Réduction de modèle basée sur des composants élémentaires pour des systèmes Thermo-Hydro-Mécaniques.

Giulia Sambataro



Thèse présentée pour obtenir le grade de

DOCTEUR
DE L'UNIVERSITÉ DE BORDEAUX

École doctorale de mathématiques et Informatique

Mathématiques appliquées et calcul scientifique

Giulia SAMBATARO

sous la direction de **Angelo IOLLO** et **Tommaso TADDEI**

Réduction de modèle basée sur des composants élémentaires pour des modèles THM.

Soutenue le 13 décembre 2022 devant le jury composé de

M. Angelo IOLLO	Professeur	Univ. Bordeaux	Directeur
M. Marc LECONTE	Ingénieur de Recherche	Andra	Invité
M. Raphaël LOUBÈRE	Directeur de Recherche	Univ. Bordeaux	Président
Mme. Cecilia PAGLIANTINI	Professeur associé	Eindhoven University of Technology	Examinatrice
M. Antoine PASTEAU	Ingénieur de Recherche	Andra	Invité
M. David RYCKELYNCK	Professeur	MINES Paristech	Rapporteur
M. Tommaso TADDEI	Chargé de Recherche	INRIA Bordeaux Sud-Ouest	Co-directeur
Mme. Irina K. TEZAUR	Directrice de Recherche	Sandia National Laboratories	Rapporteur

Component-based model order reduction procedure for large scales Thermo-Hydro-Mechanical systems

by

Giulia Sambataro

A thesis presented for the degree of
Doctor of Philosophy

Applied mathematics and scientific computing
University of Bordeaux, France

Abstract

The objective of the thesis is to develop a component-based model order reduction procedure for a class of problems in nonlinear mechanics with internal variables. The work is is motivated by applications to thermo-hydro-mechanical (THM) systems for radioactive waste disposal (this project is funded by ANDRA, the national agency for radioactive waste management). THM equations model the behaviour of temperature, pore water pressure and solid displacement in the neighborhood of geological repositories, which contain radioactive waste and are responsible for a significant thermal flux towards the Earth's surface. From a mathematical point of view, the THM system that we solve is a time-dependent and highly nonlinear coupled system; furthermore, the solution to the problem depends on several parameters, which might be related to the geometric configuration (e.g. the number of repositories, their distance or their size) or the material properties of the medium. For example, changes in the position and/or the number of the radioactive repositories might lead to significant changes in the predicted quantities of interest; we would need therefore to solve the numerical model more than once. This problem represents a *multi-query* problem and it requires the application of component-based parametrized model order reduction (CB-pMOR). First, we start from the high-fidelity finite element discretisation of the two-dimensional THM problem, we develop a monolithic projection-based ROM and we study its performance with respect to predictions. Then, we device a CB-pMOR formulation for steady problems in nonlinear mechanics. Finally, we extend the CB formulation and methodology to time-dependent nonlinear problems with internal variables, to tackle the THM problem of interest.

Keywords: model order reduction, domain decomposition, nonlinear elasticity, coupled problems.

Réduction de modèle basée sur des composants élémentaires pour des systèmes Thermo-Hydro-Mécaniques.

de

Giulia Sambataro

Thèse présentée pour obtenir le grade de
Docteur de l'Université de Bordeaux

Mathématiques appliquées et calcul scientifique
Université de Bordeaux, France

Resumé

Le travail de thèse a l'objectif de développer une procédure de réduction de l'ordre des modèles basée sur les composants pour une classe de problèmes en mécanique non linéaire avec variables internes. Le travail est motivé par des applications aux systèmes thermo-hydro-mécaniques (THM) pour le stockage des déchets radioactifs (ce projet est financé par l'ANDRA, l'agence nationale pour la gestion des déchets radioactifs). Les équations THM modélisent le comportement de la température, de la pression de l'eau interstitielle et du déplacement des solides dans le voisinage des dépôts géologiques, qui contiennent des déchets radioactifs et sont responsables d'un flux thermique important vers la surface de la Terre. D'un point de vue mathématique, le système THM que nous résolvons est un système couplé dépendant du temps et hautement non linéaire; en outre, la solution du problème dépend de plusieurs paramètres, qui peuvent être liés à la configuration géométrique (par exemple, le nombre de dépôts, leur distance ou leur taille) ou aux propriétés matérielles du milieu. Par exemple, des changements dans la position et/ou le nombre de dépôts radioactifs pourraient conduire à des changements significatifs dans les quantités prédites d'intérêt; nous aurions donc besoin de résoudre le modèle numérique plus d'une fois. Ce problème représente un problème *multi-query* et il nécessite l'application de la réduction de l'ordre des modèles paramétrés basée sur les composants (CB-pMOR). Tout d'abord, nous partons de la discrétisation par éléments finis haute-fidélité du problème THM bidimensionnel, nous développons un modèle réduit monolithique basée sur la projection de Galerkin, et nous étudions ses performances par rapport aux prédictions. Ensuite, nous proposons une formulation CB-pMOR pour des problèmes stationnaires en élasticité non linéaire. Enfin, nous étendons la formulation et la méthodologie CB aux problèmes non linéaires dépendant du temps et avec des variables internes, afin de résoudre le problème THM qui nous intéresse.

Mots clés: réduction de l'ordre des modèles, décomposition du domaine, élasticité non linéaire, problèmes couplés.

Acknowledgements

I would like to express my gratitude to Prof. Angelo Iollo and Dr. Tommaso Taddei, my research supervisors. I sincerely thank the professor for his support, encouragement and helpful criticism on this research work, and also for having created a collaborative and pleasant environment within the research team. I thank Tommaso for constantly being a trustworthy and brillant guide: his example encourages me to do my best to learn. I am grateful also for all the amount of time he dedicates to every part of my project and to my professional growth.

I would like to thank Dr. Irina Tezaur and Prof. David Ryckelynck for accepting to review my work; I also thank Dr. Cecilia Pagliantini and Dr. Loubère for accepting to participate to my examining committee.

I strongly thank Engrs. Marc Leconte and Antoine Pasteau from Andra for their kind assistance and for their trust.

A sincere thank also to Drs. Olga Mula, Angelina Roche and Robin Ryder for giving me the opportunity to collaborate to the Cemracs summer school project: it gave me the possibility to learn and appreciate new subjects in applied mathematics other than the ones related to my thesis project.

I would also like to thank my *Comité de suivi* members at the University of Bordeaux, Christelle and Dajano, for their friendly support.

Thank also to the team assistant Anne-Laure Gautier for her efficiency and to Eng. Philippe Depouilly who helped me in the setting of numerical simulations in the PlaFRim platform.

Thank to all the collegues and friends from Memphis team. I would like to include also the friends from Monc and Iop teams and also the ones from Algant group of 2021.

Thank to the new close friends I met along the way, Roberta, Kirsten and Virginie. A special thank to my long time friends Michela, Valentina and Alessandra, my dear sister and relatives.

Merci à Virginie d'avoir été mon enseignante de piano pendant ces trois dernières années. Merci pour sa sensibilité qui me touche toujours profondément, merci pour les morceaux que nous avons partagés avec dévotion et amour de la musique.

"*Là où les mots échouent, la musique parle...*"

Resumé détaillé

L'application qui motive le présent travail est la disposition et le stockage des déchets radioactifs de haute activité en milieu géologique. En France, de grandes quantités de déchets radioactifs sont générées par 1200 générateurs[1], qui comprennent des centrales nucléaires, mais aussi des universités, des hôpitaux et des centres de recherche. Cela représente une menace pour les générations actuelles et futures, car la santé humaine et l'environnement peuvent être menacés par l'émission ou la dissémination de matières radioactives.
L'Andra, — l'Agence nationale pour la gestion des déchets radioactifs[2] crée en 1979 au sein du Commissariat à l'énergie atomique (CEA)— a pour objectif de trouver, mettre en uvre et garantir des solutions sûres pour la gestion des déchets radioactifs en France. L'Andra a opté pour une solution à long terme: les conteneurs de stockage des déchets doivent isoler les matières radioactives de l'environnement jusqu'à ce que leur radioactivité ait baissé à un niveau acceptable; des conteneurs spécifiques doivent être adaptés à chaque type de déchets.

Les déchets sont stockés dans des dépôts géologiques qui sont surveillés alors que la radioactivité diminue dans le temps. La sûreté des dépôts se fonde sur trois éléments: les *packages*, les structures du dépôt (appelés *alveoli*) et le site géologique. Les colis contiennent les déchets radioactifs et sont placés à l'intérieur des alvéoles, qui sont situées horizontalement à une grande profondeur dans le sol (à environ 300 à 500 mètres); le site géologique est constitué de la région où se trouvent les alvéoles; la zone qui entoure les alvéoles constitue une barrière naturelle permanente qui empêche la propagation des déchets radioactifs. La figure 1 est une représentation schématique du stockage des déchets dans les dépôts. En raison de la température élevée des déchets

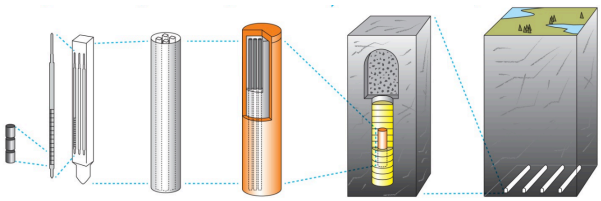

FIGURE 1: Installation en profondeur d'un stock de déchets radioactifs

radioactifs, un flux thermique est généré à l'intérieur des alvéoles: ce flux thermique entraîne ensuite la réponse mécanique et hydraulique du milieu géologique pendant plusieurs années. Ce phénomène nécessite une évaluation attentive des effets à long terme sur les zones voisines. D'un point de vue mathématique, le comportement du système est décrit par des systèmes d'équations aux dérivées partielles (EDP) couplés à grande échelle et dépendants du temps, qui prennent en compte la réponse thermique, hydraulique et mécanique du milieu géologique due à l'introduction du dépôt de déchets radioactifs.

Comme il est impossible de trouver une solution exacte pour ce système d'équations, des simulations numériques sont adoptées pour la conception et l'évaluation. La solution du problème dépend de plusieurs paramètres, qui peuvent être liés à la configuration géométrique (par exemple, le nombre d'alvéoles, leur distance ou leur taille) ou aux propriétés matérielles du milieu. Par exemple, des changements dans la position

[1] Source: "*Les essentiels de l'Inventaire national, 2019*"
[2] Site web de l'Andra: https://www.andra.fr

et/ou le nombre d'alvéoles peuvent conduire à des changements significatifs dans les quantités prédites d'intérêt telles que le déplacement de la surface terrestre environnante. Pour prendre en compte correctement l'incertitude des valeurs des paramètres, nous devons résoudre le modèle numérique pour de nombreux paramètres d'intérêt différents: ce problème est généralement appelé un problème de type *many-query*. De plus, une solution numérique efficace à ce type de problème est encore plus difficile dans un contexte *real-time*, dans lequel une solution pour des paramètres spécifiques est nécessaire rapidement.

Le problème mathématique Thermo-Hydro-Mécanique (THM) peut être écrit sous forme abstraite comme dans le système (1). Nous considérons la variable spatiale x dans le domaine de Lipschitz $\Omega \subset \mathbb{R}^d$ avec dimension $d = 2, 3$, et la variable temporelle t dans le temps $(0, T_\mathrm{f}] \subset \mathbb{R}$, où T_f est le temps final. Nous définissons en outre le vecteur de paramètres μ dans la région compacte des paramètres $\mathscr{P} \subset \mathbb{R}^P$. Étant donné un paramètre $\mu \in \mathscr{P}$, nous introduisons les variables d'état (ou primaires) $\underline{U}_\mu : \Omega \times (0, T_\mathrm{f}] \to \mathbb{R}^D$, où nous désignons par D le nombre de variables primaires; elles peuvent être considérées comme des variables qui représentent l'output d'un map paramétré de solutions évaluées à un paramètre donné $\mu \in \mathscr{P}$. Nous introduisons ensuite les variables internes (ou dépendantes) $\underline{W}_\mu : \Omega \times (0, T_\mathrm{f}] \to \mathbb{R}^{D_\mathrm{cl}}$; on denote D_cl le nombre de variables internes dans les lois de comportement dans l'équation (1); les variables internes peuvent être considérées comme des variables physiques secondaires qui contribuent à bien caractériser la dynamique physique d'un problème d'EDP donné. Nous introduisons le problème paramétré qui nous intéresse en forme abstraite: étant donné $\mu \in \mathscr{P}$, trouver $\underline{U}_\mu$ and $\underline{W}_\mu$ telle que

$$\begin{cases} \mathcal{G}_\mu(\underline{U}_\mu, \partial_t \underline{U}_\mu, \underline{W}_\mu) = 0, & \text{in } \Omega \times (0, T_\mathrm{f}], \\ \dot{\underline{W}}_\mu = \mathcal{F}_\mu(\underline{U}_\mu, \underline{W}_\mu), & \text{in } \Omega \times (0, T_\mathrm{f}], \end{cases} \tag{1}$$

avec des conditions initiales et limites appropriées. $\mathcal{G}_\mu$ est un opérateur différentiel non linéaire du second ordre dans l'espace et du premier ordre dans le temps qui est associé aux équations d'équilibre, tandis que $\mathcal{F}_\mu$ est un ensemble d'équations différentielles ordinaires (ODE) qui est associé aux lois constitutives. Nous remarquons que le système THM est hautement non-linéaire, dépendant du temps et de haute dimension; nous remarquons également qu'il appartient à une large classe de problèmes d'EDP non-linéaires non stationnaires qui sont d'un grand intérêt en mécanique des structures.

Nous considérons une approximation en dimension finie du problème (1): en fait, nous prenons un sous-espace de dimension finie $\mathcal{X}^\mathrm{hf} \subset \mathcal{X}$ de dimension N^hf. Pour résoudre le problème d'EDP discrétisé, nous utilisons la méthode des éléments finis (FE). Nous utilisons un schéma de discrétisation temporelle d'Euler implicite, avec $J_\mathrm{max} = 100$ pas de temps uniformes pour l'intervalle de temps $(0, T_\mathrm{f}]$; le caractère supérieur $(\cdot)^+$ fait référence à la nouvelle solution (au pas de temps actuel j, pour $j = 1, ..., J_\mathrm{max}$), tandis que $(\cdot)^-$ fait référence à la solution aux pas de temps précédents. Nous considérons une discrétisation par éléments finis (FE) de $\mathtt{p} = 3$ pour la composante déplacement, et une discrétisation FE de $\mathtt{p} = 2$ pour la pression et la température. Dans la figure 2 des solutions en termes de pression et de température sont représentées pour le paramètre $\mu = \bar{\mu} = [1.088 \cdot 10^3, 0.3, 21.33, 0.4558]^T$ qui est le centroïde de $\mathscr{P}$. La configuration géométrique correspond à la figure (le numéro de dépôt est $Q_\mathrm{a} = 2$).

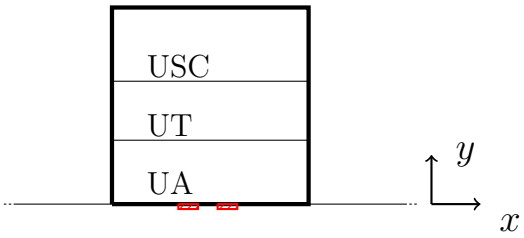

(a) configuration géométrique

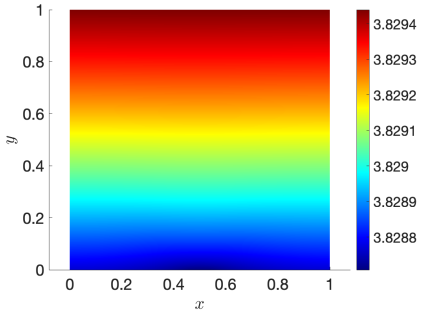

(b) $p_{\mathrm{w}}^{(J_{\max})} - p_{\mathrm{w}}^{(0)}$ [MPa]

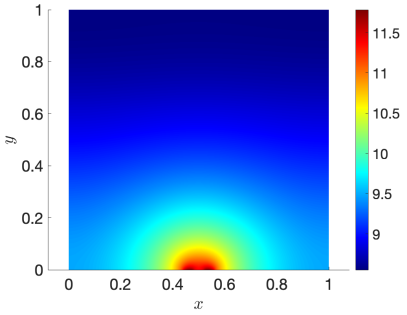

(c) $T^{(J_{\max})} - T^{(0)}$ [K]

FIGURE 2: Gaps temporels entre le temps final T_{f} et le temps initial 0 des solutions dimensionnelles en termes de pression et de température.

Les techniques de réduction de l'ordre du modèle paramétrique (pMOR) sont appliquées aux problèmes de la forme (1) pour construire un modèle de faible dimension nécessitant des temps de simulation courts et un faible stockage de données, tout en gardant sous contrôle l'erreur d'approximation entre la solution *reduced-order* et la solution *full-order* (calculée à partir d'une discrétisation haute-fidélité de l'EDP paramétrée). Les méthodes de base réduite (RB) représentent une instance particulière des modèles d'ordre réduit: la solution RB est obtenue par une *projection* (figure 3) du problème haute-fidélité sur un petit sous-espace. Cette dernière est réalisée par un petit nombre de fonctions de base globales, construites pour le problème spécifique à traiter, plutôt que par un nombre beaucoup plus important de fonctions de base.

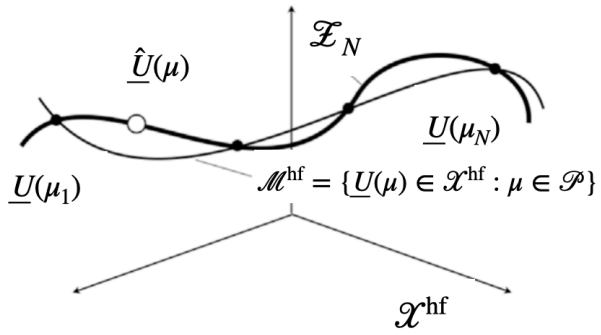

FIGURE 3: Les snapshots sur la manifold paramétrique $\mathscr{M}^{\mathrm{hf}}$ pour un cas stationnaire avec un seul paramètre ($P = 1$). Adaptation de la figure 19.2 dans [Qua17].

Les méthodes RB sont utilisées dans cette thèse dans le but de calculer, de manière peu coûteuse, une approximation à basse dimension de la solution de l'EDP.

L'élément essentiel d'une méthode RB est la procédure *offline/online*. La solution du modèle d'ordre complet est nécessaire pour quelques instances des paramètres au

cours d'une étape *offline* (également appelée *training*) exigeante en termes de calcul, afin de construire un espace réduit de solutions de base et de construire le modèle d'ordre réduit (ROM); le modèle d'ordre réduit permet une prédiction rapide du champ de solution pour de nouvelles instances des paramètres au cours de l'étape *online* (ou *prediction*).

Les choix les plus courants pour la construction de la base réduite sont les algorithmes *proper orthogonal decomposition* (POD) et *greedy*. À la base de la stratégie de découplage hors ligne/en ligne, il y a la possibilité d'exploiter une décomposition *affine* des EDP paramétrées, (au moins de manière approximative). Nous disons que $\mathcal{G}_\mu$ est paramétriquement affine si elle peut être exprimée comme la somme des coefficients dépendant des paramètres fois des formes indépendantes des paramètres, c'est-à-dire

$$\mathcal{G}_\mu(\cdot,\cdot,\cdot) = \sum_{q=1}^{Q} \Theta_{\mu,q} \mathcal{G}_q(\cdot,\cdot,\cdot) \tag{2}$$

où les coefficients $\mathbf{\Theta}_\mu$ sont des fonctions à valeur réelle dépendant du paramètre qui peuvent être facilement évaluées pour tout $\mu \in \mathcal{P}$, et $\mathcal{G}_q(\cdot,\cdot,\cdot)$, pour $q = 1,\dots,Q$, sont des formes indépendantes des paramètres. En règle générale, les premiers termes doivent être calculés pour tout paramètre donné $\mu \in \mathcal{P}$, mais les derniers termes indépendants des paramètres seront calculés et stockés une fois pour toutes pendant une étape hors ligne éventuellement coûteuse: cela rend le calcul en ligne beaucoup plus léger pour tout paramètre de test. Nous remarquons que pour l'efficacité du calcul, il est essentiel que $Q \in \mathbb{N}$ soit relativement petit. Malheureusement, la majorité des problèmes mathématiques d'intérêt, comme dans le cas du système THM dans (1), présentent une non-linéarité élevée et une dépendance paramétrique non affine, de sorte que l'approximation des résidus non linéaires $\mathcal{G}_\mu$ n'admet pas une décomposition hors ligne/en ligne efficace (en particulier, indépendante de N^{hf}). Dans ce cas, nous devons introduire un niveau supplémentaire de réduction, appelé *hyper-réduction*. Pour le formes faibles $\mathcal{G}_\mu(\cdot,\cdot)$, l'évaluation des résidus nécessite une intégration sur le domaine spatial Ω. L'objectif est d'éviter que la complexité de calcul de la ROM résultante ne se mette à l'échelle de la dimension N^{hf} de la discrétisation haute-fidélité, ce qui est, en général, prohibitif en termes de calcul. Nous aimerions obtenir un temps d'opération qui s'échelonne avec $\mathcal{O}(N)$. Nous identifions deux catégories distinctes de méthodes d'hyper-réduction. Une première catégorie commence par interpoler la forme résiduelle dans $\mathcal{G}_\mu(\cdot,\cdot)$ en utilisant des fonctions empiriques, puis elle intègre les résidus interpolés; la deuxième catégorie évalue directement les intégrales résiduelles dans $\mathcal{G}_\mu(\cdot,\cdot)$ en utilisant des règles de quadrature empiriques. La première catégorie comprend la méthode d'interpolation empirique (EIM), pour laquelle nous nous référons à [Bar+04]; la seconde comprend l'approche d'hyper-réduction de [Ryc05] (voir également [Fri+18]), la methode energy-conserving mesh sampling and weighting (ECSW) de [FCA15] et la procédure de quadrature empirique (EQP) proposée dans [YP19a], [DY22].

Comme première étape du travail, nous avons développé et validé numériquement une procédure de réduction de l'ordre du modèle basée sur la projection de Galerkin pour le système THM introduit dans l'équation (1). Nous avons appliqué avec succès le ROM au problème paramétrique THM dans un cas bidimensionnel. Nous avons proposé un indicateur d'erreur moyenné dans le temps pour piloter le training Greedy dans la phase offline, et une procédure de quadrature empirique pour réduire les coûts en ligne. Les résultats démontrent la précision du ROM avec moins de 1% (pour une dimension de l'espace réduit qui est plus de 30) sur un range de paramètres d'input prédictifs, et un facteur d'accélération de l'ordre de 10^2 fourni par le ROM par rapport aux simulations HF.

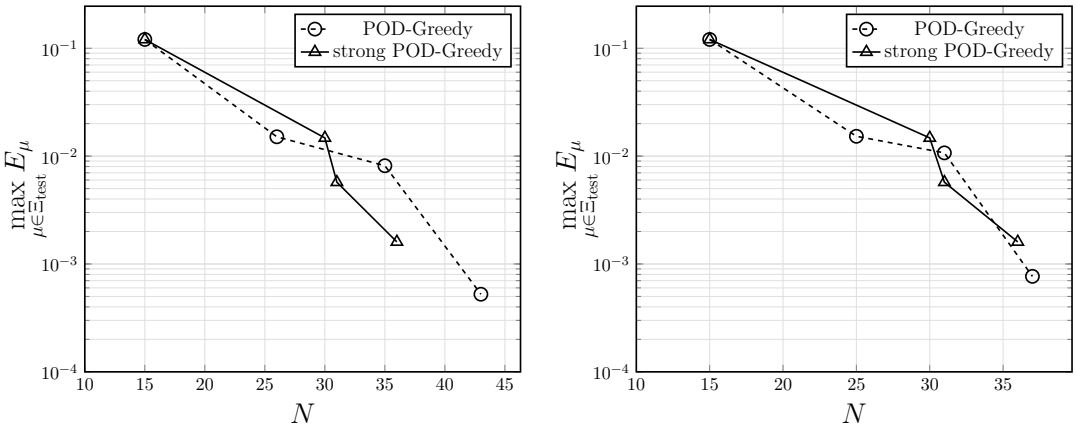

(a) H-POD Greedy (b) HA-POD Greedy

FIGURE 4: Performance out-of-sample du problème paramétrique ROM obtenu à l'aide de deux algorithmes de training (POD-Greedy et Strong POD-Greedy).

Les techniques pMOR standard reposent sur des résolutions haute-fidélité (HF) au stade de l'apprentissage, ce qui peut être inabordable pour les problèmes à très grande échelle ou dans le cas où des maillages très fins sont nécessaires pour atteindre un bon niveau de précision. En outre, les techniques pMOR standard reposent sur l'hypothèse que le champ de solution est défini sur un domaine indépendant des paramètres ou sur une famille de domaines difféomorphes. En fait, pour les systèmes comportant de nombreux paramètres géométriques, la prise en compte des changements dans la topologie du domaine nécessite des changements majeurs dans le paradigme hors ligne/en ligne de MOR.

Pour résoudre ces problèmes, plusieurs auteurs ont proposé des procédures pMOR basées sur des composants (CB), qui combinent des techniques de décomposition de domaine (DD) avec la réduction de l'ordre des modèles. Les procédures CB-pMOR visent à construire des espaces réduits locaux (dans l'espace et/ou dans le temps) qui ont un support sur une partie du domaine et à calculer une approximation globale par un couplage approprié des espaces locaux. À partir de maintenant, nous faisons référence aux méthodes pMOR standard dans un seul domaine comme l'approche *monolithique* et nous la distinguons de l'approche CB-pMOR dans laquelle la décomposition du domaine original en une partition de sous-domaines entre en jeu.

Dans la deuxième partie de la thèse, nous avons proposé une formulation CB-pMOR pour a) des EDP non linéaires stationnaires, b) des problèmes non linéaires couplés dépendants du temps. La formulation est basée sur l'overlapping de sous-domaines; elle se base sur une optimisation sous contrainte qui pénalise les sauts de solutions aux interfaces des sous-domaines. L'extension des techniques classiques de pMOR au cadre DD est conduite par l'introduction de composants *archétypes* et *instanciés*.

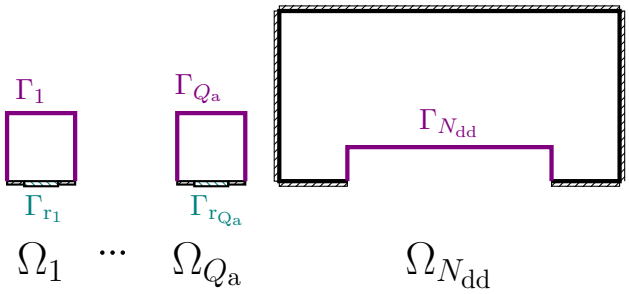

FIGURE 5: Composantes instantiées $\{\Omega_i\}_{i=1}^{N_{dd}}$ pour une valeur donnée du paramètre géométrique Q_a.

La décomposition de la solution en solutions *bubble* et *ports* et l'exploitation du principe de *static condensation* constituent un point clé pour obtenir un problème de minimisation non contraint de faible dimension.

Dans l'application de la procédure CB-pMOR à un problème d'élasticité non linéaire bidimensionnel de type neo-Hook, nous obtenons un facteur d'accélération de l'ordre de 20 par rapport à un modèle FE monolithique standard, avec une erreur de prédiction inférieure à 0.1%.

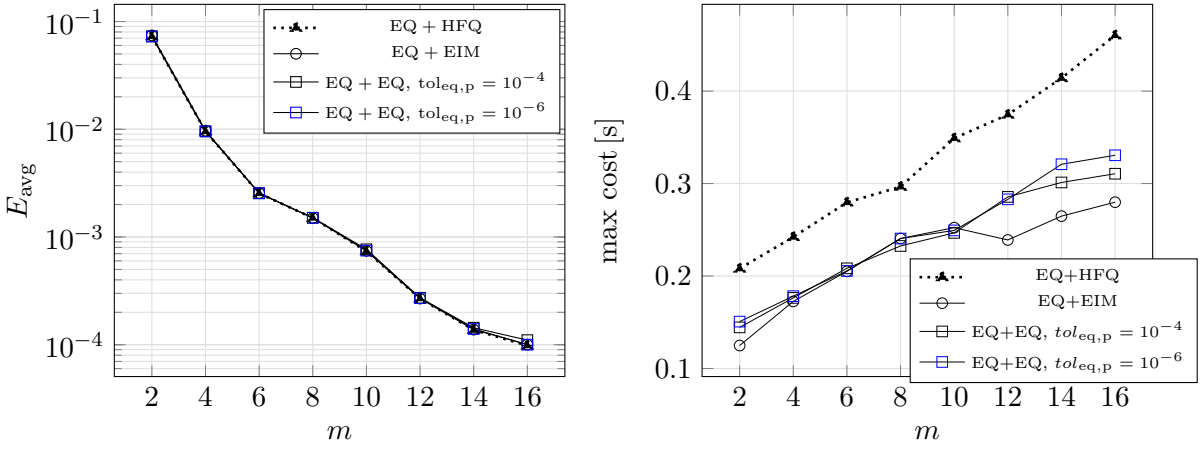

(a) (b)

FIGURE 6: hyper-réduction basée sur EIM et EQ. (a) Performance hors échantillon de la ROM OS2 hyper-réduite pour plusieurs choix de modes m, avec $n = m$. (b) Coût de calcul maximal sur l'ensemble de test. Les résultats sont basés sur la tolérance EQ $tol_{\text{eq}} = 10^{-10}$ pour les problèmes locaux et les tolérances $tol_{\text{eq,p}} = 10^{-4}$ et $tol_{\text{eq,p}} = 10^{-6}$ pour la fonction objectif (pour EQ+EQ).

Dans la troisième partie de la thèse, nous avons étendu notre formulation CB-pMOR (pour les EDP non linéaires) pour traiter le THM d'intérêt. Nous avons également exploré la performance des ROMs dans les cas out-of-sample. Nous avons doté les ROMs locales de l'hyper-réduction. Le solutions haute-fidélité sont recréées avec une erreur de prédiction de l'ordre de 0.3% ; quant à l'efficacité, notre méthode hyper-réduite réalise un bon gain en coût de calcul (de l'ordre de $13 - 22$) par rapport à une résolution monolithique pour les mêmes configurations de test out-of-sample. Nous envisageons que une implémentation basée sur la parallélisation, et une procédure EQ basée sur des points de quadrature au lieu d'éléments, peuvent apporter des facteurs d'accélération encore plus élevés.

Contents

List of Figures

List of Tables

Chapter 1

Introduction

1.1 Motivation

The application that motivates the present work is the disposal and storage of high-level radioactive waste materials in geological media. In France, large amounts of radioactive waste are generated by 1200 generators[1], which include nuclear power plants, but also universities, hospitals and research centers. This represents a concern for both present and future generations since human health and the environment may be menaced by emission or disseminaition of radioactive material.

Andra, — the French National Agency for Radioactive Waste Management[2] created in 1979 within the French Atomic Energy Commision (CEA)—has the objective of finding, implementing and guaranteeing safe solutions to radioactive waste management in France.
Andra has opted for a long-term solution: waste disposal containers must isolate radioactive materials from the environment until their radioactivity has decayed to an acceptable level; specific containers should be adapted to each particular type of waste.

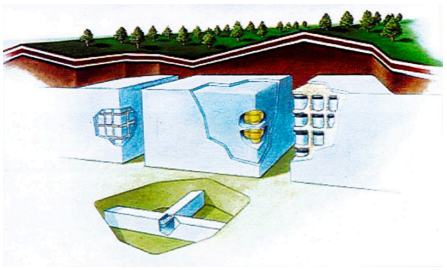

FIGURE 1.1: Multi-barrier design for a surface facility

Waste is disposed in geological repositories that are monitored while radioactivity decreases in time. Repository safety is based on three components: the *packages*, the repository structures (dubbed *alveoli*) and the geological site. The packages contain the radioactive waste and are placed inside the alveoli, which are located horizontally deep underground (at approximately 300 to 500 meters); the geological site consists in the region where the arrays of the alveoli are located; the area that surrounds the alveoli provides a permanent natural barrier that prevents the spread of radioactive waste. Figure 1.2 is a schematic representation of waste disposal in the repositories.

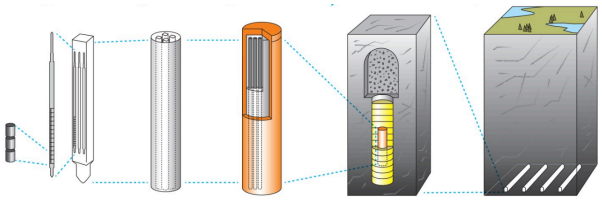

FIGURE 1.2: Multi-barrier disposal concept

[1]Source: "*Les essentiels de l'Inventaire national, 2019*"
[2]Andra website: https://www.andra.fr

Due to the large temperature of the radioactive waste, a thermal flux is generated inside the alveoli: the thermal flux then drives the mechanical and hydraulic response of the geological medium over the course of several years. This phenomenon requires a careful assessment of the long-term effects on neighboring areas. From a mathematical viewpoint, the system behaviour is described by time-dependent large scale coupled systems of partial differential equations (PDEs), which take into account the thermal, hydraulic and mechanical response of the geological medium due to the introduction of radioactive waste repository.

Since an exact solution for this system of equations is impossible to find, numerical simulations are adopted for design and assessment. The solution to the problem depends on several parameters, which might be related to the geometric configuration (e.g. the number of alveoli, their distance or their size) or to the material properties of the medium. For example, changes in the position and/or in the number of alveoli might lead to significant changes in the predicted quantities of interest such as the displacement of the surrounding Earth surface. To properly take into account uncertainty in the parameters values, we need to solve the numerical model for many different parameters of interest: this problem is usually referred to as a *many-query* problem. Furthermore, an efficient numerical solution to this type of problem is even more challenging in a *real-time* context, in which a solution for specific parameters is needed rapidly.

Standard computational methods often require prohibitively large computational costs to achieve sufficiently accurate numerical solutions for real-time, many-query applications. This is mainly due to two reasons: the high number of degrees of freedom (and of field variables) to achieve a satisfactory accuracy, and the strong coupling among nonlinear equations. The purpose of this thesis is to overcome these computational obstacles by the application of model order reduction (MOR) methods, which during the last few decades, have proved to be successful in providing low-complexity high-fidelity surrogate models that allow rapid and accurate simulations under parameter variation.

1.2 Methodology overview

The mathematical Thermo-Hydro-Mechanical (THM) problem can be written in abstract form as in system (1.1). We consider the spatial variable x in the Lipschitz domain $\Omega \subset \mathbb{R}^d$ with dimension $d = 2, 3$, and the time variable t in the time internal $(0, T_\mathrm{f}] \subset \mathbb{R}$, where T_f is the final time. We further define the vector of parameters μ in the compact parameter region $\mathscr{P} \subset \mathbb{R}^P$. Given a parameter $\mu \in \mathscr{P}$, we introduce the state (or primary) variables $\underline{U}_\mu : \Omega \times (0, T_\mathrm{f}] \to \mathbb{R}^D$, where we denote as D the number of primary variables; they can be thought of as variables that represent the output of a parametrized solution map evaluated at a given parameter $\mu \in \mathscr{P}$. We then introduce internal (or dependent) variables $\underline{W}_\mu : \Omega \times (0, T_\mathrm{f}] \to \mathbb{R}^{D_\mathrm{cl}}$, where we denote as D_cl the number of internal variables in the constitutive laws in equation (1.1); internal variables can be thought of as secondary physical variables that contribute to well characterise the physical dynamics of a given PDE problem. We introduce the parameterised problem of interest: given $\mu \in \mathscr{P}$, find $\underline{U}_\mu$ and $\underline{W}_\mu$ such that

$$\begin{cases} \mathcal{G}_\mu(\underline{U}_\mu, \partial_t \underline{U}_\mu, \underline{W}_\mu) = 0, & \text{in } \Omega \times (0, T_\mathrm{f}], \\ \dot{\underline{W}}_\mu = \mathcal{F}_\mu(\underline{U}_\mu, \underline{W}_\mu), & \text{in } \Omega \times (0, T_\mathrm{f}], \end{cases} \tag{1.1}$$

with suitable initial and boundary conditions.
Here, $\mathcal{G}_\mu$ is a nonlinear second-order in space, first-order in time differential operator

that is associated with the equilibrium equations, while $\mathcal{F}_\mu$ is a set of ordinary differential equations (ODEs) that is associated with the constitutive laws: we specify the operators $\mathcal{G}_\mu$ and $\mathcal{F}_\mu$ for the problem of interest in chapter 3. We remark that the THM system is highly nonlinear, time-dependent and high-dimensional; also, we remark that it belongs to a large class of nonlinear unsteady PDE problems which is of broad interest in structural mechanics.

We consider a finite dimensional approximation of problem (1.1): indeed, we take a finite dimensional subspace $\mathcal{X}^{\text{hf}} \subset \mathcal{X}$ of dimension N^{hf}. We refer to this approximation as *high-fidelity* discretization; to solve the discretized PDE problem we employ the finite-element (FE) method, which is the most popular discretization technique for structural engineering design and analysis.

Parametric model order reduction (pMOR) techniques are applied to problems of form (1.1) to construct a model of low dimension requiring short simulation times and low data storage, but still keeping the approximation error between the *reduced-order* solution and the so called *full-order* one (computed from a high-fidelity discretization of the parametrized PDE) under control. Reduced basis (RB) methods represent a particular instance of reduced order models: the RB solution is obtained through a *projection* of the high-fidelity problem onto a small subspace. This latter is made by a small number of global basis functions, constructed for the specific problem at hand, rather than by a much larger number of basis functions. RB methods are used overall this thesis with the aim of computing, in a cheap way, a low-dimensional approximation of the PDE solution. Many works are associated with projection-based model order reduction: we cite, without any purpose of completeness, [HRS+16; QMN15] and [RHP08].

The essential constituent of a RB method is the *offline/online* procedure. The solution to the full-order model is needed for a few instances of the parameters during a computationally demanding *offline* stage (also called *training* stage), in order to construct a reduced space of basis solutions and to build the reduced order model (ROM); the constructed ROM enables rapid predictions of the solution field for new instances of the parameters during the *online* (or *prediction*) stage. Figure 1.3 schematically illustrates the use of ROMs to run faster reduced-order simulations for new parameters with respect to the use of full-order models.

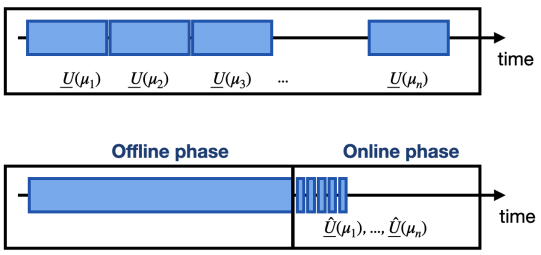

FIGURE 1.3: Comparison between simulations time with a full-dimensional model (at the top) and a reduced model (at the bottom).

The most common choices for the construction of the reduced basis are the *proper orthogonal decomposition* (POD) and the *greedy* algorithms. POD is also popular in multivariate statistical analysis, where it is called *principal component analysis*, or in the theory of stochastic processes under the name of *Karhunen-Loève* decomposition, see e.g., [LK10; GWZ14]; we refer also to [Aub91; BHL93] for the first applications of POD in scientific computing, in particular in the simulation of turbulent flows, and to [BBI09; Vol11] for more recent works. The Greedy method, which was originally

introduced in [Pru+02; Ver+03], is based on the idea of constructing the reduced basis space in an offline iterative procedure which requires at each step a maximization of the current error over the parameter space. For the purpose of numerical computation, this maximization is performed over a finite training set obtained through a discretization of the parameter set. In chapter 2 we explain the construction of a RB approximation by both POD and greedy methods. Also, in chapter 2 we explain all the features that better characterize RB methods; as a starting point, the high-fidelity discretization of the parametrized PDE, then the Galerkin projection and the derivation of a priori/a posteriori error bounds for the error between the solution obtained by a full-order model and a reduced-order model.

At the foundation of the offline/online decoupling strategy there is the possibility to exploit an *affine* decomposition of parametrized PDEs, (at least in an approximate way). We say that $\mathcal{G}_\mu$ is parametrically affine if it can be expressed as the sum of parameter-dependent coefficients times parameter-independent forms, i.e.

$$\mathcal{G}_\mu(\cdot,\cdot,\cdot) = \sum_{q=1}^{Q} \Theta_{\mu,q}\mathcal{G}_q(\cdot,\cdot,\cdot), \tag{1.2}$$

where coefficients $\boldsymbol{\Theta}_\mu$ are parameter-dependent real-valued functions that can be readily evaluated for any $\mu \in \mathscr{P}$, and $\mathcal{G}_q(\cdot,\cdot,\cdot)$, for $q = 1,\dots,Q$, are parameter-independent forms. As a general principle, former terms have to be computed for any given parameter $\mu \in \mathscr{P}$, but the latter parameter-independent terms will be computed and stored once and for all during a possibly expensive offline stage: this makes online computation much lighter for any test parameter. We notice that for computational efficiency it is critical that $Q \in \mathbb{N}$ is relatively small. The decomposition (1.2) is possible, for example in the case of elliptic PDEs that are at most quadratically nonlinear in the solution U_μ: the computational cost for the online stage depends on the dimension of the reduced-basis space, which is typically small, and on Q, but it is independent of the dimension N^{hf} of the underlying high-fidelity finite element approximation. Unfortunately, the majority of mathematical problems of interest, as in the case of the THM system in (1.1), feature a high nonlinearity and a nonaffine parametric dependence, so that the approximation of nonlinear residuals $\mathcal{G}_\mu$ does not admit an efficient (in particular, a N^{hf}-independent) offline/online decomposition. In this case we must introduce a further level of reduction, called *hyper-reduction*. In chapter 2, we provide a detailed description of two hyper-reduction techniques.

As just mentioned, standard pMOR techniques rely on high-fidelity (HF) solves at the training stage, which might be unaffordable for very large-scale problems or in the case where very fine meshes are needed to reach a good level of accuracy. Furthermore, standard pMOR techniques rely on the assumption that the solution field is defined over a parameter-independent domain or over a family of diffeomorphic domains. In fact, for systems with many geometric parameters, dealing with changes in domain topology requires major changes to the offline/online paradigm of MOR.

To provide a concrete example, let us consider a PDE problem as in form (1.1) to be solved in a domain as the one in figure 1.4, in which the red boundaries model the presence of radioactive waste repositories and are associated with a certain type of boundary condition in problem (1.1).

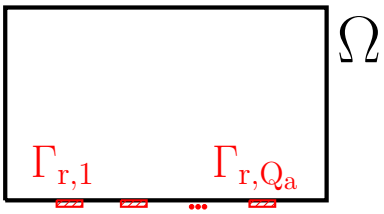

FIGURE 1.4: Domain Ω and boundaries $\Gamma_{\mathrm{r},1}, \ldots, \Gamma_{\mathrm{r},Q_\mathrm{a}}$ that can vary in number and position.

Despite its simplicity, if the position and/or the number of the repositories — which we denote as Q_a — change, the solution to problem (1.1) becomes prohibitive for the standard ROMs introduced so far: if the number of repositories is sufficiently large, we would indeed end-up with a very high-dimensional parametrization, which would require several full-order solves. Furthermore, solutions for different numbers of repositories are defined over different meshes and satisfy different sets of boundary conditions: therefore, they cannot be considered into a single reduced space. Figure 1.5 shows two example of domains defined by two different geometric configurations.

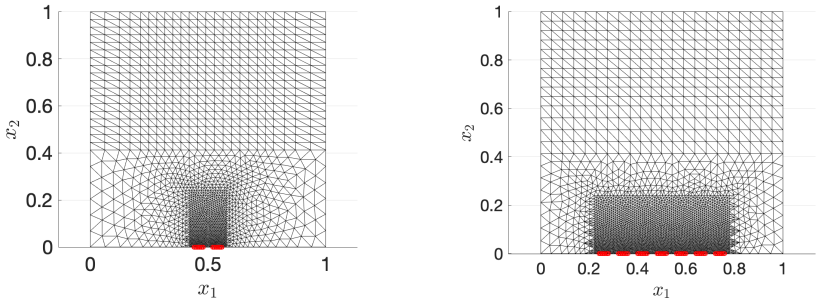

FIGURE 1.5: Two computational domains defined by two different values of geometric parameter Q_a.

To address these issues, several authors have proposed component-based (CB) pMOR procedures, which combine domain decomposition (DD) techniques with model order reduction. CB-pMOR procedures aim to construct local (in space and/or in time) reduced spaces that have support on a portion of the domain and compute a global approximation by suitable coupling of the local spaces. From now on, we refer to the standard pMOR methods in a single domain as the *monolithic* approach and we distinguish it from the CB-pMOR approach in which the decomposition of the original domain into a partition of subdomains comes into play.

CB-pMOR strategies consist of two distinct building blocks: (i) a rapid and reliable DD strategy for online global predictions, and (ii) a localized training strategy exclusively based on local solves for the construction of the local reduced bases. In this work, in particular in chapters 5 and 6, we focus exclusively on the first area of research (i). We refer to [BP22; ST22] and [HCC21, section 8.1.7] for recent works on localized training for nonlinear elliptic PDEs. We propose in chapter 5 and chapter 6 a general component-based pMOR procedure for steady and unsteady problems, respectively. In this work, the domain decomposition is based on *overlapping* subdomains: as we show in chapter 5, overlapping domain decomposition methods feature a simplified imposition of the continuity conditions of solutions at the interface boundaries among subdomains. Therefore, it is desirable in the case of non-linear problems requiring demanding implementations.

The adoption of a component-based reduction method requires a suitable adaptation of the offline/online decomposition introduced so far, since the MOR methodology has to be extended to a component-based framework. The key point of the CB-pMOR approach we use in this work is the concept of *archetype* and *instantiated* domains. Archetype components are reference components which are built for a certain user-defined fixed value of geometric parameters. The instantiated components are the actual components which are created for each parameter of interest; they are connected through predefined interface boundaries (or faces) named *ports* to form a global synthesized system. We could also think of the concept of archetype and instantiated components by using an analogy with the principle of object-oriented programming: archetype components would play the role of classes, user-defined data types that act as the blueprint for individual objects (which represent the instantiated components). Using this analogy, we could say that the components that form a global system are instances (of archetype components, designed as classes) created with specifically defined geometric data.
Considering the global system in figure 1.4, we identify two archetype components, depicted in figure 1.6: the first component in 1.6(a) refers to a generic region close to a repository, while component in 1.6(b) can be interpreted as a generic portion of the interior of the domain or of the boundary without the repository boundary. Port boundaries are depicted in purple for each archetype component and denoted as $\Gamma^{\mathrm{a}}_{\mathrm{int}}$ and $\Gamma^{\mathrm{a}}_{\mathrm{ext}}$.

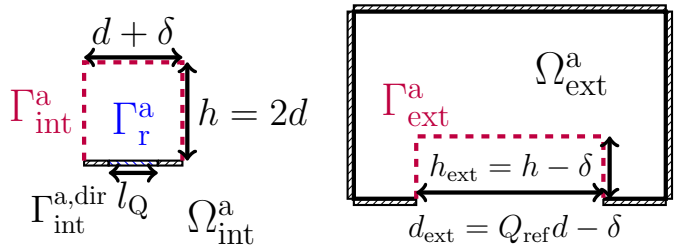

(a) "internal" archetype component (b) "external" archetype component

FIGURE 1.6: Example of archetype components for the global system in figure 1.4.

Given a library of archetype components and given a new system configuration (in our case determined by the geometric parameter Q_{a}), we can generate the full system by creating instantiations of the archetype components. In figure 1.7 the global domain Ω is decomposed into an overlapping partition $\{\Omega_i\}_{i=1}^{N_{\mathrm{dd}}}$ for a given value of the geometric parameter Q_{a}; next to the instantiated subdomains, the corresponding "internal" and the "external" archetype components are depicted.

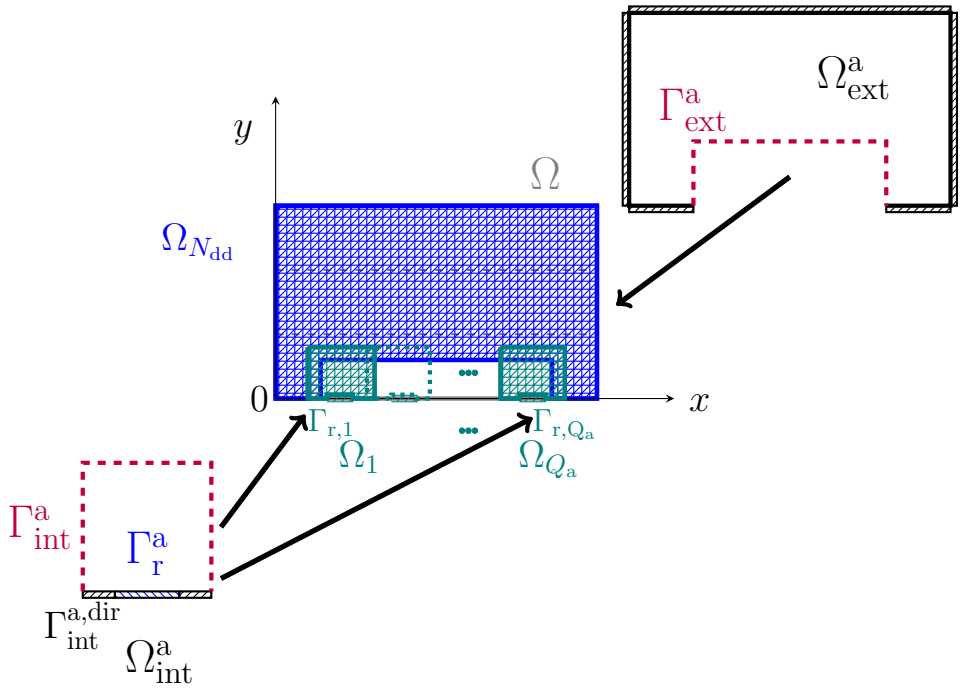

FIGURE 1.7: Instantiated components $\{\Omega_i\}_{i=1}^{N_{\mathrm{dd}}}$ for a given value of geometric parameter Q_{a}.

The offline/online MOR subdivision which was introduced in the case of monolithic ROM would be substantially adapted as follows.

1. During the offline stage, a library of archetype components is defined and local reduced-order bases (ROBs) and local ROMs are built; this stage requires HF solves and may thus be relatively expensive, but it is carried out only once as a library preprocessing step.

2. During the online stage, local components are instantiated to form the global system and the global solution is estimated by coupling local ROMs. In this stage, the user may instantiate any of the archetype components and assign to each component instantiation the desired parameter values; this phase is supposed to be much less expensive.

In chapter 5 we explain the development of the CB-pMOR procedure proposed in this work: we describe the component-based formulation of a preliminary PDE problem and we show how the identification of port edges in the instantiated components plays a key role in enabling the decomposition of solutions and in guaranteeing the efficiency of the whole CB-pMOR method.

1.3 Objectives of this work

The aim of this thesis work is the development of a CB-pMOR procedure for THM systems. The application of a CB-pMOR approach to problems of the form (1.1) requires a significant effort in terms of choice and adaptation of methods and in terms of numerical implementation. To proceed while keeping the degree of difficulty under control, this work is divided into three main phases in the following way.

I. First, a projection-based monolithic MOR technique is developed for problems of the form (1.1) with particular emphasis on THM systems that are fully described

in chapter 3. The approach is characterised by an offline/online splitting to reduce the *marginal* cost (that is the cost in the limit of many queries), and it relies on Galerkin projection to devise a reduced-order model (ROM), which is built by an adaptive sampling to reduce offline training costs; furthermore, we rely on hyper-reduction to speed up the assembly of the ROM during the online stage.

II. Second, we design a CB-pMOR formulation for parametrized nonlinear elliptic PDEs based on overlapping subdomains. To validate the methodology, a preliminary test case is used: all the numerical investigations are made for a two-dimensional neo-Hookean nonlinear mechanics problem that shares the same geometric configuration (depicted in figure 1.6) with the THM problem studied in the first part of the work.

III. Third, the CB-pMOR methodology proposed in the second part is extended to the THM system, which is fully described in chapter 3. This part of the work requires the adaptation of the techniques presented in the second part to the case of coupled, non-stationary problems with internal variables of the form (1.1). Also in this part all the methods are validated by numerical investigations.

1.4 Contributions of the thesis

The contributions of the present thesis are summarized as follows:

- the development of a POD-Greedy technique for coupled problems with internal variables, in the context of projection-based MOR. In particular, we develop a time-average a posteriori error indicator, a greedy sampling (based on the proposed indicator) and a hyper-reduction technique based on an element-wise empirical quadrature procedure;
- the development of a new CB-pMOR formulation for parametrized PDEs based on overlapping subdomains; this part is completed by the theoretical discussion of the well-posedness of the CB mathematical formulation and the a priori error analysis for linear coercive problems;
- the adaptation of the proposed CB formulation to unsteady coupled problems with internal variables.

1.5 Structure of the thesis

In addition to the introductory and concluding chapters, this manuscript consists of five main chapters organized as follows.

1. Chapter 2 provides an overview of the model order reduction framework that is later employed and further developed in the remainder of the thesis for the construction of ROMs. In particular, we introduce the POD, the greedy method for stationary problems (and the POD-greedy); we also present the Galerkin projection method used during the training and prediction stages, respectively. In addition, we present hyper-reduction techniques to deal with nonlinear problems and a rapid and reliable error indicator to be used in the training phase.
2. In chapter 3 we present in more details the THM problem: we describe the physical assumptions that are used to derive the model; we present the mathematical formulation and its numerical finite-element discretization; we also show the solution field for a fixed parametric configuration.

3. The first contribution of this thesis is presented in chapter 4, where we develop a projection-based monolithic MOR procedure for the THM system.

4. In chapter 5 the second contribution of the thesis is presented: a general CB-pMOR procedure for steady PDEs based on overlapping subdomains.

5. In chapter 6 the component-based approach presented in chapter 5 is extended to problems of the form (1.1). This represents the last contribution of this thesis.

Chapter 2

Model order reduction methods

In this chapter we present in a self-contained way the main features of model order reduction methods that are applied in this thesis; methodology sections in chapters 4, 5 and 6 show the careful adaptation of this general methodology to handle challenging applications in different contexts: in chapter 4, to handle coupled problems with internal variables, and in chapters 5 and 6 in a CB setting.

2.1 Galerkin ROMs for unsteady PDEs

2.1.1 Problem formulation

We introduced the physical domain Ω and the temporal interval $(0, T_\mathrm{f}]$ at the beginning of section 1.2. We denote as $(\mathcal{X}, \|\cdot\|)$ a suitable Hilbert space defined in Ω; we consider $H^1_0(\Omega) \subset \mathcal{X} \subset H^1(\Omega)$. By (w, v), we denote the inner product in $\mathcal{X}$ for all $w, v \in \mathcal{X}$, and by $\|w\| = \sqrt{(w, w)}$ its induced norm for all $w \in \mathcal{X}$. We denote by $\mathcal{X}'$ the dual space of $\mathcal{X}$.
To present the pMOR methodology that is considered in this work, we focus on a parabolic problem in variational form. We denote as $\mathcal{X}_0$ the test set such that $\mathcal{X}_0 = \{v \in \mathcal{X} : v|_{\Gamma_\mathrm{dir}=0}\}$, where Γ_dir denotes the portion of the boundary associated with Dirichlet boundary conditions and $g_\mathrm{dir} \in H^{1/2}(\Gamma_\mathrm{dir})$; we denote the time derivative as $\partial_t u_\mu = \frac{\partial u}{\partial t} \in L^2(0, T_\mathrm{f}; \mathcal{X}_0^{-1})$.

We consider problems of the form: find $u_\mu \in C^0(0, T_\mathrm{f}; L^2(\Omega)) \cap L^2(0, T_\mathrm{f}; \mathcal{X})$ s.t.

$$(\partial_t u_\mu, v)_{L^2(\Omega)} + \mathcal{G}_\mu(u_\mu, v) = 0 \ \ \forall v \in \mathcal{X}_0, \tag{2.1}$$

with suitable initial and boundary conditions: $u_\mu(x, 0) = u_0$ for $(x, \mu) \in \Omega \times \mathcal{P}$, and $T_0 u_\mu = g_\mathrm{dir}$. Here, $T_0 : \mathcal{X} \to H^{1/2}(\Gamma_\mathrm{dir})$ is the trace operator such that $T_0 v = v|_{\Gamma_\mathrm{dir}}$ for all $v \in \mathcal{X} \cap C^0(\bar{\Omega})$; to simplify the presentation, we consider a parameter and time independent Dirichlet datum. We recall that the parameter μ belongs to a compact parameter region $\mathcal{P} \subset \mathbb{R}^P$, with $P \geq 1$, as introduced in section 1.2. Here, $\mathcal{G} : \mathcal{X} \times \mathcal{X}_0 \times \mathcal{P} \to \mathbb{R}$ is a linear or nonlinear parametrized variational form, which we suppose to be time-invariant: the definition of $\mathcal{G}_\mu$ for the THM system is specified in the following chapter 3.

2.1.2 High-fidelity discretization

We introduce the time grid $0 = t^{(0)} < t^{(1)} < \ldots < t^{(J_\mathrm{max})} = T_\mathrm{f}$ such that $t^{(j)} = j\Delta t$. Given the domain $\Omega \in \mathbb{R}^\mathrm{d}$, we define the triangulation $\{\mathtt{D}_k\}_{k=1}^{N_\mathrm{e}}$, where N_e denotes the total number of elements, the nodes $\{x_j^\mathrm{hf}\}_{j=1}^{N^\mathrm{hf}}$ and the connectivity matrix $\mathtt{T} \in \mathbb{N}^{N_\mathrm{e}, n_\mathrm{lp}}$ such that $\mathtt{T}_{k,i} \in \{1, \ldots, N^\mathrm{hf}\}$ is the index of the i-th node of the k-th element of the mesh and n_lp is the number of degrees of freedom in each element. The high-fidelity

space $\mathcal{X}^{\text{hf}}$ is defined in the following way:

$$\mathcal{X}^{\text{hf}} := \text{span}\{\zeta_i \mathbf{e}_j \; i = 1, \dots, N^{\text{hf}}, j = 1, \dots, D\}$$

where $\{\zeta_i\}_{i=1}^{N^{\text{hf}}}$ is the continuous Lagrangian FE basis. Given $v \in \mathcal{X}^{\text{hf}}$, we denote by $\mathbf{v}$ the corresponding FE vector. We remark that $\mathcal{X}^{\text{hf}}$ is a finite dimensional space, although high-dimensional: the solution in $\mathcal{X}^{\text{hf}}$ obtained by a high-fidelity discretization of (2.1) is assumed to be a sufficiently accurate approximation to $u_\mu \in \mathcal{X}$ solving (2.1). We consider the simplest case in which the number D of state variables is equal to one; in chapters 3 and 4 we extend the definitions to the case $D > 1$ which corresponds to vector-valued state variables. The elemental restriction operator $\mathbf{E}_k : \mathbb{R}^{N^{\text{hf}}} \to \mathbb{R}^{n_{\text{lp}}}$ is defined as

$$\left(\mathbf{E}_k \mathbf{u}_\mu^{(j)}\right)_i = u_\mu^{(j)}(x^{\text{hf}}_{\mathtt{T}_{k,i}}), \quad i = 1, \dots, n_{\text{lp}}, \; k = 1, \dots, N_{\text{e}}. \tag{2.2a}$$

Furthermore, we introduce the quadrature points $\{x^{\text{hf,q}}_{q,k}\}_{q,k} \subset \Omega$, such that $x^{\text{hf,q}}_{q,k}$ is the q-th quadrature point of the k-th element of the mesh, with $q = 1, \dots, n_{\text{q}}$, and the operators $\mathbf{E}^{\text{qd}}_k : \mathbb{R}^{N^{\text{hf}}} \to \mathbb{R}^{n_{\text{q}}}$ and $\mathbf{E}^{\text{qd},\nabla}_k : \mathbb{R}^{N^{\text{hf}}} \to \mathbb{R}^{n_{\text{q}},d}$ such that

$$\left(\mathbf{E}^{\text{qd}}_k \mathbf{u}_\mu^{(j)}\right)_q = u_\mu^{(j)}(x^{\text{hf,q}}_{q,k}), \quad \left(\mathbf{E}^{\text{qd},\nabla}_k \mathbf{u}_\mu^{(j)}\right)_{q,i} = \frac{\partial}{\partial x_i} u_\mu^{(j)}(x^{\text{hf,q}}_{q,k}), \tag{2.2b}$$

where $q = 1, \dots, n_{\text{q}}$, $k = 1, \dots, N_{\text{e}}$ and $i = 1, \dots, d$.

We denote by $\{u_\mu^{(j)}\}_{j=1}^{J_{\max}}$ the high-fidelity solution trajectory for the parameter $\mu \in \mathcal{P}$; $u_\mu^{(j)}$ is an approximation of the true solution at time $t^{(j)}$ and for $\mu \in \mathcal{P}$. Notice that script hf is neglected in the solution for a matter of simplicity in the notation. If we resort to an implicit Euler time scheme, the high-fidelity discretization of problem (2.1) can be written as follows: for $j = 1, \dots J_{\max}$ find

$$\begin{cases} \left(\frac{\mathbf{u}_\mu^{(j)} - \mathbf{u}_\mu^{(j-1)}}{\Delta t}, \mathbf{v}\right)_{L^2(\Omega)} + \mathcal{G}_\mu\left(\mathbf{u}_\mu^{(j)}, \mathbf{v}\right) = 0 \;\; \forall v \in \mathcal{X}_0^{\text{hf}}, \\ \mathbf{u}_\mu^{(j)}\left(\mathtt{I}_{\text{dir}}, t^{(j)}\right) = \mathbf{g}_{\text{dir}}, \\ \mathbf{u}_\mu(\cdot, 0) = \mathbf{u}_0, \end{cases} \tag{2.3}$$

where $\mathbf{g}_{\text{dir}} \in \mathbb{R}^{|\mathtt{I}_{\text{dir}}|}$ is the Dirichlet datum, $\mathtt{I}_{\text{dir}} \subset \{1, \dots, N^{\text{hf}}\}$ are the indices associated with Dirichlet boundary Γ_{dir} and $\mathcal{X}_0^{\text{hf}} = \{v \in \mathcal{X}^{\text{hf}} : \mathbf{v}(\mathtt{I}_{\text{dir}}) = \mathbf{0}\}$. Notice that the discussion can be trivially extended to other time discretization schemes; nevertheless, in this work, we exclusively consider the implicit Euler method for time discretization. Once introduced the high-fidelity discretization of problem (2.1), we can define the *solution manifold* as the set of high-fidelity solutions for all values of the parameter μ in the parameter domain $\mathcal{P}$:

$$\mathcal{M} = \{u_\mu^{(j)} \in \mathcal{X}^{\text{hf}} : \mu \in \mathcal{P}, j \in \{1, \dots, J_{\max}\}\} \subset \mathcal{X}^{\text{hf}}. \tag{2.4}$$

We can possibly restrict the solution trajectories to the set of sampling times that we denote as $\mathtt{I}_s$. The definition presented in (2.4) is an important concept since the ROMs aim at finding reduced solutions that approximate the high-fidelity solution manifold defined in (2.4). The high-fidelity solutions found for a suitably chosen finite sample of parameters $\Xi_{\text{train}} = \{\mu_1, \dots, \mu_{n_{\text{train}}}\}$ and times in $\mathtt{I}_s$ are called *snapshots*: they form the set

$$\mathcal{M}_{\text{train}} = \{u_\mu^{(j)} \in \mathcal{X}^{\text{hf}} : \mu \in \Xi_{\text{train}}, j \in \mathtt{I}_s \subset \{1, \dots, J_{\max}\}\} \tag{2.5}$$

and they are used to generate an N-dimensional reduced basis. We remark that the solution of the high-fidelity discretization (2.3) might be potentially very expensive since a large number of degrees of freedom N^{hf} might be needed to achieve a sufficiently accurate approximation of the continuous solution of (2.1). This ends up in a large computational cost if the solution needs to be estimated for many parameter values. The reduced basis method seeks to speed up computations in the limit of many queries without sacrificing the accuracy with respect to the high-fidelity solution.

2.1.3 Reduced Basis method

As pointed out in the introduction section in chapter 1, the reduced basis (RB) method is adopted in this work to accurately and efficiently generate an approximate solution to a parametrized PDE as the one in (2.1). That reduced solution is typically obtained in a subspace that approximates the solution manifold $\mathcal{M}$. A low number $N \ll N^{\text{hf}}$ of problem-dependent basis functions $\{\zeta_n\}_{n=1}^N$ is generated from a suitable set of snapshots. The associated reduced basis space is given by $\mathcal{Z}_N = \text{span}\{\zeta_1, \dots, \zeta_N\} \subset \mathcal{X}^{\text{hf}}$. For now, we consider the reduced basis space $\mathcal{Z}_N$ as given; in section 2.2, we describe different techniques commonly used for its costruction during the offline stage, and in 2.3 how to efficiently recover the reduced basis solution during the online stage. To simplify notation, we now denote as $\mathfrak{u}_\mu = \{u_\mu^{(j)}\}_{j=1}^{J_{\max}}$ the trajectories associated with the high-fidelity snapshots at all time steps for a given parameter $\mu \in \mathcal{P}$. The approximate solution at computation times $j = 1, \dots, J_{\max}$ is denoted by $\hat{\mathfrak{u}}_\mu = \{\hat{u}_\mu^{(j)}\}_{j=1}^{J_{\max}} \subset \mathcal{Z}_N$. For each parameter $\mu \in \mathcal{P}$ and each time index $j = 1, \dots, J_{\max}$, the ansatz of problem (2.1) has the following form:

$$\hat{u}_\mu^{(j)} = Z_N \alpha_\mu^{(j)} = \sum_{n=1}^{N} \left(\alpha_\mu^{(j)}\right)_n \zeta_n. \tag{2.6}$$

The summation is done over $N \ll N^{\text{hf}}$; the real-valued time and parameter-dependent coefficients $\{\alpha_\mu^{(j)}\}_{j \in \mathtt{I}_s}$ are called *reduced solutions*, with $\alpha_\mu^{(j)} : \mathcal{P} \to \mathbb{R}^N$.

We notice that operator $Z_N : \mathbb{R}^N \to \mathcal{Z}_N = \text{span}\{\zeta_n\}_{n=1}^N$ is linear; indeed, in this work, we restrict ourselves to *linear approximation* methods. In order to establish whether the manifold $\mathcal{M}$ can be accurately approximated using a low-dimensional linear space $\mathcal{Z}_N$, we need to introduce the notion of *Kolmogorov n-width* $d_n(\mathcal{M})$.

The Kolmogorov n-width measures the reconstruction performance of the optimal n-dimensional linear space $\mathcal{Z}_n \subset \mathcal{X}^{\text{hf}}$: it measures the best achievable accuracy in the $\mathcal{X}^{\text{hf}}$ norm when all possible elements are approximated by elements in a n-dimensional subspace $\mathcal{Z}_n \subset \mathcal{X}^{\text{hf}}$; it is defined in the following way:

$$d_n(\mathcal{M}) := \inf_{\substack{\mathcal{Z}_n \subset \mathcal{X}^{\text{hf}}, \\ \dim(\mathcal{Z}_n) = n}} \sup_{u_\mu \in \mathcal{M}} \inf_{v_n \in \mathcal{Z}_n} \|u_\mu - v_n\|. \tag{2.7}$$

The faster the decay in the Kolmogorov $n-$width with n, the better is the approximability of a solution manifold in a n-dimensional linear space. For a wide range of parameterized elliptic and parabolic problems, the Kolmogorov $n-$ width often decays exponentially, allowing for (acceptably) low-dimensional and accurate linear approximations. In the numerical applications in this work we rely on linear compressibility of the solution manifold. We observe that theoretical considerations on the behaviour of the Kolmogorov n-width are limited to some types of parametrized solution mappings, in particular analytic or nonlinear olomorphic mappings (we refer to [QMN15] and [CD16]).

There is an alternative class of methods, called *nonlinear approximation* methods, which rely on approximations that do not come from linear spaces but rather from nonlinear manifolds (the application of these methods is beyond the scope of this thesis; we cite [IL14], [LC20] and [Tad20]).

The offline/online decomposition presented in algorithm 1 aims at reducing the marginal (in the sense of many queries) cost associated with the solution to (2.3). Several issues should be addressed. First, we should discuss how to choose *training*

Algorithm 1 The RB method: offline/online decomposition

Offline stage:

1: compute $\mathfrak{u}_{\mu_1}, \dots \mathfrak{u}_{\mu_{n_{\text{train}}}}$ using a FE solver;

2: construct the reduced space $\mathcal{Z}_N = \text{span}\{\zeta_n\}_{n=1}^N$;

3: compute and store online structures;

Online stage: for a given $\bar{\mu} \in \mathcal{P}$

4: compute $\hat{\mathfrak{u}}_{\bar{\mu}}$ by solving a suitable ROM;

5: estimate the error between $\mathfrak{u}_{\bar{\mu}}$ and $\hat{\mathfrak{u}}_{\bar{\mu}}$.

parameters in $\Xi_{\text{train}} = \{\mu_1, \dots, \mu_{n_{\text{train}}}\} \subset \mathcal{P}$, and build the reduced space $\mathcal{Z}_N$ based on the snapshots sets $\{\mathfrak{u}_{\mu_1}, \dots \mathfrak{u}_{\mu_{n_{\text{train}}}}\}$. Second, we should discuss how to efficiently compute the solution $\hat{\mathfrak{u}}_\mu$ for a given $\mu \in \mathcal{P}$. Third, we should discuss how to rapidly and accurately estimate the error. In the numerical simulations, we consider the error metric $L^2(0, T_\text{f}; \mathcal{X}^{\text{hf}})$, which we define as follows:

$$E_\mu := \frac{\left\|\hat{\mathfrak{u}}_\mu - \mathfrak{u}_\mu\right\|_J}{\left\|\mathfrak{u}_\mu\right\|_J}. \tag{2.8}$$

where

$$\|\mathfrak{v}\|_J = \sqrt{\sum_{j=1}^{J_{\max}} (t^{(j)} - t^{(j-1)}) \|v^{(j)}\|^2}, \quad \forall \mathfrak{v} = \{v^{(j)}\}_{j=1}^{J_{\max}}.$$

Note that $\|\cdot\|_J$ is an approximation of the norm $L^2(0, T_\text{f}; \mathcal{X}^{\text{hf}})$. The just mentioned three issues, which could be referred to as "reduced space construction", "reduced formulation" and "*a posteriori* error estimation", are discussed in sections 2.2, 2.3 and 2.4, respectively.

2.2 Construction of the reduced space

In this section we should address the issue of i) sampling the parametric space $\mathcal{P}$ in order to select suitable training parameters; ii) constructing the reduced basis from a given set of snapshots. A greedy approach explained in section 2.2.1 is often used for point i), while among data compression techniques we use proper orthogonal decomposition (POD) method, illustrated in section 2.2.2. The time-dependent nature of problems (2.3) requires some adaptations of the methods that are used to tackle both parameters selection and data compression. Indeed, application of POD to time-parameter manifolds might end up in very high-dimensional data structures; moreover, to obtain the snapshots for a fixed parameter μ, a complete time-trajectory needs to be computed and suitable time instants need to be selected. A convenient approach consists in suitably combining the greedy method with POD in the so-called *POD-greedy* procedure; we provide details about the POD-greedy in section 2.2.3.

2.2.1 Greedy algorithm

For time-dependent PDEs, the underlying idea of the greedy procedure is the selection of a set of parameters $\{\mu_1, \dots, \mu_N\}$ and timesteps $\mathtt{I}^\star$ so to compute corresponding high-fidelity solutions $\left\{\{u^{(j)}_{\mu_1}\}_{j\in\mathtt{I}^\star}, \dots, \{u^{(j)}_{\mu_N}\}_{j\in\mathtt{I}^\star}\right\}$ that could adequately represent the parametrically induced manifold $\mathcal{M}$. The first version of the greedy algorithm is the *strong greedy*: here, retained parameters selection is based on the *best-fit* (bf) error:

$$E^{\mathrm{bf,(j)}}_{\mu,N} = \left\|u^{(j)}_\mu - \Pi_{\mathcal{Z}_N} u^{(j)}_\mu\right\|, \tag{2.9}$$

where the projection operator $\Pi_{\mathcal{Z}_N} : \mathcal{X}^{\mathrm{hf}} \to \mathcal{Z}_N$ is such that

$$\Pi_{\mathcal{Z}_N}\left(u^{(j)}_\mu\right) = \arg\min_{v\in\mathcal{Z}_N} \left\|u^{(j)}_\mu - v\right\| \text{ for each } j = 1, \dots, J_{\max}.$$

For each iteration $n_{\mathrm{c}} = 1, \dots, N_{\mathrm{count}}$ of a greedy algorithm, we should have to compute parameter $\mu^\star$ and time step $j^\star$ in order to construct a suitable reduced basis. For a time-dependent problem, selection of parameter $\mu^\star$ can be made by fixing a time step $j = J_{\max}$, as done in [GP05]:

$$\mu^\star = \arg\max_{\mu\in\Xi_{\mathrm{train}}} E^{\mathrm{bf},(J_{\max})}_{\mu,n_{\mathrm{c}}}. \tag{2.10}$$

On the contrary, selection of a new timestep is done over all computational times, computing the best fit error for the currently selected parameter $\mu^\star$:

$$j^\star = \arg\max_{j=1,\dots,J_{\max}} \left(E^{\mathrm{bf},(j)}_{\mu^\star,n_{\mathrm{c}}} - E^{\mathrm{bf},(j-1)}_{\mu^\star,n_{\mathrm{c}}}\right). \tag{2.11}$$

The strong greedy search iterations at (2.10) and (2.11) require the computation of the best fit error $E^{\mathrm{bf}}_{\mu,n_{\mathrm{c}}}$ at iteration n_{c} for each parameter in the training set Ξ_{train}: therefore, the evaluation of the best-fit error requires (many) expensive evaluations of the high-fidelity solutions, even in the case in which the parametric set Ξ_{train} has a low cardinality $|\Xi_{\mathrm{train}}| = n_{\mathrm{train}}$. A further simplification is adopted in the weak greedy: the best-fit error defined in (2.9) is replaced by an inexpensive *a posteriori* error indicator Δ_μ such that

$$\left\|\mathfrak{u}_\mu - \Pi_{\mathcal{Z}_{n_{\mathrm{c}}}}\hat{\mathfrak{u}}_\mu\right\|_J \le \Delta_\mu \quad \forall\mu\in\mathscr{P}, \tag{2.12}$$

where $\hat{\mathfrak{u}}_\mu = \left\{\hat{u}^{(j)}_\mu\right\}_{j=1}^{J_{\max}}$ and $\hat{u}^{(j)}_k = \Pi_{\mathcal{Z}_{n_{\mathrm{c}}}} u^{(j)}_k$ for each $j = 1, \dots, J_{\max}$.

We observe that, to be efficient, a greedy algorithm must be supported by an error indicator that provides an estimate of the error induced by replacing the high-fidelity space $\mathcal{X}^{\mathrm{hf}}$ with the reduced basis space $\mathcal{Z}_{n_{\mathrm{c}}}$, i.e. (2.12) holds. If the error indicator Δ_μ can be evaluated efficiently, the computation of $\mu^\star$ can be significantly accelerated since no high-fidelity solution is required at this step and the evaluation of the error indicator is embarassingly parallelizable. In section 2.4 we discuss the choice of the error indicator.

We also note that the convergence results for the greedy approximation have been established in [Bin+11] and [Buf+12]. In these works, the authors analyze the *a priori* convergence of the greedy algorithm; in particular, they show that if the underlying problem allows an exponentially small Kolmogorov $n-$width, then the greedy reduced basis approximation converges exponentially fast to the high-fidelity approximation. In [Haa13] the study on *a priori* convergence rates of [Bin+11] and [Buf+12] is extended to time-dependent problems, which are typically approximated by the POD-Greedy algorithm, as mentioned at the beginning of section 2.2.

2.2.2 Proper Orthogonal Decomposition

We present here the POD procedure based on the *method of snapshots* ([Sir87]). The POD technique takes the set of snapshots, which are computed by high-fidelity solves for given parameters in a parametric training set Ξ_{train}, and it generates a set of uncorrelated variables called *POD modes*. The first modes retain most of the information content (that we precise in the following) present in all the given snapshots. Given the high-fidelity snapshots $\{\mathbb{u}_{\mu_1}, \dots, \mathbb{u}_K\}$, we can define the snapshots matrix $\mathbf{S} = [\mathbf{u}_1, \dots, \mathbf{u}_{n_{\text{train}}}] \in \mathbb{R}^{N^{\text{hf}}, n_{\text{train}}}$, where $n_{\text{train}} = J_{\max} K$. We suppose that the number of degrees of freedom associated with the high-fidelity discretization is much bigger than the number of training parameters, thus $N^{\text{hf}} \gg n_{\text{train}}$; this assumption characterizes the *method of snapshots*. Given the snapshots database $\mathbf{S}$, the reduced space is defined as the subspace of rank N which minimizes, in the least squares sense, the difference between the snapshots and their orthogonal projections onto this subspace:

$$\begin{aligned} \min_{\mathcal{Z}_N = \text{span}\{\zeta_1, \dots, \zeta_N\}} E(\zeta_1, \dots \zeta_N) &:= \frac{1}{n_{\text{train}}} \sum_{k=1}^{n_{\text{train}}} \|u_k - \hat{u}_k\|^2 \\ \text{subject to } (\zeta_i, \zeta_j) &= \delta_{i,j} \ \forall i, j = 1, \dots, N \end{aligned} \tag{2.13}$$

where $\hat{u}_k^{(j)} = \Pi_{\mathcal{Z}_N} u_k^{(j)}$ for $j = 1, \dots, J_{\max}$, $k = 1, \dots, K$. The minimization problem in (2.13) can be cast in matrix form as follows

$$\begin{aligned} \min_{\mathbf{Z}_N} E &= \|\mathbf{S} - \mathbf{Z}_N \mathbf{Z}_N^T \mathbf{X} \mathbf{S}\|_{F_X}^2 \\ \text{subject to } \mathbf{Z}_N^T \mathbf{X} \mathbf{Z}_N &= \mathbb{1}_N \end{aligned} \tag{2.14}$$

where $\mathbb{1}_N$ denotes the $N \times N$ identity matrix and $\|A\|_{F_X}^2 = Tr(\mathbf{A}^T \mathbf{X} \mathbf{A})$ denotes the Frobenius norm associated with the previously introduced inner product in $\mathcal{X}$ and the induced norm matrix $\mathbf{X}$ s.t. $(u, u) = \mathbf{u}^T \mathbf{X} \mathbf{u}$. Since matrix $\mathbf{X}$ is symmetric positive definite (SPD), the Cholesky decomposition can be employed to factorize $\mathbf{X} = \mathbf{X}^{1/2} (\mathbf{X}^{1/2})^T$. By considering the change of variables $\tilde{\mathbf{S}} = (\mathbf{X}^{1/2})^T \mathbf{S}$ and $\tilde{\mathbf{Z}}_N = (\mathbf{X}^{1/2})^T \mathbf{Z}_N$, the minimization problem in (2.14) can be written as

$$\begin{aligned} \min_{\tilde{\mathbf{Z}}_N} E &= \|\tilde{\mathbf{S}} - \tilde{\mathbf{Z}}_N \tilde{\mathbf{Z}}_N^T \tilde{\mathbf{S}}\|_F^2 \\ \text{subject to } \tilde{\mathbf{Z}}_N^T \tilde{\mathbf{Z}}_N &= \mathbb{1}_N \end{aligned} \tag{2.15}$$

where $\|A\|_F^2 = Tr(\mathbf{A}^T \mathbf{A})$ is the Frobenius norm. The POD based on the *method of snapshots* relies on a singular value decomposition (SVD) of $\tilde{\mathbf{S}}^T \tilde{\mathbf{S}} \in \mathbf{R}^{n_{\text{train}}, n_{\text{train}}}$ and on application of *Schmidt-Eckart-Young-Mirsky* theorem on $\tilde{\mathbf{S}}$: having $\tilde{\mathbf{S}} \in \mathbb{R}^{N^{\text{hf}}, n_{\text{train}}}$, we can identify orthogonal matrices $\mathbf{U} \in \mathbb{R}^{N^{\text{hf}}, N^{\text{hf}}}$ and $\mathbf{V} \in \mathbb{R}^{n_{\text{train}}, n_{\text{train}}}$ and a diagonal matrix with non-negative real numbers on the diagonal that we denote as $\mathbf{\Sigma} \in \mathbb{R}^{N^{\text{hf}}, n_{\text{train}}}$. Matrix $\mathbf{\Sigma}$ is uniquely determined by $\tilde{\mathbf{S}}$ if the singular values (i.e. the numbers on the diagonal of $\mathbf{\Sigma}$) are listed in descending order. Now the metod of snapshots consideres the SPD correlation matrix

$$\tilde{\mathbf{S}}^T \tilde{\mathbf{S}} = (\mathbf{U} \mathbf{\Sigma} \mathbf{V}^T)^T (\mathbf{U} \mathbf{\Sigma} \mathbf{V}^T) = \mathbf{V} \mathbf{\Sigma}^2 \mathbf{V}^T.$$

where $\mathbf{V}$ and $\mathbf{\Sigma}$ are obtained from the SVD of $\tilde{\mathbf{S}}^T\tilde{\mathbf{S}} \in \mathbb{R}^{n_{\text{train}},n_{\text{train}}}$, and $\mathbf{U} = \tilde{\mathbf{S}}\mathbf{V}\mathbf{\Sigma}^{-1}$: the basis functions can be thus constructed as

$$\mathbf{Z}_N = \tilde{\mathbf{S}} \begin{bmatrix} V_{1,1} & V_{1,N} \\ \vdots & \vdots \\ V_{n_{\text{train}},1} & V_{n_{\text{train}},N} \end{bmatrix} \begin{bmatrix} \sigma_1 & & 0 \\ & \ddots & \\ 0 & & \sigma_N \end{bmatrix}^{-1}.$$

where $N \leq n_{\text{train}}$. E in (2.15) is also referred to as *POD energy*; it is also equivalent to the sum of squares of the singular values that correspond to the neglected POD modes:

$$E = \sum_{i=N+1}^{n_{\text{train}}} \sigma_i^2. \tag{2.16}$$

Therefore we can select the maximum dimension N of the reduced basis Z_N such that the POD energy is below a user-defined threshold, that is

$$E \leq \epsilon_{\text{POD}}, \tag{2.17}$$

with $\epsilon_{\text{POD}} \in (0, 1)$. By using definition (2.16) and by diving both left and right hand side terms in (2.17) by the sum of all the squared singular values $\sum_{k=1}^{n_{\text{train}}} \sigma_k^2$, we obtain that the desidered N is the minimum dimension such that

$$\frac{\sum_{k=1}^{n_{\text{train}}} \sigma_k^2 - \sum_{k=1}^{N} \sigma_k^2}{\sum_{k=1}^{n_{\text{train}}} \sigma_k^2} \leq \frac{\epsilon_{\text{POD}}}{\sum_{k=1}^{n_{\text{train}}} \sigma_k^2} = tol_{\text{pod}}, \tag{2.18}$$

that can be written in the following way:

$$I(N) := \frac{\sum_{k=1}^{N} \sigma_k^2}{\sum_{k=1}^{n_{\text{train}}} \sigma_k^2} \geq 1 - tol_{\text{pod}}. \tag{2.19}$$

Here, $I(N)$ is the *Relative Information Content* (RIC): it represents the energy retained by the first N POD modes, while the energy associated with neglected ones is equal to tol_{pod}, which is desiderable to be small.

As stated in (2.13), the POD allows the construction of a reduced basis that is optimal in a l^2-sense over the parameter space. However, its main limitation lies in the large computational cost: the construction of the reduced basis requires the computation of a potentially large number n_{train} of high-fidelity solutions to ensure a satisfactory accuracy. A proper choice of N is not known or predictable for a general problem: this lack of information could result in a substantial computational overhead associated with the fact that a large number of high-fidelity solves is required but the majority of the resulting solutions do not contribute to the construction of the reduced basis. This fact motivates the attempt to build the reduced basis by the use of an iterative approach.

2.2.3 POD-Greedy algorithm

The POD-Greedy algorithm was introduced in [HO08] and analysed in [Haa13]: the approach combines proper orthogonal decomposition (POD [BHL93; BBI09; Vol11]) to compress temporal trajectories with a greedy search driven by an error indicator to explore the parameter domain. In this work, similarly to Ref. [Fic+18], we rely on a time-averaged error indicator to drive the greedy search; furthermore, we test two different compression strategies to update the POD basis at each greedy iteration.
The POD-greedy sampling procedure requires the set of training parameters Ξ_{train}, an error tolerance tol_{loop}, a POD tolerance tol_{pod} and the maximum number of iterations $N_{\text{count,max}}$. At each iteration we search the currently worst-resolved parameter $\mu^\star \in \Xi_{\text{train}}$ using an error indicator Δ_μ that is specified in section 2.4; following [HO08], POD with respect to time is performed to compress the error trajectory and the POD modes (retained based on tolerance tol_{pod}) are added to the current basis Z. At each iteration we need to perform a data compression step. Indeed, greedy and POD methods described in sections 2.2 explore the set of training parameters, Ξ_{train} whose cardinality is denoted as n_{train}.

The computation of the high-fidelity snapshots in a possibly high-dimensional parameteric set may end-up in storing big data structures and may therefore cause memory issues. Data compression techniques, explained in section 2.2.4, are used to solve this issue. We summarize the data compression routine by the following expression

$$\left[Z',\ \boldsymbol{\lambda}'\right] = \texttt{data-compression}\left(Z,\ \boldsymbol{\lambda}, \mathbb{u}_{\mu^\star}, (\cdot,\cdot), tol_{\text{pod}}\right),$$

which takes as input the current ROB and the POD eigenvalues $\boldsymbol{\lambda} = [\lambda_1, \dots, \lambda_N]^T$, and returns the updated ROB Z' and the updated eigenvalues $\boldsymbol{\lambda}'$.

Algorithm 2 POD-Greedy

Require: $\Xi_{\text{train}} = \{\mu^{(k)}\}_{k=1}^{n_{\text{train}}}$, tol_{loop}, tol_{pod}, $N_{\text{count,max}}$.

1: $\mathcal{Z} = \emptyset$, $\boldsymbol{\lambda} = \emptyset$, $\mu^\star = \mu^{(1)}$.
2: **for** $n_{\text{count}} = 1, \dots, N_{\text{count,max}}$ **do**
3: Compute HF snapshots $\mathbb{u}_{\mu^\star}$.
4: $[Z\ \boldsymbol{\lambda}] = \texttt{data-compression}(Z,\ \boldsymbol{\lambda}, \mathbb{u}_{\mu^\star}, (\cdot,\cdot), tol_{\text{pod}})$. ▷ section 2.2.4.
5: Construct the ROM with error indicator. ▷ section 2.3, 2.4
6: **for** $j = k : n_{\text{train}}$ **do**
7: Solve the ROM for $\mu = \mu^{(k)}$ and compute Δ_μ.
8: **end for**
9: $\mu^\star = \arg\max_{\mu \in \Xi_{\text{train}}} \Delta_\mu$. ▷ Greedy search
10: **if** $\Delta_{\mu^\star} < tol_{\text{loop}}$ **then**, ▷ Termination condition
11: `break`,
12: **end if**.
13: **end for**
return ROB Z_N and the ROM coefficients $\mu \in \mathcal{P} \mapsto \{\widehat{\boldsymbol{\alpha}_\mu}^{(j)}\}_{j=1}^{J_{\max}}$.

Notice that at line 9 selection of parameter $\mu^\star$ relies on an error indicator for each parameter in the training set and it does not require the computation of the best fit error (2.9).
For a time dependent problem as (2.1), the greedy search should be made over selected

time steps as well as over the parametric set Ξ_{train}. At line 4 information about high-fidelity solutions in time is compressed so we do not have to explicitly compute selected time steps as in a classical greedy method, as presented in (2.11).
We also observe that a considerable reduction in the computational cost of the reduced basis construction is given by the fact that only n_{count} high-fidelity solutions are computed in the POD-Greedy approach, in contrast to the n_{train} solutions needed for the classical POD basis generation (in almost all cases $n_{\text{train}} \gg N_{\text{count,max}} \geq n_{\text{c}}$).

2.2.4 Data compression methods

The POD method introduced in section 2.2.2 is widely used for the construction of low-dimensional approximation spaces from the high-dimensional set of snapshots. For large-scale applications and an increasing number of snapshots, however, the computation of the POD basis often becomes prohibitively expensive. Indeed, all snapshots vectors have to be computed and stored before starting the POD computation. For large problems, this might be impossible due to insufficient memory. This issue motivates the use on incremental versions of the POD. We consider two different data compression strategies: a hierarchical POD (H-POD) and a hierarchical approximate POD (HAPOD). Both techniques have been considered in several previous works: we refer to Ref.[Haa17, section 3.5] for H-POD and to [HLR18] for HAPOD; HAPOD is also related to incremental singular value decomposition in linear algebra [Bra03]. Here, we review the two approaches for completeness. We introduce notation

$$[\mathbf{Z},\ \boldsymbol{\lambda}] = \texttt{POD}\left(\{\mathbb{u}_k\}_{k=1}^{n_{\text{train}}}, (\cdot,\cdot), tol_{\text{pod}}\right)$$

to refer to the application of POD to the snapshot set $\{\mathbb{u}_k\}_{k=1}^{n_{\text{train}}}$, with inner product $(\cdot,\cdot)$, and tolerance tol_{pod} (cf. (2.18)), with $\mathbf{Z} = [\boldsymbol{\zeta}_1, \dots, \boldsymbol{\zeta}_N]$, and $\mathbf{Z}'\mathbf{X}\mathbf{Z} = \mathbb{I}_N$; we also have that $\boldsymbol{\lambda} = [\lambda_1, \dots, \lambda_N]^T = [\sigma_1^2, \dots, \sigma_N^2]^T$, and $\lambda_1 \geq \lambda_2 \dots \geq \lambda_N$. Given $\mathbf{Z}$ and the snapshots $\mathbb{u}_{\mu^\star}$, H-POD considers the update:

$$\mathbf{Z}' = [\mathbf{Z}, \mathbf{Z}^{\text{new}}], \quad \mathbf{Z}^{\text{new}} = \texttt{POD}\left(\Pi_{\mathcal{Z}^\perp}\mathbb{u}_{\mu^\star}, (\cdot,\cdot), tol_{\text{pod}}\right). \tag{2.20a}$$

Note that the approach does not require to input the POD eigenvalues $\boldsymbol{\lambda}$ from the previous iterations. We observe that the approach leads to a sequence of nested spaces — that is, the updated ROB contains the ROB of the previous iteration — and it returns an orthonormal basis of the reduced space. In our experience, the choice of the tolerance tol_{pod} is extremely challenging: since (2.18) depends on the relative energy content of the snapshot set, the update (2.20a) with fixed tolerance tol_{pod} might lead to an excessively large (resp., small) number of modes when $\max_j \|u_\mu^{(j)} - \Pi_{\mathcal{Z}_N} u_\mu^{(j)}\|$ is small (resp., large). For this reason, we propose to choose the number of new modes N^{new} using the criterion:

$$N^{\text{new}} := \min\left\{ M \,:\, \max_{j\in \mathtt{I}_s} \frac{\left\|\Pi_{(\mathcal{Z}\oplus\mathcal{Z}_M^{\text{new}})^\perp}\mathbf{u}_{\mu^\star}^{(j)}\right\|}{\left\|\mathbf{u}_{\mu^\star}^{(j)}\right\|} \leq tol_{\text{pod}},\ \ \mathcal{Z}_M^{\text{new}} = \text{span}\{\boldsymbol{\zeta}_m^{\text{new}}\}_{m=1}^M \right\}. \tag{2.20b}$$

Note that this choice enforces that the in-sample relative projection error is below a certain threshold for all snapshots computed during the greedy iterations.

HAPOD considers the update

$$[\mathbf{Z}', \boldsymbol{\lambda}'] = \texttt{POD}\left(\{\mathbf{u}_{\mu^\star}^{(j)}\}_{j\in\mathtt{I}_s} \cup \{\sqrt{\lambda}_n\boldsymbol{\zeta}_n\}_{n=1}^N, (\cdot,\cdot), tol_{\text{pod}}\right). \tag{2.21}$$

Note that in (2.21) we have to use $\sqrt{\lambda}_n$ which correspond to the square roots of eivgenvalues of the correlation matrix $\mathbf{C} = \mathbf{S}^T\mathbf{X}\mathbf{S}$. Note that the approach (2.21) does not in general lead to hierarchical (nested) spaces. As discussed in Ref. [HLR18, section 3.3], which refers to (2.21) as to *distributed HAPOD*, it is possible to relate the performance of the reduced space obtained using HAPOD to the performance of the POD space associated with the snapshot set $\{\mathbf{u}_{\mu_n}^{(j)} : n = 1, \dots, N_{\text{count,max}}, j \in \mathtt{I}_s\}$: we refer to the above-mentioned paper for a thorough discussion.

2.3 Reduced formulation

2.3.1 Galerkin projection

Given a parameter $\mu \in \mathscr{P}$, the estimation of $\hat{\mathfrak{u}}_\mu$ is done by projection of the discretized PDE (2.3) into a suitable reduced space. We denote by $\mathscr{R}_\mu$ the residual associated with (2.3), that is,

$$\mathscr{R}_\mu(u_\mu^{(j)}, u_\mu^{(j-1)}, v) = \left(\frac{u_\mu^{(j)} - u_\mu^{(j-1)}}{\Delta t}, v\right)_{L^2(\Omega)} + \mathcal{G}_\mu(u_\mu^{(j)}, v).$$

Given the N-dimensional space $\mathcal{Z}_N$, the reduced basis approximation is sought as follows: for any given $\mu \in \mathscr{P}$, we seek $\hat{u}_\mu \in C^0(0, T_\text{f}; L^2(\Omega)) \cap L^2(0, T_\text{f}; \mathcal{Z}_N)$ s.t.

$$\left(\frac{\hat{u}_\mu^{(j)} - \hat{u}_\mu^{(j-1)}}{\Delta t}, v\right)_{L^2(\Omega)} + \mathcal{G}_\mu(\hat{u}_\mu^{(j)}, v) = 0 \ \forall v \in \mathcal{Z}_N, \tag{2.22}$$

with $\left(\hat{u}_\mu^{(0)}, v\right)_{L^2(\Omega)} = (u_0, v)_{L^2(\Omega)} \ \forall v \in \mathcal{Z}_N$ and with $T_0\hat{u}_\mu = g_\text{dir}$. Expression in (2.22) correspond to the enforcement of the orthogonality between the residual and the reduced subspace $\mathcal{Z}_N$. In algebraic form, for each time index $j = 1, \dots, J_\text{max}$, we can write the residual vector $\hat{\mathbf{R}}_\mu^\text{hf} \in \mathbb{R}^N$ and Jacobian matrix $\hat{\mathbf{J}}_\mu^\text{hf} \in \mathbb{R}^{N,N}$:

$$\left(\hat{\mathbf{R}}_\mu^\text{hf}(\hat{\mathbf{u}}_\mu^{(j)})\right)_n = \mathscr{R}\left(\hat{\mathbf{u}}_\mu^{(j)}, \boldsymbol{\zeta}_n\right) \ \text{for}\, n = 1, \dots, N \tag{2.23}$$

$$\left(\hat{\mathbf{J}}_\mu^\text{hf}(\hat{\mathbf{u}}_\mu^{(j)})\right)_{n,n'} = \frac{\partial}{\partial \alpha_{n'}^{(j)}}\left(\hat{\mathbf{R}}_\mu^\text{hf}(\hat{\mathbf{u}}_\mu^{(j)})\right)_n \ \text{for}\, n, n' = 1, \dots, N, \tag{2.24}$$

for each time index $j = 1, \dots, J_\text{max}$, where $\text{span}\{\zeta_1, \dots, \zeta_N\} = \mathcal{Z}_N$ and $\{\boldsymbol{\alpha}_\mu^{(j)}\}_{j \in \mathtt{I}_s}$ are defined in section 2.1.3. From the algebraic expressions of residual and Jacobian in (2.23) and (2.24) it is possible to notice that the Galerkin projection stated in (2.22) leads to a system of N equations, where $N \ll N^\text{hf}$.
We remark also that the assembling of the $N \times N$ system associated with the ROM (2.22) requires the integration over the whole FE mesh and thus its computational cost scales with the total number of elements N_e.
We also observe that, for the (solid mechanics) problems considered in this work, the Galerkin projection preserves the numerical stability properties of the discrete system to which it is applied, (and if the time integrator is energy conserving, it is guaranteed to be unconditionally stable), as shown in [FCA15]. Therefore, no instability or deterioration in accuracy are expected to appear over time. For certain types of hyperbolic systems of equations, as in the compressible flows applications in [KA12], the numerical stability of the ROM (based on the Galerkin method) is not guaranteed, as a consequence of the fact that the Hamiltonian structure in the projection-based ROM is no more preserved.

This topic is beyond the scope of the present thesis; we remind to [BR06], [HPR21], [GWW17] and [BGH21] for a thorough discussion.

2.3.2 Hyper-reduction techniques

As mentioned in chapter 1, in the context of projection-based MOR, hyper-reduction methods are employed to reduce the online assembling cost of variational forms that are nonaffine in the parameters and nonlinear in the unknown variable. For weak forms $\mathcal{G}_\mu(\cdot,\cdot)$, the evaluation of residuals requires the integration over the spatial domain Ω. The aim is to prevent the computational complexity of the resulting ROM from scaling with the dimension N^{hf} of the high-fidelity discretization, which is, in general, computationally prohibitive. We would like to achieve an operation time that scales with $\mathcal{O}(N)$. In general, when the solution cost of ROM for a test parameter $\mu \in \mathcal{P}$ is independent of the dimension of the FOM, we say that the ROM is *online efficient*.

We identify two distinct categories of hyper-reduction methods. A first category first intepolates the residual form in $\mathcal{G}_\mu(\cdot,\cdot)$ using empirical functions, then it integrates the interpolated residuals; the second category directly evaluates the residual integrals in $\mathcal{G}_\mu(\cdot,\cdot)$ by using empirical quadrature rules. The first category includes Empirical Interpolation Method (EIM), for which we refer to [Bar+04]; the second includes the hyper-reduction approach in [Ryc05] (see also [Fri+18]), the energy-conserving mesh sampling and weighting (ECSW) approach in [FCA15] and the empirical quadrature procedure (EQP) proposed in [YP19a], [DY22].

Empirical interpolation method

The EIM method is employed to recover online N^{hf}-independence even in the case where the variational form $\mathcal{G}_\mu(\cdot,\cdot)$ does not admit an efficient offline/online decomposition. To do that, we introduce the interpolation operator $\mathcal{I}_Q : C(\Omega) \to \mathcal{W}_Q$ associated with a Q-dimensional linear space $\mathcal{W}_Q = \text{span}\{\psi_q\}_{q=1}^Q \subset C(\Omega)$:

$$\mathcal{I}_Q[v](x_q) = v(x_q) \text{ for } q = 1, \dots, Q \tag{2.25}$$

for all $v \in C(\Omega)$ and points $\{x_q\}_{q=1}^Q \subset \bar{\Omega}$. The objective of EIM is to determine an approximation space $\mathcal{W}_Q$ and Q points $\{x_q\}_{q=1}^Q$ such that $\mathcal{I}_Q[u_\mu]$ accurately approximates u_μ for all $u_\mu \in \mathcal{M}$. Algorithm 3 summarizes the EIM procedure: the algorithm takes as input snapshots $\{\mathbb{u}_k\}_{k=1}^{n_{\text{train}}}$ of the manifold $\mathcal{M}$ and returns the functions $\{\psi_q\}_{q=1}^Q$, the interpolation points $\{x_q\}_{q=1}^Q$ and the matrix $\mathbf{B} \in \mathbb{R}^{Q,Q}$ such that $\mathbf{B}_{q,q'} = \psi_q(x'_q)$. We have that for all $v \in C(\Omega)$

$$\mathcal{I}_Q[v] = \sum_{q=1}^{Q} (\boldsymbol{\alpha}(v))_q \, \psi_q, \quad \text{with } \boldsymbol{\alpha}(v) = \mathbf{B}^{-1} \begin{bmatrix} v(x_1) \\ \vdots \\ v(x_Q) \end{bmatrix}.$$

Algorithm 3 Empirical interpolation method

Inputs: $\{\mathbb{u}_k\}_{k=1}^{n_{\text{train}}} \subset \mathcal{X}^{\text{hf}}$
Outputs:$\{\psi_q\}_{q=1}^{Q}$, $\mathbf{B} \in \mathbb{R}^{Q,Q}$, $\{x_q\}_{q=1}^{Q}$

1: Build the POD space $\zeta_1, \dots, \zeta_Q$ based on the snapshots $\{\mathbf{u}_k^{(j)}\}$ for $k = 1, \dots, n_{\text{train}}$, $j = 1, \dots, J_{\max}$
2: $x_1 := \arg\max_{x \in \bar{\Omega}} |\zeta_1(x)|$, $\psi_1 = \frac{1}{\zeta_1(x_1)}\zeta_1$, $(\mathbf{B})_{1,1} = 1$
3: **for** $q = 2, \dots, Q$ **do**
4: $\quad r_q = \zeta_q - \mathcal{I}_{q-1}\zeta_q$
5: $\quad x_q := \arg\max_{x \in \bar{\Omega}} |r_q(x)|$
6: $\quad$ Define $\psi_q := \frac{1}{r_q(x_q)} r_q$ and update $(B)_{q,q'} = \psi_q(x_{q'})$
7: **end for**

We observe that Algorithm 3 can be applied to the nonaffine terms of the PDE (see [Gre+07], Lemmas 2.1 – 2.3) or to the discrete FE residual vector (cf. [CS10b], [CS10a]). In algorithm 10 in chapter 5 we discuss the extension of EIM procedure to vector-values fields emerging from PDEs to solve for a number $D > 1$ of unknown variables.

Empirical quadrature method

In order to reduce assembly costs, we aim at preventing integration over the whole domain: we define the indices associated with the "sampled elements" $\mathtt{I}_{\text{eq}} \subset \{1, \dots, N_{\text{e}}\}$. In view of the introduction of EQ technique, we write the residual as the sum of local (elementwise) contributions, for each time index $j = 1, \dots, J_{\max}$:

$$\mathcal{R}\left(\mathbf{u}_\mu^{(j)}, \boldsymbol{\psi}\right) = \sum_{k=1}^{N_{\text{e}}} r_k^{\text{hf}}\left(\mathbf{E}_k \mathbf{u}_\mu^{(j)}, \mathbf{E}_k \boldsymbol{\psi}\right) \tag{2.26}$$

and we denote it with the acronym hf to indicate that a *high-fidelity quadrature rule* has been employed. In algebraic form we have that (2.23) holds.

We define the EQ residual:

$$\mathcal{R}_\mu^{\text{eq}}\left(\mathbf{u}_\mu^{(j)}, \boldsymbol{\psi}\right) = \sum_{k \in \mathtt{I}_{\text{eq}}} \rho_k^{\text{eq}}\, r_{\mu,k}^{\text{hf}}\left(\mathbf{E}_k \mathbf{u}_\mu^{(j)},\ \mathbf{E}_k \boldsymbol{\psi}\right) \tag{2.27}$$

where $\boldsymbol{\rho}^{\text{eq}} = [\rho_1^{\text{eq}}, ..., \rho_{N_{\text{e}}}^{\text{eq}}]^T$ is a sparse vector of positive weights such that $\rho_k^{\text{eq}} = 0$ if $k \notin \mathtt{I}_{\text{eq}}$. The algebraic form of the EQ residual is the following:

$$\left(\widehat{\mathbf{R}}_\mu^{\text{eq}}(\hat{\mathbf{u}}_\mu^{(j)})\right)_n = \mathcal{R}^{\text{eq}}(\hat{\mathbf{u}}_\mu^{(j)}, \psi_n) \text{ for } n = 1, \dots, N. \tag{2.28}$$

The residuals $\widehat{\mathbf{R}}_\mu^{\text{hf}}(\cdot)$ defined in (2.23) and $\widehat{\mathbf{R}}_\mu^{\text{eq}}(\cdot)$ in (2.28) satisfy

$$\widehat{\mathbf{R}}_\mu^{\text{hf}}(\boldsymbol{\alpha}) = \mathbf{G}(\boldsymbol{\alpha})\ \boldsymbol{\rho}^{\text{hf}}, \quad \widehat{\mathbf{R}}_\mu^{\text{eq}}(\boldsymbol{\alpha}) = \mathbf{G}(\boldsymbol{\alpha})\ \boldsymbol{\rho}^{\text{eq}}, \tag{2.29}$$

where $\mathbf{G} \in \mathbb{R}^{N,N_{\text{e}}}$ can be explicitly derived using the same approach as in [TZ21] and $\boldsymbol{\rho}^{\text{hf}} = [1, \dots, 1]^T$.

As in [YP19a], we reformulate the problem of finding the sparse weights $\boldsymbol{\rho}^{\text{eq}} \in \mathbb{R}^{N_{\text{e}}}$ as the problem of finding a vector $\boldsymbol{\rho}^{\text{eq}}$ such that:

1. the number of nonzero entries in $\boldsymbol{\rho}^{\mathrm{eq}}$, which we denote by $\|\boldsymbol{\rho}^{\mathrm{eq}}\|_0$, is as small as possible;

2. the entries of $\boldsymbol{\rho}^{\mathrm{eq}}$ are non-negative;

3. (*constant-function constraint*) the constant function is integrated accurately:

$$\left|\sum_{k=1}^{N_{\mathrm{e}}} \rho_k^{\mathrm{eq}} |\mathtt{D}_k| - |\Omega|\right| \ll 1; \tag{2.30}$$

4. (*manifold accuracy constraint*) the empirical and high-fidelity quadrature residuals are close at operating conditions:

$$\left\| \left(\mathbf{J}_\mu^{\mathrm{hf}}\left(\boldsymbol{\alpha}_{\mathrm{train}}^{(j)}\right)\right)^{-1} \left(\widehat{\mathbf{R}}_\mu^{\mathrm{hf}}\left(\boldsymbol{\alpha}_{\mathrm{train}}^{(j)}\right) - \widehat{\mathbf{R}}_\mu^{\mathrm{eq}}\left(\boldsymbol{\alpha}_{\mathrm{train}}^{(j)}\right)\right) \right\|_2 \ll 1, \tag{2.31}$$

   for $j \in \mathtt{I}_{\mathrm{s}}$ and for suitable choices of $\{\boldsymbol{\alpha}_{\mathrm{train}}^{(j)}\}_j$ that have to be discussed.

We observe that a similar problem was already introduced in Refs. [FCA15; Far+14]. Compared to these works, we here add the constant-function constraint that is found to improve the accuracy of the weights when the integrals are close to zero due to the cancellation of the function to be integrated in different parts of the domain (cf. [YP19a]).

Note that the constant accuracy constraint is also important to bound the ℓ^1 norm of the empirical weigths, we have indeed

$$\left|\sum_{k=1}^{N_{\mathrm{e}}} \rho_k^{\mathrm{eq}} |D_k|\right| \leq \left|\sum_{k=1}^{N_{\mathrm{e}}} (\rho_k^{\mathrm{eq}} - \rho_k^{\mathrm{hf}}) |D_k|\right| + \sum_{k=1}^{N_{\mathrm{e}}} \rho_k^{\mathrm{hf}} |D_k| = \left|\sum_{k=1}^{N_{\mathrm{e}}} \rho_k^{\mathrm{eq}} |D_k| - |\Omega|\right| + |\Omega|.$$

Exploiting (B.6), we can restate the previous requirements as a sparse representation problem:

$$\text{find } \boldsymbol{\rho}^{\mathrm{eq}} \in \arg\min_{\boldsymbol{\rho}\in\mathbb{R}^{\mathrm{N_e}}} \|\boldsymbol{\rho}\|_0 \text{ s.t. } \begin{cases} \boldsymbol{\rho} \geq \mathbf{0} \\ \|\mathbf{C}\boldsymbol{\rho} - \mathbf{b}\|_* \leq \delta, \end{cases} \tag{2.32}$$

for a suitable choice of the matrix $\mathbf{C}$, the vector $\mathbf{b}$, the norm $\|\cdot\|_*$, and the tolerance δ. Since the optimization problem (2.32) is NP-hard, several authors have proposed computational methods to find approximate solutions to (2.32) in polynomial time. To provide concrete references, [YP19a] considers a ℓ^1 relaxation of (2.32) with $\|\cdot\|_\star = \|\cdot\|_{\ell^\infty}$, and resorts to linear programming to find an approximate solution; here, following Farhat et al. [FCA15], we approximate the solution to (2.32) by solving the inexact non-negative least squares (NNLS) problem

$$\min_{\boldsymbol{\rho}\in\mathbb{R}^{N_{\mathrm{e}}}} \|\mathbf{C}\boldsymbol{\rho} - \mathbf{b}\|_2 \text{ s.t. } \boldsymbol{\rho} \geq \mathbf{0}. \tag{2.33}$$

A thorough comparison between the reduced quadrature approaches in [FCA15] and [YP19a] is beyond the scope of this work we refer to [SH11] for a detailed analysis of the performance of NNLS and a comparison with LP for a stochastic sparse representation problem with Gaussian disturbances.

In this work, we rely on the Matlab function `lsqnonneg` that implements the Greedy algorithm proposed in [LH74] and takes as input the matrix $\mathbf{C}$, the vector $\mathbf{b}$, and a tolerance tol_{eq}:

$$\boldsymbol{\rho}^{\mathrm{eq}} = \mathtt{lsqnonneg}(\mathbf{C}, \mathbf{b}, tol_{\mathrm{eq}}).$$

The same algorithm to find the sparse weights $\boldsymbol{\rho}^{\mathrm{eq}}$ given the matrices $\mathbf{C}, \mathbf{b}$ has been first considered in [FCA15]: for large-scale problems, a parallelised extension of the algorithm was introduced and successfully applied to hyper-reduction in [Cha+17].

We conclude this section on hyper-reduction by the following observation: as explained in [FCA15], the ECSW approach is able to preserve the numerical stability of the time integrator chosen for the solution of the reduced order problem. In [HPR21], the discrete EIM method is shown to result in a loss of the Hamiltonian structure of parametric time-dependent Hamiltonian systems: as a consequence, long-time accuracy and stability of the reduced-order solutions may be affected and suitable conditions on the reduced basis matrix are required to ensure the preservation of the Hamiltonian structure.

2.4 *A posteriori* error estimation

Due to the absence of sharp *a priori* estimates of the error between the ROM solution and the high-fidelity solution, we need a rapid and reliable error indicator to i) assess the accuracy of the ROM during the online stage (and thus it is called *a posteriori* because it is computed after having computed the prediction), as shown at line 5 of the offline/online decomposition algorithm 1; ii) use the indicator to guide parameters selection in the training phase by an adaptive algorithm (cf. algorithm 2). In particular, we exploit the connection between the solution error and the residual error and consider a *residual-based* indicator that can be used in the POD-greedy procedure proposed at line 9 to select training parameters. Given a parameter-dependent solution trajectory $\mathfrak{u}_\mu$, we define the time-average residual:

$$\mathcal{R}^{\mathrm{hf}}_{\mathrm{avg},\mu}(\mathfrak{u}, v) := \sum_{j=1}^{J_{\max}} (t^{(j)} - t^{(j-1)})\, \mathcal{R}^{\mathrm{hf}}_{\mu}\left(\mathbf{u}^{(j)}_{\mu}, \mathbf{v}\right), \quad \forall v \in \mathcal{Y}, \tag{2.34}$$

where $\mathcal{Y} = \mathcal{X}^{\mathrm{hf}}_0$. We give a first definition for the error indicator:

$$\Delta^{\mathrm{hf}}_{\mu}(\mathfrak{u}) = \sup_{v \in \mathcal{Y}\setminus\{0\}} \frac{\mathcal{R}^{\mathrm{hf}}_{\mathrm{avg},\mu}(\mathfrak{u}, v)}{\|v\|}. \tag{2.35}$$

Indicator (2.35) is expensive to evaluate since it relies on HF quadrature and it requires the computation of the supremum over all elements of $\mathcal{X}^{\mathrm{hf}}_0$: following [Tad19], we consider the hyper-reduced error indicator

$$\Delta_{\mu}(\hat{\mathfrak{u}}) = \sup_{v \in \mathcal{Y}_M\setminus\{0\}} \frac{\widehat{\mathcal{R}}^{\mathrm{eq,r}}_{\mathrm{avg},\mu}(\hat{\mathfrak{u}}, v)}{\|v\|}, \tag{2.36}$$

where $\mathcal{Y}_M$ is an M-dimensional empirical test space, while $\mathcal{R}^{\mathrm{eq,r}}_{\mathrm{avg},\mu}$ is defined by replacing $\mathcal{R}^{\mathrm{hf}}_{\mu}$ in (2.35) with a suitable sparse weighted residual of the form (2.27), defined over the elements $\mathtt{I}_{\mathrm{eq,r}} \subset \{1, \dots, N_{\mathrm{e}}\}$. Notice that the empirical quadrature employed for the error indicator (2.36) may be in general different from the quadrature rule used to evaluate (2.27) in order to solve the ROM.

Given the ROM solution $\widehat{\mathfrak{u}}_\mu$, the test space $\mathcal{Y}_M$ should guarantee that

$$\sup_{v \in \mathcal{Y}\setminus\{0\}} \frac{\widehat{\mathcal{R}}^{\mathrm{hf}}_{\mathrm{avg},\mu}(\widehat{\mathfrak{u}}_\mu, v)}{\|v\|} \approx \sup_{v \in \mathcal{Y}_M\setminus\{0\}} \frac{\widehat{\mathcal{R}}^{\mathrm{hf}}_{\mathrm{avg},\mu}(\widehat{\mathfrak{u}}_\mu, v)}{\|v\|}, \quad \forall \mu \in \mathcal{P}, \tag{2.37}$$

which implies that $\mathcal{Y}_M$ should be an approximation of the space of Riesz elements $\mathcal{M}_{\text{test}} := \{\widehat{\psi}_\mu \,:\, \mu \in \mathcal{P}\}$ with

$$\left(\widehat{\psi}_\mu, v\right) \;=\; \widehat{\mathcal{R}}^{\text{hf}}_{\text{avg},\mu}\left(\widehat{\mathbb{u}}_\mu, v\right), \quad \forall\, v \in \mathcal{X}^{\text{hf}}_0. \tag{2.38}$$

On the other hand, the empirical quadrature rule should ensure that

$$\widehat{\mathcal{R}}^{\text{eq,r}}_{\text{avg},\mu}\left(\widehat{\mathbb{u}}_\mu \psi_m\right) \;\approx\; \widehat{\mathcal{R}}^{\text{hf}}_{\text{avg},\mu}\left(\widehat{\mathbb{u}}_\mu \psi_m\right), \quad \forall\, \mu \in \mathcal{P},\; m = 1, \ldots, M, \tag{2.39}$$

where $\psi_1, \ldots, \psi_M$ is an orthonormal basis of $\mathcal{Y}_M$.

Several authors (e.g., [HO08]) have considered the time-discrete $L^2(0, T_{\text{f}}; \mathcal{Y}')$ residual indicator

$$\Delta^{\text{hf},2}_\mu(\mathbb{u}) \;=\; \sqrt{\sum_{j=1}^{J_{\max}} \left(t^{(j)} - t^{(j-1)}\right) \left(\sup_{v \in \mathcal{Y}\setminus\{0\}} \frac{\mathcal{R}^{\text{hf}}_\mu(u^{(j)}, v)}{\|v\|_{\mathcal{Y}}}\right)^2}. \tag{2.40}$$

We observe that we could apply the same ideas considered in section 2.3.2 to devise a hyper-reduced counterpart of the residual indicator (2.40). However, we find that the test space $\mathcal{Y}_M$ and the empirical quadrature rule should be accurate for all parameters and for all time steps: as a result, the resulting test space $\mathcal{Y}_M$ might be significantly higher dimensional and the quadrature rule might be significantly less sparse, for the desired accuracy. For this reason, in chapter 4, we investigate the effectivity of a time-averaged error indicator extended from (2.36) to take into account vector state variables ($D > 1$) and problems with internal variables.

Chapter 3

The Thermo-Hydro-Mechanical problem

In this chapter we extensively describe the THM system that is considered in this work. In section 3.2 we introduce relevant notation and definitions and in section 3.3 we introduce the geometrical configuration; in section 3.4 we present the equilibrium equations and the constitutive laws together with the initial conditions and the description of all the parameters of interest. In section 3.5 we describe the numerical discretization and finally in section 3.5.1 the problem parametrization.

3.1 Physical assumptions

Porous materials are characterized by an internal structure and closed and open pores, filled with one or more fluids. The geomaterial can be represented by soil, rock or concrete, and the fluid by water, water vapour and dry air. The solid and fluid phases interact between the constituents of the porous medium. Porous media theory has been of interest of research for a considerable time (see, e.g., [De 96]). The model we consider in this work is an adaptation of the one discussed in [Gra09a] and [Gra09b]. The fundamental hypothesis is that the porous medium is *fully-saturated-in-liquid*: this means that we do not have to take into account heat convection, but only heat conduction in the physical description of the model. Furthermore, the solid is deformable, resulting in a coupling of fluid, solid and thermal fields. The second assumption is that the solid undergoes small displacements. We remark that in this work the porous medium is seen at a macroscopic scale and thus the constituents are assumed to be chemically non-reacting: this means that temperatures of all the constituents at a point in the medium are equal; although, temperature is not supposed to be uniform throughout the medium. We resort to a *Lagrangian* formulation of the solid. In this case, the computed stress and deformation state are referred to the material configuration rather than to the current position in space; information about the straining and deformation of the material are contained in the deformation gradient tensor (which is presented in the mechanical equilibrium laws in (3.4)). We resort to an *Eulerian* formulation for the liquid: liquid-related variables are represented by functions depending on space variable and time. The resulting mathematical model is of the form introduced in (1.1); the radioactive waste repositories are located at the bottom of the domain, as shown in the drawing 1.2 and in figure 3.1, which is equipped with spatial axes. The numerical discretization of THM system throughout the thesis refers to a two-dimensional domain: we employ a *plane strain*

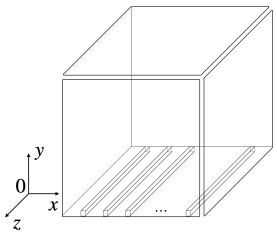

FIGURE 3.1: geometric three-dimensional sketch.

simplification. The repository's length along the z axis is considered exceedingly large with respect to the other two dimensions along x and y; applied forces act in the x-y plane and do not vary along the z direction (this is a typical situation for tunnels as well as bars that are compressed along one of their lengths).

3.2 Fundamental definitions

We consider the spatial variable x in the Lipschitz domain $\Omega \subset \mathbb{R}^d$ with $d = 2$ and the time variable t in the time interval $(0, T_\mathrm{f})$, where T_f is the final time.
We first introduce the *state variables* and the *internal* variables. The state variables, denoted as $\underline{U} = [\underline{u}^\mathrm{T}, p_\mathrm{w}, T]^\mathrm{T}$, represent solid displacement, water pressure and temperature and are reported in Table 1; the internal variables $\underline{W} = [\rho_\mathrm{w}, \varphi, h_\mathrm{w}, Q, \underline{M}_\mathrm{w}^\mathrm{T}, m_\mathrm{w}]^\mathrm{T}$ represent dependent physical quantities and are illustrated in Table 2, together with the corresponding SI units.

	SI unit	description
$\underline{u}$	m	solid displacement
p_w	Pa	water pressure
T	K	temperature

TABLE 3.1: primary variables

	SI unit	label
ρ_w	$\mathrm{kg} \cdot \mathrm{m}^{-3}$	water density
φ	%	Eulerian porosity
h_w	$\mathrm{J} \cdot \mathrm{Kg}^{-1}$	mass enthalpy of water
Q	Pa	non-convected heat
$\underline{M}_\mathrm{w}$	$\mathrm{kg} \cdot \mathrm{m}^{-2} \cdot \mathrm{s}^{-1}$	mass flux
m_w	$\mathrm{kg} \cdot \mathrm{m}^{-3}$	mass input

TABLE 3.2: dependent variables

We denote the Cauchy stress tensor by $\underline{\underline{\sigma}}$[Pa], and we define the volumetric deformation $\epsilon_\mathrm{V} = tr(\underline{\underline{\epsilon}})$ where $\underline{\underline{\epsilon}}$ is the strain tensor: $\underline{\underline{\epsilon}} = \nabla_\mathrm{s}\underline{u} = \frac{1}{2}\left(\nabla\underline{u} + \nabla\underline{u}^T\right)$. We also provide in Table 3.3 the characteristic parameters that we use for the non-dimensionalisation.

	SI unit	value
$\bar{t}$	s	$3.15 \cdot 10^7$
$\bar{H}$	m	77.3
σ_0	Pa	$11.3 \cdot 10^6$
ρ_0	$\mathrm{kg} \cdot \mathrm{m}^{-3}$	2450
T_ref	K	297.5
$\overline{\Delta T}$	K	30

TABLE 3.3: characteristic constants

Due to the plane-strain assumption, we have that the components of the strain tensor $\underline{\underline{\epsilon}}$ related to strain in direction z are equal to 0: we can write $\underline{\underline{\epsilon}} = \begin{bmatrix} \epsilon_{xx} & \epsilon_{xy} \\ \epsilon_{xy} & \epsilon_{yy} \end{bmatrix}$ and $\epsilon_{xz} = \epsilon_{yz} = \epsilon_{zz} = 0$.

3.3 Geometry configuration

A schematic representation of the domain is shown in Figure 3.2(a). The geological repositories, modelled as boundary conditions, are depicted in red at the bottom of the domain, in the case of two activated alveoli. In the vertical (y) direction, the domain is split into three layers: a clay layer denoted as UA ("*unité argilleuse*"), a transition layer UT ("*unité de transition*") and a silt-carbonate layer USC ("*unité silto-carbonatée*"). Layers UA, UT and USC are associated with different material properties, thus the physical parameters in the THM system are expected to assume different values in the domain in Figure 3.2(a): in table 3.4 their dimensional values are specified. The non-dimensional widths of the layers UA, UT and USC are, respectively, 0.4127, 0.1979, 0.3894. In Figure 3.2(b) a finite element grid is shown and denoted as $\mathcal{T}_1$: the number of degrees of freedom for the first state component (solid displacement) is $N^{\mathrm{u}} = 40430$, while for water pressure and temperature is $N^{\mathrm{p}} = N^{\mathrm{t}} = 9045$.

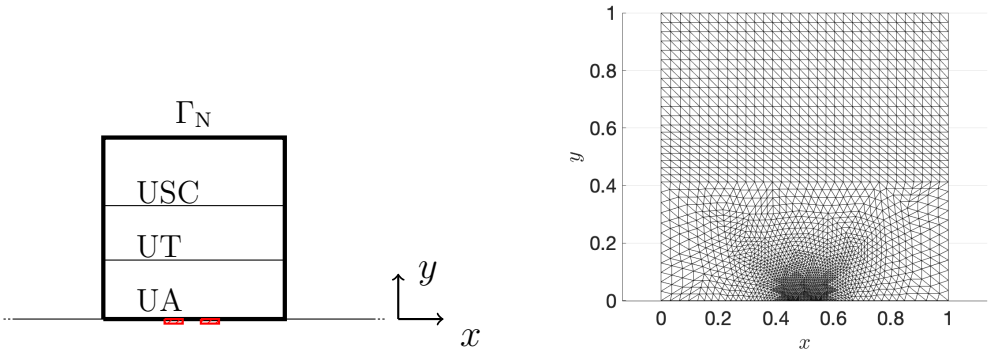

(a) (b)

FIGURE 3.2: geometric configuration: (a) the non-dimensional domain, (b): the mesh $\mathcal{T}_1$. The size of each alveoulus is equal to $l_Q = 3.09\,[\mathrm{m}]$, while the distance between consecutive alveoli is equal to $l = 6.18\,[\mathrm{m}]$.

The grid is refined in the proximity of the alveoli to better capture the relevant features of the solution.

3.4 Mathematical problem

3.4.1 Equilibrium equations

Local equilibrium of the thermo-dhynamics is assumed and macroscopic balance equations are considered to derive governing equations: the superscripts $(\cdot)^{\mathrm{m}}$, $(\cdot)^{\mathrm{h}}$,$(\cdot)^{\mathrm{t}}$ refer to quantities associated with the mechanical, hydraulic and thermal behaviours, respectively. Then, we present the constitutive laws that are considered, which link material properties to displacement, pressure and temperature, and finally we present the boundary conditions. To clarify the presentation, we report in Table 3.4 the parameters that enter in the constitutive laws.

Mechanics We denote by $\underline{F}_{\mathrm{m}} = -\frac{g}{\gamma}\underline{e}_2$ (where $\gamma = \frac{\sigma_0}{\rho_0 H}$) the mechanical force with g defined in Table 3.4 and we specify that $\underline{n}$ (resp. $\underline{t}$) is the unitary outward normal (resp. tangential) vector in the domain depicted in Figure 3.2(a). Linear elasticity is assumed for the deformation process in porous media. The linear momentum balance

equation can be written in terms of stress tensor as

$$\underline{\underline{\sigma}} = \underline{\underline{\sigma'}} + \sigma_{\mathrm{p}} \mathbb{1}, \tag{3.1}$$

where $\underline{\underline{\sigma'}}$ is the *effective* stress tensor of the porous medium and $\mathbb{1}$ is the identity tensor; $\sigma_{\mathrm{p}}\mathbb{1}$ is the *generalized* stress. The decomposition in (3.1) is due to the fact that stresses applied to a saturated porous medium are partly distributed to the solid skeleton and partly to the pore fluid. The former stresses are responsible for skeletal (i.e. solid) deformations: for this reason, they are called effective; the latter are associated with the fluid flows, they are thus called generalized. The effective stress tensor is defined as follows:

$$\begin{aligned} \underline{\underline{\sigma}} =& 2\mu' \underline{\underline{\epsilon}} + \lambda \mathrm{tr}(\underline{\underline{\epsilon}}) \mathbb{1} - (2\mu + 3\lambda)\alpha_{\mathrm{s}} \Delta \mathrm{T} \mathbb{1} \\ =& 2\mu' \nabla_{\mathrm{s}} \underline{u} + (\lambda \nabla \cdot \underline{u} - (2\mu + 3\lambda)\alpha_{\mathrm{s}} \Delta T)\, \mathbb{1}, \end{aligned} \tag{3.2}$$

where α_{s} is the thermal expansion coefficient of the solid and $\Delta T = T - T_{\mathrm{ref}}$. Notice that the stress $\underline{\underline{\sigma}}$ it is linked to the primary and internal variables by the linear law (3.2). Lamé constants μ', λ satisfy

$$\begin{aligned} \mu' &= \frac{E}{2(1+\nu)}, \\ \lambda &= \frac{E\nu}{(1+\nu)(1-2\nu)}, \end{aligned}$$

and E and ν are introduced in Table 3.4. The generalized stress tensor is given by

$$\sigma_{\mathrm{p}} = -b p_{\mathrm{w}}, \tag{3.3}$$

known as Biot-Terzaghi relation; we notice from (3.3) that the solid is assumed to be isotropic. We thus introduce the equilibrium of mechanical forces:

$$\begin{cases} -\nabla \cdot \underline{\underline{\sigma}} = \rho \underline{F}_{\mathrm{m}} & \text{in } \Omega, \\ \underline{\underline{\sigma}}\, \underline{n} = \underline{g}_{\mathrm{m,N}} & \text{on } \Gamma_{\mathrm{N}}, \\ \underline{u} \cdot \underline{n} = 0 & \text{on } \partial\Omega \setminus \Gamma_{\mathrm{N}}, \\ (\underline{\underline{\sigma}}\, \underline{n}) \cdot \underline{t} = 0 & \text{on } \partial\Omega \setminus \Gamma_{\mathrm{N}}, \end{cases} \tag{3.4}$$

where Γ_{N} is depicted in Figure 3.2(a). The Neumann datum $\underline{g}_{\mathrm{m,N}}$ is given by $\underline{g}_{\mathrm{m,N}} = -\underline{e}_2$. To solve equation (3.4) we shall also define the homogenized density $\rho = \rho^0 + m_{\mathrm{w}}$, where ρ^0 is the initial homogenized density and m_{w} is the input mass, which is introduced below: this definition exploits the fact that the porous medium's density is composed by two phases, liquid and solid. Using plane-strain assumption, stress tensor can be written as $\underline{\underline{\sigma}} = \begin{bmatrix} \sigma_{1,1} & \sigma_{1,2} \\ \sigma_{1,2} & \sigma_{2,2} \end{bmatrix}$ where each component is given by relation (3.2).

Hydraulics We state the mass conservation of water as follows

$$\begin{cases} \partial_t m_{\mathrm{w}} + \nabla \cdot \underline{M}_{\mathrm{w}} = 0 & \text{in } \Omega \\ \underline{M}_{\mathrm{w}} \cdot \underline{n} = 0 & \text{on } \partial\Omega \end{cases} \tag{3.5a}$$

Water mass is coupled to solid displacement through the following constitutive law:

$$m_{\mathrm{w}} = \rho_{\mathrm{w}}(1+\epsilon_{\mathrm{V}})\,\varphi - \rho_{\mathrm{w}}^{0}\varphi^{0}.$$

Volumetric change of pore pressure due to change in the stress field is represented by $\partial_t\, m_{\mathrm{w}}$ in equation (3.5a). We assume the flow can be represented by Darcy law: thus the muss flux $\underline{M}_{\mathrm{w}}$ is given by

$$\underline{M}_{\mathrm{w}} = -\gamma\,(\nabla p_{\mathrm{w}} - \rho_{\mathrm{w}}\underline{F}_{\mathrm{m}}). \tag{3.5b}$$

and

$$\gamma = \rho_{\mathrm{w}}\frac{\kappa_{\mathrm{w}}\,\sigma_0\,\bar{t}}{\rho_0\mu_{\mathrm{w},0}\,\bar{H}^2}\exp\left(-\frac{1808.5}{T_{\mathrm{ref}}+\overline{\Delta T}\,T}\right) \tag{3.5c}$$

where κ_{w} is the intrinsic permeability of the porous medium and $\mu_{\mathrm{w}} = \mu_{\mathrm{w},0}\exp\left(\frac{1808.5}{T_{\mathrm{ref}}+\overline{\Delta T}\,T}\right)$ is the dynamic viscosity.

Heat transfer Finally we consider the energy balance:

$$\begin{cases} h_{\mathrm{w}}\partial_t\, m_{\mathrm{w}} + \partial_t\, Q + \nabla\cdot\left(h_{\mathrm{w}}\underline{M}_{\mathrm{w}} + \underline{q}\right) - \underline{M}_{\mathrm{w}}\cdot\underline{F}_{\mathrm{m}} = \Theta & \text{in}\,\Omega \\ \left(h_{\mathrm{w}}\underline{M}_{\mathrm{w}} + \underline{q}\right)\cdot\underline{n} = g_{\mathrm{t,N}} & \text{on}\,\partial\Omega \end{cases} \tag{3.6a}$$

where Q is the non-convective heat, $\underline{q}$ is the thermal flux and is given by the Fick law

$$\underline{q} = -\Lambda\nabla T, \tag{3.6b}$$

with $\Lambda = \mathrm{diag}(\lambda_1, \lambda_2)$. If we denote by $\Gamma_{\mathrm{r}} \subset \partial\Omega$ the region associated with the alveoli, $g_{t,N}$ is equal to

$$g_{t,N} = \frac{P_{\mathrm{t}} n_c \bar{t}}{l_Q \bar{H}^2 \sigma_0}\exp\big(-t/\tau\big)\mathbb{1}_{\Gamma_{\mathrm{r}}} = C_{\mathrm{al}}\exp\big(-t/\tau\big)\mathbb{1}_{\Gamma_{\mathrm{r}}}, \tag{3.7}$$

where $n_c\,[\%]$ is the density of the radioactive waste stock in each alveolus (equal to 45 anisters), $P_{\mathrm{t}} = 31.4\,[\mathrm{W}]$ is the unitary termic power at the initial time, $l_Q = 3.09\,[\mathrm{m}]$ is the size of each alveolus, $\sigma_0, \bar{H}, \bar{t}$ are introduced in Table 3.3 and $\tau = \frac{\bar{t}}{\log(0.112)}\,[\mathrm{s}]$ is a characteristic decay time.

3.4.2 Constitutive laws

We introduce the evolution equation for the water density

$$\frac{d\rho_{\mathrm{w}}}{\rho_{\mathrm{w}}} = \frac{dp_{\mathrm{w}}}{K_{\mathrm{w}}} - 3\alpha_{\mathrm{w}}dT$$

where $\alpha_{\mathrm{w}} = \alpha_{\mathrm{w}}(T)$ is the thermal expansion coefficient of water and it is reported in table 3.4; K_{w} is the bulk modulus of water. We state the evolution equation for the eulerian porosity

$$\frac{d\varphi}{b-\varphi} = d\epsilon_{\mathrm{V}} - 3\alpha_{\mathrm{s}}dT + \frac{dp_{\mathrm{w}}}{K_{\mathrm{s}}},$$

where b and α_{s} have been introduced and K_{s} is the bulk modulus of the solid, that is $K_{\mathrm{s}} = \frac{E}{3(1-2\nu)}$. We then introduce the evolution equation for enthalpy

$$dh_{\mathrm{w}} = C_{\mathrm{w}}^{\mathrm{p}}\,dT + (\beta_h^{\mathrm{p}} - 3\alpha_{\mathrm{w}}T)\frac{dp_{\mathrm{w}}}{\rho_{\mathrm{w}}},$$

where $C_{\mathrm{w}}^{\mathrm{p}}$ is the heat capacity at constant pressure. Finally, we introduce the evolution equation for the non-convective heat

$$\delta Q = \left(\beta_Q^{\epsilon} + 3\alpha_{\mathrm{s}} K_0\, T\right)\, d\epsilon_{\mathrm{V}} \,-\, \left(\beta_Q^{\mathrm{p}} + 3\alpha_{\mathrm{w,m}} T\right)\, dp_{\mathrm{w}} \,+\, C_{\epsilon}^{0}\, dT,$$

where K_0 is the drained bulk modulus (which is the bulk modulus that is measured at constant pore fluid pressure). Notice that δQ is an inexact differential (i.e., it depends on the path). We resume all the constitutive relations in the following system:

$$\begin{cases} \dfrac{d\rho_{\mathrm{w}}}{\rho_{\mathrm{w}}} \,=\, \dfrac{dp_{\mathrm{w}}}{K_{\mathrm{w}}} \,-\, 3\alpha_{\mathrm{w}} dT, & \text{(3.8a)} \\ \dfrac{d\varphi}{b \,-\, \varphi} \,=\, d\epsilon_{\mathrm{V}} \,-\, 3\alpha_{\mathrm{s}} dT + \dfrac{dp_{\mathrm{w}}}{K_{\mathrm{s}}}, & \text{(3.8b)} \\ dh_{\mathrm{w}} = C_{\mathrm{w}}^{\mathrm{p}}\, dT \,+\, (\beta_h^{\mathrm{p}} - 3\alpha_{\mathrm{w}} T)\dfrac{dp_{\mathrm{w}}}{\rho_{\mathrm{w}}}, & \text{(3.8c)} \\ \delta Q = \left(\beta_Q^{\epsilon} + 3\alpha_{\mathrm{s}} K_0\, T\right)\, d\epsilon_{\mathrm{V}} \,-\, \left(\beta_Q^{\mathrm{p}} + 3\alpha_{\mathrm{w,m}} T\right)\, dp_{\mathrm{w}} \,+\, C_{\epsilon}^{0}\, dT, & \text{(3.8d)} \\ m_{\mathrm{w}} = \rho_{\mathrm{w}}(1 + \epsilon_{\mathrm{V}})\, \varphi - \rho_{\mathrm{w}}^{0} \varphi^{0}. & \text{(3.8e)} \end{cases}$$

Here, we have $\beta_h^{\mathrm{p}} = 1 - 3\alpha_{\mathrm{w}} T_{\mathrm{ref}}$, $\beta_Q^{\epsilon} = 3\alpha_{\mathrm{s}} K_0 T_{\mathrm{ref}}$, $\beta_Q^{\mathrm{p}} = 3\alpha_{\mathrm{w,m}} T_{\mathrm{ref}}$.
The parameters in (3.8a)-(3.8e) are defined in Table 3.4. We remind that layers UA, UT, USC are depicted in Figure 3.2(a).

3.4.3 Initial conditions

To set the initial conditions, we consider the case of deactivated repositories: therefore, we set thermal flux equal to zero and we set a constant temperature $T_0 = T_{\mathrm{ref}}$ in Ω, where the reference temperature is defined in Table 3.3. We aim at finding the initial values of the primary variables $\underline{u}$ and p_{w} that correspond to the equilibium solutions of a preliminary problem: here, the Neumann boundary condition for the energy equation is zero, that is, $g_{\mathrm{t,N}} = 0$, and temperature is costant and equal to the reference value T_{ref} (in Table 3.3).
We then seek $\underline{u}_0$, $p_{\mathrm{w},0}$ such that the initial solution vector $\underline{U}_0 = [\underline{u}_0^{\mathrm{T}}, p_{\mathrm{w},0}, T_0]^{\mathrm{T}}$ satisfies the equilibrium equations (3.4), (3.5a) and (3.6a) with thermal flux $g_{\mathrm{t,N}}$ equal to 0 on the domain boundary $\partial\Omega$. Towards this end, we first observe that (3.8a) reduces to

$$\frac{d\rho_{\mathrm{w}}}{\rho_{\mathrm{w}}} = \frac{dp_{\mathrm{w}}}{K_{\mathrm{w}}} \tag{3.9}$$

that brings to $p_{\mathrm{w}} = \rho_{-\infty} \exp\left(\frac{1}{K_{\mathrm{w}}}(p_{\mathrm{w}} - p_{-\infty})\right)$. If we assume that $\rho_{\mathrm{w}} = \rho_{-\infty} = \rho_{\mathrm{w},0}$, we find $p_{\mathrm{w}} = p_{-\infty}$; furthermore, by substituting these assumptions into the hydraulic equilibrium equation we find

$$p_{\mathrm{w},0}(x, y) = p_{\mathrm{w,top}} + \rho_{\mathrm{w},0} g(1 - y) \tag{3.10}$$

where $p_{\mathrm{w,top}}$ is a datum for water pressure that is defined at the top boundary of the domain $(0, 1) \times \{1\}$. Finally, we search for $\underline{u}_0$ as the solution to the equilibrium equation of mechanical forces:

$$\int_{\Omega} 2\mu' \nabla_{\mathrm{s}} \underline{u}_0 \,:\, \nabla_{\mathrm{s}} \underline{v} + \lambda(\nabla \cdot \underline{u}_0)(\nabla \cdot \underline{v}) - b p_{\mathrm{w},0} \nabla \cdot \underline{v} - \rho^0 \underline{F}_{\mathrm{m}} \cdot \underline{v}\, dx = \int_{\Gamma_{\mathrm{N}}} \underline{g}_{\mathrm{m,N}} \cdot \underline{v}\, dx, \tag{3.11}$$

for all $\underline{v} \in \mathcal{X}^{\mathrm{u}}$, such that $\underline{v} \cdot \underline{n}|_{\partial\Omega \setminus \Gamma_{\mathrm{N}}} = 0$.

	SI unit	description	reference value	formula
g	$\mathrm{m}\cdot\mathrm{s}^{-2}$	gravity acceleration	9.81	
E	Pa	Young's modulus	$11.4\cdot10^9$ UA $12.3\cdot10^9$ UT $20\cdot10^9$ USC	
ν	%	Poisson's ratio	0.3	
μ'	Pa	Lamé parameter,		$\frac{E}{2(1+\nu)}$
λ	Pa	Lamé parameter		$\frac{E\nu}{(1+\nu)(1-2\nu)}$
b	%	Biot coefficient	0.6	
α_s	K^{-1}	solid thermal expansion coefficient	$1.28\cdot10^{-5}$	
α_0	K^{-1}	expansion coefficient	$1.28\cdot10^{-5}$	
κ_w	m^2	intrinsic permeability of porous medium	10^{-21}	
μ_w	$\mathrm{MPa}\cdot\mathrm{s}$	dynamic viscosity		$\mu_\mathrm{w}=\mu_{\mathrm{w},0}\exp(\frac{1808.5}{T})$
$\mu_{\mathrm{w},0}$	$\mathrm{MPa}\cdot\mathrm{s}$	dynamic viscosity coefficient	$2.1\cdot10^{-12}$	
K_s	Pa	bulk modulus of the solid		$K_\mathrm{s}=\frac{E}{3(1-2\nu)}$
K_w	Pa	bulk modulus of water	$2\cdot10^9$	
C_w^p	$\mathrm{J}\cdot\mathrm{kg}^{-1}\cdot\mathrm{K}^{-1}$	heat capacity at constant pressure	4180	
K_0	Pa	drained bulk modulus		$K_0=(1-b)K_\mathrm{s}$
α_w	K^{-1}	thermal expansion coefficient of water		$\alpha_\mathrm{w}=9.52\cdot10^{-5}\log(T-273)-2.19\cdot10^{-4}$
$\alpha_{\mathrm{w,m}}$		dilation coefficient		
C_σ^s	$\mathrm{J\ kg}^{-1}\cdot\mathrm{K}$	specific heat at constant stress	537 UA 603 UT 640 USC	
ρ^0	$\mathrm{Kg}\cdot\mathrm{m}^{-3}$	porous medium initial density	2450 UA 2450 UT 2500 USC	
ρ_w^0	$\mathrm{Kg}\cdot\mathrm{m}^{-3}$	initial water density	10^3	
φ^0	%	initial Eulerian porosity	0.25 UA 0.21 UT 0.19 USC	
h_w^0	$\mathrm{m}^2\cdot\mathrm{s}^{-2}$	initial water enthalpy		$h_\mathrm{w}^0=\frac{p_\mathrm{w}^0-p_\mathrm{atm}}{\rho_\mathrm{w}^0}$
ρ_s	$\mathrm{Kg}\cdot\mathrm{m}^{-3}$	density ratio		$\rho_\mathrm{s}=\frac{\rho^0-\rho_\mathrm{w}^0\varphi^0}{1-\varphi^0}$
C_ϵ^0	$\mathrm{Pa}\cdot\mathrm{K}^{-1}$	specific heat at constant deformation		$C_\epsilon^0=(1-\varphi)\rho_\mathrm{s}C_\sigma^s+\varphi\rho_w C_w^p-9TK_0\alpha_\mathrm{s}^2$
Λ		thermic conductivity tensor		$\Lambda=\mathrm{diag}(\lambda_1,\lambda_2)$
λ_1	$\mathrm{Wm}^{-1}\mathrm{K}^{-1}$	thermic conductivity component	1.5 UA 1.5 UT 1.3 USC	
λ_2	$\mathrm{Wm}^{-1}\mathrm{K}^{-1}$	thermic conductivity component	1 UA 1 UT 1.3 USC	
Θ	$\mathrm{Pa}\cdot\mathrm{s}^{-1}$	volumetric heat sources		

TABLE 3.4: parameters of the constitutive laws.

3.5 Numerical discretization

We resort to an implicit Euler time discretization scheme, with $J_\mathrm{max}=100$ uniform time steps for the non-dimensional time interval $(0,t_\mathrm{f}]$, with $t_\mathrm{f}=1$; the superscript $(\cdot)^+$ refers to the new solution (at the current time step j, for $j=1,...,J_\mathrm{max}$), while $(\cdot)^-$ refers to the solution at the previous time steps. We notice that we cannot use an explicit time scheme since the solid mechanics equilibrium law (3.4) is steady: indeed, a singular mass matrix would be associated with the coupled system (composed of the equilibrium equations in section 3.4.1 and the constitutive laws in section 3.4.2). We also observe that the adopted implicit scheme does not require limitations to the time discretization step Δt to ensure numerical stability.

State variables are defined in the nodes of the mesh, while the internal variables are defined in the quadrature points. We denote by $\mathcal{X}$ and $\mathcal{W}$ suitable Hilbert spaces in Ω for $\underline{U}$ and $\underline{W}$. We denote by $\mathcal{X}^\mathrm{hf}=\mathcal{X}^{\mathrm{hf,u}}\times\mathcal{X}^{\mathrm{hf,p}}\times\mathcal{X}^{\mathrm{hf,t}}$ the high-fidelity space associated with the state variable $\underline{U}=[\underline{u}^\mathrm{T},p_\mathrm{w},T]^\mathrm{T}$ and $\mathcal{W}^\mathrm{hf}$ a suitable high-fidelity

space for the internal variables $\underline{W}$. From now on we omit the superscript hf from the high-fidelity spaces. We aim at finding $\underline{U}^+ \in \mathcal{X}$ and $\underline{W}^+ \in \mathcal{W}$ such that

$$\begin{cases} \displaystyle\int_\Omega 2\mu' \nabla_{\mathrm{s}} \underline{u}^+ : \nabla_{\mathrm{s}} \underline{v} + \left(\lambda \nabla \cdot \underline{u}^+ - (2\mu' + 3\lambda)\,\alpha_{\mathrm{s}} T^+ - b p_{\mathrm{w}}^+\right) \nabla \cdot \underline{v} - \left(\rho^0 + m_{\mathrm{w}}^+\right) \underline{F}_{\mathrm{m}} \cdot \underline{v}\, dx \\ \qquad\qquad = \displaystyle\int_{\Gamma_{\mathrm{N}}} \underline{g}_{\mathrm{m,N}}^+ \cdot \mathbf{v}\, dx; \\ \displaystyle\int_\Omega \frac{1}{\Delta t}(m_{\mathrm{w}}^+ - m_{\mathrm{w}}^-)\,\psi + \gamma^+ (\nabla p_{\mathrm{w}}^+ - \rho_{\mathrm{w}}^+ \underline{F}_{\mathrm{m}}) \cdot \nabla \psi\, dx = 0; \\ \displaystyle\int_\Omega \left(\frac{h_{\mathrm{w}}}{\Delta t}(m_{\mathrm{w}}^+ - m_{\mathrm{w}}^-) + \frac{1}{\Delta t}(Q^+ - Q^-) + \gamma^+ (\nabla p_{\mathrm{w}}^+ - \rho_{\mathrm{w}}^+ \underline{F}_{\mathrm{m}}) \cdot \underline{F}_{\mathrm{m}}\right) \xi - \\ \qquad\qquad \left(-h_{\mathrm{w}}^- (\nabla p_{\mathrm{w}}^+ - \rho_{\mathrm{w}}^+ \underline{F}_{\mathrm{m}}) + \underline{q}^+\right) \cdot \nabla \xi \\ \qquad\qquad = \displaystyle\int_\Omega \Theta^+ \xi\, dx - \int_{\partial\Omega} g_{\mathrm{t,N}}^+ \xi\, dx; \end{cases} \tag{3.12}$$

for all $\underline{v} \in \mathcal{X}^{\mathrm{u}}$ such that $\underline{v} \cdot \underline{n}|_{\partial\Omega \setminus \Gamma_N} = 0$, $\psi \in \mathcal{X}^{\mathrm{p}}$, $\xi \in \mathcal{X}^{\mathrm{t}}$, where

$$\begin{cases} \rho_{\mathrm{w}}^+ = \rho_{\mathrm{w}}^- \exp\left(\dfrac{p_{\mathrm{w}}^+ - p_{\mathrm{w}}^-}{K_{\mathrm{w}}} - 3\alpha_{\mathrm{w}}(T^+ - T^-)\right); \\ \varphi^+ = b - (b - \varphi^-) \exp\left(-(\epsilon_{\mathrm{V}}^+ - \epsilon_{\mathrm{V}}^-) + 3\alpha_0 (T^+ - T^-) - \dfrac{1}{K_s}(p_{\mathrm{w}}^+ - p_{\mathrm{w}}^-)\right); \\ h_{\mathrm{w}}^+ = h_{\mathrm{w}}^- + C_{\mathrm{w}}^{\mathrm{p}} (T^+ - T^-) + \dfrac{\beta_h^{\mathrm{p}} - 3\alpha_{\mathrm{w}} T^+}{\rho_{\mathrm{w}}^+} (p_{\mathrm{w}}^+ - p_{\mathrm{w}}^-); \\ Q^+ = Q^- + \left(\beta_Q^\epsilon + 3\alpha_{\mathrm{s}} K_0 \dfrac{1}{2}(T^+ + T^-)\right)(\epsilon_{\mathrm{V}}^+ - \epsilon_{\mathrm{V}}^-) - \left(\beta_Q^{\mathrm{p}} + 3\alpha_{\mathrm{w,m}}^+ \dfrac{1}{2}(T^+ + T^-)\right)(p_{\mathrm{w}}^+ - p_{\mathrm{w}}^-) \\ \qquad\qquad + C_\epsilon^{0,+} (T^+ - T^-); \\ m_{\mathrm{w}}^+ = \rho_{\mathrm{w}}^+ (1 + \epsilon_{\mathrm{V}}^+)\,\varphi^+ - \rho_{\mathrm{w}}^0\,\varphi^0. \end{cases} \tag{3.13}$$

We remark that integrals in system (3.12)-(3.13) depend on internal variables at the current times $t^{(j)}$ and at the previous times $t^{(j-1)}$, for $j = 1, ..., J_{\max}$. We consider a $\mathtt{p} = 3$ Finite Element (FE) discretization for the displacement component, and a $\mathtt{p} = 2$ FE discretization for both pressure and temperature. Indeed, as discussed in Ref. [Gra09b], to prevent numerical instabilities, we firstly choose a continuous piecewise polynomial of higher degree to approximate the displacement and a lower degree approximation for pressure and temperature; this implementative choise is empirically proven not to be strictly necessary, (in chapter 6 the same degree $\mathtt{p} = 2$ is also used for all the state variables and no instabilities appear in the solutions during the computational time steps).
We equip the FE space $\mathcal{X}$ with the weighted inner product

$$(\underline{U}, \underline{U}') = \frac{1}{\lambda_{\mathrm{u}}} \sum_{d=1}^{2} (\underline{u}_d, \underline{u}_d')_{H^1(\Omega)} + \frac{1}{\lambda_{\mathrm{p}}} (p_{\mathrm{w}}, p_{\mathrm{w}}')_{H^1(\Omega)} + \frac{1}{\lambda_{\mathrm{t}}} (T, T')_{H^1(\Omega)}, \tag{3.14}$$

where the coefficients $\lambda_{\mathrm{u}}, \lambda_{\mathrm{p}}, \lambda_{\mathrm{t}}$ are the largest eigenvalues of the Gramian matrices $\mathbf{C}^{\mathrm{u}}$, $\mathbf{C}^{\mathrm{p}}$, $\mathbf{C}^{\mathrm{t}}$ associated to displacement, pressure and temperature, respectively. Similarly to [TZ21], the inner product (3.14) is motivated by the need for properly taking into account the contributions of displacement, pressure and temperature, which are characterised by different magnitudes. Notice that all the variables are non-dimensionalized.

3.5.1 Parameterization

We consider a vector of four non-dimensional parameters: the Young's modulus E and the Poisson's ratio ν in the region UA, the thermic factor τ and the constant C_{al} in (3.7). For all parameters, we define the non-dimensional parameter domain $\mathscr{P}$ by considering variations of $\pm 15\%$ with respect to the nominal values reported in Table 3.4 that are non-dimensionalized; (we omit the the non-dimensionalizations of the state equations and constitutive laws: non-dimensional state, internal variables and parameters can be computed by using the characteristic constants in table 3.3).

3.6 Solution fields

In figure 3.3 the solutions to problem (3.12), (3.13) are depicted for $\mu = \bar{\mu} = [1.088 \cdot 10^3, 0.3, 21.33, 0.4558]^T$ that is the centroid of the parametric set $\mathscr{P}$. The geometric configuration corresponds to figure 3.2(b) (the number of repositories is $Q_{\text{a}} = 2$). For completeness of results, the time evolution of dimensional pressure and temperature is evaluated at different points in mesh $\mathcal{T}_1$ (cf. figure 3.2(b)) that correspond to three points at $x = \bar{x} = 0.46$ (which is the center of a repository) and $y_1 = 0.0$, $y_2 = 0.2$, $y_3 = 1.0$.

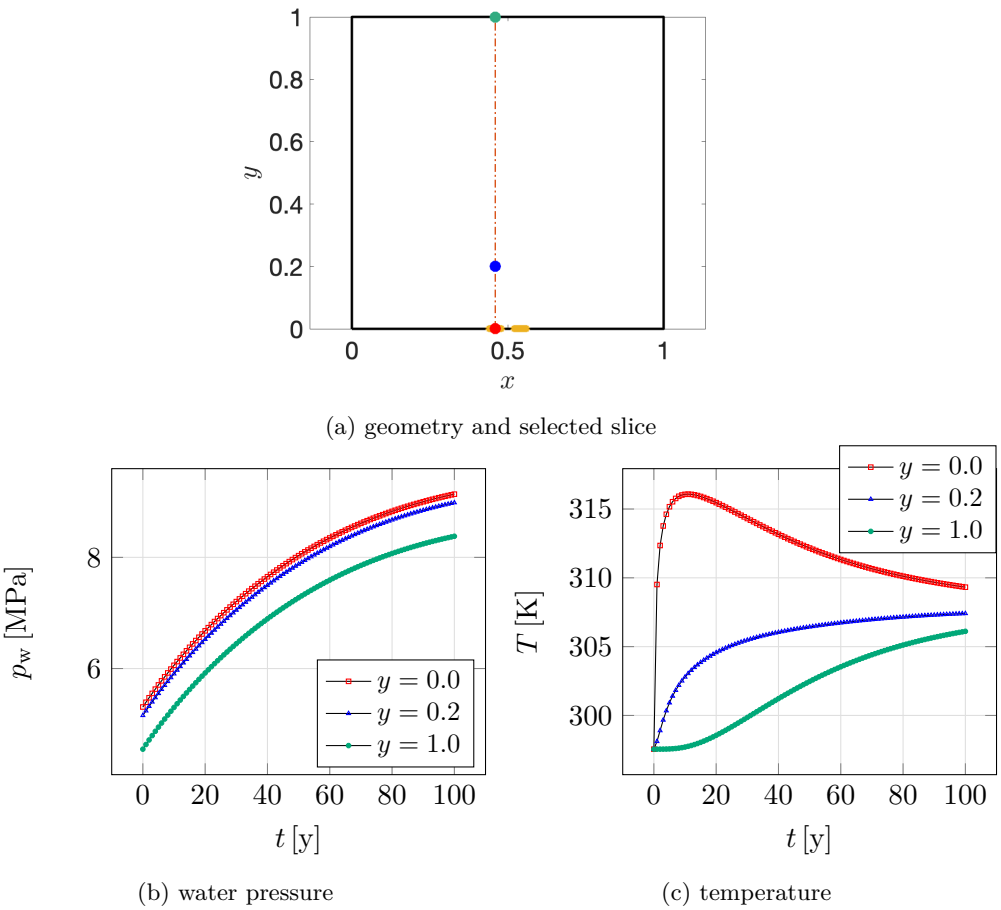

(a) geometry and selected slice

(b) water pressure

(c) temperature

FIGURE 3.4: Time evolution of (b): water pressure, (c): temperature at three different points in a vertical slice (a).

Time evolution of water pressure and temperature is an interesting phenomenon to be observed: as already described in chapter 1, the inclusion of radioactive storage

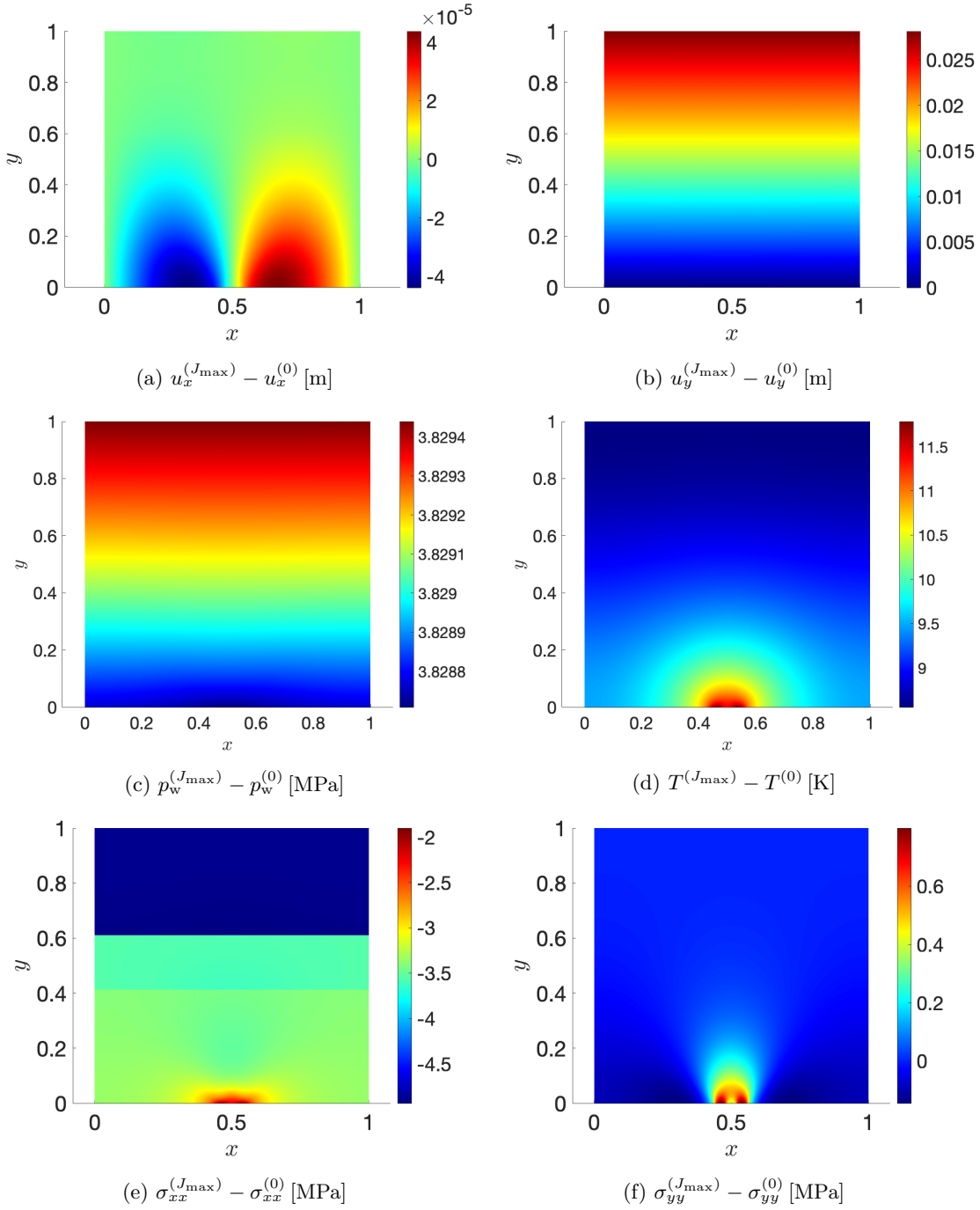

(a) $u_x^{(J_{\max})} - u_x^{(0)}$ [m]

(b) $u_y^{(J_{\max})} - u_y^{(0)}$ [m]

(c) $p_{\mathrm{w}}^{(J_{\max})} - p_{\mathrm{w}}^{(0)}$ [MPa]

(d) $T^{(J_{\max})} - T^{(0)}$ [K]

(e) $\sigma_{xx}^{(J_{\max})} - \sigma_{xx}^{(0)}$ [MPa]

(f) $\sigma_{yy}^{(J_{\max})} - \sigma_{yy}^{(0)}$ [MPa]

FIGURE 3.3: Time gaps of dimensional solutions. (a): horizontal displacement $u_x^{(J_{\max})} - u_x^{(0)}$; (b): vertical displacement $u_y^{(J_{\max})} - u_y^{(0)}$; (c): pressure $p_{\mathrm{w}}^{(J_{\max})} - p_{\mathrm{w}}^{(0)}$ (d): temperature $T^{(J_{\max})} - T^{(0)}$ (e): total horizontal component of stress $\sigma_{xx}^{(J_{\max})} - \sigma_{xx}^{(0)}$; (f): total vertical component of stress $\sigma_{yy}^{(J_{\max})} - \sigma_{yy}^{(0)}$.

at the bottom of the domain directly causes a thermal flow in the repository area (compare figure 3.2(b) and equation (3.6a)), which leads to an increase in pressure and temperature in time. The temperature is then expected to decrease until it returns to the starting value over a very long period of time.

In figure 3.5 we depict the solutions slices at points s.t. $0 \leq x \leq 1$, $y = \bar{y} = 0.2$ and

at the final time step $j = J_{\max}$: these solutions are computed by solving the discretized problem (3.12),(3.13) in mesh $\mathcal{T}_1$ with $\mathtt{p} = 3$ FE polynomial order for displacement and $\mathtt{p} = 2$ order for pressure and temperature. In addition, solutions at the same spatial points and at the same time step are also computed by using a coarser mesh, which we denote $\mathcal{T}_2$ to distinguish it from $\mathcal{T}_1$. Mesh $\mathcal{T}_2$ is characterized by $N^{\mathrm{u}} = 2076$ degrees of freedom for displacement and $N^{\mathrm{p}} = N^{\mathrm{t}} = 1488$ for water pressure and temperature, and it is associated with $\mathtt{p} = 2$ FE discretization for displacement component and $\mathtt{p} = 1$ discretization for both pressure and temperature.

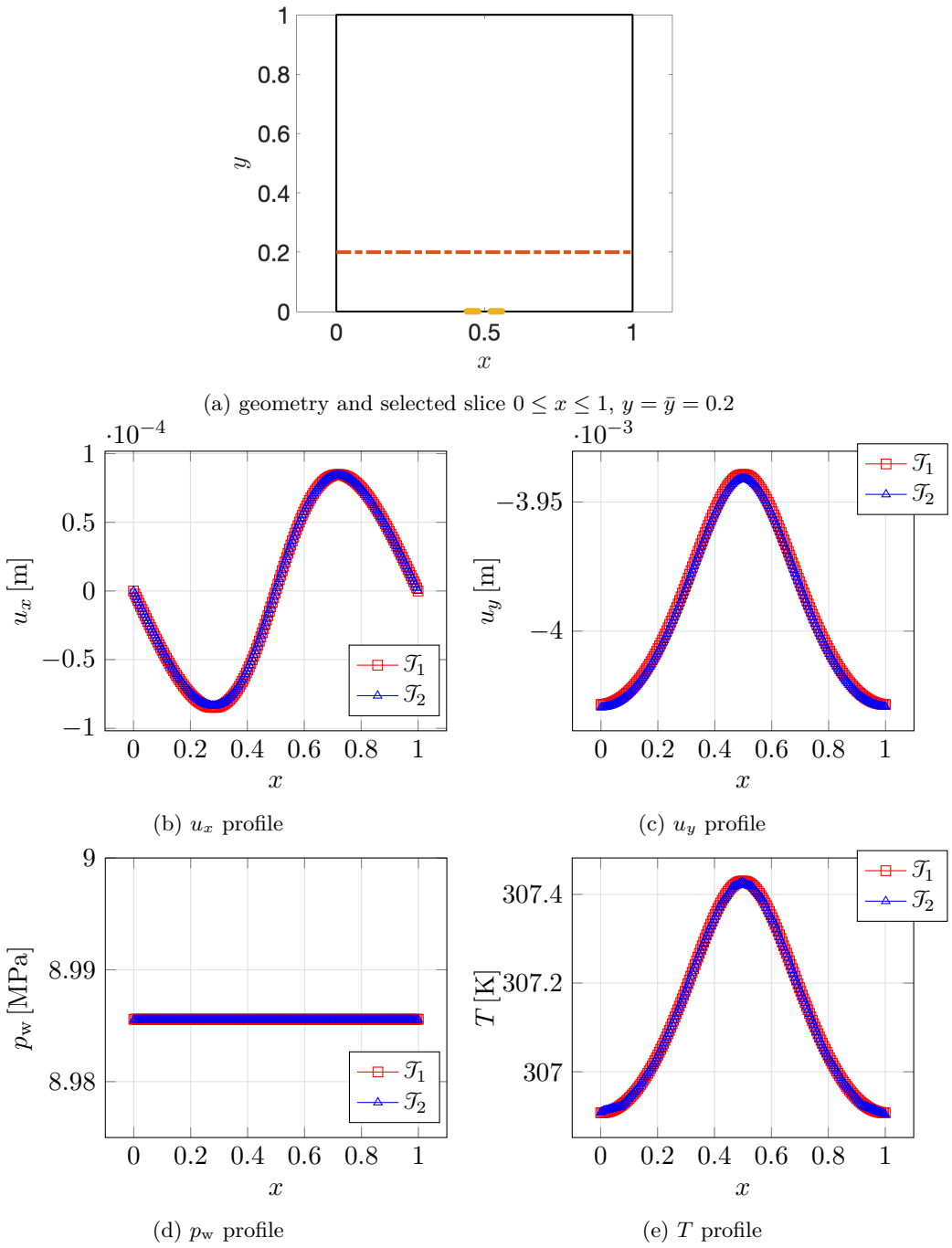

(a) geometry and selected slice $0 \leq x \leq 1$, $y = \bar{y} = 0.2$

(b) u_x profile

(c) u_y profile

(d) p_{w} profile

(e) T profile

FIGURE 3.5: Dimensional solutions at final time at points depicted in figure 3.5(a).

State variables associated with different space discretizations are coincident. In the following, we refer to mesh $\mathcal{T}_1$ for numerical investigations.

3.7 Conclusions

In this chapter we presented the THM coupled problem in a geothermal porous medium: we introduced in section 3.4 the mathematical formulation as well as in section 3.5 its FE discretization; in section 3.6 FE solutions are computed for fixed parametric configuration $\bar{\mu} \in \mathcal{P}$ and the evolution of state variables (cf. table 3.1) and total stress (cf. equation (3.1)) is depicted in space and time. In chapter 4, a monolithic projection-based ROM is built for the THM problem: to do that, we apply (and extend when required) the methods described for a general time-dependent parabolic PDE in chapter 2.

Chapter 4

A monolithic model reduction method for the THM problem

In this chapter we develop a projection-based monolithic model order reduction technique for the THM system introduced in chapter 3. The proposed methodology is an extension of the RB technique for parabolic problems introduced in chapter 2 to problems with internal variables. The outline of this chapter is the following. First, in section 4.1, we provide a survey on MOR works on nonlinear problems in mechanics; in section 4.2 we introduce the numerical discretization of the THM system, introduced in chapter 3 in a compact form. In section 4.3, we illustrate the application of MOR techniques (cf. chapter 2) to a general class of nonlinear problems with internal variables; the proposed methodology can be applied to a broad class of structural mechanics problems with internal variables. To simplify the presentation, we first discuss the solution reproduction problem and then we extend the approach to the parametric case; finally, in section 4.4 we show numerical results for a two-dimensional THM system to illustrate and validate the proposed methodology.

4.1 Relation with previous works

Our methodology is characterised by an offline/online splitting to reduce the marginal cost, and relies on Galerkin projection to devise a ROM for the solution coefficients. We rely on hyper-reduction (cfr. section 2.3.2) to speed up the assembly of the ROM during the online stage, and we rely on adaptive sampling to reduce the offline training costs. In this chapter we adopt a POD-Greedy technique (cf. section 2.2) for THM systems; we emphasize that our method can be applied to a broad class of coupled problems with internal variables. In section 4.3.2 we extend the time-average *a posteriori* error indicator introduced in section 2.4 to problems with internal variables and we compare the latter with a more standard discrete $L^2(0, T_\mathrm{f}; \mathcal{X}')$ dual residual in terms of computational and memory costs and effectivity. This is crucial for the efficiency of the adaptive method. Second, we apply a greedy sampling (based on the proposed error indicator) to effectively explore the parameter domain. Third, we introduce in this framework a hyper-reduction technique based on an element-wise empirical quadrature procedure, which generalizes the technique introduced in section 2.3.2. The key feature of EQ is to recast the problem of hyper-reduction as a sparse representation problem and then resort to state-of-the-art techniques in machine learning and signal processing to estimate the solution to the resulting optimisation problem and ultimately determine a sparse quadrature rule. Here, we rely on the approach employed in [TZ21], which combines the methods in [FCA15; Yan19] and relies on non-negative least-squares to estimate the solution to the sparse representation problem. As discussed in section 4.3 in chapter 4, the presence of internal variables requires several changes to the EQ approach in [TZ21]. Our approach relies on a different treatment of primary and internal

variables compared to the works in [Far+14; ZAF17], as explained in section 4.3.2. In section 4.3 we clarify to what extent the management of internal variables requires a careful adaptation of the MOR technique illustrated in [TZ21] and we briefly compare our treatment of internal variables with [Far+14; ZAF17].

We emphasise that several other hyper-reduction techniques have been proposed in the literature including the empirical interpolation method (EIM [Bar+04]) and its discrete variant [CS10b], the approach in [Ryc09], and Gappy-POD [Car+13; Wil06]. We also refer to [Cas+20; HCF17] for further empirical (or reduced) quadrature procedures for problems in nonlinear mechanics. A thorough comparison of state-of-the-art hyper-reduction techniques is beyond the scope of this work.

The POD-Greedy algorithm was explained in section 2.2: the approach combines POD to compress temporal trajectories with a greedy search driven by an error indicator to explore the parameter domain. Similarly to [Fic+18], we rely on a time-averaged error indicator as the one introduced in section 2.4 to drive the greedy search; furthermore, we test two different compression strategies to update the POD basis at each greedy iteration.

We further observe that the development of online-efficient adaptive ROMs for problems of the form (1.1) is extremely limited in the literature. Relevant examples include the works in [Ryc09; MRC13; LF17], which, however, do not consider adaptive sampling. As regards the application of MOR to THM systems, we recall the recent contributions by Larion *et al.* [Lar+20] and [Lar+22]: note, however, that the two cited works deal with a linearized THM model without internal variables. For completeness, we also refer to [FG20] and [Nas+22] for reduced basis applications to (thermo)-hydro-mechanical problems; we notice that in [FG20] a linear elasticity problem is used for the numerical investigations. The work in [Nas+22] makes some fundamental physical simplifications and the constitutive laws introduced in section 3.4.2 are not considered in the hydro-mechanical system; furthermore, no hyper-reduction techniques are employed.

4.2 Formulation

4.2.1 Notation

The theoretical setting is introduced at the beginning of section 1.2. We recall that D is the number of state variables in the generalized formulation (1.1). Given $\underline{U} \in \mathcal{X}$, we denote by $\mathbf{U} \in \mathbb{R}^{N^{\mathrm{hf}},D}$ the corresponding matrix of coefficients such that $(\mathbf{U})_{j,\ell} = \left(\underline{U}(x_j^{\mathrm{hf}})\right)_\ell$ for $j = 1, \dots, N^{\mathrm{hf}}$ and $\ell = 1, \dots, D$; notation $\mathbf{U}(:,\ell)$ refers to the ℓ^{th} column of the matrix $\mathbf{U}$. As in chapter 2, to simplify notation, we neglect hf index from solution notation. Notice that in principle we should write $\underline{\mathbf{U}}$ to indicate the finite element vector corresponding to vector state variables $\underline{U} \in \mathcal{X}$, but, for a matter of simplicity in the notation, we prefer writing it as $\mathbf{U}$.

For the THM problem described in chapter 3, the state solution vector $\underline{U}$ contains the displacement $\underline{u}$, the water pressure p_{w} and the temperature T; we thus have that $D = 2 + d$ holds for the total number of state variables.

4.2.2 Finite element discretization

We denote by $\{\underline{U}_\mu^{(j)}\}_{j=1}^{J_{\max}} \subset \mathcal{X}^{\mathrm{hf}}$ the FE approximation of the state variables at all times, that is, the ℓ^{th} column of $\mathbf{U}_\mu^{(j)}$ is the approximation of the ℓ^{th} state variable at time $t^{(j)}$. On the other hand, we denote by $\mathbf{W}_\mu^{(j)} \in \mathbb{R}^{n_{\mathrm{q}},N_{\mathrm{e}},D_{\mathrm{cl}}}$ the tensor associated

with the evaluation of the internal variables at time $t^{(j)}$ in the quadrature points:

$$\left(\mathbf{W}_\mu^{(j)}\right)_{q,k,\ell} = \left(\underline{W}_\mu^{(j)}(x_{q,k}^{\mathrm{hf,q}})\right)_\ell, \quad q = 1,\dots,n_\mathrm{q},\ k = 1,\dots,N_\mathrm{e},\ \ell = 1,\dots,D_\mathrm{cl}.$$

Given $\ell \in \{1,\dots,D\}$, we extend the definition of Dirichlet nodes and boundary conditions introduced for a generic PDE in equation (2.3) in the case $D = 1$: we denote by $\mathtt{I}_\mathrm{dir}^\ell \subset \{1,\dots,N^\mathrm{hf}\}$ the indices associated with Dirichlet boundary conditions (if any) of the ℓ^th state component, and we denote by $\mathbf{g}_{\mathrm{dir},\ell}^{(j)} \in \mathbb{R}^{|\mathtt{I}_\mathrm{dir}^\ell|}$ the vector that contains the value of the ℓ^th state component at each Dirichlet node at time $t^{(j)}$.

The FE discretisation of the THM system (3.13) can be written in a compact fashion as follows: for $j = 1, 2, \dots$, find $\underline{U}_\mu^{(j)}$, $\underline{W}_\mu^{(j)}$ such that

$$\begin{cases} \mathcal{R}_\mu^\mathrm{hf}\left(\mathbf{U}_\mu^{(j)},\ \mathbf{U}_\mu^{(j-1)},\ \mathbf{W}_\mu^{(j)},\ \mathbf{W}_\mu^{(j-1)},\ \mathbf{V}\right) = 0, \quad \forall \underline{V} \in \mathcal{X}_0^\mathrm{hf}; \\ \mathbf{U}_\mu^{(j)}(\mathtt{I}_\mathrm{dir}^\ell, \ell) = \mathbf{g}_{\mathrm{dir},\ell}^{(j)}, \quad \ell = 1,\dots,D; \\ \left(\mathbf{W}_\mu^{(j)}\right)_{q,k,\ell} = \mathcal{F}_{\mu,\ell}^\mathrm{hf}\left(\left(\mathbf{E}_k^{\mathrm{qd},\star}\mathbf{U}_\mu^{(j)}\right)_{q,\cdot},\ \left(\mathbf{E}_k^{\mathrm{qd},\star}\mathbf{U}_\mu^{(j-1)}\right)_{q,\cdot},\ \left(\mathbf{W}_\mu^{(j-1)}\right)_{q,k,\cdot}\right), \\ \qquad\qquad q = 1,\dots,n_\mathrm{q}, k = 1,\dots,N_\mathrm{e}, \ell = 1,\dots,D_\mathrm{cl}. \end{cases} \tag{4.1}$$

where $\mathcal{X}_0^\mathrm{hf} := \{\underline{V} \in \mathcal{X}^\mathrm{hf} : \mathbf{V}(\mathtt{I}_\mathrm{dir}^\ell, \ell) = 0,\ \ell = 1,\dots,D\}$ is the test space for all state equations. Note that $\mathcal{R}_\mu^\mathrm{hf}$ and $\underline{\mathcal{F}}_\mu^\mathrm{hf}$ are the discrete counterparts of the operators $\mathcal{G}_\mu$ and $\underline{\mathcal{F}}_\mu$ in (1.1), for $\mu \in \mathcal{P}$.

Note that the constitutive laws are stated in the quadrature points of the mesh and the internal fields should be computed in the quadrature points of the mesh. Dirichlet boundary conditions are imposed via a lifting; Neumann boundary conditions are introduced in the weak formulation associated to the first equation in system (4.1) via the Greens formula. We refer to equations (3.12), (3.13) for the particular form of problem (4.1) associated to the THM system of interest.

Remark 1. *As discussed in section 3.5, to avoid instabilities, it might be necessary to use polynomials of degree κ for displacement and $\kappa - 1$ for pressure and temperature: as a result, we should introduce separate restriction operators (introduced in (2.2)) and separate FE spaces for the different components of the state $\{\underline{U}_\mu^{(j)}\}_j$; We choose to not explicitly address this issue to simplify notation: we remark that the extension to κ-$(\kappa-1)$ discretisations is computationally tedious but methodologically straightforward.*

The underlying problem in (4.1) is second-order in space and first-order in time. At each time step, following [Gra09b], we solve (4.1) for $\underline{U}_\mu^{(j)}$ using a Newton's method with line search; the method requires the computation of the Jacobian associated with $\mathcal{R}^\mathrm{hf}$ and the solution to a coupled linear system of size $N^\mathrm{hf} \cdot D$.

In view of the introduction of the MOR methodology, in particular the hyper-reduction procedure, we write the residual $\mathcal{R}^\mathrm{hf}$ as the sum of local contributions: extension of expression (2.26) for the THM system reads

$$\begin{aligned} &\mathcal{R}_\mu^\mathrm{hf}\left(\mathbf{U}_\mu^{(j)},\ \mathbf{U}_\mu^{(j-1)},\ \mathbf{W}_\mu^{(j)},\ \mathbf{W}_\mu^{(j-1)},\ \mathbf{V}\right) = \\ &\sum_{k=1}^{N_\mathrm{e}} r_{\mu,k}^\mathrm{hf}\left(\mathbf{E}_k\mathbf{U}_\mu^{(j)},\ \mathbf{E}_k\mathbf{U}_\mu^{(j-1)},\ \left(\mathbf{W}_\mu^{(j)}\right)_{\cdot,k,\cdot},\ \left(\mathbf{W}_\mu^{(j-1)}\right)_{\cdot,k,\cdot},\ \mathbf{E}_k\mathbf{V}\right). \end{aligned} \tag{4.2}$$

As explained in section 2.3.2, this decomposition provides the foundation of our hyper-reduction procedure.

4.3 Methodology

We propose a time-marching Galerkin ROM based on linear approximations: we refer to section 2.1.3 for an introduction to the reduced basis method. More precisely, we consider approximations of the form (2.6) where the reduced solution is denoted as $\underline{\widehat{U}}_\mu^{(j)}$ for each time index $j = 1, \dots, J_{\max}$.
In presence of non-homogeneous Dirichlet conditions, it is convenient to consider affine approximations of the form $\underline{\widehat{U}}_\mu^{(j)} = \underline{H}\mathbf{g}^{(j)} + \underline{Z}\,\widehat{\boldsymbol{\alpha}}_\mu^{(j)}$, where $\underline{H}$ is a suitable lifting operator (see, e.g., [TZ21]) and $\mathcal{Z} \subset \mathcal{X}_0$: since in this work we consider homogeneous Dirichlet conditions, we do not address the treatment of non-homogeneous conditions. We consider a single reduced basis $\underline{Z}$ for all state variables in $\{\underline{U}_\mu^{(j)}\}_{j=1}^{J_{\max}}$; the choice of the inner product is discussed in section 3.5 (cf. Eq. (3.14)).

As explained in section 2.3 for a general unsteady PDE, the Galerkin ROM is obtained by projecting (4.1) onto the reduced space $\mathcal{Z}$: this leads to a nonlinear system of N equations at each time step. To reduce assembly costs, it is important to avoid integration over the whole integration domain. Towards this end, we define the indices associated with the "sampled elements" $\mathtt{I}_{\mathrm{eq}} \subset \{1, \dots, N_{\mathrm{e}}\}$ and we define the EQ residual:

$$\begin{aligned} &\mathcal{R}_\mu^{\mathrm{eq}}\left(\mathbf{U}_\mu^{(j)},\ \mathbf{U}_\mu^{(j-1)},\ \mathbf{W}_\mu^{(j)},\ \mathbf{W}_\mu^{(j-1)},\ \mathbf{V}\right) = \\ &\sum_{k \in \mathtt{I}_{\mathrm{eq}}} \rho_k^{\mathrm{eq}}\, r_{\mu,k}^{\mathrm{hf}}\left(\mathbf{E}_k\mathbf{U}_\mu^{(j)},\ \mathbf{E}_k\mathbf{U}_\mu^{(j-1)},\ \left(\mathbf{W}_\mu^{(j)}\right)_{\cdot,k,\cdot},\ \left(\mathbf{W}_\mu^{(j-1)}\right)_{\cdot,k,\cdot},\ \mathbf{E}_k\mathbf{V}^{(j)}\right) \end{aligned} \tag{4.3a}$$

where $\boldsymbol{\rho}^{\mathrm{eq}} = [\rho_1^{\mathrm{eq}}, ..., \rho_{N_{\mathrm{e}}}^{\mathrm{eq}}]^T$ is a sparse vector of positive weights such that $\rho_k^{\mathrm{eq}} = 0$ if $k \notin \mathtt{I}_{\mathrm{eq}}$. In conclusion, the Galerkin ROM reads as follows: for $j = 1, 2, \dots$, find $(\underline{\widehat{U}}_\mu^{(j)}, \underline{\widehat{W}}_\mu^{(j)})$ such that

$$\begin{cases} \mathcal{R}_\mu^{\mathrm{eq}}\left(\widehat{\mathbf{U}}_\mu^{(j)},\ \widehat{\mathbf{U}}_\mu^{(j-1)},\ \widehat{\mathbf{W}}_\mu^{(j)},\ \widehat{\mathbf{W}}_\mu^{(j-1)},\ \mathbf{V}\right) = 0, \quad \forall\, V \in \mathcal{Z}; \\ \left(\widehat{\mathbf{W}}_\mu^{(j)}\right)_{q,k,\ell} = \mathcal{F}_{\mu,\ell}^{\mathrm{hf}}\left(\left(\mathbf{E}_k^{\mathrm{qd},\star}\widehat{\mathbf{U}}_\mu^{(j)}\right)_{q,\cdot},\ \left(\mathbf{E}_k^{\mathrm{qd},\star}\widehat{\mathbf{U}}_\mu^{(j-1)}\right)_{q,\cdot},\ \left(\widehat{\mathbf{W}}_\mu^{(j-1)}\right)_{q,k,\cdot}\right), \\ \qquad\qquad q = 1, \dots, n_{\mathrm{q}}, k \in \mathtt{I}_{\mathrm{eq}}, \ell = 1, \dots, D_{\mathrm{cl}}. \end{cases} \tag{4.3b}$$

Note that the internal variables need to be computed only in the sampled elements. Furthermore, computation of (4.3b) only requires the storage of the ROB in the sampled elements, $\{\mathbf{E}_k\boldsymbol{\zeta}_n : n = 1, \dots, N, k \in \mathtt{I}_{\mathrm{eq}}\}$: provided that $|\mathtt{I}_{\mathrm{eq}}| \ll N_{\mathrm{e}}$, this leads to significant savings in terms of online assembly costs and also in terms of online memory costs.

In the remainder of this section, the methodology introduced in chapter 2 is adopted for the construction of the ROB $\underline{Z}$ (*data compression*), the empirical quadrature rule $\boldsymbol{\rho}^{\mathrm{eq}}$ (*hyper-reduction*) and also the error indicator. To simplify the presentation, in section 4.3.1 we focus on the solution reproduction problem, while in section 4.3.2 we discuss the extension to the parametric problem.

4.3.1 Solution reproduction problem

The solution reproduction problem refers to the task of reproducing the results obtained for a fixed value of the parameter $\bar{\mu}$. It is of little practical interest; however, it represents the first step towards the implementation of an effective ROM for the parametric problem. Algorithm 4 summarises the procedure: during the offline stage,

Algorithm 4 Solution reproduction problem: offline/online decomposition

Offline stage:

1: compute $\{\mathbf{U}_{\bar{\mu}}^{(j)}\}_{j\in \mathtt{I}_\mathrm{s}}$, $\mathtt{I}_\mathrm{s} \subset \{1,\dots,J_{\max}\}$;

2: construct the ROB $\underline{Z}$;

3: construct the weights $\boldsymbol{\rho}^{\mathrm{eq}}$.

Online stage:

4: compute $\{\widehat{\boldsymbol{\alpha}}_{\bar{\mu}}^{(j)}\}_{j=1}^{J_{\max}}$ by solving the ROM (4.3).

we compute the HF solution to (4.1) for a given parameter and we store snapshots of the state variables at select time steps $\mathtt{I}_\mathrm{s} \subset \{1,\dots,J_{\max}\}$; then, we use this piece of information to build a ROM for the state; then, during the online stage, we query the ROM for the same value of the parameter considered in the offline stage. Note that during the offline stage we store the state variables in a subset of the time steps and we do not store internal variables: this choice is motivated by the fact that for practical problems memory constraints might prevent the storage of all snapshots; in addition, internal variables might not be computed explicitly by available HF codes.

Construction of the ROB $\underline{Z}$ at line 2 by POD is described in section 2.2.2; we remark that the POD modes depend on the choice of the inner product in $\mathcal{X}^{\mathrm{hf}}$, that is discussed in section 3.5 for the THM problem. As for the computation of empirical quadrature weights at line 3, the algorithm to find the sparse weigths $\boldsymbol{\rho}^{\mathrm{eq}}$ is described in section 2.3.2; in the following we specify its use in the occurrence of internal variables.

Hyper-reduction

Following expressions (2.23) and (2.28), we specify the algebraic form of the algebraic reduced residuals associated with the HF and empirical quadrature rules:

$$\begin{cases} \left(\widehat{\mathbf{R}}_\mu^{\mathrm{hf}}\left(\boldsymbol{\alpha};\boldsymbol{\beta},\mathbf{W}'\right)\right)_n := \mathcal{R}_\mu^{\mathrm{hf}}\left(\mathbf{Z}\,\boldsymbol{\alpha},\ \mathbf{Z}\,\boldsymbol{\beta},\ \mathbf{W}_\mu^\star,\ \mathbf{W},\ \boldsymbol{\zeta}_n\right), \quad n=1,\dots,N, \\ \left(\widehat{\mathbf{R}}_\mu^{\mathrm{eq}}\left(\boldsymbol{\alpha};\boldsymbol{\beta},\mathbf{W}'\right)\right)_n := \mathcal{R}_\mu^{\mathrm{eq}}\left(\mathbf{Z}\,\boldsymbol{\alpha},\ \mathbf{Z}\,\boldsymbol{\beta},\ \mathbf{W}_\mu^\star,\ \mathbf{W}',\ \boldsymbol{\zeta}_n\right), \quad n=1,\dots,N, \end{cases}$$

where $\boldsymbol{\alpha},\boldsymbol{\beta}\in\mathbb{R}^N$, $\mathbf{W}'\in\mathbb{R}^{n_\mathrm{q},N_\mathrm{e},D_\mathrm{cl}}$, and $\mathbf{W}_\mu^\star = \mathbf{W}_\mu^\star(\boldsymbol{\alpha},\boldsymbol{\beta};\mathbf{W}')$ is obtained by substituting in $(4.1)_3$. We further introduce the Jacobians $\mathbf{J}_\mu^{\mathrm{hf}}(\cdot),\mathbf{J}_\mu^{\mathrm{eq}}(\cdot)$ such that

$$\begin{aligned} \left(\mathbf{J}_\mu^{\mathrm{hf}}(\boldsymbol{\alpha};\boldsymbol{\beta},\mathbf{W}')\right)_{n,n'} &:= \frac{\partial}{\partial\alpha_{n'}}\left(\widehat{\mathbf{R}}_\mu^{\mathrm{hf}}\left(\boldsymbol{\alpha};\boldsymbol{\beta},\mathbf{W}'\right)\right)_n, \\ \left(\mathbf{J}_\mu^{\mathrm{eq}}(\boldsymbol{\alpha};\boldsymbol{\beta},\mathbf{W}')\right)_{n,n'} &:= \frac{\partial}{\partial\alpha_{n'}}\left(\widehat{\mathbf{R}}_\mu^{\mathrm{eq}}\left(\boldsymbol{\alpha};\boldsymbol{\beta},\mathbf{W}'\right)\right)_n, \end{aligned}$$

for $n,n' = 1,\dots,N$. We observe that the computation of the Jacobian involves the derivatives with respect to the constitutive laws in $\underline{\mathcal{F}}_\mu^{\mathrm{hf}}$.

Remark 2. *The presence of internal variables complexifies the application of EQ procedures (cf. section 2.3.2). Indeed, the general problem formulation in Equation (4.1) (and Equations (3.12)-(3.13) for the specific problem of interest) shows the dependence of the residual on state and internal variables both at the current time and at the previous time step. Therefore, in order to compute the entries of* $\mathbf{C},\mathbf{b}$ *associated with (2.31), we should prescribe the triplets* $\left\{\left(\boldsymbol{\alpha}_{\mathrm{train}}^{(j)},\boldsymbol{\alpha}_{\mathrm{train}}^{(j-1)},\mathbf{W}_{\mathrm{train}}^{(j-1)}\right)\right\}_{j\in\mathcal{I}_\mathrm{s}}$*: knowledge of*

the primary and internal variables at time j and $j-1$ for $j \in \mathtt{I}_s$ is thus necessary to construct residuals at each time step.

A first option, which was considered in Ref. [Far+14], is to store state and internal variables $\{\underline{U}_\mu^{(j)}, \underline{U}_\mu^{(j-1)}, \underline{W}_\mu^{(j-1)}\}$ at all select time steps $j \in \mathtt{I}_s$. This choice might lead to very large offline memory costs — which scale with $\left(n_{\mathrm{q}} N_{\mathrm{e}} D_{\mathrm{cl}} + 2N^{\mathrm{hf}} D\right) |\mathtt{I}_{\mathrm{s}}|$ — and might require modifications to the HF solver, but it does not require the solution to the ROM with HF quadrature.

An alternative approach, which is considered in this work, is to use HF data to build the ROB for the state variables, solve the ROM (4.3) with HF quadrature to obtain $\{\widehat{\boldsymbol{\alpha}}_{\mathrm{hf},\mu}^{(j)}, \widehat{\mathbf{W}}_{\mathrm{hf},\mu}^{(j)}\}_j$, and then set $\boldsymbol{\alpha}_{\mathrm{train}}^{(j)} = \widehat{\boldsymbol{\alpha}}_{\mathrm{hf},\mu}^{(j)}$ and $\mathbf{W}_{\mathrm{train}}^{(j)} = \widehat{\mathbf{W}}_{\mathrm{hf},\mu}^{(j)}$. This choice contributes to reduce offline memory costs and might also avoid modifications to the HF solver; however, it increases offline computational costs. In the section dedicated to numerical results, in particular in Table 4.1, we report computational costs of ROM solves based on HF and empirical quadrature.

We emphasize that the other pieces of our approach — Galerkin projection, POD-Greedy algorithm, time-averaged residual indicator — can cope with both strategies. The decision should thus be based on the particular software architecture considered and on the design constraints.

4.3.2 Parametric problem

In order to extend our methodology to parametric problems, we should address two challenges. First, we should explore the parameter domain $\mathcal{P}$ in an efficient way; second, we should devise a compression strategy to combine information from different parameters.

We choose to adopt the adaptive strategy — the so called POD-Greedy method— which is described in section 2.2.3 (cf. Algorithm 2). The POD-Greedy algorithm takes as input a discretisation of $\mathcal{P}$ denoted as Ξ_{train}, a tolerance tol_{loop} for the outer greedy loop, a tolerance tol_{pod} for the data compression step, and the maximum number of greedy iterations $N_{\mathrm{count,max}}$ — we here prescribe the termination condition based on the error indicator; we refer to the pMOR literature for other termination conditions.

We observe that the high-fidelity snapshots computation at line 3 can be summarized by the following building block:

$$\left[\{\mathbf{U}_\mu^{(j)}\}_{j\in\mathtt{I}_{\mathrm{s}}}\right] = \texttt{FE-solve}(\mu)$$

that represents the FE solver for the high-fidelity discretization in (4.1); it takes as input the vector of parameters and returns the snapshot set associated with the sampling times $\mathtt{I}_{\mathrm{s}} \subset \{1, \dots, J_{\max}\}$ (without saving internal variables, as pointed out in remark 2). Line 4, corresponding to a data compression step, can be rewritten in the following way, in the occurence of internal variables:

$$\left[\underline{Z}',\ \boldsymbol{\lambda}'\right] = \texttt{data-compression}\left(\underline{Z},\ \boldsymbol{\lambda}, \{\mathbf{U}_{\mu^\star}^{(j)}\}_{j\in\mathtt{I}_{\mathrm{s}}}, (\cdot,\cdot), tol_{\mathrm{pod}}\right);$$

it takes as input the current ROB and the POD eigenvalues $\boldsymbol{\lambda} = [\lambda_1, \dots, \lambda_N]^T$, and returns the updated ROB Z' and the updated eigenvalues $\boldsymbol{\lambda}'$. Finally, we observe that construction of the ROM comprises both the construction of the Galerkin ROM and of the error indicator. In the remainder of this section, we discuss each element of the procedure.

We remark that the presence of internal variables requires further modifications of the ROM also in the implementation of an adaptive strategy. Ref. [Far+14] is an

example of a POD setting: the training parameters are choosen *a priori* and for these selected configurations the primary and the internal variables are stored; then, a POD is performed over the primary snapshots. In the present work, the chosen adaptive strategy requires the computation of error indicators. In mode detail, the computation of the dual residual requires either the knowledge of internal and primary variables at each computational time step, or the solution of a ROM.

Time-averaged error indicator

Once having defined trajectories $\mathbb{U}_\mu = \{\underline{U}_\mu^{(j)}\}_{j=1}^{J_{\max}}$ and $\mathbb{W}_\mu = \{\underline{W}_\mu^{(j)}\}_{j=1}^{J_{\max}}$, for a given parameter $\mu \in \mathcal{P}$, time-averaged residual (2.34) can be extended as follows

$$\mathcal{R}^{\mathrm{hf}}_{\mathrm{avg},\mu}\left(\mathbb{U}_\mu, \mathbb{W}_\mu, \underline{V}\right) := \sum_{j=1}^{J_{\max}} \left(t^{(j)} - t^{(j-1)}\right) \mathcal{R}^{\mathrm{hf}}_\mu\left(\underline{U}_\mu^{(j)}, \underline{U}_\mu^{(j-1)}, \underline{W}_\mu^{(j)}, \underline{W}_\mu^{(j-1)}, \underline{V}\right), \quad \forall\, \underline{V} \in \mathcal{X}_0^{\mathrm{hf}}. \tag{4.4}$$

Error indicator in (2.35)(based on high-fidelity quadrature) now depends on both state and internal trajectories:

$$\Delta^{\mathrm{hf}}_\mu\left(\mathbb{U}_\mu, \mathbb{W}_\mu\right) = \sup_{\underline{V} \in \mathcal{X}_0^{\mathrm{hf}} \setminus \{0\}} \frac{\mathcal{R}^{\mathrm{hf}}_{\mathrm{avg},\mu}\left(\mathbb{U}_\mu, \mathbb{W}_\mu, \underline{V}\right)}{\|\underline{V}\|}. \tag{4.5}$$

In an analogous form, error indicator (2.36) based hyper-reduction can be written as follows:

$$\Delta_\mu\left(\mathbb{U}_\mu, \mathbb{W}_\mu\right) = \sup_{\underline{V} \in \mathcal{Y}_M \setminus \{0\}} \frac{\mathcal{R}^{\mathrm{eq,r}}_{\mathrm{avg},\mu}\left(\mathbb{U}_\mu, \mathbb{W}_\mu, \underline{V}\right)}{\|\underline{V}\|}, \tag{4.6}$$

where $\mathcal{Y}_M \subset \mathcal{X}_0^{\mathrm{hf}}$ is an M-dimensional empirical test space, while $\mathcal{R}^{\mathrm{eq,r}}_{\mathrm{avg},\mu}$ is defined by replacing $\mathcal{R}^{\mathrm{hf}}_\mu$ in (4.4) with a suitable sparse weighted residual of the form (4.3a), defined over the elements $\mathtt{I}_{\mathrm{eq,r}} \subset \{1, \ldots, N_{\mathrm{e}}\}$. In our implementation, we compute the error indicator during the time iterations — as opposed to after having computed the whole solution trajectory. Algorithm 5 provides the complete online solution and residual indicator computations. We find that computation of Δ_μ requires to compute the internal variables $\widehat{\mathbb{W}}_\mu$ in the elements $\mathtt{I}_{\mathrm{eq}} \cup \mathtt{I}_{\mathrm{eq,r}}$ at each time iteration (cf. (4.3b)), and it requires to store the trial ROB Z in $\{\mathtt{D}_k : k \in \mathtt{I}_{\mathrm{eq}} \cup \mathtt{I}_{\mathrm{eq,r}}\}$ and the test basis $\underline{Y} = [\underline{\psi}_1, \ldots, \underline{\psi}_M]$ in $\{\mathtt{D}_k : k \in \mathtt{I}_{\mathrm{eq,r}}\}$.

Algorithm 5 Online solution and residual computations

1: Initial state and internal variables; set $\widehat{\mathbf{R}}_\mu^{\mathrm{avg}} = \mathbf{0}$.
2: **for** $j = 1, \ldots, J_{\max}$ **do**
3: Compute $\widehat{\boldsymbol{\alpha}}_\mu^{(j)}$ by solving (4.3b).
4: Compute $\left(\widehat{\mathbf{W}}_\mu^{(j)}\right)_{\cdot,k,\cdot}$ for all $k \in \mathtt{I}_{\mathrm{eq,r}}$ using $(4.3b)_2$.
5: Assemble $\widehat{\mathbf{R}}_\mu^{(j)} \in \mathbb{R}^M$ such that $\left(\widehat{\mathbf{R}}_\mu^{(j)}\right)_m = \mathcal{R}_\mu^{\mathrm{eq,r}}\left(\underline{\widehat{U}}_\mu^{(j)}, \underline{\widehat{U}}_\mu^{(j-1)}, \underline{\widehat{W}}_\mu^{(j)}, \underline{\widehat{W}}_\mu^{(j-1)}, \underline{\psi}_m\right)$ for $m = 1, \ldots, M$.
6: Update $\widehat{\mathbf{R}}_\mu^{\mathrm{avg}} = \widehat{\mathbf{R}}_\mu^{\mathrm{avg}} + (t^{(j)} - t^{(j-1)})\widehat{\mathbf{R}}_\mu^{(j)}$.
7: **end for**
return $\{\widehat{\boldsymbol{\alpha}}_\mu^{(j)}\}_j$ and $\Delta_\mu = \|\widehat{\mathbf{R}}_\mu^{\mathrm{avg}}\|_2$.

ROM construction

In order to devise an actionable ROM, we should discuss (i) the choice of the EQ rule $\boldsymbol{\rho}^{\mathrm{eq}}$, (ii) the choice of the test space $\mathcal{Y}$ and of the EQ rule $\boldsymbol{\rho}^{\mathrm{eq,r}}$ in (4.6). In view of the presentation of the computational procedure, we define the ROM solution with HF quadrature $(\widehat{\mathbb{U}}_\mu^{\mathrm{hf}}, \widehat{\mathbb{W}}_\mu^{\mathrm{hf}})$; we denote by $\mathbf{C}_\mu \in \mathbb{R}^{K\cdot N, N_{\mathrm{e}}}$ the EQ matrix associated with the manifold accuracy constraints in (2.31) for $\mu \in \mathcal{P}$; we further define the vector $\mathbf{c} = [|\mathtt{D}_1|, \dots, |\mathtt{D}_{N_{\mathrm{e}}}|]^T$ associated with the constant function accuracy constraint. Given the test reduced basis $\psi_1, \dots, \psi_M$, we define $\mathbf{G}_\mu^{\mathrm{r}} \in \mathbb{R}^{M, N_{\mathrm{e}}}$ such that

$$\left(\mathbf{G}_\mu^{\mathrm{r}} \boldsymbol{\rho}_{\mathrm{hf}}\right)_m = \mathcal{R}_{\mathrm{avg},\mu}^{\mathrm{eq,r}}\left(\widehat{\mathbb{U}}_\mu^{\mathrm{hf}}, \widehat{\mathbb{W}}_\mu^{\mathrm{hf}}, \underline{\psi}_m\right), \quad \forall\, \mu \in \mathcal{P},\ m = 1, \dots, M. \tag{4.7}$$

We further define the unassembled average residual $\mathbf{R}_\mu^{\mathrm{avg,un}} \in \mathbb{R}^{n_{\mathrm{lp}}, N_{\mathrm{e}}, D_{\mathrm{eq}}}$: we observe that $\mathbf{R}_\mu^{\mathrm{avg,un}}$ might be employed to build the FE residual and ultimately compute the Riesz representers $\widehat{\psi}_\mu$ in (2.38), and also, given $\mathcal{Y}$, to compute $\mathbf{G}_\mu^{\mathrm{r}}$.

We focus on the construction of the ROM at the n_{c}-th iteration of the POD Greedy algorithm. We define $\Xi^\star = \{\tilde{\mu}^{(j)}\}_{j=1}^{n_{\mathrm{rom}}} = \{\mu^{\star,(i)}\}_{i=1}^{n_{\mathrm{c}}} \cup \{\tilde{\mu}^{(j)}\}_{j=1}^{n_{\mathrm{train,eq}}}$, where $\mu^{\star,(1)}, \dots, \mu^{\star,(n_{\mathrm{c}})}$ are the parameters sampled by the greedy algorithm and $\tilde{\mu}^{(1)}, \dots, \tilde{\mu}^{(n_{\mathrm{train,eq}})}$ are independent identically distributed samples from the uniform distribution over $\mathcal{P}$. Algorithm 6 summarises the computational procedure as implemented in our code: the test space $\mathcal{Y}$ is built using POD as in Ref. [Tad19], while the EQ weights $\boldsymbol{\rho}_{\mathrm{eq,r}}$ are obtained using the non-negative least-squares method.

Algorithm 6 Construction of the ROM

1: **for** $\mu \in \Xi^\star$ **do**
2: Solve the ROM with HF quadrature and compute $\mathbf{C}_\mu$ and $\mathbf{R}_\mu^{\mathrm{avg,un}}$.
3: **end for**
4: Assemble $\mathbf{C} = \begin{bmatrix} \mathbf{C}_{\tilde{\mu}^{(1)}} \\ \vdots \\ \mathbf{C}_{\tilde{\mu}^{(n_{\mathrm{rom}})}} \\ \mathbf{c}^T \end{bmatrix} \in \mathbb{R}^{K\cdot N\cdot n_{\mathrm{rom}}, N_{\mathrm{e}}}$ and set $\boldsymbol{\rho}^{\mathrm{eq}} = \mathtt{lsqnonneg}(\mathbf{C}, \mathbf{C}\boldsymbol{\rho}^{\mathrm{hf}}, tol_{\mathrm{eq}})$.
5: Compute the Riesz representers $\{\widehat{\underline{\psi}}_\mu\}_{\mu\in\Xi_\star}$ using (2.38).
6: Define the empirical test space $\mathcal{Y} = \mathrm{span}\{\underline{\psi}_m\}_{m=1}^M$ as $[\{\underline{\psi}_m\}_{m=1}^M] = \mathtt{POD}\left(\{\widehat{\underline{\psi}}_\mu\}_{\mu\in\Xi_\star}, (\cdot,\cdot), tol_{\mathrm{pod,res}}\right)$.
7: Assemble $\mathbf{G} = \begin{bmatrix} \mathbf{G}_{\tilde{\mu}^{(1)}} \\ \vdots \\ \mathbf{G}_{\tilde{\mu}^{(n_{\mathrm{rom}})}} \\ \mathbf{c}^T \end{bmatrix} \in \mathbb{R}^{M\cdot n_{\mathrm{rom}}, N_{\mathrm{e}}}$ and set $\boldsymbol{\rho}^{\mathrm{eq,r}} = \mathtt{lsqnonneg}(\mathbf{G}, \mathbf{G}\boldsymbol{\rho}^{\mathrm{hf}}, tol_{\mathrm{eq,r}})$.

4.4 Numerical results

We measure performance of the ROM using the following discrete $L^2(0, T_\mathrm{f}; \mathcal{X}^\mathrm{hf})$ relative error; (see also (2.8)).

$$E_\mu := \frac{\sqrt{\sum_{j=1}^{J_\mathrm{max}} \left(t^{(j)} - t^{(j-1)}\right) \left\|\underline{U}_\mu^{(j)} - \widehat{\underline{U}}_\mu^{(j)}\right\|^2}}{\sqrt{\sum_{j=1}^{J_\mathrm{max}} \left(t^{(j)} - t^{(j-1)}\right) \left\|\underline{U}_\mu^{(j)}\right\|^2}} \tag{4.8}$$

for any $\mu \in \mathcal{P}$. Similarly, we denote by E_μ^u, E_μ^p and E_μ^t the discrete relative $L^2(0, T_\mathrm{f}; \mathcal{X}^\mathrm{hf})$ errors associated with the estimate of displacement, pressure and temperature, respectively.
In all the numerical tests, for both the in-sample and out-of-sample predictions, we consider a constant time increment $\Delta t = 0.01$ and a total number of 100 computational times; the time increments for solutions storage and for solution computation are equal, i.e. $\Delta t_\mathrm{s} = \Delta t = 0.01$.

4.4.1 Solution reproduction problem

We first present numerical results for a fixed configuration of parameters $\bar{\mu} \in \mathcal{P}$ to validate the ROM described in section 4.3. We consider $\bar{\mu}$ equal to the centroid of $\mathcal{P}$. Notice that the solution fields corresponding to the physical configuration associated with parameter $\bar{\mu}$ are depicted in section 3.6. We perform data compression based on the whole set of snapshots, i.e. $|I_\mathrm{s}| = J_\mathrm{max} = 100$.

Data compression: POD

In Figure 4.1 we compare performance of the global POD based on the weighted inner product $(\cdot, \cdot)$ (introduced in formula (3.14)) with the performance of the component-wise POD. More precisely, we define Z such that

$$[Z, \boldsymbol{\lambda}] = \texttt{POD}\left(\{\underline{U}_{\bar{\mu}}^{(j)}\}_{j \in I_\mathrm{s}}, (\cdot, \cdot), tol_\mathrm{pod}\right), \tag{4.9}$$

and we then extract reduced basis associated to the single state variables of interest, that is, we extract the displacement, pressure and temperature components Z^u, Z^p, Z^t.

Then, we denote the "optimal" (in a discrete L^2 sense) spaces

$$[\underline{Z}^{u,\mathrm{opt}}, \boldsymbol{\lambda}^{u,\mathrm{opt}}] = \texttt{POD}\left(\{\underline{u}_{\bar{\mu}}^{(j)}\}_{j \in \mathtt{I}_\mathrm{s}}, (\cdot, \cdot)_{H^1}, tol_\mathrm{pod}\right); \tag{4.10}$$

$$[\underline{Z}^{p,\mathrm{opt}}, \boldsymbol{\lambda}^{p,\mathrm{opt}}] = \texttt{POD}\left(\{p_{\bar{\mu}}^{(j)}\}_{j \in \mathtt{I}_\mathrm{s}}, (\cdot, \cdot)_{H^1}, tol_\mathrm{pod}\right); \tag{4.11}$$

$$[\underline{Z}^{T,\mathrm{opt}}, \boldsymbol{\lambda}^{T,\mathrm{opt}}] = \texttt{POD}\left(\{T_{\bar{\mu}}^{(j)}\}_{j \in \mathtt{I}_\mathrm{s}}, (\cdot, \cdot)_{H^1}, tol_\mathrm{pod}\right), \tag{4.12}$$

that are found through $D_\mathrm{eq} - 1$ PODs over displacement, pressure and temperature.

In Figure 4.1(a) we show the behaviour of the POD eigenvalues in (4.9); in Figure 4.1(b), (c), (d) we compare the relative projection errors associated with $\underline{Z}^\mathrm{u}$ and $\underline{Z}^{\mathrm{u,opt}}$, $\underline{Z}^\mathrm{p}$, $\underline{Z}^{\mathrm{p,opt}}$ and $\underline{Z}^\mathrm{t}$ and $\underline{Z}^{\mathrm{t,opt}}$. We observe that the projection errors are nearly the same for all the three state variables: this observation suggests to consider a single reduced space to approximate the solution field. For this reason, the predictive errors

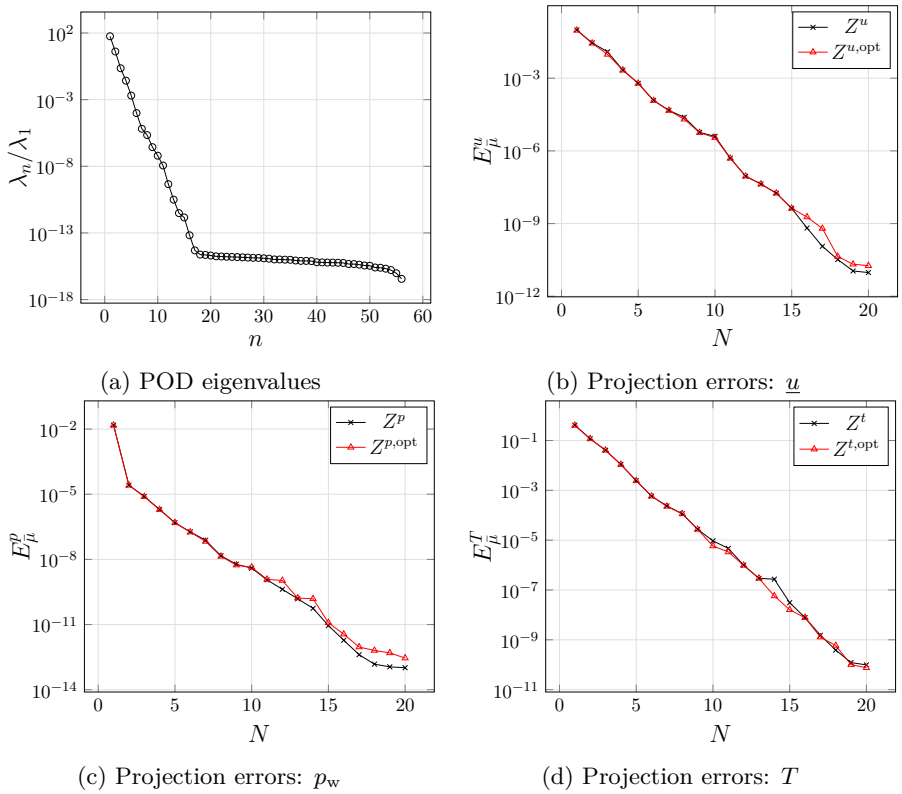

(a) POD eigenvalues

(b) Projection errors: $\underline{u}$

(c) Projection errors: p_{w}

(d) Projection errors: T

FIGURE 4.1: solution reproduction problem. (a): exponential decay of POD eigenvalues. (b), (c), (d): projection errors computed through (4.9) (in black) and (4.10)-(4.12)(in red) for increasing numbers of POD modes.

are computed over the whole vector of solutions (rather than on the single solutions components) by the weighted norm that is associated with the weighted inner product in (3.14).

Hyper-reduction

In Figure 4.2(a) we show the performance of the Galerkin ROM with and without hyper-reduction. We distinguish between the high-fidelity quadrature rule, abbreviated as HFQ, and the empirical quadrature rule for several tolerances tol_{eq}. We also add as a reference, the relative projection error. Figure 4.2(b) shows the percentage of selected elements $\frac{\hat{\text{Q}}}{N_{\text{e}}} \times 100\%$ for the same choices of the tolerance tol_{eq}. We observe that the empirical quadrature procedure is able to significantly reduce the size of the mesh used for online calculations without compromising accuracy. The plateau for $N \gtrsim 14$ is due to the tolerance of the Newton iterative solver.

In Figure 4.3, we show the selected grid elements for two choices of the EQ tolerance value tol_{eq} and for $N = 12$. We observe that the sampled elements are distributed over the whole domain with a slight prevalence of elements in the proximity of the alveoli.

We report in Table 4.1 the computational costs associated to the solution of system (3.12)-(3.13) through the high-fidelity solver and the ROM with high-fidelity quadrature and empirical quadrature, for the solution reproduction problem. We consider a reduced space of size $N = 12$; we also set $tol_{\text{eq}} = 10^{-14}$. The values in Table 4.1 are the computational speedup, that is, speedup $= \frac{\text{HF cost}}{\text{ROM cost}}$ where HF cost is the computational time of solving the high-fidelity solver and ROM cost is the computational time associated to the ROM (we specify in different rows if with HFQ or EQ). The speedup

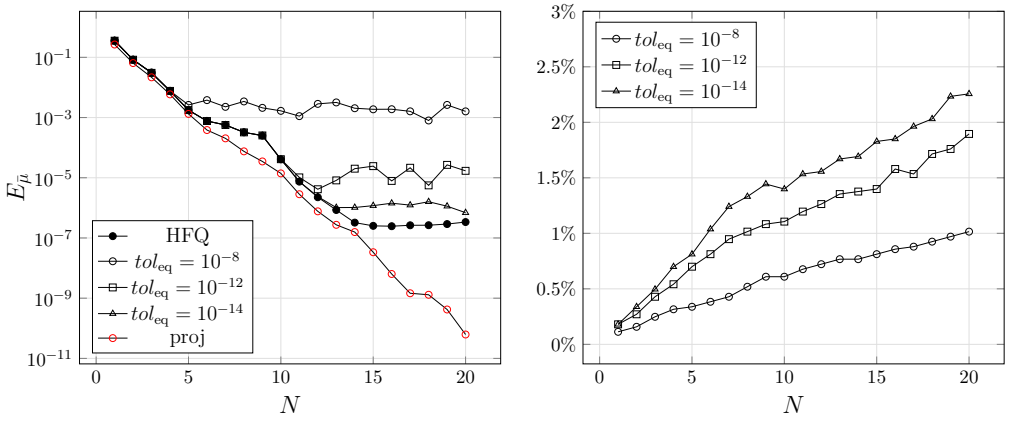

(a) Errors (b) Selected elements

FIGURE 4.2: solution reproduction problem. (a): errors associated to projection error (proj), Galerkin with high-fidelity quadrature (HFQ) and Galerkin with empirical quadrature for several choices of tol_{eq} with respect to the ROM dimension N. (b): percentage of selected elements for several tol_{eq}.

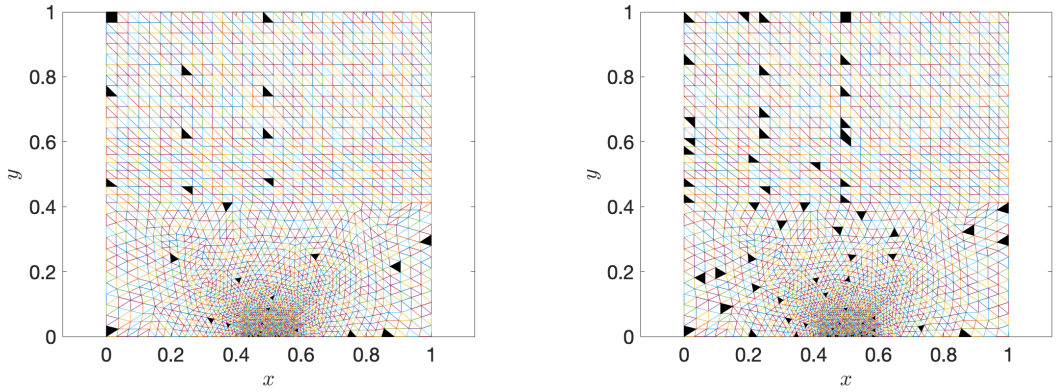

(a) $tol_{\text{eq}} = 10^{-8}$ (b) $tol_{\text{eq}} = 10^{-14}$

FIGURE 4.3: solution reproduction problem. Reduced mesh for two choices of the empirical quadrature tolerance.

associated to the ROM with high-fidelity quadrature is almost 2 and is more than 50 times lower than the speedup of the hyper-reduced ROM. For this model problem, the cost associated with ROM with HFQ is comparable with the cost of the HF solver. As discussed in Remark 2, the choice of solving a ROM with high-fidelity quadrature significantly increases the offline computation costs.

4.4.2 Parametric problem

We present results for the parametric case. We denote by $\Xi_{\text{train}} \subset \mathcal{P}$ the training set used to build the ROM and by $\Xi_{\text{test}} \subset \mathcal{P}$ the test set used to assess performance. Both sets consist of independent identically distributed samples of a uniform distribution in $\mathcal{P}$, with $|\Xi_{\text{train}}| = n_{\text{train}} = 50$ and $|\Xi_{\text{test}}| = n_{\text{test}} = 10$. We also set $tol_{\text{pod}} = 10^{-7}$ in (2.18) and in (2.20b) for data compression, and we set $tol_{\text{pod,res}} = 10^{-5}$ in algorithm 6 for the construction of the empirical test space. We consider $n_{\text{train,eq}}$ additional EQ parameters for the construction of the ROM and the computation of the error indicator, as described in section 4.3.2; we set $n_{\text{train,eq}} = 5$.

	speedup
HF	1
ROM with HFQ	1.87
ROM with EQ	104.60

TABLE 4.1: solution reproduction problem: relative computational costs of the ROM with high-fidelity quadrature and empirical quadrature.

We set the same EQ tolerance for both the construction of the trial and test spaces: $tol_{\text{eq}} = tol_{\text{eq,r}} = 10^{-12}$. The corresponding selected elements are denoted as Q and Q_{r}. We set $I_{\text{s}} \subset \{1, ..., J_{\max}\}$ with $|I_{\text{s}}| = 20$. EQ rules are depicted using the tolerance $tol_{\text{eq}} = 10^{-12}$ (cf . Algorithm 6).

Error estimation

In Figure 4.4 we compare the dual residual and several EQ errors for each parameter μ in the training set Ξ_{train} and for different dimensions of the reduced space that is progressively updated during the execution of the POD-Greedy algorithm. In particular, we show results in two cases: the hierarchical POD-Greedy (H-POD) and the hierarchical approximate POD-Greedy (denoted as HA-POD). Figures 4.4a and 4.4b show for both H-POD and HA-POD to what extent the residual-based error indicator defined in (4.6) is correlated with the relative error (4.8). We observe that for values of the indicators that are larger than 10^{-3}, correlation is very high, while for smaller values correlation is much weaker.

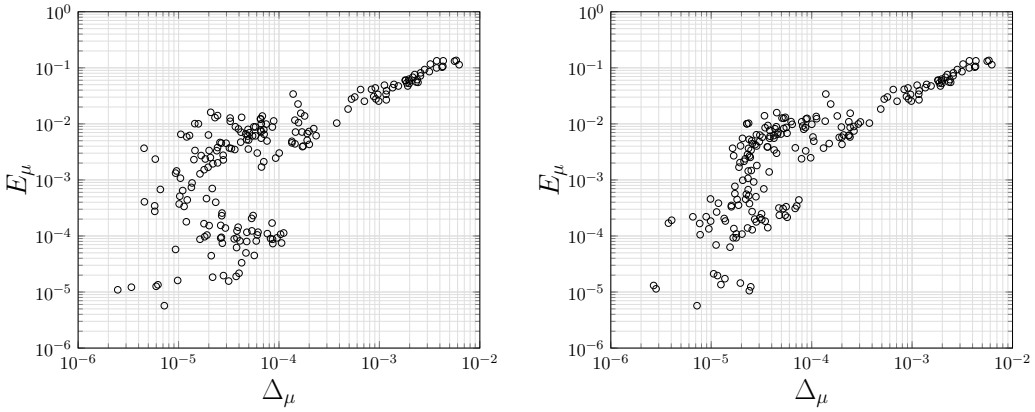

(a) H-POD (b) HA-POD

FIGURE 4.4: parametric problem: correlation between the time-average residual indicator (4.6) and true relative errors (4.8).

To provide a a concrete reference, in Figure 4.5 we investigate the correlation between the relative error (4.8) and the time-discrete $L^2(0, T_{\text{f}}; \mathcal{X}'_{\text{hf},0})$ residual indicator defined in (2.40): we observe that the indicator in (2.40) is significantly more accurate, particularly for small values of the error. As stated in section 4.3, the residual indicator (2.40) is considerably more expensive in terms of both memory and computational costs.

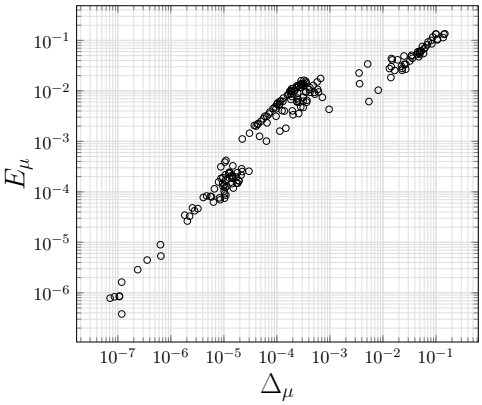

FIGURE 4.5: parametric problem: correlation between residual indicator (2.40) and true relative errors 4.8.

POD-Greedy sampling

In Figures 4.6 and 4.7 we show the POD-Greedy algorithm convergence history, for both the hierarchical and approximate hierarchical PODs. At each iteration of the algorithm, until convergence, the error indicator Δ_μ is illustrated with respect to training parameter indices $\mathcal{I}_{\text{train}} = \{1, ..., |\Xi_{\text{train}}|\}$. At each iteration the selected parameter $\mu^\star$ is marked in red, while the previously selected parameters are marked in green. We also report the dimension of the updated reduced space and the number of sampled elements.

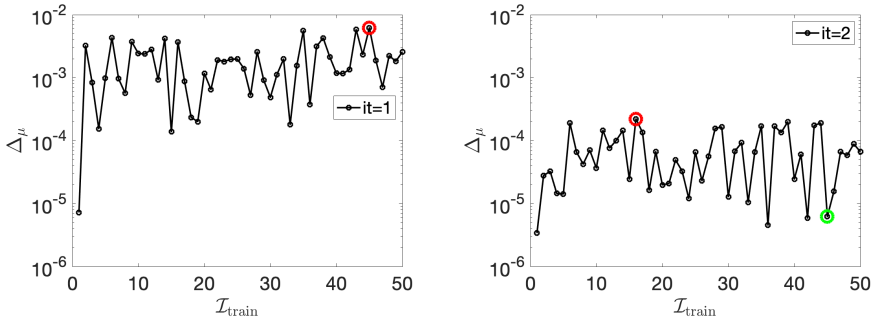

(a) Iteration it = 1; $N = 15$, $Q = 74$, $Q_r = 16$

(b) Iteration it = 2; $N = 26$, $Q = 123$, $Q_r = 18$

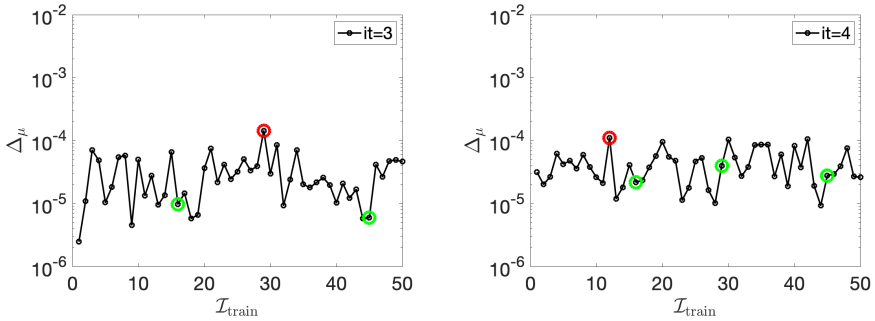

(c) Iteration it = 3; $N = 35$, $Q = 155$, $Q_r = 22$

(d) Iteration it = 4; $N = 43$, $Q = 169$, $Q_r = 18$

FIGURE 4.6: parametric problem: POD-Greedy algorithm convergence history in the H-POD case.

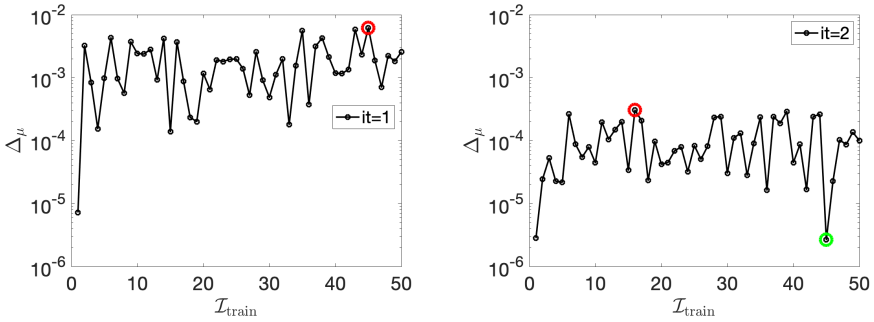

(a) it = 1; $N = 15, Q = 74, Q_{\text{r}} = 16$

(b) it = 2; $N = 25, Q = 120, Q_{\text{r}} = 19$

(c) it = 3; $N = 31, Q = 135, Q_{\text{r}} = 21$

(d) Iteration it = 4; $N = 37, Q = 156, Q_{\text{r}} = 19$

FIGURE 4.7: parametric problem: POD-Greedy algorithm convergence history in the HA-POD case.

Prediction tests

In Figure 4.8, we assess out-of-sample performance of the proposed method. More precisely, we show the behaviour of the maximum relative error (4.8) over the test set $\max_{\mu \in \Xi_{\text{test}}} E_{\mu}$ for both H-POD Greedy and HA-POD Greedy. To provide a relevant benchmark, we compare results with the H-POD Greedy and HA-POD Greedy algorithms based on the exact errors (strong POD-Greedy). For this particular example, we observe that the proposed method is effective to generate accurate ROMs: in particular, the Greedy procedures based on the time-averaged error indicator are comparable in terms of performance with the corresponding strong POD-Greedy algorithms.

4.5 Conclusions

In this chapter we developed and numerically validated a Galerkin projection-based model order reduction procedure for the THM system introduced in equation (1.1) and fully described in chapter 3. We remark that this approach may be extended to other problems of the form (1.1), to demonstrate its generality and its relevance for continuum mechanics applications. We successfully applied the underlying ROM to the parametric THM problem in a two-dimensional case. We proposed a time-averaged error indicator to drive the offline Greedy sampling, and an empirical quadrature procedure to reduce online costs.

The approach discussed in this chapter relies on the assumption that the computational domain is parameter-independent — monolithic MOR. Therefore, it cannot handle parameter-induced topology changes: in particular, it cannot handle changes of

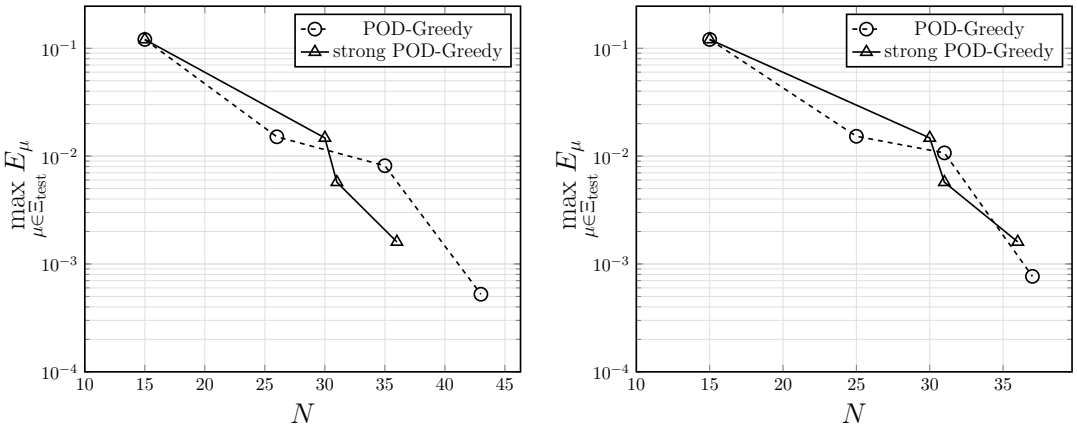

(a) H-POD Greedy

(b) HA-POD Greedy

FIGURE 4.8: parametric problem:out-of-sample performance of the ROM parametric problem obtained using the POD-Greedy algorithm. Comparison with strong POD Greedy.

the number Q_{a} of repositories (cf. figure 3.2). In the remainder of this thesis, we develop a component-based extension of the present method to deal with these important scenarios.

Chapter 5

A one-shot overlapping Schwarz method for component-based model reduction: application to nonlinear elasticity

In this chapter we develop a CB-pMOR formulation for nonlinear PDEs: in particular, we consider a nonlinear elasticity problem. This chapter is organised as follows: in section 5.1 we introduce the domain-decomposition formulation in a simplified case and we describe the link between a classical overlapping DD method and the proposed method; in section 5.2 we present the formulation for general nonlinear PDEs in arbitrary geometries and we introduce the model problem; in section 5.3 we discuss the construction of local approximation spaces, hyper-reduction of the local models and of the objective function; in section 5.5 we investigate performance of our method for a nonlinear elasticity problem.

5.1 One-shot overlapping Schwarz method

5.1.1 The foundations of the method

We first introduce the formulation in the simplified case of two instantiated components Ω_1, Ω_2, depicted in figure 5.1. We consider a steady problem of the type

$$\text{find } u \in \mathcal{X} : \mathcal{G}_\mu(u_\mu, v) = 0 \ \ \forall v \in \mathcal{Y}, \tag{5.1}$$

with (or without) Dirichlet boundary conditions on a portion of the domain $\Gamma_{\text{dir}} \subset \partial\Omega$. If $\mathcal{X} = H^1$, the test space $\mathcal{Y}$ is set equal to $H^1_{\Gamma_{\text{dir}},0}$.

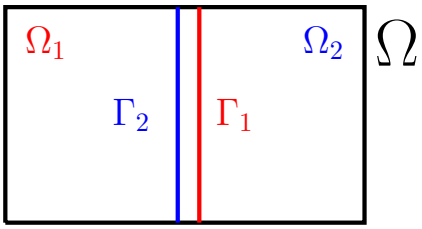

FIGURE 5.1: configuration considered for illustration in section 5.1 and for the analysis of the linear coercive problem in section 5.4.

We start presenting the component-based formulation of a given PDE problem of the form of (5.1) without any level of reduction. To simplify notation, we do not distinguish

between archetype and instantiated components introduced in chapter 1, that is, we only consider a given geometric configuration and local instantiated components to form a global system Ω depicted in black in figure 5.1. In section 5.2, we present the formulation in the general setting: there we distinguish between archetype components (in which local ROBs and local ROMs are built) and instantiated components in which we actually solve the PDE problem by coupling local ROMs.

We denote by $\mathcal{X}_i \subset H^1(\Omega_i)$ a suitable Hilbert space in Ω_i. We introduce the concept of *port* spaces and *bubble* spaces for each instantiated component $i = 1, 2$. A port space is the space of traces of a local solution on port (or interior boundaries), which are introduced in chapter 1 and depicted in figure 1.7 for a given geometric configuration. A bubble space is the space of functions of $\mathcal{X}$ that vanish at port boundaries. We depict in Figure 5.2 a schematic sketch of the bubble and port nodes of a representative FE mesh for the instantiated components considered in this simplified case.

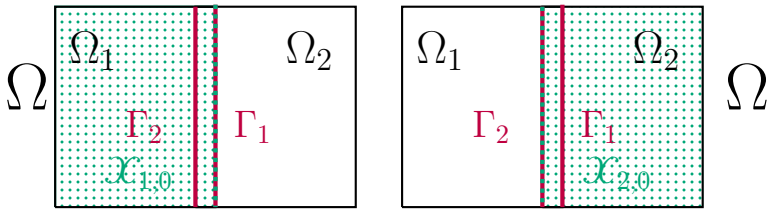

(a) bubble and port in Ω_1 (b) bubble and port in Ω_2

FIGURE 5.2: Sketch of bubble and port nodes associated with (a):$\mathcal{X}_{1,0}$, Γ_1 and (b):$\mathcal{X}_{2,0}$, Γ_2.

This solution decomposition is important, as we explain in section 5.3, since it enables the dimensionality reduction of local problems and it enables effective parallelization of the online solver. The bubble space $\mathcal{X}_{i,0}$ and the port space $\mathcal{U}_i$ are respectively defined as follows: $\mathcal{X}_{i,0} = \{v \in \mathcal{X}_i : v|_{\Gamma_i} = 0\}$ and $\mathcal{U}_i = \{v|_{\Gamma_i} : v \in \mathcal{X}_i\}$, for $i = 1, 2$.

Then, we introduce the *overlapping Schwarz* (OS) iterations as

$$\begin{cases} \text{find } u_1^{(k)} \in \mathcal{X}_1 : \mathcal{G}_1(u_1^{(k)}, v) = 0 \ \ \forall v \in \mathcal{X}_{1,0}, \ \ u_1^{(k)}|_{\Gamma_1} = u_2^{(k-1)}; \\ \text{find } u_2^{(k)} \in \mathcal{X}_2 : \mathcal{G}_2(u_2^{(k)}, v) = 0 \ \ \forall v \in \mathcal{X}_{2,0}, \ \ u_2^{(k)}|_{\Gamma_2} = \begin{cases} u_1^{(k)} \\ u_1^{(k-1)}, \end{cases} \end{cases} \tag{5.2}$$

for $k = 1, 2, \ldots$. Here, $u_i^{(k)}$ denotes the state estimate at the k-th iteration in the i-th subdomain, while $\mathcal{G}_1, \mathcal{G}_2$ are the variational forms associated with the PDE of interest in Ω_1, Ω_2. The first method that was developed by Schwarz is characterized by the condition $u_2^{(k)} = u_1^{(k)}$ on Γ_2 in (5.2): with this choice, the algorithm is named *multiplicative* Schwarz or also *Gauss-Seidel* Schwarz method, to point out the natural connection of this method with the classical Gauss-Seidel iterative method for solving linear systems. More than a century later, starting in the mid 1980's, the potential of Schwarz's idea for parallelizing numerical solvers for boundary value problems was recognized: the algorithm that implements statement (5.2) can be generalized to many subdomains and involves the solution of subproblems of smaller sizes. However, to make it a parallel algorithm that is easily extensible to many subdomains, the boundary condition $u_2^{(k)} = u_1^{(k-1)}$ has to be choosen in (5.3): this is the *additive* Schwarz method, also referred to as *Jacobi-Schwarz* method.

It can be proven that if the global problem (cf. (5.1)) is well-posed and the overlap region is non empty, the Schwarz method applied to problem of the form (5.1) converges, at least for linear coercive problems. We refer to some books on the convergence properties of the classical Schwarz method (both in the multiplicative and additive variants): [QV99], [Smi97], [TW04]. When the convergence of the algorithm is guaranteed, the convergence rate increases if the measure of the overlapping region $|\Omega_1 \cap \Omega_2|$ increases. The convergence of the OS iterations to a limit state $(u_1^\star, u_2^\star)$ implies that $\|u_1^\star - u_2^\star\|_{L^2(\Gamma_1 \cup \Gamma_2)} = 0$. We thus propose to consider the formulation

$$\min_{u_1 \in \mathcal{X}_1, u_2 \in \mathcal{X}_2} \|u_1 - u_2\|_{L^2(\Gamma_1 \cup \Gamma_2)} \quad \text{s.t.} \;\; \mathcal{G}_i(u_i, v_i) = 0 \;\; \forall\, v_i \in \mathcal{X}_{i,0}, \;\; i = 1, 2. \tag{5.3}$$

Formulation (5.3) is a *constrained* optimization statement that penalizes the jump at the components' interfaces Γ_1 and Γ_2, subject to the approximate (in a sense to be defined) satisfaction of the PDE in each instantiated component Ω_1 and Ω_2.
We note that a penalization on the port boundaries, rather that on the whole overlap region, is considered in the formulation (5.3): we conjecture and empirically verify in the numerical tests that the penalization over the ports is sufficient to ensure stability. In the remainder we further comment on the choice of the formulation in view of the introduction of hyper-reduction techniques.

Clearly, the pair $(u_1^\star, u_2^\star)$ is a solution to (5.3); in section 5.4, we show that the solution to (5.3) is unique and depends continuously on the data for linear coercive problems. Note that for linear problems the solution to (5.3) can be computed directly without the need for an iterative scheme: we thus refer to our approach as the one-shot (OS) overlapping Schwarz (OS) method and we use the abbreviation OS2[1]

In order to recast (5.3) into an *unconstrained* problem, we denote by $u_1^{\mathrm{p}}, u_2^{\mathrm{p}}$ the port solutions, that is the restrictions of u_1 and u_2 to the corresponding ports Γ_1 and Γ_2;

Port solutions can be extended over the whole local domains by means of extension operators $\mathtt{E}_i : \mathcal{U}_i \to \mathcal{X}_i$.

For a differential equation that admits a unique solution, the knowledge of the solution at the ports suffices to uniquely characterize the solution in Ω. Indeed, local, distinct and well-defined boundary value problems would need to be solved: the difficulty level of this task would only be related to the difficulty of solving the localized problems. This consideration suggests the idea of representing bubble solutions as the evaluation of a local map, which we call a *port-to-bubble* solution map, at the port solution: the key idea is that each local port-to-bubble map $\mathtt{F}_i : \mathcal{U}_i \to \mathcal{X}_{i,0}$, for $i = 1, 2$, is uniquely determined by the corresponding port solution. It follows that given a local port solution $w \in \mathcal{U}_i$, we can rewrite each local variational form as follows:

$$\mathcal{G}_i(\mathtt{F}_i(w) + \mathtt{E}_i w, v_i) = 0 \;\; \forall\, v_i \in \mathcal{X}_{i,0}, \tag{5.4}$$

Then, we obtain the unconstrained OS2 statement:

$$\min_{u_1^{\mathrm{p}} \in \mathcal{U}_1, u_2^{\mathrm{p}} \in \mathcal{U}_2} \mathfrak{f}(u_1^{\mathrm{p}}, u_2^{\mathrm{p}}) := \|\mathtt{F}_1(u_1^{\mathrm{p}}) + \mathtt{E}_1 u_1^{\mathrm{p}} - \mathtt{F}_2(u_2^{\mathrm{p}}) - \mathtt{E}_2 u_2^{\mathrm{p}}\|^2_{L^2(\Gamma_1 \cup \Gamma_2)}. \tag{5.5}$$

The present derivation can be viewed as a *static condensation* of bubble degrees of freedom and is similar in scope to the approach in [HKP13]. Following taxonomy from the optimization literature, we might view our approach as *black-box* — as opposed to *all-at-once* [HK10, section 1.1].

[1] More rigorously, we should consider the acronym OSOS or $(\mathrm{OS})^2$; however, we opted for OS2 to simplify the notation.

5.1.2 Relation with previous works

The literature on CB-pMOR and reduced-order model/full-order model (ROM-FOM) coupling is extremely vast: CB-pMOR strategies have been presented in [KOH11; HKP13; HCC21; IQR16; MC21; Peg+21] and also recently reviewed in [Buh+20]; ROM/FOM coupling strategies have been proposed for a broad range of applications including compressible flows [CDV11; LA03; Luc+01; Rif+21] incompressible flows [BCI13; Ber+18; WST09], and structural mechanics [CDM15; Ker+13; RR14] — these methods do not distinguish between archetype and instantiated components and do not necessarily involve the training of a library of local ROMs. Recently, several authors have proposed to couple iterative Schwarz DD strategies with local non-intrusive ROMs based on neural network approximations [Che+21a; Li+19].

The OS2 statement presented in (5.3) shares several features with the minimization formulation first proposed in [DH79] in the domain decomposition literature, for coercive linear elliptic PDEs. We recognise some similarities also with [Cas+22] and [BTM22], which are focused on the coupling of projection-based MOR models and high-fidelity models in non-overlapping and overlapping partitions. Rather than [Cas+22] and [BTM22], the present work is characterized by the introduction of static condensation and the use of archetype components for the definition of configuration-independent ROBs.

The OS2 statement presented in (5.3) is also tightly linked to the method proposed in [DB15] for the coupling of local and nonlocal diffusion models (see also [BR09]): as in [DB15], we interpret the OS2 statement as a control problem; while in [DB15] the controls are the nonlocal volume constraint and the local boundary condition, in this work the controls are the local solutions at ports. We also observe that the authors of [DB15] do not exploit the nonlinear least-square structure of the problem and rely on a quasi-Newton scheme to approximate the solution. We show that the choice of using the port solutions as control variables enables the definition of configuration-independent archetype components and is thus key for CB-pMOR.

Our approach is related to the Galerkin-free approach proposed in [BTI09] and further developed in [Ber+18]. The authors consider a HF model in the region of interest and rely on a low-dimensional expansion for the far-field; instead of projecting the equations in the far-field onto a low-dimensional test space, they simply rely on the objective function to compute the far-field solution coefficients (Galerkin-free). Exploiting notation introduced in the previous section, we can state the methods in [BTI09; Ber+18] as:

$$\min_{u_1 \in \mathcal{X}_1, w_2 \in \mathcal{Z}_2} \|u_1 - u_2\|_{L^2(\Omega_1 \cap \Omega_2)} \quad \text{s.t.} \quad \mathcal{G}_1(u_1, v_1) = 0 \; \forall \, v_1 \in \mathcal{X}_{1,0},$$

where $\mathcal{X}_1$ denotes the HF space in Ω_1 and $\mathcal{Z}_2$ denotes the reduced-order space in Ω_2. The approach presented in this work is more general, more robust and also leads to more efficient online calculations, at the price of a much more involved implementation.

Our approach is linked to the minimum residual formulation in [HCC21]: the authors consider a minimization statement in which continuity of solution and fluxes is enforced as a constraint in the formulation, while the global dual residual enters directly in the objective function. The imposition of continuity in the objective function removes compatibility requirements at ports and allows the use of independent spaces in each archetype component; in particular, the use of an overlapping partition allows us to neither explicitly enforce continuity of the solution at ports nor to enforce continuity of normal fluxes. For highly-nonlinear PDEs, we found that this feature remarkably simplifies the implementation of our method and ultimately increases its flexibility.

Finally, the OS2 approach can be interpreted as an alternative to the partition-of-unity method (PUM, [BM97]) considered in [ST22]. Given local approximation spaces, PUM relies on the introduction of a partition of unity to define a global approximation space, and on Galerkin projection to devise the ROM for the deployed system. PUM has strong theoretical guarantees both in terms of approximation and in terms of quasi-optimality properties. Similarly to OS2, PUM requires efficient mesh interpolation to achieve online efficiency. The major difference between OS2 and PUM is that PUM relies on a global variational formulation based on a single model: on the other hand, since in OS2 local models are independent of each other, OS2 can be used to couple different models in different regions of the domain.

5.2 Formulation

5.2.1 Preliminary definitions

We use the superscript $(\cdot)^{\mathrm{a}}$ to indicate quantities and spaces defined for a given archetype component; we further denote by ℓ a generic element of the library $\mathscr{L}$ of archetype components. We define the archetype components $\{\Omega^{\mathrm{a}}_\ell\}_{\ell\in\mathscr{L}} \subset \mathbb{R}^d$; we denote by $\Gamma^{\mathrm{a,dir}}_\ell$ the open subset of $\partial\Omega^{\mathrm{a}}_\ell$ where we impose Dirichlet boundary conditions, and we denote by Γ^{a}_ℓ the portion of $\partial\Omega^{\mathrm{a}}_\ell$ that lies inside the computational domain ("port"). For each archetype component $\ell \in \mathscr{L}$, we define the local discrete high-fidelity finite element space $\mathcal{X}^{\mathrm{a}}_\ell \subset [H^1_{0,\Gamma^{\mathrm{a,dir}}_\ell}(\Omega^{\mathrm{a}}_\ell)]^D$ where we recall that D denotes the number of state variables. Each archetype component is endowed with a bubble space $\mathcal{X}^{\mathrm{a}}_{\ell,0} = \{\underline{v} \in \mathcal{X}^{\mathrm{a}}_\ell : \underline{v}|_{\Gamma^{\mathrm{a}}_\ell} = 0\}$, and a port space $\mathcal{U}^{\mathrm{a}}_\ell = \{\underline{v}|_{\Gamma^{\mathrm{a}}_\ell} : \underline{v} \in \mathcal{X}^{\mathrm{a}}_\ell\} \subset [H^{1/2}(\Gamma^{\mathrm{a}}_\ell)]^D$. We endow $\mathcal{X}^{\mathrm{a}}_\ell$ with the inner product $(\cdot,\cdot)_\ell$ and the induced norm $\|\cdot\|_\ell = \sqrt{(\cdot,\cdot)_\ell}$ and we define $N^{\mathrm{a}}_\ell = \dim(\mathcal{X}^{\mathrm{a}}_\ell)$.

To define port solutions over the whole local (archetype) domains and enable the solution decomposition into bubble and port contributions, we adopt the continuous extension operator $\mathtt{E}^{\mathrm{a}}_\ell : \mathcal{U}^{\mathrm{a}}_\ell \to \mathcal{X}^{\mathrm{a}}_\ell$ such that

$$(\mathtt{E}^{\mathrm{a}}_\ell \underline{w}, \underline{v})_\ell = 0 \quad \forall\, \underline{v} \in \mathcal{X}^{\mathrm{a}}_{\ell,0}, \;\; \mathtt{E}^{\mathrm{a}}_\ell \underline{w}\big|_{\Gamma^{\mathrm{a}}_\ell} = \underline{w}, \qquad \forall\, \underline{w} \in \mathcal{U}^{\mathrm{a}}_\ell; \tag{5.6}$$

in this way $\mathtt{E}^{\mathrm{a}}_\ell \underline{u}^{\mathrm{p}}_\ell \in \mathcal{X}^{\mathrm{a}}_\ell$. We consider the standard H^1 inner product, that is $(\underline{w},\underline{v})_\ell = \int_{\Omega^{\mathrm{a}}_\ell} \nabla\underline{w}\cdot\nabla\underline{v} + \underline{w}\cdot\underline{v}\,dx$.

We define the vector of local parameters μ_ℓ in the parameter region $\mathscr{P}_\ell$, which include geometric and material parameters that identify the physical model in any instantiated component of type ℓ.

5.2.2 Problem formulation

We define the variational form $\mathcal{G}^{\mathrm{a}}_\ell : \mathcal{X}^{\mathrm{a}}_\ell \times \mathcal{X}^{\mathrm{a}}_{\ell,0} \times \mathscr{P}_\ell \to \mathbb{R}$ such that

$$\mathcal{G}^{\mathrm{a}}_\ell(\underline{w},\underline{v};\mu_\ell) = \sum_{k=1}^{N^{\mathrm{e}}_\ell} \int_{\mathtt{D}_{\ell,k}} \eta^{\mathrm{a,e}}_\ell(\underline{w},\underline{v};\mu_\ell)\,dx \;+\; \int_{\partial\mathtt{D}_{\ell,k}} \eta^{\mathrm{a,f}}_\ell(\underline{w},\underline{v};\mu_\ell)\,dx \tag{5.7}$$

where N^{e}_ℓ is the number of mesh elements, $\{\mathtt{D}_{\ell,k}\}_{k=1}^{N^{\mathrm{e}}_\ell}$ denote the elements of the FE mesh for the archetype component Ω^{a}_ℓ and the element and facet forms $\eta^{\mathrm{a,e}}_\ell$ and $\eta^{\mathrm{a,f}}_\ell$ encode the dependence on the problem of interest: we provide their definition for the problem considered in the numerical examples in (5.11). Furthermore, for any $\ell \in \mathscr{L}$,

we define the parametric mapping $\Phi^{\mathrm{a}}_\ell : \Omega^{\mathrm{a}}_\ell \times \mathcal{P}_\ell \to \mathbb{R}^d$ that describes the deformation of the archetype component ℓ for the parameter value $\mu_\ell \in \mathcal{P}_\ell$.

A physical system with N_{dd} components is uniquely described by a function $\mathtt{L} : \{1, \dots, N_{\mathrm{dd}}\} \to \mathcal{L}$ that associates to each instantiated component $i \in \{1, \dots, N_{\mathrm{dd}}\}$ the corresponding archetype component $\mathtt{L}_i \in \mathcal{L}$, and the set of N_{dd} labels $\{\mathtt{L}_i\}_{i=1}^{N_{\mathrm{dd}}} \subset \mathcal{L}$, and the set of parameters $\mu := (\mu_1, \dots, \mu_{N_{\mathrm{dd}}}) \in \mathcal{P} := \bigotimes_{i=1}^{N_{\mathrm{dd}}} \mathcal{P}_{\mathtt{L}_i}$. Given $\mu \in \mathcal{P}$, we define

(i) the mappings $\{\Phi_i\}_{i=1}^{N_{\mathrm{dd}}}$ such that $\Phi_i = \Phi^{\mathrm{a}}_{\mathtt{L}_i}(\cdot; \mu_i)$ for $i = 1, \dots, N_{\mathrm{dd}}$;

(ii) the instantiated overlapping partition $\{\Omega_i = \Phi_i(\Omega^{\mathrm{a}}_{\mathtt{L}_i})\}_{i=1}^{N_{\mathrm{dd}}}$, the global open domain $\Omega \subset \mathbb{R}^d$ such that $\overline{\Omega} = \bigcup_i \overline{\Omega}_i$, the ports $\Gamma_i = \Phi_i(\Gamma^{\mathrm{a}}_{\mathtt{L}_i})$ and the Dirichlet boundaries $\Gamma^{\mathrm{dir}}_i = \Phi_i(\Gamma^{\mathrm{a,dir}}_{\mathtt{L}_i})$, for $i = 1, \dots, N_{\mathrm{dd}}$;

(iii) the deployed FE full, bubble, and port spaces $\mathcal{X}_i = \{\underline{v} \circ \Phi_i^{-1} : \underline{v} \in \mathcal{X}^{\mathrm{a}}_{\mathtt{L}_i}\}$, $\mathcal{X}_{i,0} = \{\underline{v} \circ \Phi_i^{-1} : \underline{v} \in \mathcal{X}^{\mathrm{a}}_{\mathtt{L}_i,0}\}$, and $\mathcal{U}_i = \{\underline{v}|_{\Gamma_i} : \underline{v} \in \mathcal{X}_i\}$, for $i = 1, \dots, N_{\mathrm{dd}}$;

(iv) the extension operators $\mathtt{E}_i : \mathcal{U}_i \to \mathcal{X}_i$ such that $\mathtt{E}_i \underline{w} = \mathtt{E}^{\mathrm{a}}_{\mathtt{L}_i}(\underline{w} \circ \Phi_i) \circ \Phi_i^{-1}$ for $i = 1, \dots, N_{\mathrm{dd}}$;

(v) the deployed variational forms $\mathcal{G}_i : \mathcal{X}_i \times \mathcal{X}_{i,0} \to \mathbb{R}$ such that

$$\mathcal{G}_i(\underline{w}, \underline{v}) \;=\; \mathcal{G}^{\mathrm{a}}_{\mathtt{L}_i}(\underline{w} \circ \Phi_i, \underline{v} \circ \Phi_i; \mu_i). \tag{5.8}$$

Given $i = 1, \dots, N_{\mathrm{dd}}$, we further define the set of neighboring elements $\mathrm{Neigh}_i = \{j : \Omega_j \cap \Omega_i \neq \emptyset, j \neq i\}$, and the partition of Γ_i $\{\Gamma_{i,j} = \Gamma_i \cap \Omega_j : j \in \mathrm{Neigh}_i\}$. Note that, exploiting the previous definitions, the condition $x \in \Gamma_{i,j} \cap \Gamma_{j,i}$ implies that $x \in \partial\Omega_i \cap \Omega_i$: since Ω_i is an open open sets, $\partial\Omega_i \cap \Omega_i = \emptyset$ and thus $\Gamma_{i,j} \cap \Gamma_{j,i} = \emptyset$ for any $i, j = 1, \dots, N_{\mathrm{dd}}$.

Given the archetype mesh $\mathcal{T}^{\mathrm{a}}_\ell = \left(\{x^{\mathrm{a,v}}_{\ell,j}\}_{j=1}^{N^{\mathrm{v}}_\ell}, \mathtt{T}_\ell\right)$, with nodes $\{x^{\mathrm{a,v}}_{\ell,j}\}_{j=1}^{N^{\mathrm{v}}_\ell}$, connectivity matrix $\mathtt{T}_\ell$ and elements $\{\mathtt{D}_{k,\ell}\}_{k=1}^{N^{\mathrm{e}}_\ell}$, we denote by $\underline{u}$ a generic element of $\mathcal{X}_\ell$ and we denote by $\mathbf{u} \in \mathbb{R}^{DN^{\mathrm{v}}_\ell}$ the corresponding FE vector associated with the Lagrangian basis of $\mathcal{T}^{\mathrm{a}}_\ell$, for all $\ell \in \mathcal{L}$. Following [TZ21], we pursue a discretize-then-map treatment of parameterized geometries: given the mesh $\mathcal{T}^{\mathrm{a}}_{\mathtt{L}_i}$, we state the local variational problems in the deformed mesh $\Phi_i\left(\mathcal{T}^{\mathrm{a}}_{\mathtt{L}_i}\right) = \left(\{\Phi_i\left(x^{\mathrm{a,v}}_{j,\mathtt{L}_i}\right)\}_{j=1}^{N^{\mathrm{v}}_{\mathtt{L}_i}}, \mathtt{T}_{\mathtt{L}_i}\right)$. In section 5.3.2, we discuss the hyper-reduced formulation of the local problems. Note that if $(\mathcal{T}^{\mathrm{a}}_\ell, \mathbf{u})$ is associated with the element $u \in \mathcal{X}_\ell$, then $(\Phi_i(\mathcal{T}^{\mathrm{a}}_\ell), \mathbf{u})$ approximates $\underline{u} \circ \Phi^{-1}$.
We observe that the parametric mapping is supposed to be bijective in Ω^{a}_ℓ and bi-lipschitz. In this work, the deformation of archetype components (cf. figure 1.7) is described by piecewise linear maps that retain the structured features of the archetype components to the instantiated ones. A nonlinear mapping could be considered as well: we observe that in that case i) a more computationally demanding mesh interpolation would derive from unstructured instantiated grids; ii) in a discretize-then-map context, the computation of variational operators in the instantiated meshes would not require the computation of mapping derivatives.

5.2.3 Model problem

We illustrate the many elements of the formulation for the two-dimensional (plane stress) nonlinear (neo-Hookean) elasticity problem considered in the numerical experiments in section 5.5. The problem shares the same geometric configuration with the

THM problem that we describe in chapter 3 and we solve in chapter 4 for a monolithic configuration. We can consider the neo-Hookean study case as a preliminary model problem for the study of CB-pMOR techniques; we extend the methodology to unsteady coupled systems in chapter 6. Notice that in this chapter we consider a different model from the elasticity law for the solid in the THM system (cf. the equilibrium of mechanical forces in section 3.4.1). We remark that the numerical methods presented in this chapter are as well applicable to different types of constituive laws, for example to solid-mechanics models with time-dependency and plasticity.

We consider the constitutive law for the first Piola Kirchhoff stress tensor

$$P(\underline{u}) = \lambda_2 \left(F(\underline{u}) - F(\underline{u})^{-T}\right) + \lambda_1 \log\left(\det(F(\underline{u}))\right) F(\underline{u})^{-T}. \tag{5.9a}$$

Here, $F(\underline{u}) = \mathbb{1} + \nabla \underline{u}$ is the deformation gradient associated with the displacement $\underline{u}$, λ_1, λ_2 are the Lamé constants given by

$$\lambda_1 = \frac{E\nu}{1-\nu^2}, \qquad \lambda_2 = \frac{E}{2(1+\nu)}, \tag{5.9b}$$

where E is the Young's modulus, and ν is the Poisson's ratio. We consider the domain $\Omega = (0,1)^2$ depicted in Figure 5.3; we set $\nu = 0.3$ and we consider $E = E_k$ in ω_k for $k = 1, 2, 3$. We prescribe normal homogeneous Dirichlet conditions on the left and right boundaries; homogeneous Dirichlet conditions on the bottom boundary Γ_{btm} and the Neumann conditions:

$$P(\underline{u})\underline{n}\big|_{\Gamma_{\text{top}}} = \underline{g}_{\text{top}} := \begin{bmatrix} 0 \\ -4x_1(1-x_1) \end{bmatrix}, \quad P(\underline{u})\underline{n}\big|_{\Gamma_{\text{r,q}}} = \underline{g}_{\text{r}} := -s \begin{bmatrix} 0 \\ 1 \end{bmatrix}, \quad q = 1, \dots, Q_{\text{a}} \tag{5.9c}$$

with $s > 0$.

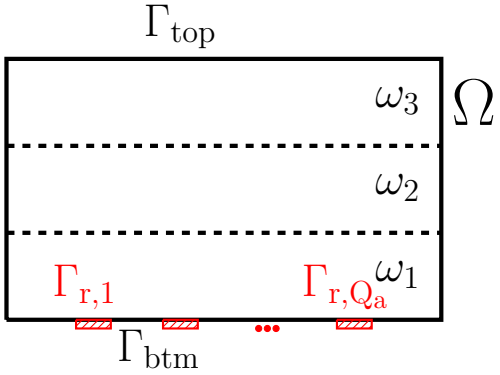

FIGURE 5.3: global system. Γ_{top} and $\Gamma_{\text{r,1}}, \dots, \Gamma_{\text{r,Q_a}}$ are associated with the stress conditions; the regions $\{\Gamma_{\text{r},q}\}_q$ are of equal size $\ell_{\text{r}} > 0$, and the distance between consecutive regions is constant and equal to $\ell > \ell_{\text{r}}$.

The system of equations below summarizes the problem: we seek the solution $u : \Omega \to \mathbb{R}^2$ to the system

$$\begin{cases} -\nabla \cdot P(\underline{u}) = 0 & \text{in } \Omega \\ \underline{u} \cdot \underline{n} = 0 & \text{on } \{0,1\} \times (0,1) \\ P(\underline{u})\underline{n} = \underline{g}_{\mathrm{r}} & \text{on } \Gamma_{\mathrm{r}} \\ P(\underline{u})\underline{n} = \underline{g}_{\mathrm{top}} & \text{on } \Gamma_{\mathrm{top}} \\ \underline{u} = \underline{0} & \text{on } \Gamma_{\mathrm{btm}} = (0,1) \times \{0\} \setminus \Gamma_{\mathrm{r}} \end{cases} \tag{5.10}$$

where $\Gamma_{\mathrm{r}} = \bigcup_{q=1}^{Q_{\mathrm{a}}} \Gamma_{\mathrm{r,q}}$. Our goal is to estimate the solution to (5.10) for any choice of the Young's moduli (E_1, E_2, E_3) associated with the regions $\omega_1, \omega_2, \omega_3$ in $[25, 30] \times [10, 20]^2$, any value of $s \in [0.4, 1]$ in (5.9c), and any $Q_{\mathrm{a}} \in \{2, \dots, 7\}$. Note that variations of Q_{a} induce topological changes that prevent the application of standard monolithic techniques.

We introduce the library of components $\Omega^{\mathrm{a}}_{\mathrm{int}}$ and $\Omega^{\mathrm{a}}_{\mathrm{ext}}$ depicted in Figure 1.6; in Figure 5.4 we show examples of instantiated components and we identify the corresponding ports. We denote by $\delta > 0$ the size of the overlap. The mapping $\Phi^{\mathrm{a}}_{\mathrm{int}}$ associated with the internal component is a simple horizontal shift, while the mapping $\Phi^{\mathrm{a}}_{\mathrm{ext}}$ associated with the external component consists in a piecewise-linear map in the horizontal direction and the identity map in the vertical direction. The internal component is uniquely described by the vector of parameters $\mu_{\mathrm{int}} = [E_1, s, x_{\mathrm{shift}}]$ where x_{shift} denotes the magnitude of the horizontal shift; the external component is described by the vector of parameters $\mu_{\mathrm{ext}} = [E_1, E_2, E_3, \ell_{\mathrm{ext}}]$ with $\ell_{\mathrm{ext}} = Q_{\mathrm{a}}\ell - \delta$. We then introduce the variational forms:

$$\begin{cases} \mathcal{G}^{\mathrm{a}}_{\mathrm{int}}(\underline{w}, \underline{v}; \mu_{\mathrm{int}}) = \displaystyle\int_{\Omega^{\mathrm{a}}_{\mathrm{int}}} \eta^{\mathrm{a,e}}_{\mathrm{int}}(\underline{w}, \underline{v}; \mu_{\mathrm{int}})\, dx + \int_{\Gamma^{\mathrm{a}}_{\mathrm{r}}} \eta^{\mathrm{a,f}}_{\mathrm{int}}(\underline{w}, \underline{v}; \mu_{\mathrm{int}})\, dx, \\ \mathcal{G}^{\mathrm{a}}_{\mathrm{ext}}(\underline{w}, \underline{v}; \mu_{\mathrm{ext}}) = \displaystyle\int_{\Omega^{\mathrm{a}}_{\mathrm{ext}}} \eta^{\mathrm{a,e}}_{\mathrm{ext}}(\underline{w}, \underline{v}; \mu_{\mathrm{ext}})\, dx + \int_{\Gamma^{\mathrm{a}}_{\mathrm{top}}} \eta^{\mathrm{a,f}}_{\mathrm{ext}}(\underline{w}, \underline{v}; \mu_{\mathrm{ext}})\, dx. \end{cases} \tag{5.11a}$$

Explicit expressions of $\eta^{\mathrm{a,e}}_{\ell}$ and $\eta^{\mathrm{a,f}}_{\ell}$ can be obtained by resorting to change-of-variable formulas: given the mapping Φ, we denote by $\nabla_\Phi = \nabla\Phi^{-T}\nabla$ the corresponding "mapped" gradient and we define $\nabla_{\mathrm{s},\Phi} = \frac{1}{2}\left(\nabla_\Phi + \nabla_\Phi^T\right)$ and $\underline{\underline{F}}_\Phi = \mathbb{1} + \nabla_\Phi$. Then, we have (we omit dependence on the parameter to shorten notation)

$$\begin{aligned} &\eta^{\mathrm{a,e}}_{\mathrm{int}}(\underline{w}, \underline{v}) = \eta^{\mathrm{a,e}}_{\mathrm{ext}}(\underline{w}, \underline{v}) = P(F_\Phi(\underline{w})) : \nabla_{\mathrm{s},\Phi}\underline{v} \det(\nabla\Phi), \\ &\eta^{\mathrm{a,f}}_{\mathrm{int}}(\underline{w}, \underline{v}) = \underline{v} \cdot \left(\underline{g}_{\mathrm{r}} \circ \Phi\right) \|\nabla\Phi\widehat{\mathbf{t}}\|_2, \quad \eta^{\mathrm{a,f}}_{\mathrm{ext}}(\underline{w}, \underline{v}) = \underline{v} \cdot \left(\underline{g}_{\mathrm{top}} \circ \Phi\right) \|\nabla\Phi\widehat{\mathbf{t}}\|_2, \end{aligned} \tag{5.11b}$$

where $\widehat{\mathbf{t}}$ denotes the tangent vector to the surface.

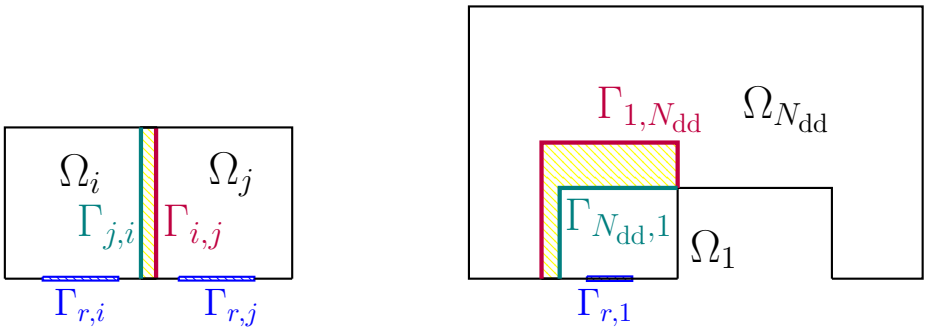

(a) instantiated "internal" components

(b) instantiated "internal" and "external components

FIGURE 5.4: geometrical configuration. Examples of deployed components. (a): $i, j = 1, \ldots, Q_{\mathrm{a}}$, (b): $i = 1$, $j = N_{\mathrm{dd}} = Q_{\mathrm{a}} + 1$. The overlap area is marked in yellow.

5.2.4 Hybridized statement

High-dimensional formulation

We generalize below the OS2 statement introduced in section 5.1. Given the set of parameters $\mu = (\mu_1, \ldots, \mu_{N_{\mathrm{dd}}}) \in \mathcal{P} = \bigotimes_{i=1}^{N_{\mathrm{dd}}} \mathcal{P}_{\mathtt{L}_i}$, we propose the CB full-order model: find $\underline{u}^{\mathrm{hf}} = (\underline{u}_1^{\mathrm{hf}}, \ldots, \underline{u}_{N_{\mathrm{dd}}}^{\mathrm{hf}}) \in \mathcal{X} := \bigotimes_{i=1}^{N_{\mathrm{dd}}} \mathcal{X}_i$ to minimize

$$\min_{\underline{u} \in \mathcal{X}} \frac{1}{2} \sum_{i=1}^{N_{\mathrm{dd}}} \sum_{j \in \mathrm{Neigh}_i} \|\underline{u}_i - \underline{u}_j\|^2_{L^2(\Gamma_{i,j})} \quad \text{s.t. } \mathcal{G}_i(\underline{u}_i, \underline{v}_i) = 0 \ \ \forall \underline{v}_i \in \mathcal{X}_{i,0}, \ i = 1, \ldots, N_{\mathrm{dd}}. \tag{5.12}$$

Note that (5.12) reduces to (5.3) for the case of two overlapping components.

To derive the hybridized formulation, we define the port-to-bubble maps $\mathtt{F}_i : \mathcal{U}_i \to \mathcal{X}_{i,0}$ such that, given $w \in \mathcal{U}_i$,

$$\mathcal{G}_i^{\circ}\left(\mathtt{F}_i(\underline{w}) + \mathtt{E}_i \underline{w}, \underline{v}\right) = 0 \quad \forall v \in \mathcal{X}_{i,0}. \tag{5.13a}$$

Note that (5.13a) corresponds to the FE solution to a localized PDE problem with datum w on Γ_i. Then, we rewrite (5.12) as the unconstrained least-square problem: find $\underline{u}^{\mathrm{hf,p}} = (\underline{u}_1^{\mathrm{hf,p}}, \ldots, \underline{u}_{N_{\mathrm{dd}}}^{\mathrm{hf,p}}) \in \mathcal{U} := \bigotimes_{i=1}^{N_{\mathrm{dd}}} \mathcal{U}_i$ to minimize

$$\min_{\underline{u}^{\mathrm{p}} \in \mathcal{U}} \frac{1}{2} \sum_{i=1}^{N_{\mathrm{dd}}} \sum_{j \in \mathrm{Neigh}_i} \|\underline{u}_i^{\mathrm{p}} - \mathtt{E}_j \underline{u}_j^{\mathrm{p}} - \mathtt{F}_j(\underline{u}_j^{\mathrm{p}})\|^2_{L^2(\Gamma_{i,j})}. \tag{5.13b}$$

Minimization problem (5.13b) reads as a nonlinear least-square problem; in the following we devise a low-dimensional reduced-order approximation of (5.13b) based on Galerkin projection of the port-to-bubble maps.

Reduced-order formulation

For all $\ell \in \mathcal{L}$, we introduce the low-dimensional archetype bubble and port spaces $\mathcal{Z}_\ell^{\mathrm{a,b}} \subset \mathcal{X}_{\ell,0}$, $\mathcal{Z}_\ell^{\mathrm{a,p}} \subset \mathcal{U}_\ell$ and the extended port spaces $\mathcal{W}_\ell^{\mathrm{a,p}} = \{\mathtt{E}_\ell \underline{\zeta} : \underline{\zeta} \in \mathcal{Z}_\ell^{\mathrm{a,p}}\} \subset \mathcal{X}_\ell$; we denote by n and m the dimensions of the bubble and port spaces, respectively; for simplicity, we assume that the dimension of the spaces is the same for all archetype components. We also define the archetype ROBs $\underline{Z}_\ell^{\mathrm{a,b}} : \mathbb{R}^n \to \mathcal{Z}_\ell^{\mathrm{a,b}}$ and $\underline{W}_\ell^{\mathrm{a,b}} : \mathbb{R}^m \to$

$\mathcal{W}_\ell^{\mathrm{a,b}}$. Given the deployed system, we introduce the instantiated (or deployed) bubble and port spaces $\mathcal{Z}_i^{\mathrm{b}} = \{\underline{\zeta} \circ \Phi_i^{-1} : \underline{\zeta} \in \mathcal{Z}_{\mathrm{L}_i}^{\mathrm{a,b}}\}$ and $\mathcal{W}_i^{\mathrm{p}} = \{\underline{\zeta} \circ \Phi_i^{-1} : \underline{\zeta} \in \mathcal{W}_{\mathrm{L}_i}^{\mathrm{a,p}}\}$ with ROBs $\underline{Z}_i^{\mathrm{b}} = [\underline{\zeta}_{i,1}^{\mathrm{b}}, \dots, \underline{\zeta}_{i,n}^{\mathrm{b}}] : \mathbb{R}^n \to \mathcal{Z}_i^{\mathrm{b}}$ and $\underline{W}_i^{\mathrm{p}} = [\underline{\psi}_{i,1}^{\mathrm{p}}, \dots, \underline{\psi}_{i,m}^{\mathrm{p}}] : \mathbb{R}^m \to \mathcal{W}_i^{\mathrm{p}}$, respectively. Then, we define the ansatz:

$$\widehat{\underline{u}}_i(\widehat{\alpha}_i, \widehat{\beta}_i) = \underline{Z}_i^{\mathrm{b}} \widehat{\alpha}_i + \underline{W}_i^{\mathrm{p}} \widehat{\beta}_i, \quad i = 1, \dots, N_{\mathrm{dd}}. \tag{5.14}$$

We observe that $\widehat{\underline{u}}_i^{\mathrm{b}} = \underline{Z}_i^{\mathrm{b}} \widehat{\alpha}_i$ should approximate the bubble field $\underline{u}|_{\Omega_i} - \mathtt{E}_i(\underline{u}|_{\Gamma_i})$, while $\widehat{\underline{u}}_i^{\mathrm{p}} = \underline{W}_i^{\mathrm{p}} \widehat{\beta}_i$ is an approximation of the (extended) port field $\mathtt{E}_i(\underline{u}|_{\Gamma_i})$: we refer to $\widehat{\underline{u}}_i^{\mathrm{b}}, \widehat{\underline{u}}_i^{\mathrm{p}}$ as to the bubble and port estimates of the solution field in the i-th component.

To obtain the low-dimensional formulation, we introduce the local residuals[2] (cf. (5.7), (5.8) and (5.11))

$$\widehat{\mathbf{R}}_i^{\mathrm{hf}} : \mathbb{R}^n \times \mathbb{R}^m \to \mathbb{R}^n \quad \text{s.t.} \quad \left(\widehat{\mathbf{R}}_i^{\mathrm{hf}}(\boldsymbol{\alpha}_i, \boldsymbol{\beta}_i)\right)_j = \mathcal{G}_i\left(\widehat{\underline{u}}_i(\boldsymbol{\alpha}_i, \boldsymbol{\beta}_i), \underline{\zeta}_{i,j}^{\mathrm{b}}\right), \tag{5.15a}$$

for $i = 1, \dots, N_{\mathrm{dd}}$, $j = 1, \dots, n$, and the approximate port-to-bubble maps $\widehat{\mathtt{F}}_i^{\mathrm{hf}} : \mathbb{R}^m \to \mathbb{R}^n$ such that $\widehat{\mathbf{R}}_i^{\mathrm{hf}}\left(\widehat{\mathtt{F}}_i^{\mathrm{hf}}(\boldsymbol{\beta}_i), \boldsymbol{\beta}_i\right) = \mathbf{0}$. Computation of the port-to-bubble maps $\{\widehat{\mathtt{F}}_i^{\mathrm{hf}}\}_i$ is expensive due to the need to integrate over the whole computational mesh. We thus replace the residuals $\{\widehat{\mathbf{R}}_i^{\mathrm{hf}}\}_i$ with the empirical quadrature (EQ) approximations $\{\widehat{\mathbf{R}}_i^{\mathrm{eq}}\}_i$ and we define the hyper-reduced port-to-bubble maps $\widehat{\mathtt{F}}_i^{\mathrm{eq}} : \mathbb{R}^m \to \mathbb{R}^n$ such that

$$\widehat{\mathbf{R}}_i^{\mathrm{eq}}\left(\widehat{\mathtt{F}}_i^{\mathrm{eq}}(\boldsymbol{\beta}_i), \boldsymbol{\beta}_i\right) = \mathbf{0}. \tag{5.15b}$$

We discuss in section 5.3.2 the hyper-reduction strategy employed to construct the approximate residuals $\widehat{\mathbf{R}}_i^{\mathrm{eq}}$; here, we observe that the gradient of the port-to-bubble map can be obtained by differentiating (5.15b):

$$\nabla \mathtt{F}_i^{\mathrm{eq}}(\boldsymbol{\beta}_i) = -\left(\partial_{\boldsymbol{\alpha}_i} \widehat{\mathbf{R}}_i^{\mathrm{eq}}\right)^{-1} \partial_{\boldsymbol{\beta}_i} \widehat{\mathbf{R}}_i^{\mathrm{eq}}\Big|_{(\boldsymbol{\alpha}_i, \boldsymbol{\beta}_i) = (\widehat{\mathtt{F}}_i^{\mathrm{eq}}(\boldsymbol{\beta}_i), \boldsymbol{\beta}_i)} \tag{5.15c}$$

We remark that the existence and well-posedness of the port-to-bubble maps (5.15b) is conditioned to the existence of solutions to the nonlinear systems of equations $\widehat{\mathbf{R}}_i^{\mathrm{hf}} = \mathbf{0}$ and to the fact that $\partial_{\boldsymbol{\alpha}_i} \widehat{\mathbf{R}}_i^{\mathrm{hf}}$ is non-singular at the optimum. It thus depends on the particular problem of interest, and might also depend on the overlapping partition considered and on the reduced-order approximation spaces.

We now focus on the objective function. We observe that

$$\begin{aligned}
&\frac{1}{2} \sum_{i=1}^{N_{\mathrm{dd}}} \sum_{j \in \mathrm{Neigh}_i} \int_{\Gamma_{i,j}} \|\widehat{\underline{u}}_i(x) - \widehat{\underline{u}}_j(x)\|_2^2 \, dx \\
&= \frac{1}{2} \sum_{i=1}^{N_{\mathrm{dd}}} \int_{\Gamma_i} \left(\sum_{j \in \mathrm{Neigh}_i : x \in \Omega_j} \|\widehat{\underline{u}}_i(x) - \widehat{\underline{u}}_j(x)\|_2^2 \right) dx \\
&= \frac{1}{2} \sum_{i=1}^{N_{\mathrm{dd}}} \int_{\Gamma_{\mathrm{L}_i}^{\mathrm{a}}} \left(\sum_{j \in \mathrm{Neigh}_i : \Phi_i(\widehat{x}) \in \Omega_j} \|\widehat{\underline{u}}_i(\Phi_i(\widehat{x})) - \widehat{\underline{u}}_j(\Phi_i(\widehat{x}))\|_2^2 \right) J_i^{\mathrm{bnd}}(\widehat{x}) \, d\widehat{x}
\end{aligned}$$

where $J_i^{\mathrm{bnd}} = \|\det(\nabla \Phi_i) \nabla \Phi_i^{-T} \mathbf{n}_{\mathrm{L}_i}^{\mathrm{a}}\|_2$ and $\mathbf{n}_\ell^{\mathrm{a}}$ is the outward normal to Γ_ℓ^{a}. Note that in the last identity we used the Narson formula; furthermore, to shorten notation, we omitted dependence of $\widehat{\underline{u}}_i, \widehat{\underline{u}}_j$ on bubble and port coefficients (cf. (5.14)). We introduce

[2] The superscript $^{\mathrm{hf}}$ encodes the fact that the local residuals are computed using the HF mesh.

the HF quadrature rules $\{(x^{\mathrm{p}}_{\ell,q}, \rho^{\mathrm{p}}_{\ell,q})\}_{q=1}^{N^{\mathrm{p}}_\ell}$ on the archetype ports Γ^{a}_ℓ for $\ell \in \mathcal{L}$; then, we have

$$\frac{1}{2}\sum_{i=1}^{N_{\mathrm{dd}}} \sum_{j\in \mathrm{Neigh}_i} \int_{\Gamma_{i,j}} \|\widehat{\underline{u}}_i(\boldsymbol{\alpha}_i,\boldsymbol{\beta}_i) - \widehat{\underline{u}}_j(\boldsymbol{\alpha}_j,\boldsymbol{\beta}_j)\|_2^2 \, dx \;\approx\; \frac{1}{2}\sum_{i=1}^{N_{\mathrm{dd}}} \boldsymbol{\rho}^{\mathrm{p}}_{\mathrm{L}_i} \cdot \boldsymbol{\eta}^{\mathrm{p}}_i(\boldsymbol{\alpha},\boldsymbol{\beta}) \tag{5.16a}$$

where $\boldsymbol{\alpha} = [\boldsymbol{\alpha}_1, \ldots, \boldsymbol{\alpha}_{N_{\mathrm{dd}}}] \in \mathbb{R}^N$ with $N := nN_{\mathrm{dd}}$, $\boldsymbol{\beta} = [\boldsymbol{\beta}_1, \ldots, \boldsymbol{\beta}_{N_{\mathrm{dd}}}] \in \mathbb{R}^M$, with $M = mN_{\mathrm{dd}}$, and

$$\boldsymbol{\eta}^{\mathrm{p}}_i(\boldsymbol{\alpha},\boldsymbol{\beta}) = \begin{bmatrix} \eta^{\mathrm{p}}_i\left(\Phi_i(x^{\mathrm{p}}_{\ell,1}); \boldsymbol{\alpha},\boldsymbol{\beta}\right) \\ \vdots \\ \eta^{\mathrm{p}}_i\left(\Phi_i(x^{\mathrm{p}}_{\ell,N^{\mathrm{p}}_\ell}); \boldsymbol{\alpha},\boldsymbol{\beta}\right) \end{bmatrix} \tag{5.16b}$$

with

$$\eta^{\mathrm{p}}_i\left(x;\boldsymbol{\alpha},\boldsymbol{\beta}\right) = \left(\sum_{j\in \mathrm{Neigh}_i : x\in\Omega_j} \|\widehat{\underline{u}}_i(x;\boldsymbol{\alpha}_i,\boldsymbol{\beta}_i) \;-\; \widehat{\underline{u}}_j(x;\boldsymbol{\alpha}_j,\boldsymbol{\beta}_j)\|_2^2 \right) J^{\mathrm{bnd}}_i(\Phi_i^{-1}(x)), \tag{5.16c}$$

for $i = 1, \ldots, N_{\mathrm{dd}}$.

We notice that the reduced (and hyper-reduced) formulations of the objective function introduced in (5.16a) heavily rely on the formulation (5.3), which is based on a penalization over the port boundaries. Such a formulation cannot be easily extended to the case in which a penalization is done over the whole overlapping subdomain. This consideration motivates the proposed formulation (5.3), together with the fact that stability is also preserved by a minimization over ports.

Evaluation of (5.16) is expensive due to the need to integrate over the port boundaries $\bigcup_{i=1}^{N_{\mathrm{dd}}} \bigcup_{j\in\mathrm{Neigh}_i} \Gamma_{i,j}$: we should thus replace the HF quadrature vectors $\{\boldsymbol{\rho}^{\mathrm{p}}_\ell\}_{\ell\in\mathcal{L}}$ with sparse EQ vectors $\{\boldsymbol{\rho}^{\mathrm{p,eq}}_\ell\}_{\ell\in\mathcal{L}}$. In conclusion, we obtain the discrete OS2 formulation: find $\widehat{\boldsymbol{\beta}} = [\widehat{\boldsymbol{\beta}}_1, \ldots, \widehat{\boldsymbol{\beta}}_{N_{\mathrm{dd}}}] \in \mathbb{R}^M$ such that

$$\widehat{\boldsymbol{\beta}} \in \arg\min_{\boldsymbol{\beta}\in\mathbb{R}^M} \mathfrak{f}^{\mathrm{eq}}(\boldsymbol{\beta}) \;=\; \mathfrak{F}\left(\widehat{\mathbb{F}}^{\mathrm{eq}}(\boldsymbol{\beta}),\, \boldsymbol{\beta}, \{\boldsymbol{\rho}^{\mathrm{p,eq}}_\ell\}_{\ell\in\mathcal{L}}\right) \tag{5.17a}$$

where $\widehat{\mathbb{F}}^{\mathrm{eq}} : \mathbb{R}^M \to \mathbb{R}^N$ is the full port-to-bubble map such that $\widehat{\mathbb{F}}^{\mathrm{eq}}(\boldsymbol{\beta}) = \left[\widehat{\mathbb{F}}^{\mathrm{eq}}_1(\boldsymbol{\beta}_1), \ldots, \widehat{\mathbb{F}}^{\mathrm{eq}}_{N_{\mathrm{dd}}}(\boldsymbol{\beta}_{N_{\mathrm{dd}}})\right]^T$, and

$$\mathfrak{F}\left(\boldsymbol{\alpha},\, \boldsymbol{\beta}, \{\boldsymbol{\rho}^{\mathrm{p,eq}}_\ell\}_{\ell\in\mathcal{L}}\right) = \frac{1}{2}\sum_{i=1}^{N_{\mathrm{dd}}} \boldsymbol{\rho}^{\mathrm{p,eq}}_{\mathrm{L}_i} \cdot \boldsymbol{\eta}^{\mathrm{p}}_i(\boldsymbol{\alpha},\boldsymbol{\beta}). \tag{5.17b}$$

If we denote by Q the total number of quadrature points with repetitions times the number of state variables D,

$$Q := D\left(\sum_{i=1}^{N_{\mathrm{dd}}}\sum_{q=1}^{N^{\mathrm{p}}_{\mathrm{L}_i}} \mathrm{card}\left\{j : \Phi_i(x^{\mathrm{p}}_{\mathrm{L}_i,q}) \in \Omega_j\right\} H(\rho^{\mathrm{p,eq}}_{\mathrm{L}_i,q})\right), \quad \text{with } H(x) = \begin{cases} 1 & \text{if } x > 0 \\ 0 & \text{otherwise} \end{cases} \tag{5.17c}$$

we find that there exist $\mathbf{P} \in \mathbb{R}^{Q\times N}$ and $\mathbf{Q} \in \mathbb{R}^{Q\times M}$ such that

$$\mathfrak{f}^{\mathrm{eq}}(\boldsymbol{\beta}) = \frac{1}{2}\|\mathbf{r}^{\mathrm{eq}}(\boldsymbol{\beta})\|_2^2, \quad \text{where } \mathbf{r}^{\mathrm{eq}}(\boldsymbol{\beta}) = \mathbf{P}\,\widehat{\mathbb{F}}^{\mathrm{eq}}(\boldsymbol{\beta}) + \mathbf{Q}\boldsymbol{\beta}. \tag{5.17d}$$

5.2.5 Discussion

The remarks below provide a number of comments on the OS2 statement introduced in the previous section.

Remark 3. ***Algebraic representation of the local ROBs.*** *Exploiting the notation introduced at the end of section 5.2.1, the archetype bubble ROB* $Z_\ell^{\mathrm{a,b}} : \mathbb{R}^n \to \mathcal{Z}_\ell^{\mathrm{a,b}}$ *admits the algebraic representation* $Z_\ell^{\mathrm{a,b}} : \boldsymbol{\alpha} \in \mathbb{R}^n \mapsto \left(\mathcal{T}_\ell^{\mathrm{a}}, \mathbf{Z}_\ell^{\mathrm{b}}\boldsymbol{\alpha}\right)$ *for some* $\mathbf{Z}_\ell^{\mathrm{b}} \in \mathbb{R}^{N_\ell^{\mathrm{a}} \times n}$*, while the deployed operators can be stated as* $Z_i^{\mathrm{b}} : \boldsymbol{\alpha} \in \mathbb{R}^n \mapsto \left(\Phi_i(\mathcal{T}_{L_i}^{\mathrm{a}}), \mathbf{Z}_{L_i}^{\mathrm{b}}\boldsymbol{\alpha}\right)$*, for* $i = 1, \ldots, N_{\mathrm{dd}}$*. Note that by virtue of the correspondence between archetype and deployed spaces, we do not have to explicitly instantiate — and then store — the bubble ROBs for each configuration. The same applies for the port bases.*

Remark 4. ***Extension to non-homogeneous Dirichlet conditions.*** *The OS2 formulation can readily deal with non-homogeneous Dirichlet boundary conditions. Towards this end, for* $i = 1, \ldots, N_{\mathrm{dd}}$*, given the Dirichlet datum* $\underline{g}_i^{\mathrm{dir}} : \Gamma_i^{\mathrm{dir}} \to \mathbb{R}^D$*, we introduce the lift* $\underline{u}_i^{\mathrm{dir}}$ *such that* $\underline{u}_i^{\mathrm{dir}}|_{\Gamma_i^{\mathrm{dir}}} = \underline{g}_i^{\mathrm{dir}}$*, and the ansatz*

$$\widehat{\underline{u}}_i(\widehat{\alpha}_i, \widehat{\beta}_i) \;=\; \underline{u}_i^{\mathrm{dir}} + \underline{Z}_i^{\mathrm{b}}\widehat{\alpha}_i + \underline{W}_i^{\mathrm{p}}\widehat{\beta}_i, \quad i = 1, \ldots, N_{\mathrm{dd}}.$$

Here, $\widehat{\underline{u}}_i^{\mathrm{b}} = \underline{Z}_i^{\mathrm{b}}\widehat{\alpha}_i$ *should approximate the bubble field* $\underline{u}|_{\Omega_i} - \underline{\mathcal{E}}_i((\underline{u} - \underline{u}_i^{\mathrm{dir}})|_{\Gamma_i}) - \underline{u}_i^{\mathrm{dir}}$*, while* $\widehat{\underline{u}}_i^{\mathrm{p}} = \underline{W}_i^{\mathrm{p}}\widehat{\beta}_i$ *is an approximation of the (extended) port field* $\underline{\mathcal{E}}_i((\underline{u} - \underline{u}_i^{\mathrm{dir}})|_{\Gamma_i})$*. Then, we can proceed as before to derive the reduced port-to-bubble maps and the low-dimensional OS2 formulation. We refer to [GPS07] for a thorough discussion on the imposition of Dirichlet boundary conditions in Galerkin ROMs.*

Remark 5. ***Computation of the matrices*** $\mathbf{P}, \mathbf{Q}$**.** *The matrices* $\mathbf{P}, \mathbf{Q}$ *depend on the configuration of interest but are independent of the port coefficients* $\boldsymbol{\beta}$*: they can thus be defined after having instantiated the system and before solving the optimization problem. Since the port quadrature points* $\{\Phi_i(x_{L_i,q}^{\mathrm{p}})\}_{i,q}$ *are configuration-dependent, we should resort to mesh interpolation to assemble the matrices* $\mathbf{P}$ *and* $\mathbf{Q}$*. In this work, we rely on structured meshes in the archetype components that enable logarithmic-in-*N_ℓ^{v} *FE interpolations.*

Remark 6. ***Hyper-reduction.*** *As required in CB-pMOR, hyper-reduction should be defined at the component level and is then translated to the deployed system using the mappings* $\{\Phi_i\}_i$*. From an algorithmic standpoint, an archetype component* $\ell \in \mathcal{L}$ *should be interpreted as a complex data structure that comprises (i) bubble and port ROBs; (ii) the approximate residual* $\widehat{\mathbf{R}}_\ell^{\mathrm{eq}}$ *that enables effective computations of port-to-bubble maps; (iii) the port quadrature rule* $\boldsymbol{\rho}_\ell^{\mathrm{p,eq}}$ *associated with the approximate objective function (5.17a); and (iv) a (structured) mesh structure for which efficient (i.e., logarithmic-in-*N_ℓ^{v}*) interpolation procedures are available for the computation of the matrices* $\mathbf{P}, \mathbf{Q}$*.*

5.2.6 Solution to the OS2 minimization problem

In view of the description of the numerical solution to (5.17), we observe that the Jacobian of the global port-to-bubble map $\widehat{\mathbf{F}}^{\mathrm{eq}} : \mathbb{R}^M \to \mathbb{R}^N$ is block-diagonal (cf. (5.15c)):

$$\widehat{\mathbf{J}}_{\mathbf{F}}^{\mathrm{eq}}(\boldsymbol{\beta}) = \mathrm{diag}\left[\widehat{\mathbf{J}}_{\mathbf{F}_1}^{\mathrm{eq}}(\boldsymbol{\beta}_1), \ldots, \widehat{\mathbf{J}}_{\mathbf{F}_{N_{\mathrm{dd}}}}^{\mathrm{eq}}(\boldsymbol{\beta}_{N_{\mathrm{dd}}})\right], \; \widehat{\mathbf{J}}_{\mathbf{F}_i}^{\mathrm{eq}}(\boldsymbol{\beta}_i) := -\left(\partial_{\boldsymbol{\alpha}_i}\widehat{\mathbf{R}}_i^{\mathrm{eq}}\right)^{-1}\partial_{\boldsymbol{\beta}_i}\widehat{\mathbf{R}}_i^{\mathrm{eq}}\Big|_{(\boldsymbol{\alpha}_i, \boldsymbol{\beta}_i) = (\widehat{\mathbf{F}}_i^{\mathrm{eq}}(\boldsymbol{\beta}_i), \boldsymbol{\beta}_i)}. \tag{5.18a}$$

Then, we observe that

$$\nabla \mathbf{r}^{\mathrm{eq}} = \mathbf{P}\widehat{\mathbf{J}}_{\mathrm{F}}^{\mathrm{eq}} + \mathbf{Q}, \quad \nabla \mathfrak{f}^{\mathrm{eq}} = \left(\mathbf{P}\widehat{\mathbf{J}}_{\mathrm{F}}^{\mathrm{eq}} + \mathbf{Q}\right)^T \mathbf{r}^{\mathrm{eq}}. \tag{5.18b}$$

If $N_{\mathrm{dd}} \gg m$ (as in the cases considered e.g. in [HKP13; MC21]), the Jacobian $\widehat{\mathbf{J}}_{\mathrm{F}}^{\mathrm{eq}}$ is highly sparse; note that explicit assembly of the local Jacobians requires to solve m linear systems of size n, while matrix-vector multiplications $\widehat{\mathbf{J}}_{\mathrm{F}}^{\mathrm{eq}}\mathbf{v}$ and $\mathbf{v}^T\widehat{\mathbf{J}}_{\mathrm{F}}^{\mathrm{eq}}$ require N_{dd} $n \times m$ matrix-vector multiplications and N_{dd} linear solves of size m.

The nonlinear least-squares problem (5.17) can be solved using (i) steepest-descent or quasi-Newton methods, or (ii) Gauss-Newton or Levenberg-Marquandt algorithms, [NW06].

(i) Steepest-descent or quasi Newton methods only require the explicit calculation of the objective function $\mathfrak{f}^{\mathrm{eq}}$ and its gradient $\nabla \mathfrak{f}^{\mathrm{eq}}$, which can be computed without explicitly forming $\widehat{\mathbf{J}}_{\mathrm{F}}^{\mathrm{eq}}$. However, these methods do not exploit the underlying least-square structure of the optimization problem and might thus exhibit slower convergence and/or might be more prone to divergent behaviors.

(ii) The Gauss-Newton method (GNM) reads as

$$\widehat{\boldsymbol{\beta}}^{(k+1)} = \widehat{\boldsymbol{\beta}}^{(k)} - \left(\nabla \mathbf{r}^{\mathrm{eq}}\left(\widehat{\boldsymbol{\beta}}^{(k)}\right)\right)^{\dagger} \mathbf{r}^{\mathrm{eq}}\left(\widehat{\boldsymbol{\beta}}^{(k)}\right)$$

where $(\cdot)^{\dagger}$ denotes the Moore-Penrose pseudo-inverse. The Levenberg-Marquandt algorithm (LMA) is a generalization of GNM that is typically more robust for poor choices of the initial condition. Note that GNM/LMA are the methods of choice for least-squares problems; however, they require the assembly of $\widehat{\mathbf{J}}_{\mathrm{F}}^{\mathrm{eq}}$ at each iteration.

Algorithm 7 Solution to (5.17) through the Gauss-Newton method.

Inputs: $\boldsymbol{\alpha}^{(0)} = [\boldsymbol{\alpha}_1^{(0)}, \dots, \boldsymbol{\alpha}_{N_{\text{dd}}}^{(0)}]$, $\boldsymbol{\beta}^{(0)} = [\boldsymbol{\beta}_1^{(0)}, \dots, \boldsymbol{\beta}_{N_{\text{dd}}}^{(0)}]$ initial conditions (cf. Eq. (5.22)), $tol > 0$, `maxit`.
Outputs: $\widehat{\boldsymbol{\beta}}$ port coefficients, $\widehat{\boldsymbol{\alpha}} = \widehat{\mathtt{F}}^{\text{eq}}(\widehat{\boldsymbol{\beta}})$ bubble coefficients.

1: Compute the matrices $\mathbf{P}, \mathbf{Q}$ in (5.17d).
2: Set $\widehat{\boldsymbol{\beta}}^{(0)} = \boldsymbol{\beta}^{(0)}$ and $\widehat{\boldsymbol{\alpha}} = \boldsymbol{\alpha}^{(0)}$.
3: **for** $k = 1, \dots,$ `maxit` **do**
4: **for** $i = 1, \dots, N_{\text{dd}}$ **do**
5: Compute $\boldsymbol{\alpha}_i$ s.t. $\widehat{\mathbf{R}}_i^{\text{eq}}(\boldsymbol{\alpha}_i, \boldsymbol{\beta}_i^{(k)}) = \mathbf{0}$ using Newton's method with initial condition $\widehat{\boldsymbol{\alpha}}_i$.
6: Compute $\widehat{\mathbf{J}}_{\mathtt{F}_i}^{\text{eq}}(\boldsymbol{\beta}_i^{(k)})$ (cf. (5.18)).
7: **end for**
8: Update $\widehat{\boldsymbol{\alpha}} = [\boldsymbol{\alpha}_1, \dots, \boldsymbol{\alpha}_{N_{\text{dd}}}]$.
9: Compute $\mathbf{r}^{\text{eq,(k)}} = \mathbf{P}\widehat{\boldsymbol{\alpha}} + \mathbf{Q}\widehat{\boldsymbol{\beta}}_i^{(k)}$ and $\nabla \mathbf{r}^{\text{eq,(k)}} = \mathbf{P}\widehat{\mathbf{J}}_{\mathtt{F}}^{\text{eq}} + \mathbf{Q}$.
10: Compute $\widehat{\boldsymbol{\beta}}^{(k+1)} = \widehat{\boldsymbol{\beta}}^{(k)} - \left(\nabla \mathbf{r}^{\text{eq,(k)}}\right)^{\dagger} \mathbf{r}^{\text{eq,(k)}}$
11: **if** $\|\widehat{\boldsymbol{\beta}}^{(k+1)} - \widehat{\boldsymbol{\beta}}^{(k)}\|_2 < tol \|\widehat{\boldsymbol{\beta}}^{(k)}\|_2$ **then**, `BREAK`
12: **end if**
13: **end for**
14: Return $\widehat{\boldsymbol{\beta}} = \widehat{\boldsymbol{\beta}}^{(k+1)}$ and $\widehat{\boldsymbol{\alpha}} = \widehat{\mathtt{F}}^{\text{eq}}(\widehat{\boldsymbol{\beta}})$.

In this work, we resort to GNM to solve (5.17). Algorithm 7 summarizes the overall procedure as implemented in our code; we envision that our approach can cope with LMA with only minor changes: we omit the details. Note that we update at each iteration the estimates of the bubble coefficients: this is important to speed up the solution to the local Newton problems. In addition, the algorithm requires to provide an initial guess for port and bubble coefficients; we discuss the choice of the initial condition in section 5.3 (cf. Eq. (5.22)).

As explained in [MNT04], for nonlinear least-squares problems of the form (5.17d), Gauss-Newton's method shows quadratic convergence if $\mathbf{r}^{\text{eq}}\left(\widehat{\boldsymbol{\beta}}\right) = \mathbf{0}$ and a super-linear convergence if $\|\mathbf{r}^{\text{eq}}\left(\widehat{\boldsymbol{\beta}}\right)\|_2$ is small. In the numerical results, we also investigate performance of a quasi-Newton method — the limited-memory BFGS method [NW06]. Note that the implementation of the latter follows a similar procedure as in Algorithm 7 with only minor changes: we omit the details.

Remark 7. *We remark that the internal loop at lines 4-7 in Algorithm 7 and the construction of the matrices* $\mathbf{P}, \mathbf{Q}$ *are embarrassingly parallelizable.*

We consider, as reference, the multiplicative overlapping Schwarz method. Classical OS iterations are introduced in section 5.1 for a generic PDE problem in a simple geometric setting. More precisely, we implement the iterative procedure described in Algorithm 8.

Algorithm 8 Overlapping Schwarz method.

Inputs: $\boldsymbol{\alpha}^{(0)} = [\boldsymbol{\alpha}_1^{(0)}, \dots, \boldsymbol{\alpha}_{N_{\text{dd}}}^{(0)}]$, $\boldsymbol{\beta}^{(0)} = [\boldsymbol{\beta}_1^{(0)}, \dots, \boldsymbol{\beta}_{N_{\text{dd}}}^{(0)}]$ initial conditions (cf. Eq. (5.22)), $tol > 0$, `maxit`.
Outputs: $\widehat{\boldsymbol{\beta}}$ port coefficients, $\widehat{\boldsymbol{\alpha}} = \widehat{\mathtt{F}}^{\text{eq}}(\widehat{\boldsymbol{\beta}})$ bubble coefficients.

1: Set $\widehat{\boldsymbol{\beta}}^{(0)} = \boldsymbol{\beta}^{(0)}$ and $\widehat{\boldsymbol{\alpha}} = \boldsymbol{\alpha}^{(0)}$.
2: **for** $k = 1, \dots,$ `maxit` **do**
3: Initialize $\widehat{\boldsymbol{\alpha}}^{(k)} = \widehat{\boldsymbol{\alpha}}^{(k-1)}$ and $\widehat{\boldsymbol{\beta}}^{(k)} = \widehat{\boldsymbol{\beta}}^{(k-1)}$.
4: **for** $i = 1, \dots, N_{\text{dd}}$ **do**
5: Update $\widehat{\boldsymbol{\beta}}_i^{(k)} \in \arg\min_{\boldsymbol{\beta} \in \mathbb{R}^m} \sum_{j \in \text{Neigh}_i} \|W_i^{\text{p}} \boldsymbol{\beta} - Z_j^{\text{b}} \widehat{\mathtt{F}}_j^{\text{eq}}(\widehat{\boldsymbol{\beta}}_j^{(k)}) - W_j^{\text{p}} \widehat{\boldsymbol{\beta}}_j^{(k)}\|^2_{L^2(\Gamma_{i,j})}$.
6: Update $\widehat{\boldsymbol{\alpha}}_i^{(k)} = \widehat{\mathtt{F}}_i^{\text{eq}}(\widehat{\boldsymbol{\beta}}_i^{(k)})$.
7: **end for**
8: **if** $\|\widehat{\boldsymbol{\beta}}^{(k)} - \widehat{\boldsymbol{\beta}}^{(k-1)}\|_2 < tol \|\widehat{\boldsymbol{\beta}}^{(k)}\|_2$ **then**, `BREAK`
9: **end if**
10: **end for**

We notice that since the discretization is not conforming across components, we should define the i-th port mode using projection (cf. Line 5, Algorithm 8). Note that at step i of the for loop at Lines $4-7$ we use the values of $\widehat{\boldsymbol{\beta}}_i, \dots, \widehat{\boldsymbol{\beta}}_{N_{\text{dd}}}$ at the previous iteration and the values $\widehat{\boldsymbol{\beta}}_1, \dots, \widehat{\boldsymbol{\beta}}_{i-1}$ at the current iteration: the for loop is thus not parallelizable in the multiplicative version of OS, while it is the case for the additive version of OS (cf. section 5.1.1).
In section 5.5 we compare the performance of Gauss-Newton and Quasi-Newton to the one shown by OS method with Dirichlet boundary conditions for a steady nonlinear problem.

5.3 Methodology

5.3.1 Data compression

In this work, we resort to global solves to construct the archetype ROBs $\{(\underline{Z}_\ell^{\text{a,b}}, \underline{W}_\ell^{\text{a,b}})\}_{\ell \in \mathcal{L}}$, $\underline{Z}_\ell^{\text{a,b}} = [\underline{\zeta}_{\ell,1}^{\text{a,b}}, \dots, \underline{\zeta}_{\ell,n}^{\text{a,b}}]$, $\underline{W}_\ell^{\text{a,p}} = [\underline{\psi}_{\ell,1}^{\text{a,p}}, \dots, \underline{\psi}_{\ell,n}^{\text{a,p}}]$. We generate n_{train} global configurations $\{\mu^{(k)}\}_{k=1}^{n_{\text{train}}}$ and we denote by $\{\left(\Omega_i^{(k)}, \mathtt{L}_i^{(k)}\right)\}_{i,k}$ the corresponding labeled partitions; we estimate the global solutions $\{u^{(k)}\}_{k=1}^{n_{\text{train}}}$ using a standard FE solver and we assemble the datasets

$$\mathcal{D}_\ell = \left\{ \underline{u}^{(k)}|_{\Omega_i^{(k)}} \circ \Phi_i^{(k)} \ : \ \mathtt{L}_i^{(k)} = \ell, \ k = 1, \dots, n_{\text{train}} \right\} \subset \mathcal{X}_\ell^{\text{a}}, \quad \ell \in \mathcal{L}; \tag{5.19a}$$

we further define the bubble and port datasets

$$\mathcal{D}_\ell^{\text{b}} := \left\{ \underline{w} - \mathtt{E}_\ell^{\text{a}}(\underline{w}|_{\Gamma_\ell^{\text{a}}}) \ : \ \underline{w} \in \mathcal{D}_\ell \right\}, \quad \mathcal{D}_\ell^{\text{p}} := \left\{ \mathtt{E}_\ell^{\text{a}}(\underline{w}|_{\Gamma_\ell^{\text{a}}}) \ : \ w \in \mathcal{D}_\ell \right\}; \tag{5.19b}$$

finally, we apply proper orthogonal decomposition (POD, [Vol11]) based on the method of snapshots [Sir87] with inner product $(\cdot, \cdot)_\ell$, to obtain the local approximation spaces. Algorithm 9 summarizes the computational procedure.

In view of the application of the empirical quadrature procedures described in sections 5.3.2 and 5.3.3, for all $\ell \in \mathcal{L}$ we further compute the projected coefficients $\{\boldsymbol{\alpha}_{\ell,j}\}_{j=1}^{n_{\text{train},\ell}}$, $\{\boldsymbol{\beta}_{\ell,j}\}_{j=1}^{n_{\text{train},\ell}}$

$$(\boldsymbol{\alpha}_{\ell,j})_i = \left(\underline{u}^{\text{b}}_{\ell,j}, \underline{\zeta}^{\text{a,b}}_{\ell,i}\right)_\ell, \quad \left(\boldsymbol{\beta}_{\ell,j}\right)_q = \left(\underline{u}^{\text{p}}_{\ell,j}, \underline{\psi}^{\text{a,p}}_{\ell,q}\right)_\ell, \qquad \ell \in \mathcal{L}, \tag{5.20}$$

for $i = 1, \dots, n$, $q = 1, \dots, m$, $j = 1, \dots, n_{\text{train},\ell}$, where $\underline{u}^{\text{b}}_{\ell,j}$ (resp., $\underline{u}^{\text{p}}_{\ell,j}$) denotes the j-th bubble (resp., port) solution in the dataset $\mathcal{D}^{\text{b}}_\ell$ (resp., $\mathcal{D}^{\text{p}}_\ell$).

Algorithm 9 Data compression based on global solves

Inputs: training parameters $\{\mu^{(k)}\}_{k=1}^{n_{\text{train}}}$; m, n ROB dimensions.

Outputs: $\{(\underline{Z}^{\text{a,b}}_\ell, \underline{W}^{\text{a,b}}_\ell)\}_{\ell \in \mathcal{L}}$ ROBs; $\{\boldsymbol{\alpha}^{(k)}_\ell\}_{k=1}^{n_{\text{train},\ell}}$, $\{\boldsymbol{\beta}^{(k)}_\ell\}_{k=1}^{n_{\text{train},\ell}}$ local optimal coefficients.

1: Initialize $\mathcal{D}^{\text{b}}_\ell = \mathcal{D}^{\text{p}}_\ell = \emptyset$ for $\ell \in \mathcal{L}$.
2: **for** $k = 1, \dots, n_{\text{train}}$ **do**
3: Estimate the global solution $\underline{u}_\mu$ to (5.10) using a global FE method.
4: Update the datasets $\mathcal{D}^{\text{b}}_\ell$ and $\mathcal{D}^{\text{p}}_\ell$ using (5.19b).
5: **end for**
6: Perform POD to obtain the ROBs $\underline{Z}^{\text{a,b}}_\ell = [\underline{\zeta}^{\text{a,b}}_{\ell,1}, \dots, \underline{\zeta}^{\text{a,b}}_{\ell,n}]$ and $\underline{W}^{\text{a,p}}_\ell = [\underline{\psi}^{\text{a,b}}_{\ell,1}, \dots, \underline{\psi}^{\text{a,b}}_{\ell,n}]$
7: Define the optimal coefficients $\{\boldsymbol{\alpha}^{(k)}_\ell\}_{k=1}^{n_{\text{train},\ell}}$, $\{\boldsymbol{\beta}^{(k)}_\ell\}_{k=1}^{n_{\text{train},\ell}}$ using (5.20).

We remark that the proposed approach — which was previously considered in [Peg+21] — might be highly inefficient since it requires global solves that are often unfeasible in the framework of CB-pMOR. We envision to further extend the localized training approach in [ST22] to address this issue. For practical applications, we envision that global solves should be performed using a standard FE solver and then resorting to FE interpolation routines to extract the local solutions: this procedure inevitably introduces an error at the scale of the FE mesh size between full-order and reduced-order models. Even if this error might be negligible for applications, it hinders the interpretations of the numerical investigations. To avoid this issue, in the numerical experiments, we rely on the HF model (5.13) to generate the dataset of local solutions.

5.3.2 Hyper-reduction of port-to-bubble problems

We here rely on element-wise EQ, that is we replace the residuals (5.7) in (5.15a) with the weighted residual associated with the variational form

$$\underline{\mathcal{G}}^{\text{a,eq}}_\ell(\underline{w}, \underline{v}; \mu_\ell) = \sum_{k=1}^{N^{\text{e}}_\ell} \rho^{\text{eq}}_{\ell,k} \left(\int_{\mathtt{D}_{\ell,k}} \eta^{\text{a,e}}_\ell(\underline{w}, \underline{v}; \mu_\ell)\, dx \; + \; \int_{\partial \mathtt{D}_{\ell,k}} \eta^{\text{a,f}}_\ell(\underline{w}, \underline{v}; \mu_\ell)\, dx \right), \tag{5.21}$$

where $\boldsymbol{\rho}^{\text{eq}}_\ell = [\rho^{\text{eq}}_{\ell,1}, \dots, \rho^{\text{eq}}_{\ell,N^{\text{e}}_\ell}]^T$ is a sparse vector of non-negative weights. This hyper-reduction approach, which has been considered in a number of previous works including [IST22], is discussed for completeness in A. We anticipate that the algorithm takes as input the projected coefficients (5.20) generated by Algorithm 9 and the associated local parameters, $\{(\boldsymbol{\alpha}^{(j)}_\ell, \boldsymbol{\beta}^{(j)}_\ell, \mu^{(j)}_\ell\}_{j=1}^{n_{\text{train},\ell}}$.

We remark that, as discussed in [DY22], the use of elementwise- (as opposed to pointwise-) reduced quadrature formulations leads to significantly less efficient ROMs,

particularly for high-order FE discretizations. On the other hand, elementwise reduced quadrature formulations are significantly easier to implement and can easily cope with geometry deformations [TZ21]. We refer to [Far+21; Yan21] for a thorough introduction to state-of-the-art hyper-reduction techniques.

5.3.3 Hyper-reduction of the objective function

Exploiting (5.17b), it is easy to verify that — we here stress dependence on the parameter value μ —

$$\mathfrak{F}\left(\boldsymbol{\alpha},\,\boldsymbol{\beta},\{\boldsymbol{\rho}_\ell^{\mathrm{p,eq}}\}_{\ell\in\mathcal{L}},\mu\right)=\frac{1}{2}\sum_{\ell\in\mathcal{L}}\left(\sum_{i:\mathtt{L}_i=\ell}\boldsymbol{\eta}_i^{\mathrm{p}}(\boldsymbol{\alpha},\boldsymbol{\beta},\mu)\right)\cdot\boldsymbol{\rho}_\ell^{\mathrm{p,eq}}=\frac{1}{2}\sum_{\ell\in\mathcal{L}}\sum_{j=1}^{N_{\mathrm{dd},\ell}}\left(\mathbf{G}_\ell^{\mathrm{p}}(\boldsymbol{\alpha},\boldsymbol{\beta},\mu)\boldsymbol{\rho}_\ell^{\mathrm{p,eq}}\right)_j,$$

where $N_{\mathrm{dd},\ell}$ is the number of components of type ℓ and $\{\mathbf{G}_\ell^{\mathrm{p}}\}_\ell$ are suitable matrices; to provide a concrete example, for the model problem of section 5.2.3, we have

$$\mathbf{G}_{\mathrm{int}}^{\mathrm{p}}(\boldsymbol{\alpha},\boldsymbol{\beta},\mu)=\begin{bmatrix}\left(\boldsymbol{\eta}_1^{\mathrm{p}}(\boldsymbol{\alpha},\boldsymbol{\beta},\mu)\right)^T\\ \vdots\\ \left(\boldsymbol{\eta}_{Q_{\mathrm{a}}}^{\mathrm{p}}(\boldsymbol{\alpha},\boldsymbol{\beta},\mu)\right)^T\end{bmatrix},\quad \mathbf{G}_{\mathrm{ext}}^{\mathrm{p}}(\boldsymbol{\alpha},\boldsymbol{\beta},\mu)=\left(\boldsymbol{\eta}_{Q_{\mathrm{a}}+1}^{\mathrm{p}}(\boldsymbol{\alpha},\boldsymbol{\beta},\mu)\right)^T.$$

In order to speed up the evaluation of $\mathfrak{f}^{\mathrm{eq}}$, it is necessary to build a sparse quadrature rule $\{\boldsymbol{\rho}_\ell^{\mathrm{p,eq}}\}_{\ell\in\mathcal{L}}$. In the remainder of this section, we propose two different strategies to address this task: the former relies on the solution to a suitable sparse representation problem and is tightly linked to the EQ procedure employed for hyper-reduction of the port-to-bubble maps; the latter relies on a variant of the empirical interpolation method (EIM, [Bar+04]) for vector-valued functions.

Empirical quadrature

We denote by $(\boldsymbol{\alpha}^{(k)},\boldsymbol{\beta}^{(k)})$ the projected bubble and port coefficients associated with the k-th configuration $\mu^{(k)}$ and Eq. (5.20); we further denote by $(\boldsymbol{\alpha}_0^{(k)},\boldsymbol{\beta}_0^{(k)})$ the bubble and port coefficients associated with the sample means,

$$\boldsymbol{\alpha}_0^{(k)}=\begin{bmatrix}\boldsymbol{\alpha}_{0,1}^{(k)}\\ \vdots\\ \boldsymbol{\alpha}_{0,N_{\mathrm{dd},(\mathrm{k})}}^{(k)}\end{bmatrix},\quad \boldsymbol{\beta}_0^{(k)}=\begin{bmatrix}\boldsymbol{\beta}_{0,1}^{(k)}\\ \vdots\\ \boldsymbol{\beta}_{0,N_{\mathrm{dd},(\mathrm{k})}}^{(k)}\end{bmatrix},\quad k=1,\dots,n_{\mathrm{train}},\tag{5.22a}$$

where $\boldsymbol{\alpha}_{0,i}^{(k)}=\boldsymbol{\alpha}_{\mathtt{L}_i^{(k)}}^{\mathrm{avg}}$ and $\boldsymbol{\beta}_{0,i}^{(k)}=\boldsymbol{\beta}_{\mathtt{L}_i^{(k)}}^{\mathrm{avg}}$, with

$$\boldsymbol{\alpha}_\ell^{\mathrm{avg}}:=\frac{1}{n_{\mathrm{train},\ell}}\sum_{j=1}^{n_{\mathrm{train},\ell}}\boldsymbol{\alpha}_{\ell,j},\quad \boldsymbol{\beta}_\ell^{\mathrm{avg}}:=\frac{1}{n_{\mathrm{train},\ell}}\sum_{j=1}^{n_{\mathrm{train},\ell}}\boldsymbol{\beta}_{\ell,j},\qquad\forall\,\ell\in\mathcal{L}.\tag{5.22b}$$

We anticipate that (5.22) is used in the numerical results to initialize the Gauss-Newton's algorithm.

Given the random samples $s^{(k)} \overset{\text{iid}}{\sim} \text{Uniform}(0,1)$, we define the matrices

$$\mathbf{C}_\ell = \begin{bmatrix} \mathbf{G}_\ell^{\text{p}}(\widetilde{\boldsymbol{\alpha}}^{(1)}, \widetilde{\boldsymbol{\beta}}^{(1)}, \mu^{(1)}) \\ \vdots \\ \mathbf{G}_\ell^{\text{p}}(\widetilde{\boldsymbol{\alpha}}^{(n_{\text{train}})}, \widetilde{\boldsymbol{\beta}}^{(n_{\text{train}})}, \mu^{(n_{\text{train}})}) \\ \mathbf{1}^T \end{bmatrix}, \quad \forall\, \ell \in \mathcal{L}, \tag{5.23a}$$

where $\mathbf{1}$ is the vector with entries all equal to one, and $\widetilde{\boldsymbol{\alpha}}^{(k)}$ and $\widetilde{\boldsymbol{\beta}}^{(k)}$ are random convex interpolations between the projected bubble and port coefficients $(\boldsymbol{\alpha}^{(k)}, \boldsymbol{\beta}^{(k)})$ and the initial conditions for the GNM $(\boldsymbol{\alpha}_0^{(k)}, \boldsymbol{\beta}_0^{(k)})$,

$$\widetilde{\boldsymbol{\alpha}}^{(k)} = (1 - s^{(k)})\boldsymbol{\alpha}^{(k)} + s^{(k)}\boldsymbol{\alpha}_0^{(k)}, \quad \widetilde{\boldsymbol{\beta}}^{(k)} = (1 - s^{(k)})\boldsymbol{\beta}^{(k)} + s^{(k)}\boldsymbol{\beta}_0^{(k)}, \quad k = 1, \dots, n_{\text{train}}. \tag{5.23b}$$

The first n_{train} blocks of $\mathbf{C}_\ell$ are associated to the "manifold accuracy constraints", while the last row is associated to the "constant accuracy constraint" [YP19b]. Then, we compute the empirical weights $\{\boldsymbol{\rho}_\ell^{\text{p,eq}}\}_{\ell \in \mathcal{L}}$ by approximately solving the non-negative least-square problem

$$\min_{\boldsymbol{\rho} \in \mathbb{R}^{N_\ell^{\text{p}}}} \| \mathbf{C}_\ell \left(\boldsymbol{\rho} - \boldsymbol{\rho}_\ell^{\text{p}} \right) \|_2, \quad \text{s.t. } \boldsymbol{\rho} \geq 0 \tag{5.23c}$$

up to a tolerance $tol_{\text{eq}}^{\text{obj}}$ using the Matlab function `lsqnonneg`, which implements the iterative procedure proposed in [LH74].

The choice of the port and bubble coefficients $\{(\widetilde{\boldsymbol{\alpha}}^{(k)}, \widetilde{\boldsymbol{\beta}}^{(k)})\}_k$ for the "accuracy constraints" in (5.23a) is justified by the fact that the objective function should be accurate for all port and bubble coefficients considered during the GNM iterations; this choice is found to empirically improve the conditioning of the non-negative least-square problem and ultimately improve performance — compared to the choice $\widetilde{\boldsymbol{\alpha}}^{(k)} = \boldsymbol{\alpha}^{(k)}$, $\widetilde{\boldsymbol{\beta}}^{(k)} = \boldsymbol{\beta}^{(k)}$. The constant function accuracy constraint, which was first proposed in [YP19b] for hyper-reduction of monolithic ROMs, is important to bound the ℓ^1 norm of the empirical weights; we have indeed

$$\|\boldsymbol{\rho}_\ell^{\text{p,eq}}\|_1 \leq |\mathbf{1} \cdot (\boldsymbol{\rho}_\ell^{\text{p,eq}} - \boldsymbol{\rho}_\ell^{\text{p}})| + \|\boldsymbol{\rho}_\ell^{\text{p}}\|_1 \leq \| \mathbf{C}_\ell \left(\boldsymbol{\rho}_\ell^{\text{p,eq}} - \boldsymbol{\rho}_\ell^{\text{p}} \right) \|_2 + \|\boldsymbol{\rho}_\ell^{\text{p}}\|_1, \quad \forall\, \ell \in \mathcal{L}. \tag{5.24}$$

We also observe that, even if hyper-reduction is ultimately performed at the local level, for each archetype component, the EQ procedure requires global solves to define the matrices $\{\mathbf{C}_\ell\}_\ell$.

Empirical interpolation method

The objective function $\mathfrak{F}$ is designed to penalize the jump of the solution at the components' interface. Since the jumps are dictated by the behavior of the port modes $\{\psi_{\ell,i}^{\text{a,p}}\}_{i=1}^m$ on the ports Γ_ℓ, we propose to replace the integral in (5.16) with the discrete sum

$$\frac{1}{2} \sum_{i=1}^{N_{\text{dd}}} \sum_{j \in \text{Neigh}_i} \int_{\Gamma_{i,j}} \| \widehat{\underline{u}}_i(\boldsymbol{\alpha}_i, \boldsymbol{\beta}_i) - \widehat{\underline{u}}_j(\boldsymbol{\alpha}_j, \boldsymbol{\beta}_j) \|_2^2 \, dx \approx \frac{1}{2} \sum_{q \in \mathtt{I}_\ell^{\text{p,eq}}} \left(\boldsymbol{\eta}_i^{\text{p}}(\boldsymbol{\alpha}, \boldsymbol{\beta}, \mu) \right)_q, \tag{5.25}$$

where $\mathtt{I}_\ell^{\mathrm{p,eq}} \subset \{1,\dots,N_\ell^{\mathrm{p}}\}$ are chosen so that we can adequately recover any element of $\mathcal{Z}_\ell^{\mathrm{a,p}}$ based on the information at the points $\{x_{\ell,j}^{\mathrm{p}}\}_{j\in\mathtt{I}_\ell^{\mathrm{p,eq}}}$. Note that the approximation (5.25) is an inconsistent approximation of the L^2 integral (5.16); however, we expect — and we verify numerically — that the minimization of the right-hand side of (5.25) should control the jump at elements' interfaces and ultimately ensure accurate performance.

We here rely on a variant of EIM to select the quadrature indices $\mathtt{I}_\ell^{\mathrm{p,eq}}$. EIM was first proposed in [Bar+04] to identify accurate interpolation points for arbitrary sets of scalar functions. In this work, we resort to the extension of EIM to vector-valued fields considered in [Tad19]. We refer to the MOR literature for other variants of EIM for vector-valued fields; in particular, we observe that the present algorithm returns exactly m quadrature points: we refer to [Mad+15, Algorithm 2] and to [Che+21b] for extensions of EIM that resort to over-collocation to improve performance.

Algorithm 10 reviews the computational procedure: note that, for each $\ell \in \mathcal{L}$, the algorithm takes as input the port functions $\{\underline{\psi}_{\ell,i}^{\mathrm{a,p}}\}_{i=1}^m$ and returns the indices $\mathtt{I}_\ell^{\mathrm{p,eq}}$. Given the set of indices $\mathtt{I}_\ell^{\mathrm{p,eq}}$ and the space $\mathcal{Z}_\ell^{\mathrm{a,p}}$, we denote by $\mathcal{I}_{\ell,m}$ the approximation least-square operator

$$\mathcal{I}_{\ell,m}(\underline{v}) := \mathcal{I}\left(\underline{v}; \mathtt{I}_\ell^{\mathrm{p,eq}}, \mathcal{Z}_\ell^{\mathrm{a,p}}\right) = \arg\min_{\underline{\psi}\in\mathcal{Z}_\ell^{\mathrm{a,p}}} \sum_{j\in\mathtt{I}_\ell^{\mathrm{p,eq}}} \|\underline{v}(x_{\ell,j}^{\mathrm{p}}) - \underline{\psi}(x_{\ell,j}^{\mathrm{p}})\|_2^2, \quad \forall\, v \in C(\Gamma_\ell;\mathbb{R}^D),\ \ell\in\mathcal{L}.$$

Note that for $D > 1$ $\mathcal{I}_{\ell,m}$ is not an interpolation operator.

Algorithm 10 Empirical Interpolation Method for vector-valued fields

Input: $\{\underline{\psi}_{\ell,i}^{\mathrm{a,p}}\}_{i=1}^m$, $\ell \in \mathcal{L}$

Output: $\mathtt{I}_\ell^{\mathrm{p,eq}} = \{\mathtt{i}_{\ell,1}^\star, \dots, \mathtt{i}_{\ell,m}^\star\}$

Set $\mathtt{i}_{\ell,1}^\star := \arg\max_{j\in\{1,\dots,N_\ell^{\mathrm{p}}\}} \|\underline{\psi}_{\ell,1}^{\mathrm{a,p}}(x_{\ell,j}^{\mathrm{p}})\|_2$, and define $\mathcal{I}_{\ell,1} := \mathcal{I}\left(\cdot; \{\mathtt{i}_{\ell,1}^\star\}, \mathrm{span}\{\underline{\psi}_{\ell,1}^{\mathrm{a,p}}\}\right)$

for $m' = 2,\dots,m$ **do**

Compute $\underline{r}_{m'} = \underline{\psi}_{\ell,m'}^{\mathrm{a,p}} - \mathcal{I}_{\ell,m'-1}\left(\underline{\psi}_{\ell,m'}^{\mathrm{a,p}}\right)$

Set $\mathtt{i}_{\ell,m'}^\star := \arg\max_{j\in\{1,\dots,N_\ell^{\mathrm{p}}\}} \|\underline{r}_{m'}(x_{\ell,j}^{\mathrm{p}})\|_2$

Update $\mathcal{I}_{\ell,m'} := \mathcal{I}\left(\cdot; \{\mathtt{i}_{\ell,j}^\star\}_{j=1}^{m'}, \mathrm{span}\{\underline{\psi}_{\ell,j}^{\mathrm{a,p}}\}_{j=1}^{m'}\right)$.

end for

5.4 Analysis and interpretation for linear coercive problems

We analyze the OS2 statement for linear coercive problems. To simplify the presentation, we consider the case with two subdomains depicted in Figure 5.1. We denote by $(\mathcal{X}, \|\cdot\|_\Omega)$ the global ambient space such that $H_0^1(\Omega) \subset \mathcal{X} \subset H^1(\Omega)$; given the ports Γ_1, Γ_2 (cf. Figure 5.1), we define the bubble and port spaces:

$$\mathcal{X}_{i,0} := \{v \in \mathcal{X}_i \,:\, v|_{\Gamma_i} = 0\}, \quad \mathcal{U}_i := \{v|_{\Gamma_i} \,:\, v \in \mathcal{X}_i\}, \quad i = 1,2.$$

We introduce the bilinear form $a : \mathcal{X}\times\mathcal{X} \to \mathbb{R}$ with continuity constant γ and coercivity constant $\alpha > 0$, and we introduce the linear functional $f \in \mathcal{X}'$. Then, we introduce

the model problem:

$$\text{find } u^\star \in \mathcal{X} \ : \ a(u^\star, v) = f(v) \quad \forall\, v \in \mathcal{X}. \tag{5.26}$$

In section 5.4.1, we derive the port formulation of the problem (5.26); in section 5.4.2, we present two important results for the port problem; in section 5.4.3 we exploit the results of the previous section to derive an *a priori* bound for the OS2 statement; in section 5.4.4, we comment on an alternative variational interpretation of the OS2 statement; finally, in section 5.4.5, we derive explicit estimates for two representative model problems.

Given $v \in \mathcal{X}_{i,0}$, we denote by $v^{\text{ext}} \in \mathcal{X}$ the trivial extension of v to Ω that is zero in $\Omega \setminus \Omega_i$. We assume that a and f are associated to a differential (elliptic) problem; in particular, we assume that

$$a(u, v^{\text{ext}}) = a\left(u\big|_{\Omega_i}, v\right), \quad \forall\, v \in \mathcal{X}_{i,0}. \tag{5.27}$$

Note that by construction we have $f(v^{\text{ext}}) = f\,(v)$ for all $v \in \mathcal{X}_{i,0}$.

5.4.1 Port formulation

We define the tensor-product space $\mathcal{U} = \mathcal{U}_1 \times \mathcal{U}_2$ endowed with the inner product $\langle w, v\rangle = \sum_{i=1,2}(w_i, v_i)_{H^{1/2}(\Gamma_i)}$ and the induced norm $|||\cdot||| = \sqrt{\langle \cdot, \cdot\rangle}$. We introduce the local solution operators $T_i : \mathcal{U}_i \to \mathcal{X}_i$ and $G_i : \mathcal{X}' \to \mathcal{X}_{i,0}$ such that:

$$(T_i\lambda)\,\big|_{\Gamma_i} = \lambda, \qquad a(T_i\lambda, v) = 0 \quad \forall\, v \in \mathcal{X}_{i,0}; \tag{5.28}$$

$$(G_i f)\,\big|_{\Gamma_i} = 0, \qquad a(G_i f, v) = f(v) \quad \forall\, v \in \mathcal{X}_{i,0}. \tag{5.29}$$

Since the elements of $\mathcal{X}_{i,0}$ can be trivially extended to zero in $\Omega \setminus \Omega_i$, we have that the form a is continuous and coercive in $\mathcal{X}_{i,0}$ with continuity and coercivity constants bounded from above and below by γ and α, due to the fact that $\mathcal{X}_{i,0} \subset \mathcal{X}$.

Therefore, T_i and G_i are well-defined linear bounded operators. By comparing the previous definitions with (5.13a), we note that the affine operators $F_i := T_i - E_i + G_i f$ correspond to the port-to-bubble maps that are exploited to derive the hybridized formulation in section 5.2: we have $u^\star|_{\Omega_i} = F_i\lambda_i^\star + E_i\lambda_i^\star = T_i\lambda_i^\star + G_i f$, where $\lambda_i^\star \in \mathcal{U}_i$ is equal to $u^\star|_{\Gamma_i}$.

Given the trace operators $\chi_{\Gamma_1} : \mathcal{X}_2 \to \mathcal{U}_1$, $\chi_{\Gamma_2} : \mathcal{X}_1 \to \mathcal{U}_2$, we introduce the operators $T : \mathcal{U} \to \mathcal{U}$ and $G : \mathcal{X}' \to \mathcal{U}$ such that

$$T\lambda = \begin{bmatrix} \chi_{\Gamma_1} T_2 \lambda_2 \\ \chi_{\Gamma_2} T_1 \lambda_1 \end{bmatrix}, \quad Gf = \begin{bmatrix} \chi_{\Gamma_1} G_2 f \\ \chi_{\Gamma_2} G_1 f \end{bmatrix}, \quad \forall\, \lambda \in \mathcal{U}, \quad f \in \mathcal{X}'. \tag{5.30a}$$

Finally, we introduce the port problem: find $\lambda^\star \in \mathcal{U}$ such that

$$a_{\text{p}}(\lambda^\star, v) = f_{\text{p}}(v) \quad \forall\, v \in \mathcal{U}, \ \text{ where } \ a_{\text{p}}(\lambda, v) := \langle \lambda - T\lambda, v\rangle, \ \ f_{\text{p}}(v) := \langle Gf, v\rangle. \tag{5.30b}$$

Remark 8. ***Connection with OS methods.*** *We can rewrite standard additive and multiplicative OS iterations, presented in (5.2) for the simplified problem in section 5.1, using the operators introduced in (5.30). In more detail, multiplicative OS iterations can be written as (see, e.g., [QV99, Chapter 1])*

$$\begin{bmatrix} Id & 0 \\ -\chi_{\Gamma_2} T_1 & Id \end{bmatrix} \lambda^{(k+1)} = \begin{bmatrix} 0 & \chi_{\Gamma_1} T_2 \\ 0 & 0 \end{bmatrix} \lambda^{(k)} + Gf, \qquad k = 1, 2, \ldots,$$

while additive OS iterations can be written as

$$\begin{bmatrix} Id & 0 \\ 0 & Id \end{bmatrix} \lambda^{(k+1)} = \begin{bmatrix} 0 & \chi_{\Gamma_1} T_2 \\ \chi_{\Gamma_2} T_1 & 0 \end{bmatrix} \lambda^{(k)} + Gf, \qquad k = 1, 2, \dots.$$

These identities imply that any fixed point of the OS iterations satisfies (5.30b). *As discussed in the introduction in section 5.1, this connection between OS and OS2 formulations is valid for both linear and nonlinear problems; however, the analysis is strictly restricted to the linear case.*

5.4.2 Analysis of the port problem

Proposition 1 clarifies the relationship between the variational statement (5.26) and the port problem (5.30); on the other hand, Proposition 2 is key for the analysis of the OS2 ROM. Proofs are postponed to appendix B. The results rely on the introduction of a partition-of-unity (PoU, [BM97]) $\{\phi_i\}_{i=1}^2 \subset \mathrm{Lip}(\Omega; \mathbb{R})$ associated with $\{\Omega_i\}_{i=1}^2$ such that

$$\sum_{i=1}^{2} \phi_i(x) = 1, \quad \begin{cases} 0 \le \phi_i(x) \le 1 & \forall\, x \in \Omega, \\ \phi_i(x) = 0 & \forall\, x \notin \Omega_i, \end{cases} \quad i = 1, 2.$$

Proposition 1. *Let $u^\star$ be the solution to* (5.26). *Then, $\lambda^\star = (u^\star|_{\Gamma_1}, u^\star|_{\Gamma_2})$ solves* (5.30b). *Conversely, if $\lambda^\star$ is a solution to* (5.30b), *then $u^\star = \sum_{i=1}^2 (T_i \lambda_i^\star + G_i f)\, \phi_i$ solves* (5.26).

Proposition 2. *Let the operator T in* (5.30a) *be compact. Then, the form $a_{\mathrm{p}} : \mathcal{U} \times \mathcal{U} \to \mathbb{R}$ defined in* (5.30b) *is inf-sup stable and continuous, that is*

$$\alpha_{\mathrm{p}} = \inf_{w \in \mathcal{U}} \sup_{v \in \mathcal{U}} \frac{a_{\mathrm{p}}(w, v)}{|||w||| |||v|||} > 0, \quad \gamma_{\mathrm{p}} = \sup_{w \in \mathcal{U}} \sup_{v \in \mathcal{U}} \frac{a_{\mathrm{p}}(w, v)}{|||w||| |||v|||} < \infty. \tag{5.31}$$

The proof of the compactness of the operator T depends on the underlying PDE. For several problems, including the Laplace equation, the advection-diffusion-reaction equation, the Stokes equations, and the Helmholtz equation, we can prove compactness of the operator T using Caccioppoli's inequalities: we refer to [Tad17, Appendix C] and also [SP16] for further details. We further observe that Proposition 2 does not provide an explicit relationship among the stability constant α_{p} in Proposition 2, the PDE of interest and the size of the overlap. We envision that the derivation of explicit bounds for the stability constant α_{p} in terms of the PDE of interest and the size of the overlap will shed light on the underlying properties of the OS2 formulation and might also lead to new algorithmic developments. We note that there is a vast body of works that address the derivation of sharp estimates for the convergence of overlapping Schwarz methods (see, e.g., [CHL91; CG17]): the derivation of analogous results for this setting is beyond the scope of the present thesis.

As discussed in appendix B, proofs of Propositions 1 and 2 rely on the fact that, if we introduce the spaces $\mathcal{X}_{1,2} = \{v|_{\Omega_1 \cap \Omega_2} : v \in \mathcal{X}\}$ and $\mathcal{X}_{1,2}^0 = \{v \in \mathcal{X}_{1,2} : v|_{\Gamma_1 \cup \Gamma_2} = 0\}$, the problem of finding $u \in \mathcal{X}_{1,2}$ such that

$$a(u, v) = 0 \quad \forall\, v \in \mathcal{X}_{1,2}^0, \quad u|_{\Gamma_1} = \lambda_1, \quad u|_{\Gamma_2} = \lambda_2,$$

admits a unique solution for any $(\lambda_1, \lambda_2) \in \mathcal{U}$. This result is trivial for coercive problems, but it is significantly less trivial — and requires additional assumptions — for inf-sup stable problems and is not addressed in this work. On the other hand, we envision that the analysis for nonlinear PDEs requires more sophisticated tools and is beyond the scope of this work.

5.4.3 Analysis of the OS2 statement

We consider the following OS2 formulation for the linear problem (5.26):

$$\text{find } \widehat{\lambda} = \arg\min_{\lambda\in\mathcal{Z}^{\mathrm{p}}} \left|\!\left|\!\left| \lambda - \widehat{T}\lambda - \widehat{G}f \right|\!\right|\!\right|. \tag{5.32}$$

Note that (5.32) corresponds to the OS2 statement (5.13) with the important difference that we replace the L^2 norm with the $H^{1/2}$ norm $|||\cdot|||$. In particular, in our work, the space $\mathcal{Z}^{\mathrm{p}}$ in (5.32) is given by the tensor product of the local port spaces, $\mathcal{Z}^{\mathrm{p}} = \mathcal{Z}_1^{\mathrm{p}} \times \mathcal{Z}_2^{\mathrm{p}}$, and $\widehat{T}, \widehat{G}$ are associated to the approximate local solution operators that are obtained by Galerkin projection. We further introduce the OS2 formulation with perfect local operators:

$$\text{find } \widetilde{\lambda} = \arg\min_{\lambda\in\mathcal{Z}^{\mathrm{p}}} |||\lambda - T\lambda - Gf|||. \tag{5.33}$$

We observe that (5.33) corresponds to the minimum residual formulation of the port problem (5.30); we have indeed

$$|||\lambda - T\lambda - Gf||| = \sup_{v\in\mathcal{U}} \frac{\langle \lambda - T\lambda - Gf, v\rangle}{|||v|||} = \sup_{v\in\mathcal{U}} \frac{a_{\mathrm{p}}(\lambda, v) - f_{\mathrm{p}}(v)}{|||v|||}.$$

Recalling the result in [XZ03], we thus have

$$\left|\!\left|\!\left| \lambda^\star - \widetilde{\lambda} \right|\!\right|\!\right| \le \frac{\gamma_{\mathrm{p}}}{\alpha_{\mathrm{p}}} \inf_{\lambda\in\mathcal{Z}^{\mathrm{p}}} |||\lambda^\star - \lambda|||, \tag{5.34}$$

which proves the quasi-optimality of the OS2 statement with perfect local operators (5.33).

To estimate the error $\left|\!\left|\!\left| \widehat{\lambda} - \widetilde{\lambda} \right|\!\right|\!\right|$, we resort to a perturbation analysis. We denote by $\widehat{\alpha}_{\mathrm{p}}$ and $\widehat{\gamma}_{\mathrm{p}}$ the stability and continuity constants associated with the problem (5.32): it is possible to resort to a perturbation analysis to estimate these constants; since the argument is completely standard, we omit the details. We define the quantities ε_{T} and ε_{G} as follows:

$$\varepsilon_{\mathrm{T}} := \sup_{\psi\in\mathcal{Z}^{\mathrm{p}}} \frac{\left|\!\left|\!\left| (T - \widehat{T})\psi \right|\!\right|\!\right|}{|||\psi|||}, \quad \varepsilon_{\mathrm{G}} := \left|\!\left|\!\left| (G - \widehat{G})f \right|\!\right|\!\right|. \tag{5.35}$$

Then, it is possible to show that

$$\left|\!\left|\!\left| \widetilde{\lambda} - \widehat{\lambda} \right|\!\right|\!\right| \le \frac{1}{\alpha_{\mathrm{p}}^2} \left(M\left(\gamma_{\mathrm{p}} + \widehat{\gamma}_{\mathrm{p}}\right) \frac{\left|\!\left|\!\left| \widehat{G}f \right|\!\right|\!\right|}{\widehat{\alpha}_{\mathrm{p}}} \varepsilon_{\mathrm{T}} + \sqrt{M}\left(\widehat{\gamma}_{\mathrm{p}}\varepsilon_{\mathrm{G}} + \left|\!\left|\!\left| \widehat{G}f \right|\!\right|\!\right| \varepsilon_{\mathrm{T}} \right) \right). \tag{5.36}$$

We postpone the proof of (5.36) to appendix B.

By combining (5.36) with (5.34), we obtain the following result. We observe that (5.37) is the sum of two terms: the first term is associated with the approximation properties of the port space, while the second term is directly linked to the accuracy of the local solution operators.

Proposition 3. *Let $\gamma_{\mathrm{p}}, \alpha_{\mathrm{p}}$ be the continuity and stability constants of the form a_{p} and let $\widehat{\gamma}_{\mathrm{p}}, \widehat{\alpha}_{\mathrm{p}}$ be the continuity and stability constants of the form $\widehat{a}_{\mathrm{p}}(\lambda, v) = \langle \lambda - \widehat{T}\lambda\,,\, v\rangle$.*

Given the M-dimensional space $\mathcal{Z}^{\mathrm{p}} \subset \mathcal{U}$, we have

$$\left|\!\left|\!\left| \lambda^\star - \widehat{\lambda} \right|\!\right|\!\right| \leq \frac{1}{\alpha_{\mathrm{p}}} \left(\gamma_{\mathrm{p}} \inf_{\lambda \in \mathcal{Z}^{\mathrm{p}}} \left|\!\left|\!\left| \lambda^\star - \lambda \right|\!\right|\!\right| + \frac{1}{\alpha_{\mathrm{p}}} \left(M \left(\gamma_{\mathrm{p}} + \widehat{\gamma}_{\mathrm{p}} \right) \frac{\left|\!\left|\!\left| \widehat{G} f \right|\!\right|\!\right|}{\widehat{\alpha}_{\mathrm{p}}} \varepsilon_{\mathrm{T}} + \sqrt{M} \left(\widehat{\gamma}_{\mathrm{p}} \varepsilon_{\mathrm{G}} + \left|\!\left|\!\left| \widehat{G} f \right|\!\right|\!\right| \varepsilon_{\mathrm{T}} \right) \right) \right). \tag{5.37}$$

5.4.4 Alternative variational interpretation of the OS2 statement

Following [Lio88], we might also consider the alternative variational framework of the OS limit formulation (see also [QV99, Chapter 1.5.2]): find $(u_1^{\mathrm{b}}, u_1^{\mathrm{p}}, u_2^{\mathrm{b}}, u_2^{\mathrm{p}}) \in \bigotimes_{i=1}^{2} \mathcal{X}_{i,0} \times \mathcal{U}_i$ such that

$$\begin{cases} a\left(u_i^{\mathrm{b}} + E_i u_i^{\mathrm{p}},\, v_i\right) = f(v_i) & \forall\, v_i \in \mathcal{X}_{i,0}, \quad i = 1, 2; \\ \left(u_1^{\mathrm{p}} - \chi_{\Gamma_1}\left(u_2^{\mathrm{b}} + E_2 u_2^{\mathrm{p}}\right),\, \psi_1\right)_{H^{1/2}(\Gamma_1)} + & \\ \left(u_2^{\mathrm{p}} - \chi_{\Gamma_2}\left(u_1^{\mathrm{b}} + E_1 u_1^{\mathrm{p}}\right),\, \psi_2\right)_{H^{1/2}(\Gamma_2)} = 0 & \forall\, \psi = (\psi_1, \psi_2) \in \mathcal{U}; \end{cases} \tag{5.38}$$

where E_1, E_2 are the extension operators, $u_1^{\mathrm{b}}, u_2^{\mathrm{b}}$ are the bubble solutions and $u_1^{\mathrm{p}}, u_2^{\mathrm{p}}$ are the port solutions. Given the reduced spaces $\mathcal{Z}_i^{\mathrm{b}} \subset \mathcal{X}_{i,0}$ and $\mathcal{Z}_i^{\mathrm{p}} \subset \mathcal{U}_i$, and the approximate port-to-bubble maps $\widehat{F}_i = \widehat{T}_i + \widehat{G}_i f - E_i$, for $i = 1, 2$, the reduced-order OS2 formulation can be stated as follows: find $(\widehat{u}_1^{\mathrm{b}}, \widehat{u}_1^{\mathrm{p}}, \widehat{u}_2^{\mathrm{b}}, \widehat{u}_2^{\mathrm{p}}) \in \bigotimes_{i=1}^{2} \mathcal{Z}_i^{\mathrm{b}} \times \mathcal{Z}_i^{\mathrm{p}}$ such that

$$\begin{cases} a\left(\widehat{u}_i^{\mathrm{b}} + E_i \widehat{u}_i^{\mathrm{p}},\, v_i\right) = f(v_i) & \forall\, v_i \in \mathcal{Z}_i^{\mathrm{b}}, \quad i = 1, 2; \\ \left(\widehat{u}_1^{\mathrm{p}} - \chi_{\Gamma_1}\left(\widehat{u}_2^{\mathrm{b}} + E_2 \widehat{u}_2^{\mathrm{p}}\right),\, \psi_1\right)_{H^{1/2}(\Gamma_1)} + & \\ \left(\widehat{u}_2^{\mathrm{p}} - \chi_{\Gamma_2}\left(\widehat{u}_1^{\mathrm{b}} + E_1 \widehat{u}_1^{\mathrm{p}}\right),\, \psi_2\right)_{H^{1/2}(\Gamma_2)} = 0 & \forall\, \psi = (\psi_1, \psi_2) \in \widetilde{\mathcal{Z}}^{\mathrm{p}}; \end{cases} \tag{5.39a}$$

where $\widetilde{\mathcal{Z}}^{\mathrm{p}} \subset \mathcal{U}$ is the M-dimensional space given by

$$\widetilde{\mathcal{Z}}^{\mathrm{p}} = \left\{ \left(\zeta_1^{\mathrm{p}} - \chi_{\Gamma_1} \widehat{T}_2(\zeta_2^{\mathrm{p}}),\; \zeta_2^{\mathrm{p}} - \chi_{\Gamma_2} \widehat{T}_1(\zeta_1^{\mathrm{p}}) \right) \,:\, \zeta_i^{\mathrm{p}} \in \mathcal{Z}_i^{\mathrm{p}}, i = 1, 2 \right\}, \tag{5.39b}$$

and $\widehat{T}_i \zeta$ satisfies $\widehat{T}_i \zeta = u^{\mathrm{b}}(\zeta) + E_i \zeta$ with $u_i^{\mathrm{b}}(\zeta) \in \mathcal{Z}_i^{\mathrm{b}}$ and $a(u_i^{\mathrm{b}}(\zeta) + E_i \zeta, v) = 0$ for all $v \in \mathcal{Z}_i^{\mathrm{b}}$.

The proof of (5.39) is straightforward, and it is provided for completeness in B. Note that the OS2 statement reads as a Petrov-Galerkin projection of (5.38) for a suitable choice of the test space $\widetilde{\mathcal{Z}}^{\mathrm{p}}$. We envision that (5.39) could be exploited to devise an alternative error analysis for the OS2 statement. We do not address this issue in the present work.

5.4.5 Explicit convergence rates for two one-dimensional model problems

Given $\Omega = (-1, 1)$ and the partition $\Omega_1 = (-1, \delta)$, $\Omega_2 = (-\delta, 1)$, we study the convergence of (multiplicative) OS and OS2 for the problems

$$\begin{cases} u'' = 2 & \text{in } \Omega, \\ u(-1) = u(1) = 1; \end{cases} \tag{5.40a}$$

and

$$\begin{cases} -u'' + \gamma u' = 0 & \text{in } \Omega, \\ u(-1) = 0, \quad u(1) = 1; \end{cases} \tag{5.40b}$$

in the limit $|\delta| \ll 1$. For OS2, we resort to the gradient descent method with optimal choice of the step size, and to the Gauss-Newton method (OS2-GN) — the choice of the gradient descent method is intended to simplify calculations (compared to quasi-Newton methods). The motivation of this analysis is twofold: first, we show that the use of gradient-based methods as opposed to Gauss-Newton is increasingly sub-optimal as $\delta \to 0$; second, we provide explicit estimates for the constants α_{P} and γ_{P} of Proposition 2 for two representative model problems.
We denote by $\widehat{u}_i$ the approximation of the solution in Ω_i for $i = 1, 2$; we define $\beta_1 = \widehat{u}_1(\delta)$ and $\beta_2 = \widehat{u}_2(-\delta)$. We can show that OS and OS2 iterations can be written as

$$\boldsymbol{\beta}^{(k)} = \mathbf{P}_\delta^{\mathrm{os}} \boldsymbol{\beta}^{(k-1)} + \mathbf{F}_\delta^{\mathrm{os}}, \quad \boldsymbol{\beta}^{(k)} = \mathbf{P}_\delta^{\mathrm{os2}} \boldsymbol{\beta}^{(k-1)} + \mathbf{F}_\delta^{\mathrm{os2}},$$

for $k = 1, 2, \ldots$ and suitable choices of $\left(\mathbf{P}_\delta^{\mathrm{os}}, \mathbf{F}_\delta^{\mathrm{os}}\right)$ and $\left(\mathbf{P}_\delta^{\mathrm{os2}}, \mathbf{F}_\delta^{\mathrm{os2}}\right)$. On the other hand, since the problems are linear, OS2-GN reduces to a direct method and can be stated as

$$\mathbf{A}_\delta \boldsymbol{\beta} = \mathbf{F}_\delta$$

for suitable choices of $\left(\mathbf{A}_\delta, \mathbf{F}_\delta\right)$.

In appendix B, we show that the spectral radii $\rho_\delta^{\mathrm{os}}$ and $\rho_\delta^{\mathrm{os2}}$ of the transition matrices $\mathbf{P}_\delta^{\mathrm{os}}$ and $\mathbf{P}_\delta^{\mathrm{os2}}$ satisfy

$$\begin{aligned} &\rho_\delta^{\mathrm{os}} \sim 1 - 4\delta, && \rho_\delta^{\mathrm{os2}} \sim 1 - 4\delta^2 && \text{for (5.40a)}; \\ &\rho_\delta^{\mathrm{os}} \sim 1 - 2\frac{e^\gamma + 1}{e^\gamma - 1}\gamma\delta, && \rho_\delta^{\mathrm{os2}} \sim 1 - \frac{e^\gamma + 2}{8(e^\gamma - 1)}\gamma^2\delta^2 && \text{for (5.40b)}; \end{aligned} \tag{5.41a}$$

while the condition number of the linear system associated to OS2-GN satisfies

$$\begin{aligned} &\mathrm{cond}\left(\mathbf{A}_\delta\right) = \frac{1}{\delta}, && \text{for (5.40a)}; \\ &\mathrm{cond}\left(\mathbf{A}_\delta\right) \sim \frac{4(e^\gamma - 1)}{4(e^\gamma + 2)\gamma}\delta^{-1} && \text{for (5.40b)}; \end{aligned} \tag{5.41b}$$

and the constants α_{p} and γ_{p} defined in Proposition 2 satisfy

$$\begin{aligned} &\alpha_{\mathrm{p}} = \frac{2\delta}{1+\delta}, \quad \gamma_{\mathrm{p}} = \frac{2}{1+\delta}, && \text{for (5.40a)}; \\ &\alpha_{\mathrm{p}} \sim \frac{4(e^\gamma + 2)\gamma\delta}{2(e^\gamma - 1)}, \quad \gamma_{\mathrm{p}} \sim 2, && \text{for (5.40b)}; \end{aligned} \tag{5.41c}$$

As expected, OS, OS2 and OS2-GN become increasingly ill-conditioned as δ decreases to zero; however, we observe that for small values of δ, OS exhibits significantly faster convergence rates than OS2 based on the gradient-descent method: this observation further strengthens the importance of exploiting the least-square structure of the OS2 statement.

5.5 Numerical results

5.5.1 Assessment metrics and training parameters

We train the CB-ROM based on $n_{\text{train}} = 70$ global parameters $\Xi_{\text{train}} = \{\mu^{(k)}\}_{k=1}^{n_{\text{train}}}$ such that

$$(E_1^{(k)}, E_2^{(k)}, E_3^{(k)}, s^{(k)}) \overset{\text{iid}}{\sim} \text{Uniform}\left([25,30] \times [10,20]^2 \times [0.4,1]\right), \quad Q_{\text{a}}^{(k)} \overset{\text{iid}}{\sim} \text{Uniform}\left(\{2,\dots,7\}\right);$$

on the other hand, we assess performance based on $n_{\text{test}} = 20$ out-of-sample global parameters $\Xi_{\text{test}} = \{\widetilde{\mu}^{(j)}\}_{j=1}^{n_{\text{test}}}$ generated using the same distribution. In view of the assessment, we also define the PoU $\{\phi_i\}_{i=1}^{N_{\text{dd}}} \subset \text{Lip}(\Omega;\mathbb{R})$ associated with the partition $\{\Omega_i\}_{i=1}^{N_{\text{dd}}}$ such that

$$\sum_{i=1}^{N_{\text{dd}}} \phi_i(x) = 1, \quad \begin{cases} 0 \le \phi_i(x) \le 1 & \forall\, x \in \Omega, \\ \phi_i(x) = 0 & \forall\, x \notin \Omega_i, \end{cases} \quad i = 1,\dots,N_{\text{dd}}.$$

Given $\underline{u} \in \mathcal{X} := \bigotimes_{i=1}^{N_{\text{dd}}} \mathcal{X}_i$, we define the PoU operator

$$\mathtt{P}_{\text{pu}}[\underline{u}] := \sum_{i=1}^{N_{\text{dd}}} \phi_i\, \underline{u}_i \in H^1(\Omega). \tag{5.42}$$

Note that we omit the dependence of $\{\phi_i\}_i$ and also N_{dd} on the parameter to shorten notation. Finally, we define the out-of-sample average prediction error

$$E_{\text{avg}} := \frac{1}{n_{\text{test}}} \sum_{\mu \in \Xi_{\text{test}}} \frac{\|\mathtt{P}_{\text{pu}}[\underline{u}_\mu^{\text{hf}}] - \mathtt{P}_{\text{pu}}[\widehat{\underline{u}}_\mu]\|_{H^1(\Omega)}}{\|\mathtt{P}_{\text{pu}}[\underline{u}_\mu^{\text{hf}}]\|_{H^1(\Omega)}}. \tag{5.43}$$

As mentioned in section 5.3, we here resort to the HF CB solver to generate HF data for training and test, to simplify interpretation of the numerical results. In several figures, we compare the prediction error (5.43) with the error associated with the mapped $H^1(\Omega_{\text{L}_i}^{\text{a}})$ projection of $u_\mu^{\text{hf}} \circ \Phi_i$, for $i = 1,\dots,N_{\text{dd}}$,

$$E_{\text{avg}}^{\text{sub}} := \frac{1}{n_{\text{test}}} \sum_{\mu \in \Xi_{\text{test}}} \frac{\|\mathtt{P}_{\text{pu}}[\underline{u}_\mu^{\text{hf}}] - \mathtt{P}_{\text{pu}}[\widehat{\underline{u}}_\mu^{\text{sub}}]\|_{H^1(\Omega)}}{\|\mathtt{P}_{\text{pu}}[\underline{u}_\mu^{\text{hf}}]\|_{H^1(\Omega)}}, \tag{5.44}$$

$$\left(\widehat{\underline{u}}_\mu^{\text{sub}}\right)_i = \left(\Pi_{\mathcal{Z}_{\text{L}_i}^{\text{a,b}} \cup \mathcal{W}_{\text{L}_i}^{\text{a,p}}} \underline{u}_\mu^{\text{hf}} \circ \Phi_i\right) \circ \Phi_i^{-1}, \tag{5.45}$$

for $i = 1,\dots,N_{\text{dd}}$. Note that (5.44) is not optimal — that is, it is not the relative $H^1(\Omega)$ projection error associated with the instantiated spaces — but it can be shown to be quasi-optimal exploiting [BM97, Theorem 1]. We omit the details.

We resort to a P2 FE discretization with $N_{\text{int}}^{\text{e}} = 1120$ and $N_{\text{ext}}^{\text{e}} = 3960$ elements, and $N_{\text{int}}^{\text{p}} = 272$ and $N_{\text{ext}}^{\text{p}} = 200$ port quadrature points. We emphasize that the HF component-based discretization is constructed to ensure that the local grids match exactly for $Q_{\text{a}} = Q_{\text{ref}}$; however, we remark that internal and external meshes do not lead to a global conforming discretization for any other value of Q_{a}. All simulations are performed in Matlab 2020b on a commodity laptop.

5.5.2 Reduced-order model with HF quadrature

We show the performance of the OS2 ROM without hyper-reduction. First, we show the behavior of the percentage of retained energy of the POD eigenvalues $\{\lambda_i\}$ of the

Gramian matrix associated with the snapshot set. To facilitate visualization, we show the average in-sample error $E_{\mathrm{n}} = 1 - \frac{\sum_{i=1}^{n} \lambda_i}{\sum_{j=1}^{n_{\mathrm{train}}} \lambda_j}$ for several values of n, for port and bubble components, and for the two archetype components. We observe that the POD eigenvalues decay extremely rapidly, for both components.

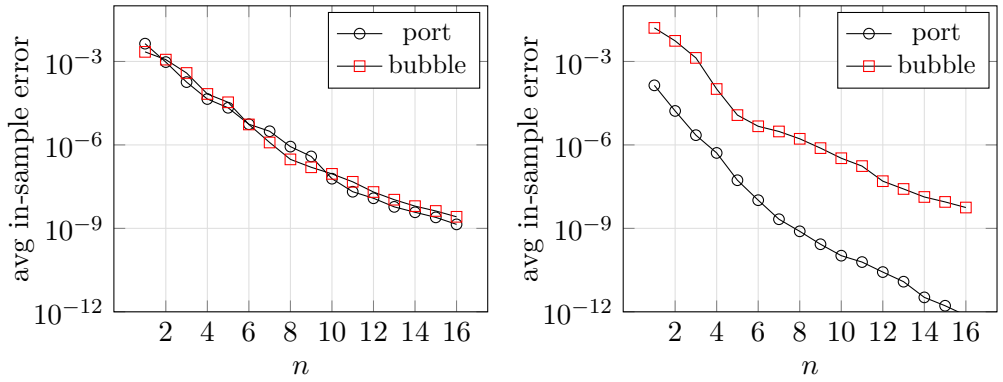

(a) $\Omega^{\mathrm{a}}_{\mathrm{int}}$ (b) $\Omega^{\mathrm{a}}_{\mathrm{ext}}$

FIGURE 5.5: behavior of the average squared in-sample error E_{n} for several values of n, for port and bubble components, and for the two archetype components.

In Figure 5.6, we compare the average error E_{avg} (5.43) associated with the OS2 ROM for several values of m, with $n = m$ and $n = 2m$, with the average error $E^{\mathrm{sub}}_{\mathrm{avg}}$ (5.44) obtained through projection. We observe that the OS2 ROM achieves near-optimal performance for all choices of the port and bubble ROBs. We also observe that doubling the number of port modes m by keeping the same number of bubble modes n does not lead to relevant differences in terms of both projection and OS2 prediction error. In the remainder of this section, we set $m = n$.

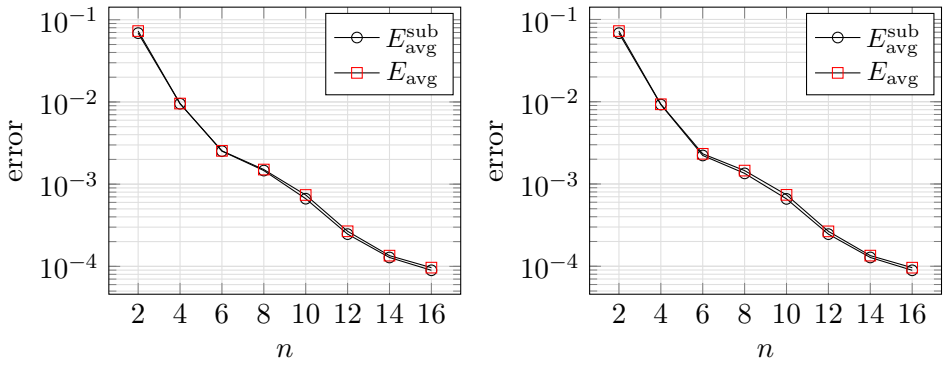

(a) $m = n$ (b) $m = 2n$

FIGURE 5.6: out-of-sample performance of OS2 ROM without hyper-reduction for several values of m, with $n = m$ and $n = 2m$; comparison with sub-optimal ("sub") average error $E^{\mathrm{sub}}_{\mathrm{avg}}$ (5.44).

Figure 5.7 shows the behavior of the solution over a vertical slice of the domain for a test configuration with $Q_{\mathrm{a}} = 7$; boundaries of the Q_{a} internal subdomains associated with repositories and the external subdomain are marked as black dots in 5.7(a); the

vertical slice, drawn as a purple dashed line, corresponds to points (x, y) such that $x = \bar{x} = 0.43$, $0 \leq y \leq 1$. Points of the slice belong to either the instantiated component Ω_3 or Ω_8 (or both). We apply the partition of unity operator (5.42) to generate globally-defined solutions. We compute therefore approximate solutions $\mathtt{P}_{\mathrm{pu}}[\hat{u}_\star^{(n=2)}]$ $\mathtt{P}_{\mathrm{pu}}[\hat{u}_\star^{(n=10)}]$ corresponding to two choices of the ROB size $n = m = 2$ and $n = m = 10$ and for subscript $\star$ corresponding to x and y components; we also compare the reduced solutions with the HF globally defined solutions $\mathtt{P}_{\mathrm{pu}}[u_\star^{\mathrm{hf}}]$. We observe that the choice $n = m = 2$ enables qualitatively accurate approximations of the vertical displacement (cf. 5.7(c)), but extremely inaccurate approximations of the horizontal displacement (cf. Figure 5.7(b), while the choice $n = m = 10$ leads to accurate predictions for both horizontal and vertical displacements.

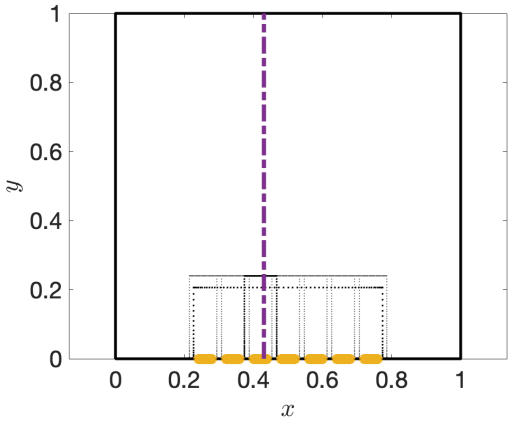

(a) geometry configuration and slice

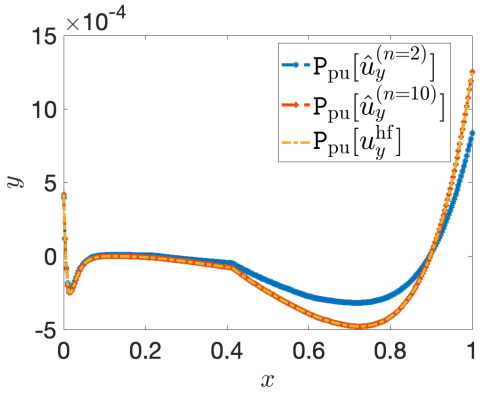

(b) horizontal displacement

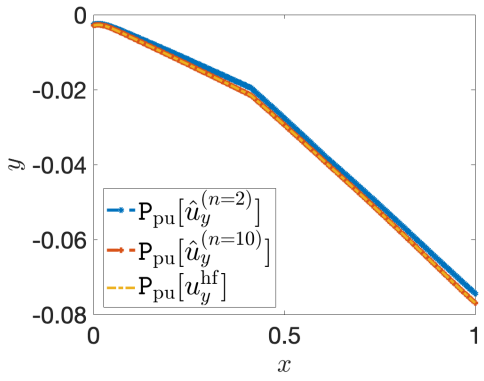

(c) vertical displacement

FIGURE 5.7: visualization of the horizontal and vertical displacement components for a vertical slice.

5.5.3 Hyper-reduction of the port-to-bubble maps

Figure 5.8 investigates the performance of the EQ rule for different tolerances tol_{eq} (cf. Appendix A): Figure 5.8(a) shows the behavior of the out-of-sample relative error E_{avg} compared to the OS2 ROM with HF quadrature (dubbed HFQ); Figures 5.8(b) and 5.8(c) show the percentage of sampled elements as a function of m, for the two archetype components and for several tolerances. We observe that for $tol_{\mathrm{eq}} \leq 10^{-10}$ the hyper-reduced OS2 ROM is as accurate as the OS2 ROM with HF quadrature for all values of m considered. We further observe that the percentage of sampled elements is between three and five times larger in the internal component — since $N^{\mathrm{e}}_{\mathrm{ext}} \approx 3.5 N^{\mathrm{e}}_{\mathrm{int}}$,

we have that the absolute number of sampled elements is nearly the same for the two components.

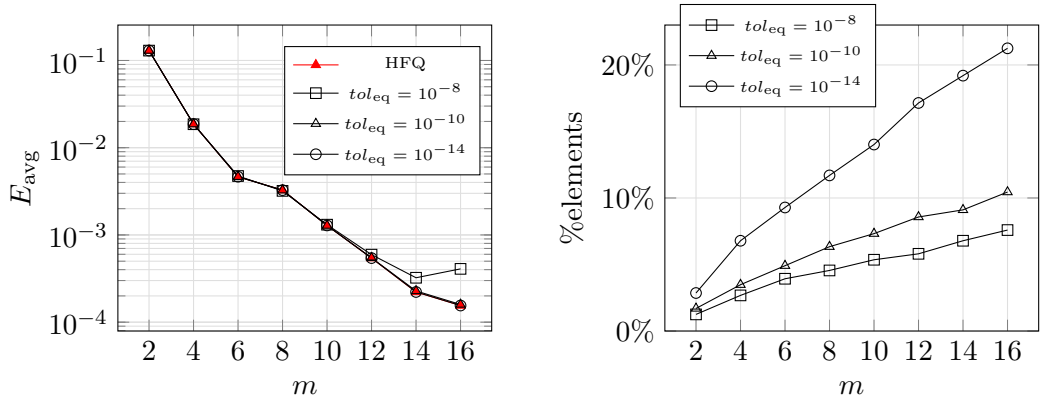

(a) E_{avg} (b) $\Omega^{\text{a}}_{\text{int}}$

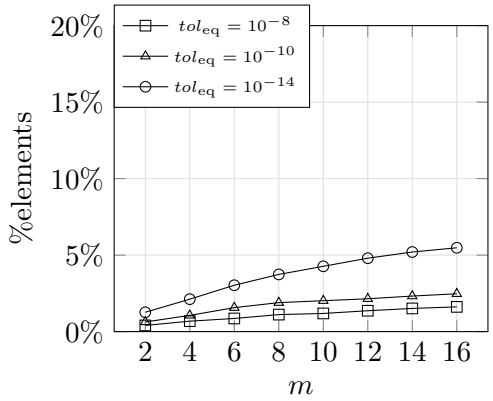

(c) $\Omega^{\text{a}}_{\text{ext}}$

FIGURE 5.8: hyper-reduction of the port-to-bubble maps for several tolerances tol_{eq} and port space sizes m, with $n = m$. (a) behavior of the average out-of-sample prediction. (b)-(c) percentage of sampled elements in $\Omega^{\text{a}}_{\text{int}}$ and $\Omega^{\text{a}}_{\text{ext}}$.

5.5.4 Hyper-reduction of the objective function

In Figure 5.9, we show the behavior of the L^∞ error

$$E^{\infty}_{\text{avg,eim}}(\ell, m) := \frac{1}{n_{\text{train},\ell}} \sum_{k=1}^{n_{\text{train},\ell}} \left\| \underline{u}^{\text{p}}_{\ell,k} - \mathcal{I}_{\ell,m}[\underline{u}^{p}_{k}] \right\|_{\infty}$$

where $\{\underline{u}^{\text{p}}_{\ell,k}\}_{k=1}^{n_{\text{train},\ell}}$ are the port fields associated with the ℓ-th component and employed to generate the port basis (cf. Algorithm 9). We observe near-exponential convergence of the L^∞ error for both components; interestingly, the interpolation error for the internal component is one order of magnitude larger than the error for the external component.

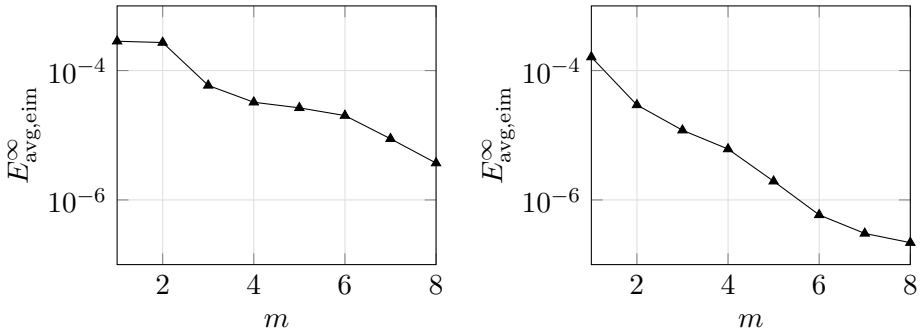

(a) $\Omega^{\text{a}}_{\text{int}}$ (b) $\Omega^{\text{a}}_{\text{ext}}$

FIGURE 5.9: application of the EIM procedure for vector-valued fields (cf. Algorithm 10). (a)-(b) behavior of the in-sample L^{∞} approximation error $E^{\infty}_{\text{avg,eim}}$ for the internal and the external component.

In Figure 5.10, we report the percentage of sampled quadrature points by the two hyper-reduction procedures. By construction, EIM selects $m_{\text{p,eq}} = m$ points; on the other hand, the number of points selected by the EQ procedure of section 5.3.3 weakly depends on the size m of the port basis.

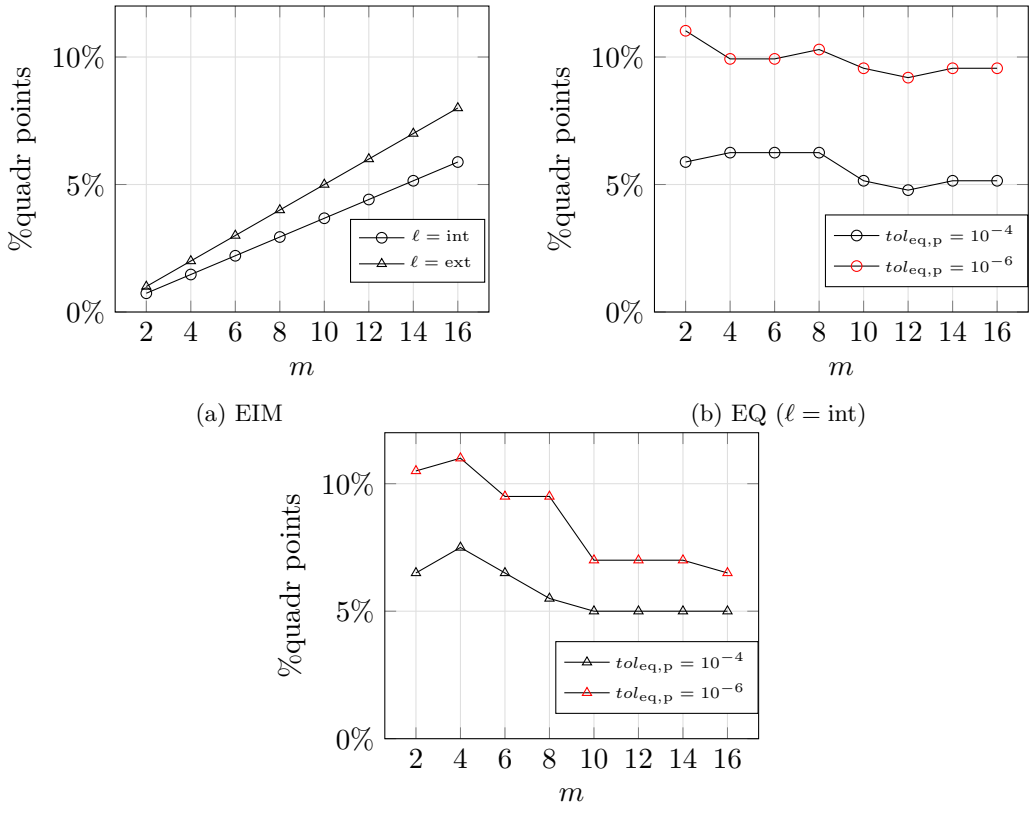

(a) EIM (b) EQ (ℓ = int)

(c) EQ (ℓ = ext)

FIGURE 5.10: hyper-reduction of the objective function for internal and external archetype components, with respect to m, with $n = m$. (a) percentage of sampled quadrature points based on EIM. (b)-(c) percentage of sampled quadrature points based on the EQ procedure, for two tolerances $tol_{\text{eq,p}}$.

In Figure 5.11, we investigate the performance of the fully hyper-reduced ROM: Figure 5.11(a) shows the behavior of the prediction error (5.43), while Figure 5.11(b)

shows the behavior of the maximum wall-clock time over the test set. We observe that the speed-up due to hyper-reduction of the objective function is of the order 1.5 for all choices of m; on the other hand, performance of the two considered hyper-reduction strategies is comparable for all tests.

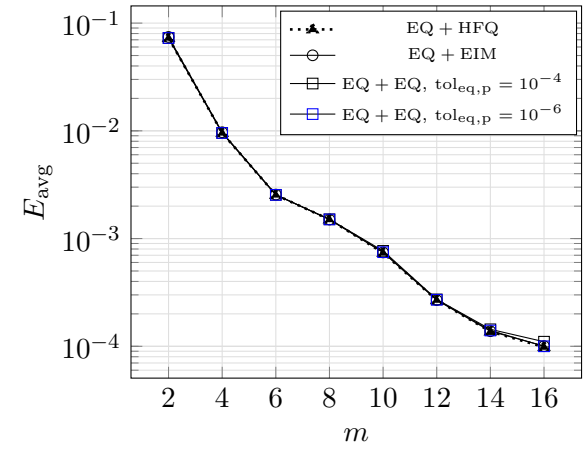

(a) out-of-sample error

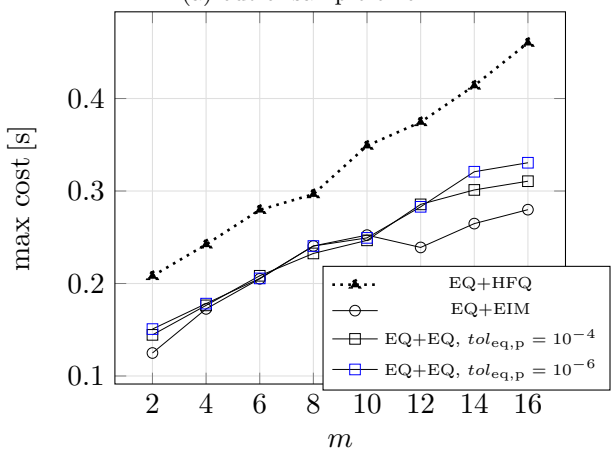

(b) computational cost

FIGURE 5.11: hyper-reduction of the objective function based on EIM and EQ. (a) out-of-sample performance of the hyper-reduced OS2 ROM for several choices of m, with $n = m$. (b) maximum computational cost over the test set. Results are based on the EQ tolerance $tol_{\text{eq}} = 10^{-10}$ for the local problems and the tolerances $tol_{\text{eq,p}} = 10^{-4}$ and $tol_{\text{eq,p}} = 10^{-6}$ for the objective function (for EQ+EQ).

In Figure 5.12 we show the speed-up factor of the hyper-reduced OS2 solvers with respect to a representative monolithic HF solver of comparable accuracy for different numbers of subdomains. The monolithic P2 FE solver runs in approximately[3] 2.7806 [s] for $N_{\text{dd}} = 2$ and in 9.9971 [s] for $N_{\text{dd}} = 8$; the CB HF solver (5.12) that is used to generate training and test data is roughly a factor three slower than the corresponding monolithic solver. We define the speed-up factor as:

$$\text{speed-up}(\text{N}_{\text{dd}}) := \frac{\text{t}_{\text{hf}}(\text{N}_{\text{dd}})}{\text{t}_{\text{OS2}}(\text{N}_{\text{dd}})}$$

[3]Computational times are based on an average over 5 tests for each number of subdomains; the computational grid has 17177 FE nodes for $N_{\text{dd}} = 2$ and it has 38637 nodes for $N_{\text{dd}} = 8$.

where t_{hf} is the estimated execution time of the monolithic HF solver averaged over 5 tests and t_{OS2} is the execution time associated with the CB ROM, averaged over the same 5 configurations, for $N_{\text{dd}} \in \{3, \dots, 8\}$. We perform hyper-reduction of the port-to-bubble maps using the tolerance $tol_{\text{eq}} = 10^{-10}$ and we consider the tolerances $tol_{\text{eq,p}} = 10^{-4}$ and $tol_{\text{eq,p}} = 10^{-6}$ for the hyper-reduction of the objective function (for the EQ+EQ case).

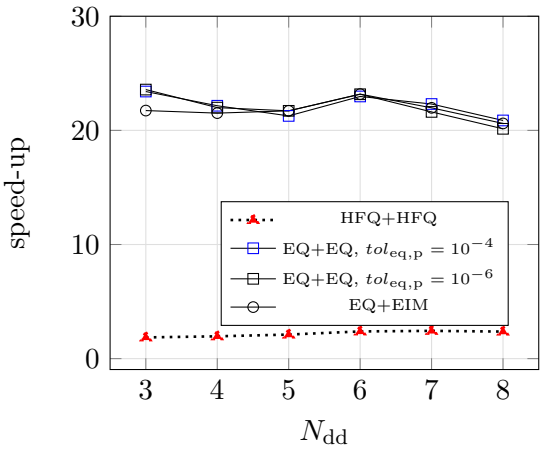

(a) $m = 8$

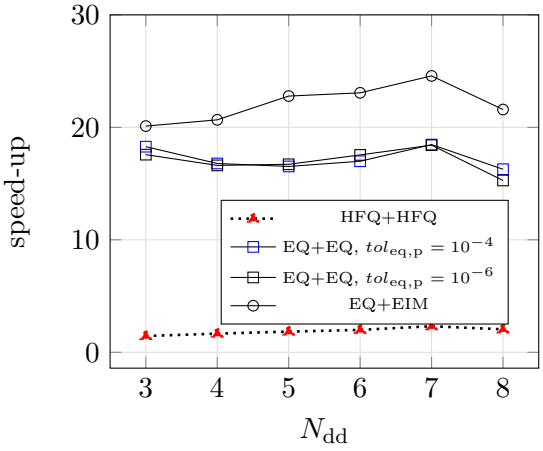

(b) $m = 16$

FIGURE 5.12: Speed-up of the OS2 ROMs with respect to the HF monolithic solver for several values of the number of subdomains. (a) performance for $m = 8$; (b) performance for $m = 16$. EQ tolerance for the port-to-bubble maps is set equal to $tol_{\text{eq}} = 10^{-10}$.

We observe that the speed-up factors depicted in Figure 5.12 depend weakly on the number of subdomains. The EIM method leads to slightly larger speed-ups than the EQ method for $m = n = 16$ (cf. Figure 5.12(b)), while performance is comparable for the case $m = n = 8$ (Figure 5.12(a)). We envision that more effective implementations of Algorithm 7 — which rely on parallelization of the port-to-bubble loop at Lines 4-7 and on pointwise EQ hyper-reduction of the port-to-bubble maps, as opposed to element-wise EQ — will lead to significantly larger speed-ups.

5.5.5 Optimization strategy: comparison between Gauss-Newton, quasi-Newton and overlapping Schwarz

We compare the performance of the Gauss-Newton method, the quasi-Newton method and the multiplicative overlapping Schwarz method with Dirichlet interface conditions presented in section 5.2.6. Numerical results are shown for various choices of the port dimension m and we set $n = m$. For Gauss-Newton and Quasi-Newton methods, we follow algorithm 7; as for OS method, we implement the iterative procedure described in Algorithm 8. We set $tol = 10^{-6}$ in Algorithm 7 (cf. Line 11) and we consider the same termination criterion for the quasi-Newton solver and the OS solver. In this test, we perform hyper-reduction at the local level (EQ tolerance 10^{-10}), but we do not hyper-reduce the objective function. Figure 5.13(a) shows the behavior of the objective

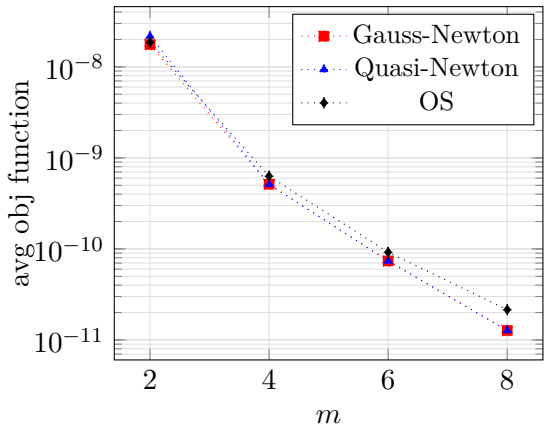

(a) average objective function

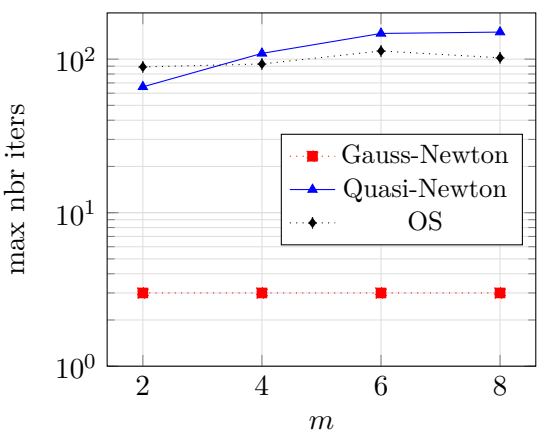

(b) maximum number of iterations

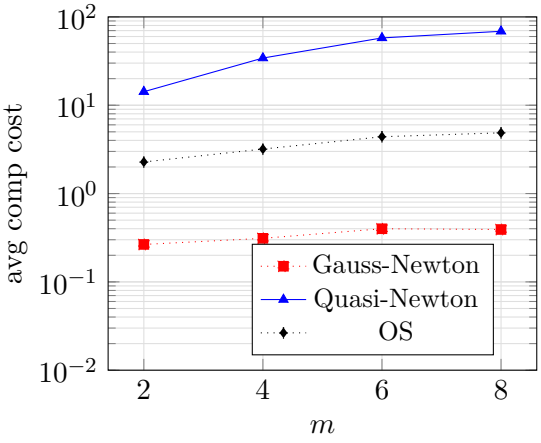

(c) average computational cost

FIGURE 5.13: comparison between OS2 with Gauss-Newton optimization and with quasi-Newton optimization, and multiplicative overlapping Schwarz methods. (a) average value of the objective function with respect to m and for $n = m$. (b) maximum number of iterations to meet the convergence criterion. (c) average wall-clock cost with respect to m and for $n = m$.

function in (5.17) with respect to the ROB sizes over the test set, while Figure 5.13(b) shows the number of iterations required to meet the termination criterion: we observe that GNM requires many fewer iterations without any deterioration in accuracy. Figure 5.13(c) shows the wall-clock average cost for the three methods: even if GNM has a slightly larger per-iteration cost, we empirically find that OS2 with GNM is significantly

more rapid than the other two approaches. Furthermore, since the OS internal loop (cf. Lines 4-7 Algorithm 8) is not parallelizable as opposed to the corresponding loop of the OS2 solver (cf. Lines 4-7 Algorithm 7), we expect significantly larger computational gains if we resort to parallel computing.

In Figure 5.14, we repeat the test of Figure 5.13 for the choice of the initial conditions $\boldsymbol{\alpha}^{(0)} = \mathbf{0}$ and $\boldsymbol{\beta}^{(0)} = \mathbf{0}$ in Algorithm 7 and Algorithm 8. We observe that OS and OS2 with GNM show similar performance with respect to all metrics. OS2 with QN exhibits a high value of the average objective function for the choice $m = n = 6$, as shown in figure 5.14(a); convergence is ensured by the satisfaction of criterion at line 11 in algorithm 7; we expect more generally, a deterioration in performance and a possibly compromised convergence.

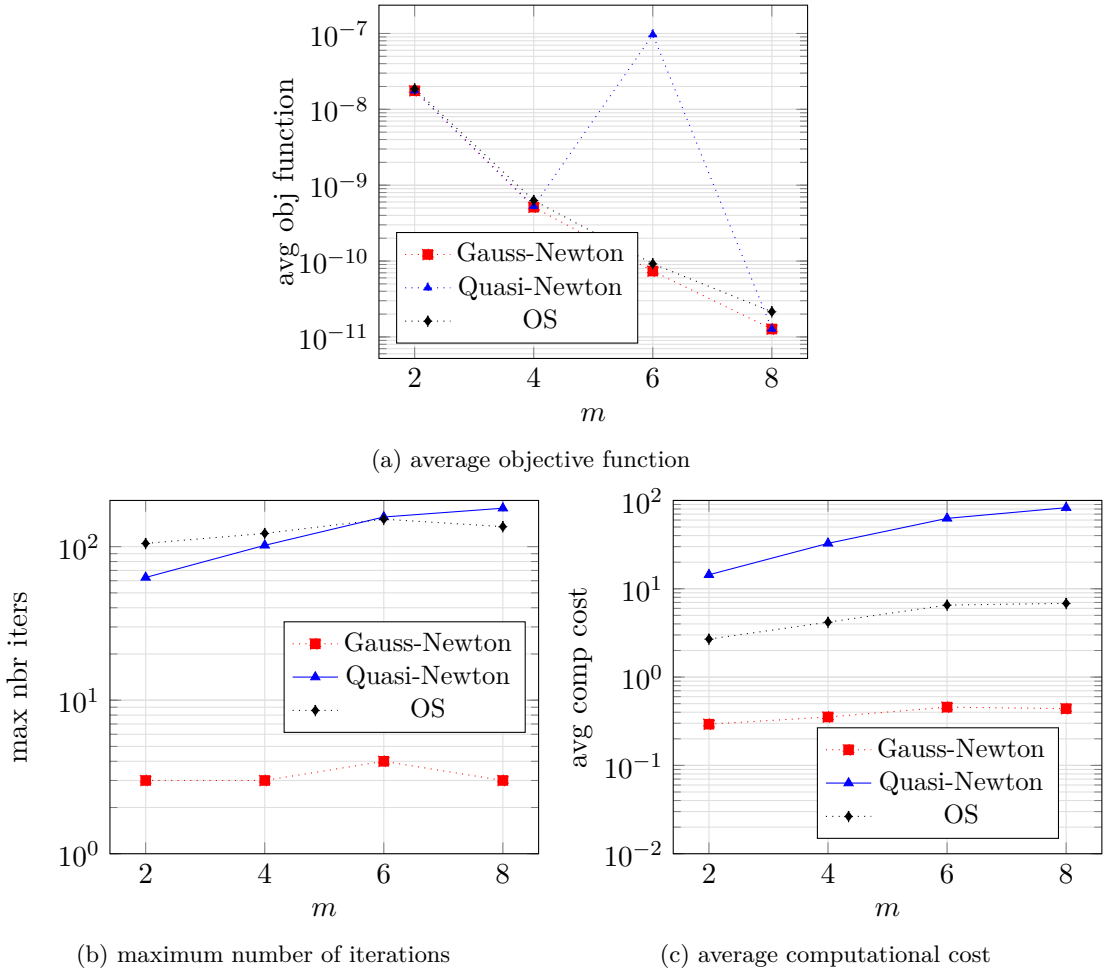

(a) average objective function

(b) maximum number of iterations

(c) average computational cost

FIGURE 5.14: comparison between Gauss-Newton, quasi-Newton methods, and multiplicative overlapping Schwarz methods with zero initial condition. (a) average value of the objective function with respect to m and for $n = m$. (b) maximum number of iterations to meet the convergence criterion. (c) average wall-clock cost with respect to m and for $n = m$.

5.5.6 Optimization strategy: convergence with respect to the overlap size

We study the performance of the multiplicative OS method and the OS2 based on Gauss-Newton with respect to the overlap size δ, as depicted in figure 5.15 for a representative case in which $Q_{\mathrm{a}} = 3$.

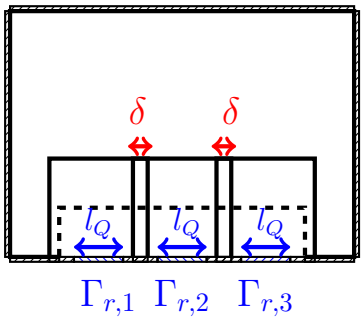

FIGURE 5.15: Example of geometric overlapping instantiated configuration for $Q_{\mathrm{a}} = 3$.

The training and test sets, as well as the parameters distributions, the out-of-sample errors and the chosen finite element spaces are defined in section 5.5.1. We perform hyper-reduction of the port-to-bubble maps based on an empirical quadrature tolerance of $tol_{\mathrm{eq}} = 10^{-10}$ and we do not perform hyper-reduction on the objective function.
In figure 5.16 the tests of figure 5.13 are repeated for different values of the overlap size $\delta = \frac{2}{3}l_{\mathrm{Q}}$, $\delta = \frac{1}{2}l_{\mathrm{Q}}$ and $\delta = \frac{1}{6}l_{\mathrm{Q}}$, where l_{Q} is depicted in figure 1.6 and denotes the repository width. The starting guess solutions for the Gauss-Newton methods are choosen according to (5.22). As in the previous results, we choose equal reduced basis sizes for the port and bubble components ($n = m$).
We can observe in figure 5.16(a) that OS2 (equipped with the GNM) and OS show comparable average values of the objective function for increasing dimensions of the reduced port and bubble spaces ($m = n$). Although, OS2 exhibits a significantly smaller number of iterations to achieve convergence with respect to OS (the order of gain in the number of iteration is about 6 for $\delta = \frac{1}{6}$). Furthermore, in the case of OS, both the maximum number of iterations in figure 5.16(b) and the average computational costs in figure 5.16(c) show a high dependence on the size of the overlap, unlike the case of OS2.

5.6 Conclusions

In this chapter we developed and numerically validated the one-shot overlapping Schwarz (OS2) approach to component-based MOR of steady nonlinear PDEs. The key features of the approach are (i) a constrained optimization statement that penalizes the jump at the components' interfaces subject to the approximate satisfaction of the PDE in each deployed (instantiated) component; (ii) the decomposition of the local solutions into a port component and bubble components, to enable effective parallelization of the online solver. Hyper-reduction of the local sub-problems and of the objective function is performed to reduce online assembly costs. We illustrate the many elements of the formulation through the application to a two-dimensional nonlinear mechanics (Neo-Hookean) PDE model; for this problem, we are able to devise a CB-ROM that reduces online costs by a factor 20 compared to a standard monolithic FE model with less than 0.1% prediction error, and without resorting to any parallelization of the online ROM

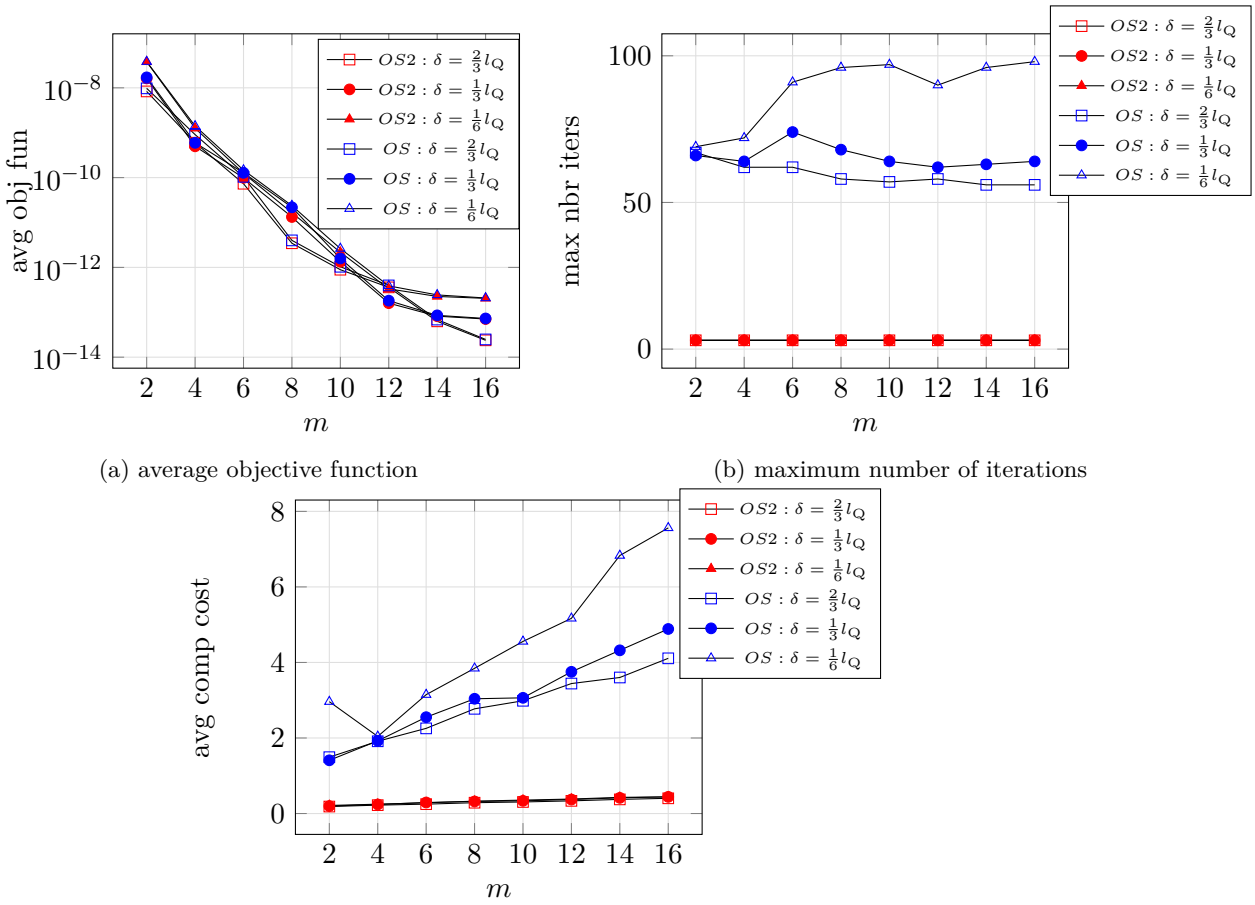

(a) average objective function

(b) maximum number of iterations

(c) average computational cost

FIGURE 5.16: Out-of-sample test: (a) average values of the objective function, (b) maximum numbers of iterations, (c) average computational cost of OS2 and OS for $\delta = \frac{2}{3}l_Q$, $\delta = \frac{1}{3}l_Q$ and $\delta = \frac{1}{6}l_Q$.

solver. We also observe that for the particular model problem considered in this paper the OS2 formulation provides acceptable results also for under-resolved ROBs.

Chapter 6

Component-based model reduction for the THM system

In this chapter we extend the CB-pMOR methodology for nonlinear PDEs that is explained in the previous chapter 5. Indeed, in chapter 5 we present a new CB formulation and we develop CB-pMOR methods that tackle steady nonlinear (or linear) parametrized problems; in this chapter both formulation and methods are adapted to face time-dependent nonlinear coupled problems, in particular the THM system of interest (cf. 3). Due to the challenging nature of the parametrized problem to solve (cf. (3.12)-(3.13)), some complexity arises in the formulation, in the methodology and in the numerical implementation. In section 6.1 the formulation that is introduced for a simpler case in section 5.2 is extended to take into account unsteady PDEs with internal variables; section 6.2 clarifies how we revise and modify the CB-pMOR methods from section 5.3 to target problems in form (3.12)-(3.13); finally, section 6.3 is dedicated to numerical investigations.

6.1 Formulation

The notation introduced in section 5.2.1 is entirely adopted in this chapter. The CB formulation, which is presented is section 5.2.2 for a general steady parametrized PDE, needs to be generalized to take into account time dependence and the presence of internal variables.
We denote as $\mathcal{W}$ a suitable Hilbert space for internal variables $\underline{W}$; we denote (as in chapters 3 and 4) the time grid associated with time interval $[0, T_\mathrm{f}]$ as $0 = t^{(0)} < \ldots < t^{(J_\mathrm{max})} = T_\mathrm{f}$. Given parameter $\mu_\ell \in \mathcal{P}$, for $\ell \in \mathcal{L}$, we define the time-dependent variational form $\mathcal{G}_\ell^{\mathrm{a},(\mathrm{j})} : \mathcal{X}_\ell^\mathrm{a} \times \mathcal{X}_{\ell,0}^\mathrm{a} \times \mathcal{P}_\ell \to \mathbb{R}$ associated with the ℓ^th archetype component:

$$\begin{aligned}\mathcal{G}_\ell^{\mathrm{a},(j)}(\underline{U}^{(j)}, \underline{V}; \mu_\ell) =& \mathcal{G}_\ell^\mathrm{a}(\underline{U}^{(j)}, \underline{U}^{(j-1)}, \underline{W}^{(j)}, \underline{W}^{(j-1)}, \underline{V}; \mu_\ell) \\ =& \sum_{k=1}^{N_\ell^\mathrm{e}} \int_{\mathtt{D}_{\ell,k}} \eta_\ell^{\mathrm{a,e}}(\underline{U}^{(j)}, \underline{U}^{(j-1)}, \underline{W}^{(j)}, \underline{W}^{(j-1)}, \underline{V}; \mu_\ell)\, dx + \\ & \int_{\partial\mathtt{D}_{\ell,k}} \eta_\ell^{\mathrm{a,f}}(\underline{U}^{(j)}, \underline{U}^{(j-1)}, \underline{W}^{(j)}, \underline{W}^{(j-1)}, \underline{V}; \mu_\ell)\, dx\end{aligned} \tag{6.1}$$

Notice the time-dependence both of the state (and internal) variables and of the variational form (6.1) itself.

The variational form (6.1) corresponds to an implicit time discretization of form $\mathcal{G}_\mu$ in (1.1) in the ℓ^th archetype component and it represents a generalized formulation for the THM system of interest (3.12). For a matter of simplicity in the notation, we omit the subscript μ on state solutions and internal variables and we omit the dependence

of the variational forms on the parameters. As in (5.11), we can rewrite the local variational forms in the two archetype components

$$\begin{cases} \mathcal{G}_{\text{int}}^{\text{a},(j)}(\underline{U}^{(j)},\underline{V}) = \displaystyle\int_{\Omega_{\text{int}}^{\text{a}}} \eta_{\text{int}}^{\text{a,e},(j)}(\underline{U}^{(j)},\underline{V})\,dx + \int_{\Gamma_{\text{r}}^{\text{a}}} \eta_{\text{int}}^{\text{a,f},(j)}(\underline{U}^{(j)},\underline{V})\,dx, \\ \mathcal{G}_{\text{ext}}^{\text{a},(j)}(\underline{U}^{(j)},\underline{V}) = \displaystyle\int_{\Omega_{\text{ext}}^{\text{a}}} \eta_{\text{ext}}^{\text{a,e},(j)}(\underline{U}^{(j)},\underline{V})\,dx + \int_{\Gamma_{\text{top}}^{\text{a}}} \eta_{\text{ext}}^{\text{a,f},(j)}(\underline{U}^{(j)},\underline{V})\,dx. \end{cases}$$

Explicit expressions of $\eta_{\text{int}}^{\text{a,e},(j)}$, $\eta_{\text{int}}^{\text{a,f},(j)}$, $\eta_{\text{ext}}^{\text{a,e},(j)}$, $\eta_{\text{ext}}^{\text{a,e},(j)}$ can be determined by writing system (3.12) in the local archetype components; we omit the details.

We can denote as $\underline{\mathbb{U}}_i$ the trajectory associated with solution $\{\underline{U}_i^{(j)}\}_{j=1}^{J_{\max}}$ for each instantiated component $i = 1,\dots,N_{\text{dd}}$ (and given parameter $\mu \in \mathcal{P}$, which is omitted from the notation).

The OS2 formulation (5.12) is generalized as follows. Given the set of parameters $\mu = (\mu_1,\dots,\mu_{N_{\text{dd}}}) \in \mathcal{P} = \bigotimes_{i=1}^{N_{\text{dd}}} \mathcal{P}_{\mathtt{L}_i}$, with labels $\{\mathtt{L}_i\}_i \subset \mathcal{L}$, find $\overrightarrow{\mathbb{U}} = \{\underline{\mathbb{U}}_1,\dots,\underline{\mathbb{U}}_{N_{\text{dd}}}\} \subset \mathcal{X} = \bigotimes_{i=1}^{N_{\text{dd}}} \mathcal{X}_i$ that solves, for each $j = 1,\dots,J_{\max}$,

$$\begin{aligned} &\min_{\overrightarrow{\mathbb{U}}\subset\mathcal{X}} \frac{1}{2}\sum_{i=1}^{N_{\text{dd}}} \sum_{f\in\text{Neigh}_{\text{i}}} \left\|\underline{U}_i^{(j)} - \underline{U}_f^{(j)}\right\|^2_{L^2(\Gamma_{if})} \\ &\qquad \text{s.t.} \\ &\mathcal{G}_i^{(j)}\left(\underline{U}_i^{(j)},\underline{V}\right) = 0 \ \ \forall \underline{V} \in \mathcal{X}_{i,0} \text{ for } i = 1,\dots,N_{\text{dd}}. \end{aligned} \tag{6.2}$$

We proceed as in section 5.2.4 to derive the hybridized form of problem (6.2). Port-to-bubble maps for problems of type (6.1) are defined for each instantiated component $i = 1,\dots,N_{\text{dd}}$ as $\mathtt{F}_i^{(j)} : \mathcal{U}_i \to \mathcal{X}_{i,0}$ such that, given port state variables $\underline{U}_{\text{p},i}^{(j)} \in \mathcal{U}_i$ and internal variables $\underline{W}_i^{(j)} \in \mathcal{W}_i$, each local variational forms assumes the following expression

$$\mathcal{G}_i^{(j)}\left(\mathtt{F}_i^{(j)}\left(\underline{U}_{\text{p},i}^{(j)}\right) + \mathtt{E}_i\left(\underline{U}_{\text{p},i}^{(j)}\right),\underline{V}\right) = 0 \ \forall \underline{V} \in \mathcal{X}_{i,0}. \tag{6.3}$$

for $j = 1,\dots,J_{\max}$. A local solution can indeed be written as

$$\underline{U}_i^{(j)} = \mathtt{F}_i^{(j)}\left(\underline{U}_{\text{p},i}^{(j)}\right) + \mathtt{E}_i\left(\underline{U}_{\text{p,i}}^{(j)}\right). \tag{6.4}$$

for $i = 1,\dots,N_{\text{dd}}$. Equation (6.3) corresponds to a time discretization of a localized PDE problem with $\underline{U}_{\text{p,i}}^{(j)}$ as a datum on the port boundary Γ_i at time $t^{(j)}$. For the solution of the nonlinear problems (6.3) that arise at each time step, we use the Newton's method with line-search.

The unconstrained formulation related to the CB full-order model (6.2) is the following: find $\overrightarrow{\mathbb{U}}_{\text{p}} = \left(\underline{\mathbb{U}}_{\text{p},1}\dots,\underline{\mathbb{U}}_{\text{p},N_{\text{dd}}}\right)$ s.t. it solves, for each $j = 1,\dots,J_{\max}$,

$$\min_{\overrightarrow{\mathbb{U}}_{\text{p}}\subset\mathcal{U}} \frac{1}{2}\sum_{i=1}^{N_{\text{dd}}} \sum_{f\in\text{Neigh}_i} \left\|\underline{U}_{\text{p},i}^{(j)} - \mathtt{E}_f\left(\underline{U}_{\text{p},f}^{(j)}\right) - \mathtt{F}_f^{(j)}\left(\underline{U}_{\text{p},f}^{(j)}\right)\right\|^2_{L^2(\Gamma_{i,f})} \tag{6.5}$$

To address the construction of ROM, we follow section 5.2.4 and for each archetype component $\ell \in \mathcal{L}$ we denote as $\mathcal{Z}_\ell^{\text{a,b}} \subset \mathcal{X}_{\ell,0}$, $\mathcal{Z}_\ell^{\text{a,rp}} \subset \mathcal{U}_\ell$, $\mathcal{Z}_\ell^{\text{a,p}} = \{\mathtt{E}_\ell\underline{\zeta} : \underline{\zeta} \in \mathcal{Z}_\ell^{\text{a,rp}}\}$ the bubble, port and extended port reduced spaces, respectively. Given the deployed system, we derive the instantiated bubble and port spaces $\mathcal{Z}_i^{\text{b}} = \{\underline{\zeta}\circ\Phi_i^{-1} : \underline{\zeta} \in \mathcal{Z}_{\mathtt{L}_i}^{\text{a,b}}\}$ and $\mathcal{Z}_i^{\text{p}} = \{\underline{\zeta}\circ\Phi_i^{-1} : \underline{\zeta} \in \mathcal{Z}_{\mathtt{L}_i}^{\text{a,p}}\}$ with ROBs $\underline{Z}_i^{\text{b}} = [\underline{\zeta}_{i,1}^{\text{b}},\dots,\underline{\zeta}_{i,n}^{\text{b}}] : \mathbb{R}^n \to \mathcal{Z}_i^{\text{b}}$ and

$\underline{Z}_i^{\mathrm{p}} = [\underline{\psi}_{i,1}^{\mathrm{p}}, \dots, \underline{\psi}_{i,m}^{\mathrm{p}}] : \mathbb{R}^m \to \mathcal{Z}_i^{\mathrm{p}}$. For each $i = 1, \dots, N_{\mathrm{dd}}$, the we can write the ansatz:

$$\hat{\underline{U}}_i^{(j)}(\hat{\alpha}_i, \hat{\beta}_i) = \underline{Z}_i^{\mathrm{b}} \hat{\alpha}_i, + \underline{Z}_i^{\mathrm{p}} \hat{\beta}_i \tag{6.6}$$

where we denote reduced bubble and port coefficients as $\hat{\alpha}_i : \mathscr{P} \times (0, T_{\mathrm{f}}] \to \mathbb{R}^n$, $\hat{\beta}_i : \mathscr{P} \times (0, T_{\mathrm{f}}] \to \mathbb{R}^m$. We recall that also in the reduced solutions parameter dependence is omitted in the notation. We can write $\hat{\underline{U}}_{i,\mathrm{b}}^{(j)} = \underline{Z}_i^{\mathrm{b}} \hat{\alpha}_i^{(j)}$ as an approximation of the bubble field $\underline{U}^{(j)}|_{\Omega_i} - \mathtt{E}_i(\underline{U}^{(j)}|_{\Gamma_i})$ and $\hat{\underline{U}}_{i,p}^{(j)} = \underline{Z}_i^{\mathrm{p}} \hat{\beta}_i^{(j)}$ as an approximation of the extended port field $\mathtt{E}_i(\underline{U}^{(j)}|_{\Gamma_i})$. We refer to $\left\{\hat{\underline{U}}_{i,\mathrm{b}}^{(j)}\right\}_{j=1}^{J_{\max}}, \left\{\hat{\underline{U}}_{i,\mathrm{p}}^{(j)}\right\}_{j=1}^{J_{\max}}$ as the bubble and port estimates of the solution field in the i-th component and we denote as $\hat{\underline{\mathbb{U}}}_{\mathrm{b,i}}$, $\hat{\underline{\mathbb{U}}}_{\mathrm{p,i}}$ their trajectories. The algebraic form of the residual $\hat{R}_i^{\mathrm{hf,(j)}} : \mathbb{R}^n \times \mathbb{R}^m \to \mathbb{R}^n$ is such that

$$\left(\hat{\mathbf{R}}_i^{\mathrm{hf},(j)}(\boldsymbol{\alpha}_i, \boldsymbol{\beta}_i)\right)_{\bar{n}} = \mathcal{G}_i^{(j)}\left(\hat{\underline{U}}_i^{(j)}(\boldsymbol{\alpha}_i, \boldsymbol{\beta}_i), \underline{\zeta}_{i,\bar{n}}^{\mathrm{b}}\right), \tag{6.7}$$

for $\bar{n} = 1, \dots, n$.
The approximate port-to-bubble $\hat{\mathtt{F}}_i^{\mathrm{hf,(j)}} : \mathbb{R}^m \to \mathbb{R}^n$ is such that

$$\hat{\mathbf{R}}_i^{\mathrm{hf,(j)}}\left(\hat{\mathtt{F}}_i^{\mathrm{hf,(j)}}(\boldsymbol{\beta}_i^{(j)}), \boldsymbol{\beta}_i^{(j)}\right) = \mathbf{0} \tag{6.8}$$

where

$$\nabla \mathtt{F}_i^{\mathrm{hf,(j)}}(\boldsymbol{\beta}_i) = -\left(\partial_{\boldsymbol{\alpha}_i} \widehat{\mathbf{R}}_i^{\mathrm{hf,(j)}}\right)^{-1} \partial_{\boldsymbol{\beta}_i} \widehat{\mathbf{R}}_i^{\mathrm{hf,(j)}}\Big|_{(\boldsymbol{\alpha}_i, \boldsymbol{\beta}_i) = \left(\widehat{\mathtt{F}}_i^{\mathrm{hf,(j)}}(\boldsymbol{\beta}_i), \boldsymbol{\beta}_i\right)}.$$

The low-dimensional OS2 problem is stated as follows: find $\hat{\boldsymbol{\beta}}^{\mathrm{hf}} = [\widehat{\boldsymbol{\beta}}_1^{\mathrm{hf}}, \dots, \widehat{\boldsymbol{\beta}}_{N_{\mathrm{dd}}}^{\mathrm{hf}}] \in \mathbb{R}^{M := m N_{\mathrm{dd}}}$ such that

$$\hat{\boldsymbol{\beta}}^{\mathrm{hf}} = \arg\min_{\boldsymbol{\beta} \in \mathbb{R}^M} \frac{1}{2} \sum_{i=1}^{N_{\mathrm{dd}}} \sum_{f \in \mathrm{Neigh}_i} \left\| \underline{Z}_i^{\mathrm{p}} \boldsymbol{\beta}_i^{(j)} - \underline{Z}_f^{\mathrm{p}} \boldsymbol{\beta}_f^{(j)} - \underline{Z}_f^{\mathrm{b}} \hat{\mathtt{F}}_f^{\mathrm{hf},(j)}\left(\boldsymbol{\beta}_f^{(j)}\right) \right\|_{L^2(\Gamma_{i,f})}^2. \tag{6.9}$$

In section 6.2.4 we discuss the extension of the hyper-reduction techniques (cf. section 5.3.2) to problem (6.9). The port-to-bubble maps are $\hat{\mathtt{F}}_i^{\mathrm{eq},(j)} : \mathbb{R}^m \to \mathbb{R}^n$ such that the high-fidelity quadrature residuals (6.8) are replaced by the following approximation:

$$\hat{\mathbf{R}}_i^{\mathrm{eq},(j)}\left(\hat{\mathtt{F}}_i^{\mathrm{eq,(j)}}\left(\boldsymbol{\beta}_i^{(j)}\right), \boldsymbol{\beta}_i^{(j)}\right) = \mathbf{0}. \tag{6.10}$$

In order to introduce the hyper-reduced version of problem (6.9), the objective function in (6.9) is written as follows:

$$\frac{1}{2} \sum_{i=1}^{N_{\mathrm{dd}}} \sum_{f \in \mathrm{Neigh}_i} \int_{\Gamma_{i,f}} \|\widehat{\underline{U}}_i^{(j)}(\boldsymbol{\alpha}_i, \boldsymbol{\beta}_i) - \widehat{\underline{U}}_f^{(j)}(\boldsymbol{\alpha}_f, \boldsymbol{\beta}_f)\|_2^2 \, dx \approx \frac{1}{2} \sum_{i=1}^{N_{\mathrm{dd}}} \boldsymbol{\rho}_{\mathrm{L}_i}^{\mathrm{p}} \cdot \boldsymbol{\eta}_i^{\mathrm{p}} \tag{6.11}$$

where (5.16b),(5.16c), (5.17b) hold. The discrete formulation (5.17a) is modified as follows:

$$\widehat{\boldsymbol{\beta}} \in \arg\min_{\boldsymbol{\beta} \in \mathbb{R}^M} \mathfrak{f}^{\mathrm{eq,(j)}}(\boldsymbol{\beta}^{(j)}) = \mathfrak{F}\left(\widehat{\mathtt{F}}^{\mathrm{eq,(j)}}\left(\boldsymbol{\beta}^{(j)}\right), \boldsymbol{\beta}^{(j)}, \{\boldsymbol{\rho}_\ell^{\mathrm{p,eq}}\}_{\ell \in \mathcal{L}}\right) \tag{6.12a}$$

where (5.17b) holds.

6.2 Methodology

6.2.1 Data compression

As discussed in chapter 5, we aim at using a localized strategy to compute the high-fidelity snapshots for the construction of local RBs. Its development is ongoing research; we show here a data compression approach that relies on the OS2 method. High-fidelity solutions to the CB full order model (6.5) need to be evaluated and stored for different training parameters $\mu \in \mathscr{P}$ and for all sampling times. Furthermore, they need to be computed for all the subdomains associated with a given partition $\{\Omega_i\}_{i=1}^{N_{\mathrm{dd}}}$. Here we present a data compression phase that is based on local solves and that is specific for time dependent problems with internal variables. We illustrate in algorithm 11 the construction of (archetype-based) bubble and port ROBs, as well as the computation of projected coefficients.

Algorithm 11 ROBs construction

Inputs: training parameters $\{\mu^{(k)}\}_{k=1}^{n_{\mathrm{train}}}$, m, n ROB dimensions.
Outputs: ROBs $\{(\underline{Z}_\ell^{\mathrm{a,b}}, \underline{Z}_\ell^{\mathrm{a,p}})\}_{\ell\in\mathcal{L}}$; local optimal coefficients $\{\boldsymbol{\alpha}_\ell^{(k)}\}_{i=1}^{n_{\mathrm{train}}}$, $\{\boldsymbol{\beta}_\ell^{(k)}\}_{i=1}^{n_{\mathrm{train}}}$.

1: Initialize $\bar{\mathscr{D}}_{\ell,1}^{\mathrm{b}} = \emptyset$, $\bar{\mathscr{D}}_{\ell,1}^{\mathrm{p}} = \emptyset$.
2: **for** $k = 1, \dots n_{\mathrm{train}}$ **do**
Snapshots computation:
3: Compute $\{\underline{U}_1^{(j)}\}_j, \dots, \{\underline{U}_{N_{\mathrm{dd}}}^{(j)}\}_j$ for $j \in \mathtt{I_s}$ by the OS2 method.
Bubble/port split:
4: Compute bubble databases $\mathscr{D}_{\ell,k}^{\mathrm{b}} = \{\underline{U}_{\mathrm{b},1}^{(j)} \dots, \underline{U}_{\mathrm{b},N_{\mathrm{dd}}}^{(j)}\}$ where $\underline{U}_{\mathrm{b},i}^{(j)} = \underline{U}_i^{(j)} - \mathtt{E}_\ell^{\mathrm{a}}(\underline{U}_i^{(j)}|_{\Gamma_\ell^{\mathrm{a}}})$, for $j \in \mathtt{I_s}$, $\ell = \mathtt{L}_i$, $i = 1, \dots, N_{\mathrm{dd}}$.
5: Compute port databases $\mathscr{D}_{\ell,k}^{\mathrm{p}} = \{\underline{U}_{\mathrm{p},1}^{(j)} \dots, \underline{U}_{\mathrm{p},N_{\mathrm{dd}}}^{(j)}\}$ where $\underline{U}_{\mathrm{p},i}^{(j)} = \mathtt{E}_\ell^{\mathrm{a}}(\underline{U}_i^{(j)}|_{\Gamma_\ell^{\mathrm{a}}})$ for $j \in \mathtt{I_s}$, $\ell = \mathtt{L}_i$, $i = 1, \dots, N_{\mathrm{dd}}$.
HAPOD update
6: $[\underline{Z}_\ell^{\mathrm{a,b}}, \lambda_\ell^{\mathrm{b}}] = \mathtt{POD}\Big(\mathscr{D}_{\ell,k}^{\mathrm{b}} \cup \bar{\mathscr{D}}_{\ell,k}^{\mathrm{b}}, (\cdot,\cdot), n\Big)$.
7: $[\underline{W}_\ell^{\mathrm{a,p}}, \lambda_{\ell,k}^{\mathrm{p}}] = \mathtt{POD}\Big(\mathscr{D}_{\ell,k}^{\mathrm{p}} \cup \bar{\mathscr{D}}_{\ell,k}^{\mathrm{p}}, (\cdot,\cdot), m\Big)$.
8: Update $\bar{\mathscr{D}}_{\ell,k+1}^{\mathrm{b}} = \Big\{\sqrt{\lambda_{\ell,\bar{n}}^{\mathrm{b}}}\underline{\zeta}_{\ell,\bar{n}}^{\mathrm{a,b}}\Big\}_{\bar{n}=1}^{n_k}$.
9: Update $\bar{\mathscr{D}}_{\ell,k+1}^{\mathrm{p}} = \Big\{\sqrt{\lambda_{\ell,\bar{m}}^{\mathrm{p}}}\underline{\psi}_{\ell,\bar{m}}^{\mathrm{a,p}}\Big\}_{\bar{m}=1}^{m_k}$.
10: **end for**

We specify that at the first iteration ($k = 1$) the POD criterion for the construction of ROBs at lines 6 and 7 is actually given by $\min\{|\mathscr{D}_{\ell,1}^{\mathrm{b}}|, n\}$, $\min\{|\mathscr{D}_{\ell,1}^{\mathrm{p}}|, m\}$, respectively, for bubble and port databases, where the cardinality of each database at each iteration k is $|\mathscr{D}_{\ell,k}^{\mathrm{b}}| = |\mathscr{D}_{\ell,k}^{\mathrm{p}}| = |\mathtt{I_s}|(N_{\mathrm{dd}} - 1)$ if $\ell = 1$ and $|\mathscr{D}_{\ell,k}^{\mathrm{b}}| = |\mathscr{D}_{\ell,k}^{\mathrm{p}}| = |\mathtt{I_s}|$ if $\ell = 2$. At each iteration $k > 1$ the bubble and port databases are enriched with n_k bubble (or m_k port) solutions that retain information from previous iterations, where n_k is s.t. $\underline{Z}_\ell^{\mathrm{a,b}} = [\underline{\zeta}_{\ell,1}^{\mathrm{a,b}}, \dots, \underline{\zeta}_{\ell,n_k}^{\mathrm{a,b}}]$ is the bubble ROB computed at iteration k, and m_k is s.t. $\underline{Z}_\ell^{\mathrm{a,p}} = [\underline{\psi}_{\ell,1}^{\mathrm{a,p}}, \dots, \underline{\psi}_{\ell,m_k}^{\mathrm{a,p}}]$ is the port ROB computed at iteration k.

Notice that we save as output also the projected coefficients, for each archetype component $\ell \in \mathcal{L}$:

$$\left(\boldsymbol{\alpha}_{\ell,\bar{j}}^{(j)}\right)_{\bar{n}} = \left(\underline{U}_{\mathrm{b,j}}^{(j)}, \underline{\zeta}_{\ell,\bar{n}}^{\mathrm{a,b}}\right)_{\ell} \text{ for } \bar{n} = 1, \dots, n,$$
$$\left(\boldsymbol{\beta}_{\ell,\bar{j}}^{(j)}\right)_{\bar{m}} = \left(\underline{U}_{\mathrm{p,j}}^{(j)}, \underline{\psi}_{\ell,\bar{m}}^{\mathrm{a,p}}\right)_{\ell} \text{ for } \bar{m} = 1, \dots, m,$$

where projections are made over all the training databases for $\bar{j} = 1, \dots, n_{\mathrm{train},\ell}$.

6.2.2 Solution to OS2 minimization problem

The Gauss-Newton algorithm that is introduced in algorithm 7 is extended in the following way. As initial conditions, we need the evaluation of state and internal variables at time 0 in the local instantiated domains. Indeed, in our implementation, the computation of high-fidelity residual $\hat{R}_i^{\mathrm{hf},(j)}(\underline{U}_i^{(j)})$ requires the knowledge of state variables at previous time $\underline{U}^{(j-1)}$ as well as internal variables at previous time $\underline{W}^{(j-1)}$. In section 6.2.3 we provide details about the computation of suitable initial conditions; for now, let us consider $\underline{U}_i^0$ and $\underline{W}_i^0$ as given, for all $i = 1, \dots, N_{\mathrm{dd}}$.

We observe that the internal for-loop block from line 4 to line 14 corresponds to the same block as in algorithm 7; here, we extend the iterative procedure in algorithm 7 due to the need of i) updating internal variables (cf. line 16), ii) updating the initial conditions (cf. line 19).

Algorithm 12 Solution to (6.9) through the Gauss-Newton method.

Inputs: $\boldsymbol{\alpha}^{(0)} = [\boldsymbol{\alpha}_1^{(0)}, \dots, \boldsymbol{\alpha}_{N_{\text{dd}}}^{(0)}]$, $\boldsymbol{\beta}^{(0)} = [\boldsymbol{\beta}_1^{(0)}, \dots, \boldsymbol{\beta}_{N_{\text{dd}}}^{(0)}]$ initial conditions (cf. Eq. (5.22)), $\mathbf{U}^{(0)}$, $\mathbf{W}^{(0)}$, $tol > 0$, `maxit`, $J_{\max}$.

Outputs: $\left\{\hat{\mathbf{U}}_1^{(j)}\right\}_{j=1}^{J_{\max}}, \dots, \left\{\hat{\mathbf{U}}_{N_{\text{dd}}}^{(j)}\right\}_{j=1}^{J_{\max}}$.

1: Compute the matrices $\mathbf{P}, \mathbf{Q}$ in (5.17d).
2: Set $\widehat{\boldsymbol{\beta}}^{(0)} = \boldsymbol{\beta}^{(0)}$ and $\widehat{\boldsymbol{\alpha}} = \boldsymbol{\alpha}^{(0)}$.
3: **for** $j = 1, \dots, J_{\max}$ **do**
4: **for** $k = 1, \dots,$ `maxit` **do**
5: **for** $i = 1, \dots, N_{\text{dd}}$ **do**
6: Compute $\boldsymbol{\alpha}_i$ s.t. $\widehat{\mathbf{R}}_i^{\text{eq},(j)}(\boldsymbol{\alpha}_i, \boldsymbol{\beta}_i^{(k)}) = \mathbf{0}$ using Newton's method with initial condition $\widehat{\boldsymbol{\alpha}}_i$, $\hat{\boldsymbol{\beta}}_i^{(0)}$
7: Compute $\widehat{\mathbf{J}}_{\mathbf{F}_i}^{\text{eq}}\left(\boldsymbol{\beta}_i^{(k)}\right)$ (cf. (5.18)).
8: **end for**
9: Update $\widehat{\boldsymbol{\alpha}} = [\boldsymbol{\alpha}_1, \dots, \boldsymbol{\alpha}_{N_{\text{dd}}}]$.
10: Compute $\mathbf{r}^{\text{eq},(k),(j)} = \mathbf{P}\widehat{\boldsymbol{\alpha}} + \mathbf{Q}\widehat{\boldsymbol{\beta}}_i^{(k)}$ and $\nabla\mathbf{r}^{\text{eq},(k),(j)} = \mathbf{P}\widehat{\mathbf{J}}_{\mathbf{F}}^{\text{eq}} + \mathbf{Q}$.
11: Compute $\widehat{\boldsymbol{\beta}}^{(k+1)} = \widehat{\boldsymbol{\beta}}^{(k)} - \left(\nabla\mathbf{r}^{\text{eq},(k),(j)}\right)^{\dagger}\mathbf{r}^{\text{eq},(k),(j)}$.
12: **if** $\|\widehat{\boldsymbol{\beta}}^{(k+1)} - \widehat{\boldsymbol{\beta}}^{(k)}\|_2 < tol\|\widehat{\boldsymbol{\beta}}^{(k)}\|_2$ **then**, `BREAK`
13: **end if**
14: **end for**
15: Save $\hat{\boldsymbol{\beta}} = \boldsymbol{\beta}^{(k+1)}$
16: Update $\mathbf{U}_i^{(j-1)}$ and $\mathbf{W}_i^{(j-1)}$ for $i = 1, \dots, N_{\text{dd}}$ to be used at line 6.
17: Update $\widehat{\boldsymbol{\alpha}}$ s.t. $\hat{\boldsymbol{\alpha}}_i = \widehat{\mathbf{F}}_i^{\text{eq},(j)}(\hat{\boldsymbol{\beta}}_i)$ to be used at line 6.
18: Store $\hat{\mathbf{U}}_i^{(j)} = \mathbf{Z}_i^{\text{b}}\hat{\boldsymbol{\alpha}}_i + \mathbf{Z}_i^{\text{p}}\hat{\boldsymbol{\beta}}_i$.
19: Save $\hat{\boldsymbol{\beta}}^{(0)} = \hat{\boldsymbol{\beta}}$.
20: **end for**
21: Return $\left\{\hat{\mathbf{U}}_1^{(j)}\right\}_{j=1}^{J_{\max}}, \dots, \left\{\hat{\mathbf{U}}_{N_{\text{dd}}}^{(j)}\right\}_{j=1}^{J_{\max}}$.

6.2.3 Initial conditions

We use the OS2 method (cf. algorithm 7) to compute the initial conditions both in the HF case and in the ROM case. In particular, we recall problem (3.11), which is stated in the global domain Ω to compute the initial displacement $\underline{u}_0$: we state (3.11) in the local archetype components $\Omega_{\text{int}}^{\text{a}}$ and $\Omega_{\text{ext}}^{\text{a}}$ by using the proper deformation maps $\Phi_{\text{int}}^{\text{a}}$ and $\Phi_{\text{ext}}^{\text{a}}$ that are introduced in section 5.2.3. We omit the dependence on the parameters μ_{int} and μ_{ext} to shorten notation and we use the following notations for mapped and symmetric gradients as in chapter 5: given a map Φ, we define $\nabla_{\Phi} = \nabla\Phi^{-T}\nabla$ and $\nabla_{\text{s},\Phi} = \frac{1}{2}\left(\nabla_{\Phi} + \nabla_{\Phi}^{T}\right)$.

In the "internal" component (which corresponds to $\ell = 1$) we should solve $\int_{\Omega^{\mathrm{a}}_{\mathrm{int}}} \eta^{\mathrm{a,e}}_{\mathrm{int}}(\underline{u}, \underline{v})dx = 0$ for all $\underline{v} \in \mathcal{X}^{\mathrm{a}}_{\ell,0}$ where, for $\Phi = \Phi^{\mathrm{a}}_{\mathrm{int}}$,

$$\begin{aligned}\eta^{\mathrm{a,e}}_{\mathrm{int}}(\underline{u}, \underline{v}) =& 2\mu'(\nabla_{\mathrm{s},\Phi}\underline{v})(\nabla_{\mathrm{s},\Phi}\underline{u})\det(\nabla\Phi) + \\ & \lambda(\nabla\Phi^{-T} : \nabla\underline{v})(\nabla\Phi^{-T} : \nabla\underline{u})\det(\nabla\Phi) + \\ & - bp_{\mathrm{w},0}\left(\nabla\phi^{-T} : \nabla\underline{v}\right)\det(\nabla\Phi) - \rho^0\underline{F}_{\mathrm{m}}\underline{v}\det(\nabla\Phi).\end{aligned}$$

In the "external" component (which corresponds to $\ell = 2$) we should solve $\int_{\Omega^{\mathrm{a}}_{\mathrm{ext}}} \eta^{\mathrm{a,e}}_{\mathrm{ext}}(\underline{u}, \underline{v})\, dx + \int_{\Gamma^{\mathrm{a}}_{\mathrm{top},\ell}} \eta^{\mathrm{a,f}}_{\mathrm{ext}}(\underline{u}, \underline{v})\, dx = 0$, for all $\underline{v} \in \mathcal{X}^{\mathrm{a}}_{\ell,0}$ s.t. $\underline{v} \cdot \underline{n}|_{\partial\Omega\setminus\Gamma^{\mathrm{a}}_{N,\ell}} = 0$. For $\Phi = \Phi^{\mathrm{a}}_{\mathrm{ext}}$, we have that $\eta^{\mathrm{a,e}}_{\mathrm{ext}}(\underline{u}, \underline{v}) = \eta^{\mathrm{a,e}}_{\mathrm{int}}(\underline{u}, \underline{v})$ and

$$\eta^{\mathrm{a,f}}_{\mathrm{ext}} = \underline{v} \cdot (\underline{g}_{\mathrm{m,N}} \circ \Phi)\|\nabla\Phi\,\hat{\mathbf{t}}\|_2.$$

We compute $\underline{u}_0$ using the Gauss-Newton method that is described in algorithm 7. Since problem (3.11) is linear in $\underline{u}_0$ (and the same holds for the corresponding local variational forms), the iterative procedure in algorithm 7 is expected to converge in only 1 iteration (cf. [MNT04]).

6.2.4 Hyper-reduction

We rely on element-wise EQ and we follow the procedure that is explained in section 5.3.2: we replace the high-fidelity discretization with the weighted residual associated with

$$\mathcal{G}^{\mathrm{a,\,eq},(j)}_{\ell}\left(\underline{U}^{(j)}, \underline{V}\right) = \sum_{k=1}^{N^{\mathrm{e}}_{\ell}} \rho^{\mathrm{eq}}_{\ell,k} \int_{\mathtt{D}_{\ell,k}} \eta^{\mathrm{a,e},(j)}_{\ell}(\underline{U}^{(j)}, \underline{V})\, dx \; + \int_{\partial\mathtt{D}_{\ell,k}} \eta^{\mathrm{a,f},(j)}_{\ell}(\underline{U}^{(j)}, \underline{V})\, dx, \tag{6.13}$$

where $\boldsymbol{\rho}^{\mathrm{eq}}_{\ell} = [\rho^{\mathrm{eq}}_{\ell,1}, \ldots, \rho^{\mathrm{eq}}_{\ell,N^{\mathrm{e}}_{\ell}}]^T$ is a sparse vector of non-negative weights. Unlike in section 5.3.2, we cannot rely on local optimal coefficients and the associated local parameters $\{\boldsymbol{\alpha}^{(j)}_{\ell,i}, \boldsymbol{\beta}^{(j)}_{\ell,i}, \mu_{\ell}\}_{i=1}^{n_{\mathrm{train}},\ell}$, $j = 1, \ldots, J_{\max}$ (which are computed from algorithm 11) for the construction of EQ matrices (cf. appendix A). Indeed, as explained in remark 2, residual (6.7) associated with equations (3.12)-(3.13) depends on state variables and internal variables both at the current time and at the previous time: we should thus prescribe $\left(\alpha^{(j)}_i, \alpha^{(j-1)}_i, \beta^{(j)}_i, \beta^{(j-1)}_i, \underline{W}^{(j-1)}_i\right)$ to compute local residuals (6.8). We recall that computation of $\underline{W}^{(j)}_i$ requires the evaluation of the discretization of $\mathcal{F}_{\mu}$ (which corresponds to constitutive laws (3.13)).
We follow the underlying idea of section 4.3.1: we solve the (local) ROM(s) with high-fidelity quadrature and generate $\{\hat{\alpha}^{(j)}_i, \hat{\beta}^{(j)}_i, \underline{\hat{W}}^{(j)}_i\}$ for all $j = 1, \ldots, J_{\max}$. The reason is due to memory costs: in the CB setting, indeed, storage of state and internal variables would be of the order of $(n_{\mathrm{q}}N^{\mathrm{e}}_{\mathrm{int}}D^{\mathrm{cl}} + N^{\mathrm{hf}}_{\mathrm{int}}D + n_{\mathrm{q}}N^{\mathrm{e}}_{\mathrm{int}}(d-1))|\mathtt{I}_{\mathrm{s}}|(N_{\mathrm{dd}} - 1)$ for all the internal components and $(n_{\mathrm{q}}N^{\mathrm{e}}_{\mathrm{ext}}D^{\mathrm{cl}} + N^{\mathrm{hf}}_{\mathrm{ext}}D + n_{\mathrm{q}}N^{\mathrm{e}}_{\mathrm{ext}}(d-1))|\mathtt{I}_{\mathrm{s}}|$ for the external component. The price to pay is an increase in the computational cost associated with the offline phase.

Hyper-reduction of the objective function in (6.12a) follows the same procedure that is explained in section 5.3.3; it suffices to adapt it to formulation (6.12a).

6.2.5 Dealing with different scales

The formulation in (6.9) is an unconstrained minimization problem in which the objective function is written in terms of port solutions at port boundaries; the solutions are of the form $\underline{U}_i^{(j)} = [\underline{u}_i^{(j)^T}, p_{\mathrm{wi}}^{(j)}, T_i^{(j)}]^T$ for each component $i = 1, \dots, N_{\mathrm{dd}}$ at all time steps $j = 1, \dots, J_{\max}$. These solutions correspond to considerably different scales. As explained in chapter 3, we introduce scaling functions that non-dimensionalize the state variables. In [PR22], this procedure is shown to have a positive impact on both POD and Galerkin or least-squares ROMs. To give a concrete example on THM applications, we recall figure 3.3 in which the time gaps of dimensional solutions are depicted for a fixed parametric configuration. The accuracy of the POD basis and the resulting ROM depends on the choice of the inner product space, in particular for vector-valued POD (i.e. $D > 1$), which has to combine variables with different scales. Therefore, a proper treatment of the solutions scales represents a significant aspect to account for, not only in error computations (compare norm definitions in section 3.5), but also in computing the algebraic form of the objective function (6.12a), both in the high-fidelity and ROM cases. In the numerical section 6.3, a monolithic coarse-mesh solution is found for a fixed parameter $\mu = \bar{\mu}$ (which is the centroid of $\mathscr{P}$) and the scaling factor of the objective function in (6.12a) corresponds to the following gap: $\max\{\mathbf{U}_{i,s}^{(J_{\max})}\} - \min\{\mathbf{U}_{i,s}^{(J_{\max})}\}$ for each $s = 1, \dots, D$ and $i = 1, \dots, N_{\mathrm{dd}}$ (both in the HF and in the ROM solves).

6.3 Numerical results

6.3.1 Assessment metrics and training parameters

We adopt two geometric discretizations. A first one, which is characterized by $N_{\mathrm{int}}^{\mathrm{e}} = 1120$ and $N_{\mathrm{ext}}^{\mathrm{e}} = 3960$ is also adopted in the numerical investigations in chapter 5; a second discretization is characterized by $N_{\mathrm{int}}^{\mathrm{e}} = 320$ and $N_{\mathrm{ext}}^{\mathrm{e}} = 1184$ elements. We notice that with respect to the mesh in figure 3.2(b) in chapter 3 (which is dedicated to the FE solution of THM system), the choice of structured meshes is motivated by the need of using mesh interpolation operators: indeed, structured meshes require an acceptably low (log-in-time) computational cost for interpolation. Unlike chapter 3, in all the following numerical results we consider FE polynomial degree $\mathtt{p} = 2$ for displacement, pressure and temperature, as in the numerical results shown in chapter 5. We aim at extending the investigation to different FE discretizations also for the component-based ROM.

We also need to take into account that in this chapter the THM system is solved for different values of interest of Q_{a} (cf. figure 5.3), while in chapter 4 a geometric setting is fixed. The parameters that are associated with the thermal flux boundary condition (3.7) are modified to take into account higher numbers of repositories $Q_{\mathrm{a}} \geq 2$. In particular, we train the CB-ROM based on $n_{\mathrm{train}} = 10$ global parameters in $\Xi_{\mathrm{train}} = \{\mu^{(k)}\}_{k=1}^{n_{\mathrm{train}}}$ such that

$$\begin{aligned}\left(E_1^{(k)}, \mu_1^{(k)}, C_{\mathrm{al}}^{(k)}, \tau^{(k)}\right) \overset{\mathrm{iid}}{\sim} \mathrm{Uniform}\big([928.1416, 1.0896 \cdot 10^3] \times [0.2760, 0.3240] \\ \times [4.9066, 5.7600] \times [0.4193, 0.4922]\big),\end{aligned} \tag{6.14}$$

and

$$Q_{\mathrm{a}}^{(k)} \overset{\mathrm{iid}}{\sim} \mathrm{Uniform}\left(\{2, \dots, 7\}\right).$$

We recall that, as in the numerical investigations in chapter 4 , we refer to non-dimensional values of parameters. Also, we recall that $E_1^{(k)}$ and $\mu_1^{(k)}$ are the values

of Young's modulus and Poisson's ratio only on region UA in figure 3.2(a). Since also geometric parameters (cf. Q_a in figure 5.3) are supposed to change, we set a a variation of the 8% of the parameters in the same training set (rather than the 15% as in the tests for the monolithic ROM in chapter 4).
We report in the following table the relative $L^2(0,T_f;H^1(\Omega))$ variation of the monolithic high-fidelity solutions for varying parameters E_1, μ_1, C_{al}, τ as in (6.14) with respect to the high-fidelity monolithic solution that is computed for the average value of μ in the same range. We consider variations of one parameter at a time in (6.14). Also, we consider a fixed geometric parameter $Q_a = 6$.

	$L^2(0,T_f;H^1(\Omega))$ solution variation
E	0.002
μ	0.0015
C_{al}	0.0462
τ	0.0312

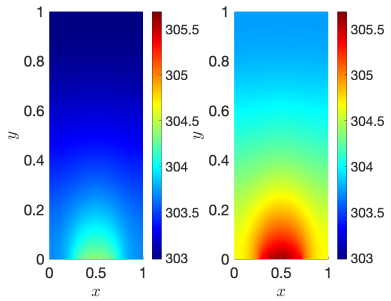

FIGURE 6.1: Two solutions (in terms of dimensional temperature $[K]$) (computed at the final time step $j = J_{max} = 20$, with $\Delta t = 0.05$) for $\tau = 0.4193$ (left) and $\tau = 0.4922$ (right) in the parametric range.

The soley variation of the physical parameter τ in the parametric range (6.14) results in a change in the order of 3% in the solution. To provide a simple example, we depict in figure 6.1 the temperature solutions at the final time step $j = J_{max} = 20$ and at the minimum and maximum values of τ in the parametric range $[0.4193, 0.4922]$. We conclude that the predictive investigation of this section is worthy of interest.

We assess performance based on $n_{test} = 5$ out-of-sample global parameters $\Xi_{test} = \{\tilde{\mu}^{(k)}\}_{k=1}^{n_{test}}$ generated by the same distribution (6.14). The non-dimensional time interval $(0, t_f]$ is divided into $J_{max} = 20$ uniform time steps of length $\Delta t = 0.05$; the high-fidelity solutions are stored in the training phase at sampling times in $\mathtt{I}_s \subseteq \{1, \dots, J_{max}\}$. We set $|\mathtt{I}_s| = 20$ and the same values for the computation and saving time-steps $\Delta t_s = \Delta t = 0.05$. We define the out-of-sample prediction error:

$$E_J := \frac{1}{n_{test}} \sum_{\mu \in \Xi_{test}} \frac{\sqrt{\sum_{j=1}^{J_{max}} (t^{(j)} - t^{(j-1)}) \left\| \mathtt{P}_{pu}[\underline{U}^{(j)}] - \mathtt{P}_{pu}[\widehat{\underline{U}}^{(j)}] \right\|^2_{H^1(\Omega)}}}{\sqrt{\sum_{j=1}^{J_{max}} (t^{(j)} - t^{(j-1)}) \left\| \mathtt{P}_{pu}[\underline{U}^{(j)}] \right\|^2_{H^1(\Omega)}}}, \tag{6.15}$$

where $\{\widehat{\underline{U}}^{(j)}\}_j$ is found by solving a ROM, by OS2, with or without hyper-reduction. The following errors are associated with solution projection: we present first the best-fit

error

$$E_J^{\mathrm{bf}} := \frac{1}{n_{\mathrm{test}}} \sum_{\mu \in \Xi_{\mathrm{test}}} \frac{\sqrt{\sum_{j=1}^{J_{\max}} (t^{(j)} - t^{(j-1)}) \left\| \mathtt{P}_{\mathrm{pu}}[\underline{U}^{(j)}] - \underline{\widehat{U}}_{\mathrm{bf}}^{(j)} \right\|_{H^1(\Omega)}^2}}{\sqrt{\sum_{j=1}^{J_{\max}} (t^{(j)} - t^{(j-1)}) \left\| \mathtt{P}_{\mathrm{pu}}[\underline{U}^{(j)}] \right\|_{H^1(\Omega)}^2}}, \tag{6.16}$$

$$\underline{\widehat{U}}_{\mathrm{bf}}^{(j)} = \Pi_{\mathcal{Z}_{\mathrm{glo}}} \mathtt{P}_{\mathrm{pu}}[\underline{U}^{(j)}] \tag{6.17}$$

where we define $\mathcal{Z}_{\mathrm{glo}} = \mathrm{span}\{\mathtt{P}_{\mathrm{pu}}[\underline{\zeta}_i \circ \Phi_i^{-1}] : \underline{\zeta}_i \in \mathcal{Z}_{\mathtt{L}_i}^{\mathrm{a,b}} \cup \mathcal{Z}_{\mathtt{L}_i}^{\mathrm{a,p}}, i = 1, \dots N_{\mathrm{dd}}\}$ for $i = 1, \dots, N_{\mathrm{dd}}$.
We add

$$E_J^{\mathrm{sub}} := \frac{1}{n_{\mathrm{test}}} \sum_{\mu \in \Xi_{\mathrm{test}}} \frac{\sqrt{\sum_{j=1}^{J_{\max}} (t^{(j)} - t^{(j-1)}) \left\| \mathtt{P}_{\mathrm{pu}}[\underline{U}^{(j)}] - \mathtt{P}_{\mathrm{pu}}[\underline{\widehat{U}}_{\mathrm{sub}}^{(j)}] \right\|_{H^1(\Omega)}^2}}{\sqrt{\sum_{j=1}^{J_{\max}} (t^{(j)} - t^{(j-1)}) \left\| \mathtt{P}_{\mathrm{pu}}[\underline{U}^{(j)}] \right\|_{H^1(\Omega)}^2}}, \tag{6.18}$$

$$\left(\underline{\widehat{U}}_{\mathrm{sub}}^{(j)}\right)_i = \left(\Pi_{\mathcal{Z}_{\mathtt{L}_i}^{\mathrm{a,b}} \cup \mathcal{Z}_{\mathtt{L}_i}^{\mathrm{a,p}}} \left(\underline{U}_i^{(j)} \circ \Phi_i \right) \right) \circ \Phi_i^{-1}, \tag{6.19}$$

that is introduced in equation (5.44) for steady problems: we recall that, unlike E_J^{bf}, the error in (6.18) is not optimal.

6.3.2 High-fidelity solution

First of all, high-fidelity solutions are shown for a fixed parametric configuration given by $\mu = \bar{\mu} = [1.088 \cdot 10^3, 0.3, 5.333, 0.4558]^T$ corresponding to the centroid of the training set and $Q_{\mathrm{a}} = 5$ corresponding to an (integer) average value for range $\{2, \dots, 7\}$. Local solutions are computed by the OS2 method applied to THM system and a a reconstruction of the solution in the global domain is found by evaluation of partition of unity operator (5.42) at the local solutions.
In figure 6.2 we depict the H^1 relative error between the high-fidelity solutions computed by OS2 method and the solution found by monolithic solver with `P2` finite element degree for displacement, pressure and temperature. The relative error for all timesteps $j = 1, \dots, J_{\max}$ can be written as follows

$$E_{\mathrm{hf}}^{(j)} = \frac{\| \mathtt{P}_{\mathrm{pu}}[\overrightarrow{U}^{(j)}] - \underline{U}^{(j)} \|_{H^1(\Omega)}}{\| \underline{U}^{(j)} \|_{H^1(\Omega)}}.$$

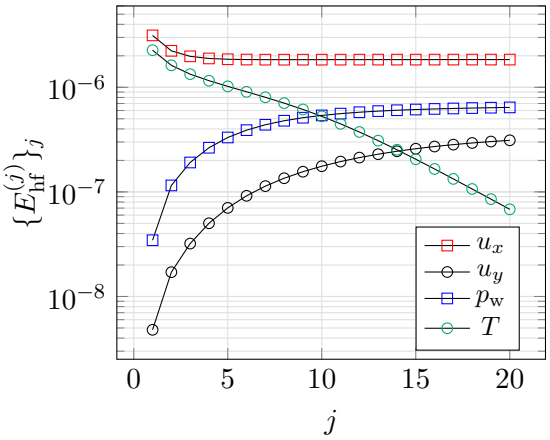

FIGURE 6.2: Error with respect to time index $j = 1, \ldots, J_{\max}$ for each state variable.

The relative (averaged in time) error is around $7.49 \cdot 10^{-4}$ by using the fine mesh and around $3.30 \cdot 10^{-3}$ by using the coarse mesh. All relative errors are under 10^{-5} for all time indices $j = 1, \ldots, J_{\max}$. We conjecture that the error in temperature is rapidly decreasing in time due to the fact that the temperature evolution is more significant in the first time steps, as depicted in figure 6.3(b), and the coupling might be weaker than the one associated with the other solution components. We would like to better investigate this aspect.

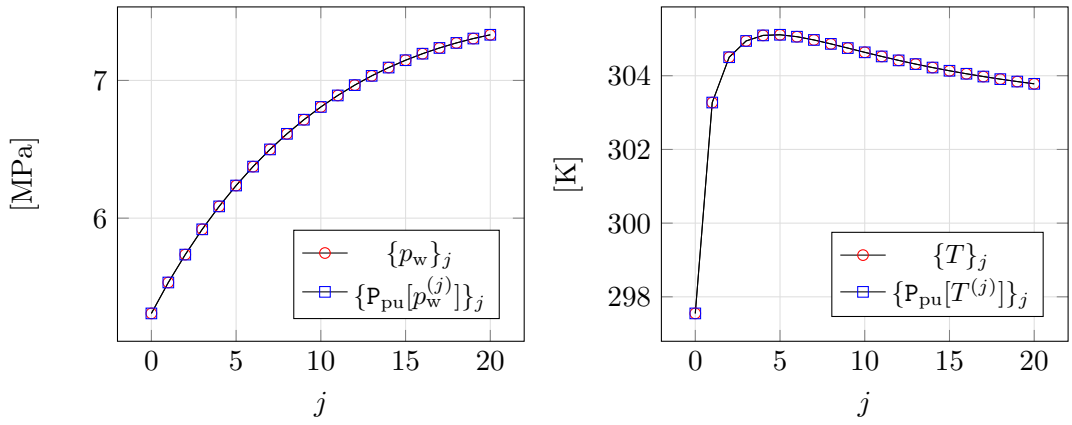

(a) pressure evolution

(b) temperature evolution

FIGURE 6.3: Dimensional temperature evolution in time, for $j = 1, \ldots, J_{\max}$; we add also the initial conditions.

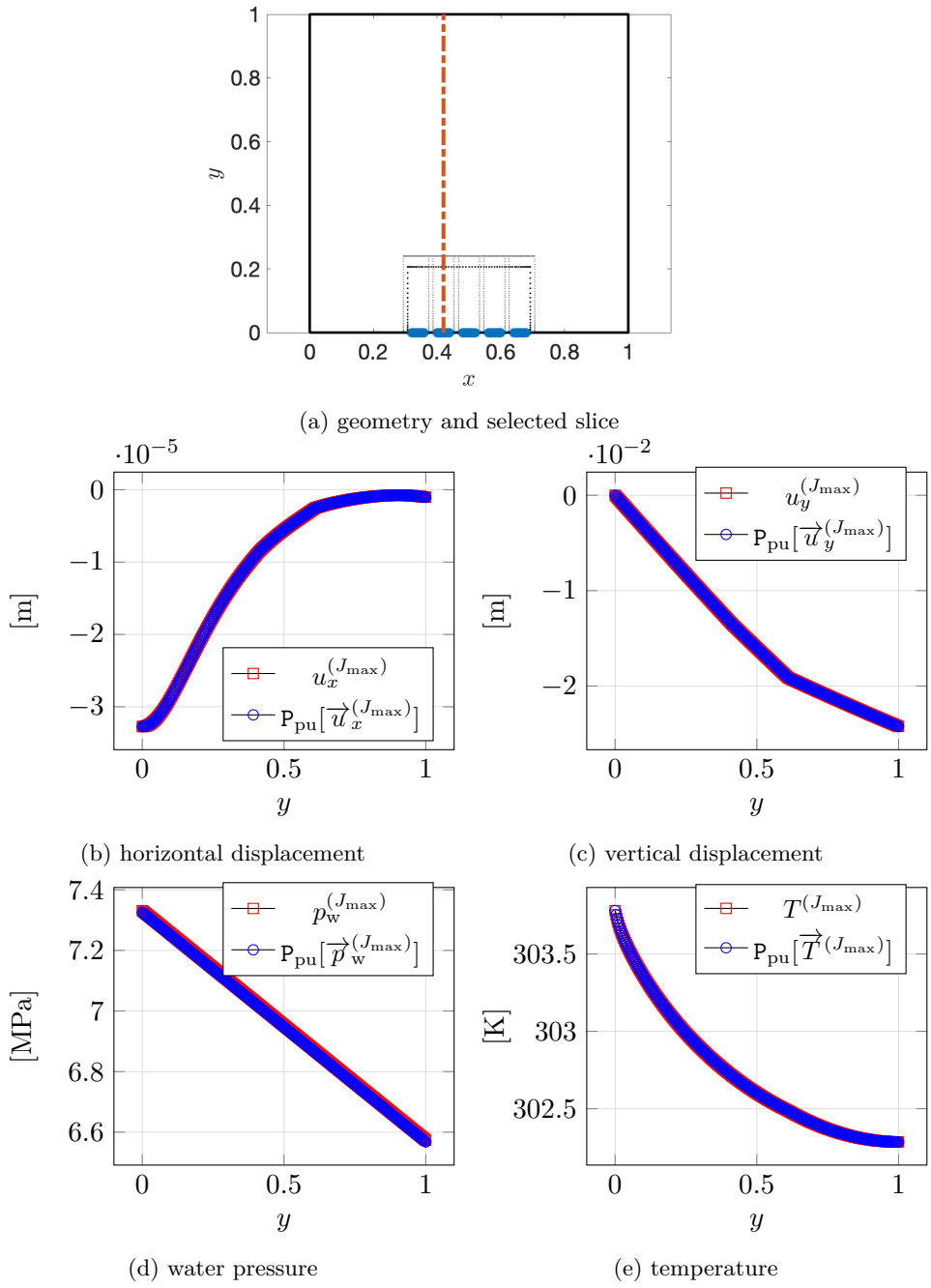

(a) geometry and selected slice

(b) horizontal displacement

(c) vertical displacement

(d) water pressure

(e) temperature

FIGURE 6.4: Dimensional solutions at points depicted in (a), s.t. $x = \bar{x} = 0.46$, $0 \leq y \leq 1$.

6.3.3 RB construction

We show the bubble and port POD eigenvalues associated with the two archetype components; the decay of the normalized eigenvalues $\lambda^{\star}_{\ell,i}/\lambda^{\star}_{\ell,1}$, for $\star \in \{\mathrm{b}, \mathrm{p}\}$ is depicted only above a threshold of 10^{-16}. We notice that the POD eigenvalues associated with the external component decay faster than the ones associated with the internal one: the solutions in the external component are expected to be less affected by the variation in parameters (cf. figure 3.2(a) and (6.14)) than the corresponding solutions in the internal components.

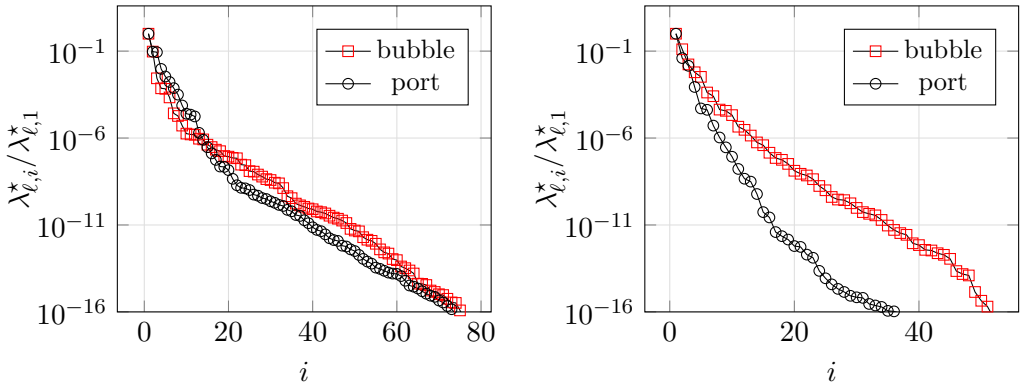

(a) $\Omega^{\mathrm{a}}_{\mathrm{int}}$ (b) $\Omega^{\mathrm{a}}_{\mathrm{ext}}$

FIGURE 6.5: Eigenvalues decay for the two archetype components: (a): $\ell = 1$, (b): $\ell = 2$.

6.3.4 Reduced order model with HF quadrature

The average in-sample error (cf. equations (2.13)) $E_{\mathrm{n}} = 1 - \frac{1}{n_{\mathrm{train}}} \sum_{i=1}^{n} \lambda_i \Big/ \sum_{j=1}^{} \lambda_j$ is depicted in figure 6.6 for several values of port modes n (and $m = n$) in the two archetype components.

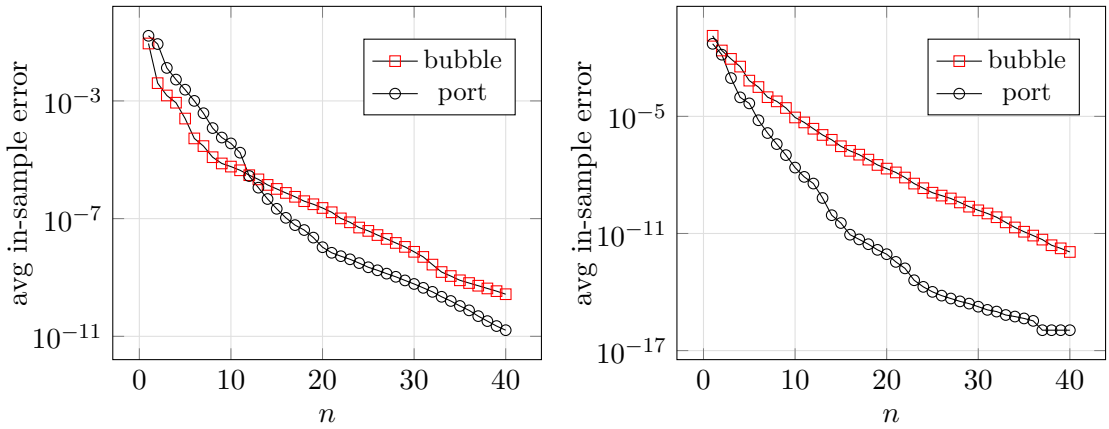

(a) $\Omega^{\mathrm{a}}_{\mathrm{int}}$ (b) $\Omega^{\mathrm{a}}_{\mathrm{ext}}$

FIGURE 6.6: behaviour of the averaged squared in-sample error E_{n} for several values of n, for port and bubble components, and for the two archetype components.

We remark that errors in figure 6.6 are squared and that they correspond to in-sample projection errors of the maximum order of 10^{-5} for the maximum number of modes $m = n = 40$.

We show the performance of the OS2 ROM without hyper-reduction. We investigate the performance in out-of-sample cases. We show the error in (6.15) between the solution found by OS2 ROM with high-fidelity quadrature and the high-fidelity solution (which is computed by OS2 method with high-fidelity solve). Also the best-fit error and the sub-optimal error (cf. (6.16) and (6.18)) are depicted with respect to increasing values of bubble and port modes ($m = n$); we recall that all errors are averaged over $n_{\mathrm{test}} = 5$ tests. We set $tol = 10^{-8}$ in algorithm 12 and we set a threshold for the

objective function value equal to 10^{-10}. We depict in figure 6.7(b) the (averaged in time) value of the objective function (cf. line 10) which is computed once Gauss-Newton's convergence criterion at line 12 is satisfied; in figure 6.7(c) the Gauss-Newton's average computational cost is shown for increasing number of modes n (and $m = n$).

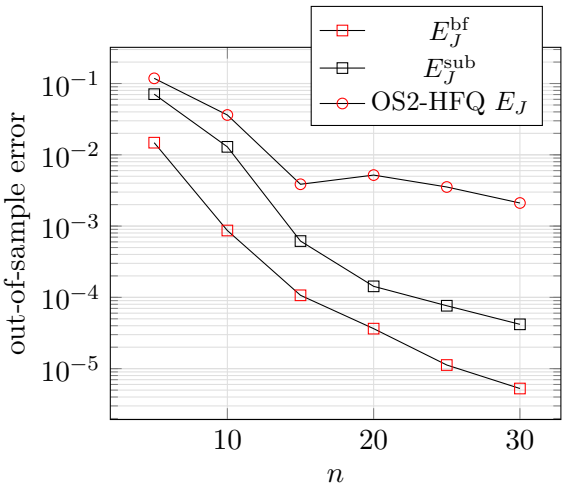

(a) out-of-sample error

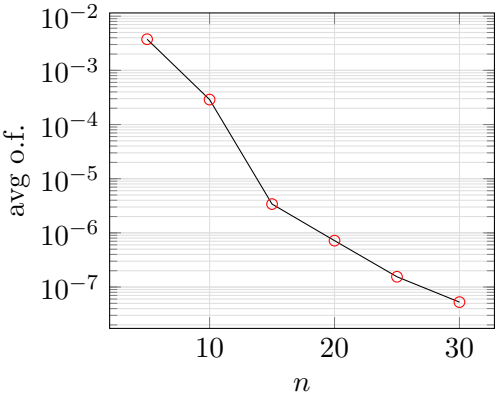

(b) average objective function

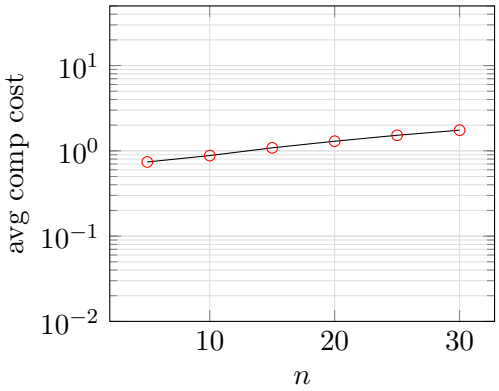

(c) average comp cost

FIGURE 6.7: (a): out-of-sample performance of OS2 ROM without hyper-reduction for several values of m, with $n = m$; (b): average (in time) objective function (6.12a) at optimality; (c): average cost on n_{test} tests and on times $\{1, \dots, J_{\max}\}$.

We observe in figure 6.7(a) a saturation of the out-of-sample error for large values of m and n, while in figure 6.7(b), for increasing values of bubble and port modes, we observe a decrease of the average objective function computed in algorithm 12. We conjecture that this different behavior might be related to the scaling of the objective function and to the difference in magnitude of the four state variables (cf. (3.14) for the choice of the norm). A thorough investigation of this aspect is currently ongoing.

In figure 6.8 the dimensional horizontal and vertical displacement, pressure and temperature are depicted at the final time step $J_{\max}$: the plots demonstrate that the OS2-ROM method (for a fixed reduced basis dimension $n = 30$ and $m = n$) provides extreemely accurate results with respect to the high-fidelity solutions. In all the cases the partition of unity operator is employed to compare solutions in the global domain Ω.

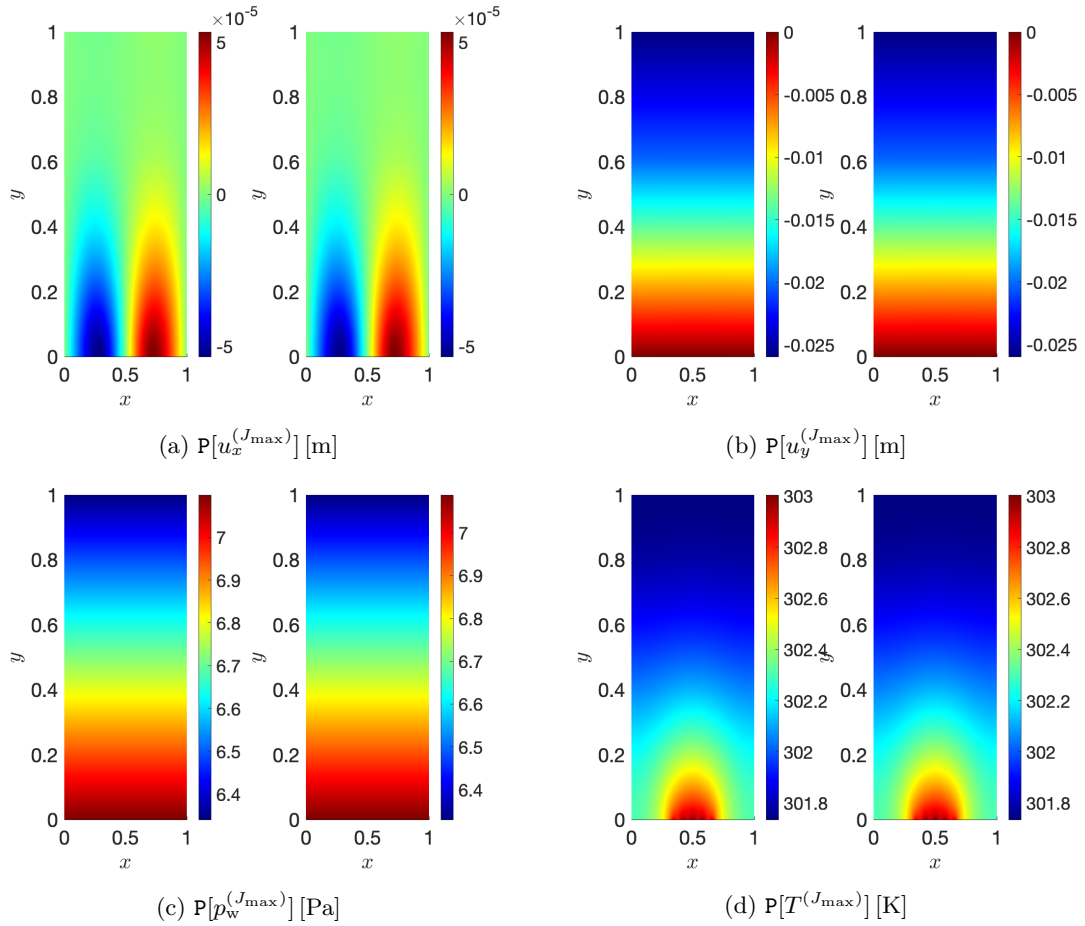

(a) $\mathtt{P}[u_x^{(J_{\max})}]$ [m]

(b) $\mathtt{P}[u_y^{(J_{\max})}]$ [m]

(c) $\mathtt{P}[p_{\mathrm{w}}^{(J_{\max})}]$ [Pa]

(d) $\mathtt{P}[T^{(J_{\max})}]$ [K]

FIGURE 6.8: Dimensional solutions at the final time $J_{\max}$ in an out-of-sample prediction test: on the left the high-fidelity solution, on the right the OS2-ROM solution found without hyper-reduction with $n = 30$ and $m = n$.

6.3.5 Hyper-reduction

In figure 6.9 we investigate the performance of the hyper-reduced ROM for the port-to-bubble maps: in 6.9(a) the out-of-sample prediction errors are depicted for several values of n, with $m = n$. We compare results obtained with empirical quadrature in local port-to-bubble maps with results obtained with high-fidelity quadrature (dubbed HFQ). Figure 6.9(b) shows the average computational time over the test set. The EQ tolerance is $tol_{\mathrm{eq}} = 10^{-14}$ (it corresponds to a percentage of sampled elements equal to 75.31% in the internal coarse mesh and 20.18% in the external coarse mesh for $n = m = 15$).

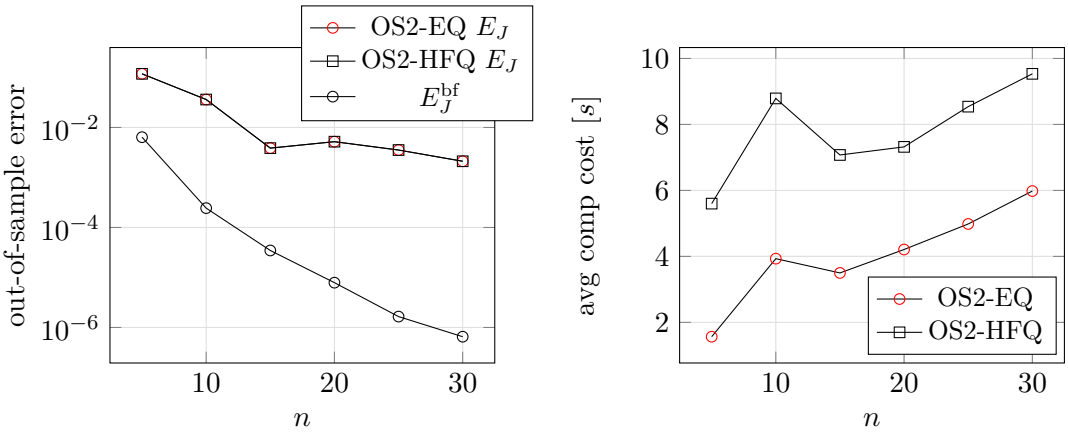

(a) error

(b) avg computational cost

FIGURE 6.9: Performance of OS2-ROM with hyper-reduction on port-to-bubble maps, based on EQ procedure with $tol_{\text{eq}} = 10^{-14}$.

The OS2 method with EQ achieves a relative error around 10^{-3} for $n \geq 15$ and $m = n$; the corresponding average computational time is around a factor $1/2$ of the cost associated with the HF quadrature rule. We also compute the speed-up factor of the hyper-reduced OS2 solver with respect to the monolithic P2 HF solve for $\mu \in \Xi_{\text{test}}$: we find an average (over n_{test} tests) value in an interval of $13 - 22$ for $n \in \{15, 20, 25, 30\}$ and $m = n$.

6.4 Conclusions

In sections 6.3.4 and 6.3.5 we investigated the ROM accuracy in out-of-sample cases with and without hyper-reduction. The OS2-ROM errors in figure 6.7(a) and in 6.9(a) present an accuracy saturation for large values of n and m compared to the projection errros (6.16). At the same time, the average value of the objective function at optimality (which is shown in the HF quadrature case in figure 6.7(b)) demonstrates good convergence properties of the OS2 procedure in algorithm 12. A thorough investigation of this aspect is currently ongoing. Nevertheless, the high-fidelity solution is recreated with a prediction error of the order of 0.3%.

We also aim to replicate the numerical results of the latter two sections 6.3.4 and 6.3.5 also in the case of finer grids.

As for the efficiency, the hyper-reduced OS2 method achieves a good gain in computational cost (in the range of $13 - 22$) with respect to a monolithic solve for the same out-of-sample test configurations. We envision that a more effective implementation of algorithm 12 — by parallelization of port-to-bubble maps at lines 5-8 and by a point-wise EQ hyper-reduction of the port-to-bubble maps, as opposed to element-wise EQ— will lead to significantly larger speed-ups.

Chapter 7

Conclusions and perspectives

In this thesis we focused in applying CB-pMOR methods for THM systems in radioactive waste applications. In particular we were interested in

1. significantly reducing the computational cost associated with the numerical simulations of parametric problems governed by PDEs;
2. developing a new CB-pMOR methodology that could handle different geometric parametrizations of the problem of interest;
3. adapting the proposed CB-pMOR methods to time-dependent coupled systems with internal variables.

To achieve these goals, at the foundation of proposed the methodology there are the ROMs, which typically consist of a training stage in which high-fidelity solution snapshots are collected to define a low-dimensional subspace, and a prediction stage, where the trial subspace is then exploited to achieve fast simulations for new input parameters.

The first contribution of this thesis concerns the development of a Galerkin projection-based model order reduction procedure for the THM system that is introduced in equation (1.1). The pMOR approach has been adapted to time-dependent nonlinear coupled problems with internal variables. The constructed ROM has been enriched with a time-averaged error indicator to drive the offline sampling and an EQ procedure to reduce online costs. The performance of the resulting ROM has been evaluated on the both reproductive and predictive tests. The results demonstrate that the accuracy of the ROM is less than 1% (for a dimension of the reduced space that is more than 25) over a range of predictive input parameters; also, the results show a significant speedup factor delivered by the ROM with respect to HF simulations.

For future perspectives, we consider the following idea.

- *Residual minimization.* The accuracy of the method could be even further improved by the residual minimization method instead of the Galerkin method.

In the second part of the thesis we proposed a CB-pMOR formulation for a) steady nonlinear PDEs, b) time-dependent coupled nonlinear problems. The formulation is based on overlapping subdomains; it relies on a constrained optimization that penalizes solutions jumps at the subdomain interfaces. The extension of classical pMOR techniques to the DD framework is driven by the introduction of archetype and instantiated components. A key point to achieve a low-dimensional unconstrained minimization problem is given by the solution decomposition into bubble and port solutions and the exploitation of the underlying principle of static condensation.

In the application in chapter 5 we achieve a speedup factor of the order of 20 compared to a standard monolithic FE model, with less than 0.1% prediction error.

In the third part of the thesis we extended our CB-pMOR formulation (for nonlinear PDEs) to tackle the THM of interest. We also explored the ROM performance both in in-sample and out-of-sample cases. We endowed the local ROMs with hyper-reduction tools and we achieved a speedup factor in the range of $13 - 22$ with respect to a monolithic P2 FE solve. We found prediction errors of the order of 0.3% in the out-of-sample cases.
Concerning the time-dependent THM problem in chapter 6, we remark the following important perspective.

- *ROM accuracy.* As explained in section 6.3.4, we are interested in the improvement of the accuracy of the Galerkin ROM method. First of all, we should better understand the importance of scaling in the objective function, and in particular further investigate the computation of the optimal scaling. Furthermore, we conjecture about drawing insights from the work in [Lin+22], which has the objective of improving the accuracy of ROM in the case of a least-squares Petrov-Galerkin method.

In addition, it would be interesting to explore some relevant perspectives to both the second and third part of the thesis.

- *Choice of the number of basis functions.* In the local ROMs, we use the same number of reduced basis functions in all the subdomains: we would better generalize the implementation and equip different archetype components with different dimensions of reduced bases. In this way, the local approach could also improve the computational complexity of the ROMs, since less local basis functions may be required to obtain accurate approximations.

- *OS methods.* We aim at better exploiting the connection between the proposed OS2 method and the (multiplicative or additive) overlapping Schwarz method, as described in section 5.1.1 for a steady PDE. Due to this fact, the extensively developed analysis on OS could be extremely useful to derive a more complete analysis (cf. section 5.4) of OS2. In particular, we are interested in the possibility of extending the connection between OS2 and OS for nonlinear and/or time-dependent problems. Also, we aim at combining our approach with the recently-developed OS method discussed in [MTP22].

- *Localized training.* We wish to devise localized training techniques to avoid the solution to global HF problems at training stage; in this regard, we aim to extend the approach in [ST22] to both steady PDEs and unsteady PDEs with internal variables.

- *Automatic partitioning.* This work is based on an *a priori* partition of the global domain, i.e. we exploit the knowledge of the parametric mapping Φ. The automatic construction of a mapping for parametrized geometries could be efficiently determined by a suitable error indicator. We refer to the model reduction literature (e.g. [Roz+19], [Las+14]) for a thorough discussion.

- *Data-fitted methods.* We aim to combine data-fitted and projection-based ROMs in the OS2 framework: we envision that the successful combination of first-principle and data-fitted models might offer new solutions for data assimilation

(state estimation) applications, for a broad range of engineering tasks.

- *Comparison with other methods.* We may be interested in comparing the OS2 method with other algorithms for PDE-constrained optimization; we cite [HK10] as a reference for different approaches for solving optimization problems with PDE constraints.

- *Non-overlapping decomposition.* We wish to investigate the possibility of generalizing our approach to non-overlapping decompositions: this requires to add in the objective function a term that penalizes the jump of the normal stresses; a deep investigation of the connection with discontinuous Galerkin methods should also be considered. We refer to the works in [GPK99] and [GL00] for optimization-based non-overlapping domain decomposition; in these works the *control* variables (i.e. the unknowns in the optimization problem) are the Neumann boundary conditions at the interface boundaries.

- *Multi-fidelity approximations.* Thanks to the extreme flexibility of the OS2 statement (the N_{dd} subproblems in (6.2) are all independent from each other), we envision to test also multi-fidelity approximations. For example, a FOM/ROM coupling could be adopted in the case of higher/lower variability of the parametrized solutions in different regions of the global domain: considering the application of this thesis, a high-fidelity model might be employed in the repository regions and a ROM in the external region (cf. figure 1.7).

- *Structure preservation.* We conjecture that the application of the OS2 method does not ensure structure preservation for Hamiltonian problems: indeed, as described in section 5.4.4, the OS2 ROM statement is equivalent to a Petrov-Galerkin formulation, which does not guarantee the conservation of the structure. We refer to [FCA15] on the explaination of structure preservation in the case of Galerkin projection and to a recent work in [HPR22] on an adaptive structure-preserving MOR approach.

Appendix A

Hyper-reduction of port-to-bubble problems

We review the element-wise EQ hyper-reduction procedure that is employed in chapter 5 to speed up the solution to the port-to-bubble problems. The approach exploits the methods first proposed in [FCA15; YP19a]: we refer to [TZ21] for further details. We recall that, for any $\ell \in \mathcal{L}$, $\{x^{\mathrm{a,v}}_{\ell,j}\}_{j=1}^{N^{\mathrm{v}}_\ell}$ are the nodes of the reference mesh of the ℓ-th component, while $\mathtt{T}_\ell \in \mathbb{N}^{N^{\mathrm{e}}_\ell \times n_{\mathrm{lp}}}$ is the connectivity matrix, with n_{lp} equal to the number of elemental degrees of freedom. We denote by $e_1, \dots, e_D$ the vectors of the canonical basis in $\mathbb{R}^D$ and we denote by $\varphi_{\ell,k,i}$ the FE basis associated with the i-th degree of freedom of the k-th element of the ℓ-th component.

Given $u \in \mathcal{X}^{\mathrm{a}}_\ell$, we denote by $\mathbf{u}^{\mathrm{un}} \in \mathbb{R}^{n_{\mathrm{lp}} \times N^{\mathrm{e}}_\ell \times D}$ the corresponding third-order tensor such that

$$u^{\mathrm{un}}_{i,k,d} = \left(u\left(x^{\mathrm{a,v}}_{\ell,\mathtt{T}_{\ell,k,i}}\right)\right)_d, \quad i = 1, \dots, n_{\mathrm{lp}}, \;\; k = 1, \dots, N^{\mathrm{e}}_\ell, \;\; d = 1, \dots, D.$$

Similarly, given the ROB basis $Z^{\mathrm{a,b}}_\ell : \mathbb{R}^n \to \mathcal{Z}^{\mathrm{a,b}}_\ell$, we denote by $\mathbf{Z}^{\mathrm{a,b,un}}_\ell \in \mathbb{R}^{n_{\mathrm{lp}} \times N^{\mathrm{e}}_\ell \times D \times n}$ the corresponding fourth-order tensor. We further define the unassembled residual associated with the field u and the parameter μ_ℓ,

$$R^{\mathrm{a,un}}_{\ell,i,k,d}(u;\mu_\ell) := \int_{\mathtt{D}_{\ell,k}} \eta^{\mathrm{a,e}}_\ell(u, \varphi_{\ell,k,i}\, e_d; \mu_\ell)\, dx + \int_{\partial\mathtt{D}_{\ell,k}} \eta^{\mathrm{a,f}}_\ell(u, \varphi_{\ell,k,i}\, e_d; \mu_\ell)\, dx,$$

for $\ell \in \mathcal{L}$, $i = 1, \dots, n_{\mathrm{lp}}$, $k = 1, \dots, N^{\mathrm{e}}_\ell$, $d = 1, \dots, D$. Then, it is easy to verify that

$$\left(\widehat{\mathbf{R}}^\star_\ell(\boldsymbol{\gamma}_\ell)\right)_j = \sum_{i,k,d} \rho^\star_{\ell,k}\, Z^{\mathrm{a,b,un}}_{\ell,i,k,d,j}\; R^{\mathrm{a,un}}_{\ell,i,k,d}(\boldsymbol{\gamma}_\ell) = \left(\mathbf{G}^{\mathrm{a}}_\ell(\boldsymbol{\gamma}_\ell)\boldsymbol{\rho}^\star_\ell\right)_j, \quad j = 1, \dots, n, \tag{A.1a}$$

where $\star \in \{\mathrm{hf}, \mathrm{eq}\}$, $\boldsymbol{\gamma}_\ell = (\boldsymbol{\alpha}_\ell, \boldsymbol{\beta}_\ell, \mu_\ell)$ denotes the triplet of bubble coefficients, port coefficients and parameter, $\mathbf{G}^{\mathrm{a}}_\ell : \mathbb{R}^n \times \mathbb{R}^m \times \mathcal{P}_\ell \to \mathbb{R}^{n \times N^{\mathrm{e}}_\ell}$ is the matrix-valued function that satisfies $\left(\mathbf{G}^{\mathrm{a}}_\ell(\boldsymbol{\gamma}_\ell)\right)_{j,k} = \sum_{i,d} Z^{\mathrm{a,b,un}}_{\ell,i,k,d,j}\; R^{\mathrm{a,un}}_{\ell,i,k,d}(\boldsymbol{\gamma}_\ell)$ for $j = 1, \dots, n$ and $k = 1, \dots, N^{\mathrm{e}}_\ell$. The latter identity implies that

$$\widehat{\mathbf{R}}^{\mathrm{hf}}_\ell(\boldsymbol{\gamma}_\ell) - \widehat{\mathbf{R}}^{\mathrm{eq}}_\ell(\boldsymbol{\gamma}_\ell) = \mathbf{G}^{\mathrm{a}}_\ell(\boldsymbol{\gamma}_\ell)\left(\boldsymbol{\rho}^{\mathrm{hf}}_\ell - \boldsymbol{\rho}^{\mathrm{eq}}_\ell\right) \tag{A.1b}$$

For any $\ell \in \mathcal{L}$, EQ procedures aim to find a vector $\boldsymbol{\rho}^{\mathrm{eq}}_\ell \in \mathbb{R}^{N^{\mathrm{e}}_\ell}$ such that (i) $\boldsymbol{\rho}^{\mathrm{eq}}_\ell$ is as sparse as possible; (ii) the constant function is integrated accurately, that is

$$\Big|\sum_{k=1}^{N^{\mathrm{e}}_\ell} \rho^{\mathrm{eq}}_{\ell,k}\, |\mathtt{D}_{\ell,k}| - |\Omega^{\mathrm{a}}_\ell|\Big| \ll 1; \tag{A.2}$$

(iii) given the training set of triplets $\Sigma_\ell^{\text{train,eq}} := \{\boldsymbol{\gamma}_\ell^{(j)}\}_{j=1}^{n_{\text{train},\ell}}$, the residual is adequately calculated for all elements of the training set,

$$\left|\mathbf{J}_\ell^{\text{b}}(\boldsymbol{\gamma}_\ell)^{-1}\left(\widehat{\mathbf{R}}_\ell^{\text{hf}}(\boldsymbol{\gamma}_\ell) - \widehat{\mathbf{R}}_\ell^{\text{eq}}(\boldsymbol{\gamma}_\ell)\right)\right| \ll 1, \quad \text{where } \mathbf{J}_\ell^{\text{b}} := \partial_{\boldsymbol{\alpha}}\widehat{\mathbf{R}}_\ell^{\text{hf}}, \quad \forall\, \boldsymbol{\gamma}_\ell \in \Sigma_\ell^{\text{train,eq}}. \tag{A.3}$$

As discussed in section 5.3.3 (cf. (5.24)), the constant accuracy constraint (A.2) is designed to control the ℓ^1 norm of the weights that is related to the stability of the quadrature rule (see, e.g., [Huy09, section 2.3]); the constraints (A.3) are directly linked to the approximation error between the ROM estimate with HF quadrature and the hyper-reduced ROM estimate (cf. [YP19a, Proposition 3.2]).

We observe that the EQ problem can be recast as a sparse representation problem of the form

$$\min_{\boldsymbol{\rho}\in\mathbb{R}^{N_\ell^{\text{e}}}} \|\boldsymbol{\rho}\|_{\ell^0}, \quad \text{s. t.} \quad \|\mathbf{C}_\ell^{\text{eq}}\left(\boldsymbol{\rho}_\ell^{\text{hf}} - \boldsymbol{\rho}_\ell^{\text{eq}}\right)\|_2 \leq tol_{\text{eq}}, \tag{A.4}$$

where $\|\boldsymbol{\rho}\|_{\ell^0}$ is the ℓ^0 norm that counts the number of non-zero entries in the vector $\boldsymbol{\rho}$, $\mathbf{C}_\ell^{\text{eq}}$ is a suitable matrix that can be readily derived from (A.2) and (A.3), and tol_{eq} is a suitable tolerance. Problem (A.4) is NP hard; however, several effective approximate strategies have been proposed in the literature to determine parsimonious quadrature rules for MOR applications, [FCA15; YP19a; Cha+17; MAB22]. In this work, we resort to the non-negative least-square algorithm implemented in the Matlab routine `lsqnonneg`, which takes as input the matrix $\mathbf{C}_\ell^{\text{eq}}$, the vector $\mathbf{b}_\ell^{\text{eq}} := \mathbf{C}_\ell^{\text{eq}}\boldsymbol{\rho}_\ell^{\text{hf}}$ and the tolerance tol_{eq}, and returns the sparse quadrature rule.

Appendix B

Proofs

B.1 Proof of Proposition 1

Proof. Let $u^\star$ be the solution to (5.26). Then, we find

$$a(u^\star|_{\Omega_i}, v) \overset{(5.27)}{=} a(u^\star, v^{\text{ext}}) = f(v^{\text{ext}}) = f(v) \;\; \forall\, v \in \mathcal{X}_{i,0};$$

therefore, $u^\star|_{\Omega_i} = T_i u^\star|_{\Gamma_i} + G_i f$. The latter implies that $\lambda^\star = (u^\star|_{\Gamma_1}, u^\star|_{\Gamma_2})$ satisfies

$$\lambda^\star - E\lambda^\star - Gf = (u^\star|_{\Gamma_1} - u^\star|_{\Gamma_1},\;\; u^\star|_{\Gamma_2} - u^\star|_{\Gamma_2}) = 0,$$

and thus that $\lambda^\star$ solves (5.30).

Let $\lambda^\star$ satisfy (5.30). We define $u_i^\star = T_i\lambda_i^\star + G_i f$ for $i = 1, 2$. If we define the space $\mathcal{X}_{1,2}^0 = \{v|_{\Omega_1\cap\Omega_2} : v \in \mathcal{X},\; v|_{\Gamma_1\cup\Gamma_2} = 0\}$, we observe that $u_1^\star, u_2^\star$ satisfy

$$u_i^\star|_{\Gamma_1} = \lambda_1^\star,\;\; u_i^\star|_{\Gamma_2} = \lambda_2^\star,\;\; a(u_i^\star, v) = f(v) \quad \forall\, v \in \mathcal{X}_{1,2}^0, \qquad i = 1, 2. \tag{B.1}$$

Since $a : \mathcal{X}_{1,2}^0 \times \mathcal{X}_{1,2}^0 \to \mathbb{R}$ is coercive, the solution to (B.1) exists and is unique: therefore, $u_1^\star = u_2^\star$ in $\Omega_1 \cap \Omega_2$. In particular, if we define $u^\star = \sum_{i=1}^2 u_i^\star$, we have $u^\star|_{\Omega_i} = u_i^\star$ for $i = 1, 2$.

Given $v \in \mathcal{X}$, we have $v\phi_i \in \mathcal{X}_{i,0}$, since, by construction, $\operatorname{supp}\phi_i \subset \overline{\Omega}_i$. We thus have

$$a(u^\star, v) = \sum_{i=1} a(u^\star, \phi_i v) = \sum_{i=1} a(u^\star|_{\Omega_i}, \phi_i v) = \sum_{i=1} a(u_i^\star, \phi_i v) = \sum_{i=1} f(\phi_i v) = f(v),$$

which is the desired result. □

B.2 Proof of Proposition 2

Proof. Continuity of a_{p} follows from the continuity of the trace operators, and the local operators T_1, T_2. We omit the details. To prove inf-sup stability of the problem, we resort to the Fredholm's alternative: since T is compact, provided that $\nu = 1$ is not an eigenvalue of T, the equation $\lambda - T\lambda = f$ admits a unique solution for any $f \in \mathcal{U}$ and there exists a constant C such that $|||\lambda||| \le C|||f|||$ (see, e.g., [Sal16, Theorem 6.6.8]). It thus suffices to prove that $T\lambda = \lambda$ only holds for $\lambda = 0$.

Towards this end, we consider the problem:

$$\text{find } w \in \mathcal{X}_{1,2} :\; a(w, v) = 0 \;\forall\, v \in \mathcal{X}_{1,2}^0, \quad w|_{\Gamma_1} = \gamma_1,\;\; w|_{\Gamma_2} = \gamma_2,$$

with $\mathcal{X}_{1,2}^0 = \{v|_{\Omega_1\cap\Omega_2} : v \in \mathcal{X}\}$, and $\mathcal{X}_{1,2}^0 = \{v|_{\Omega_1\cap\Omega_2} : v \in \mathcal{X},\; v|_{\Gamma_1\cup\Gamma_2} = 0\}$. Since $T_1\lambda_1 = \lambda_1$ on Γ_1 by definition and $T_1\lambda_1 = \lambda_2$ on Γ_2 since $T\lambda = \lambda$, we have that

$T_1\lambda_1|_{\Omega_{1,2}} = w$; similarly, we find $T_2\lambda_2|_{\Omega_{1,2}} = w$. As observed in the proof of Proposition 1, there exists a unique solution to the problem $w \in \mathcal{X}_{1,2}$: this implies that $T_1\lambda_1|_{\Omega_{1,2}} = T_2\lambda_2|_{\Omega_{1,2}}$. Given the partition of unity ϕ_1, ϕ_2 associated with $\{\Omega_i\}_{i=1}^2$, we define the field $u = \sum_{i=1}^2 \phi_i T_i \lambda_i \in \mathcal{X}$, which satisfies $u|_{\Omega_i} = T_i\lambda_i$ for $i = 1, 2$. We observe that

$$a(u,v) = \sum_{i=1}^{2} a\left(u, \phi_i v\right) \overset{(5.27)}{=} \sum_{i=1}^{2} a\left(u|_{\Omega_i}, \phi_i v\right) = \sum_{i=1}^{2} a\left(T_i\lambda_i, \phi_i v\right) = 0.$$

Since a is coercive, we must have $u \equiv 0$ and thus $\lambda \equiv 0$. □

B.3 Proofs of the estimate (5.36)

Proof. We first introduce the orthonormal basis $\{\psi_i\}_{i=1}^M$ of $\mathcal{Z}^{\mathrm{p}}$; given $\lambda \in \mathcal{Z}^{\mathrm{p}}$, we denote by $\boldsymbol{\lambda} \in \mathbb{R}^M$ the corresponding vector of coefficients such that $\lambda = \sum_{i=1}^M (\boldsymbol{\lambda})_i \psi_i$. By straightforward calculations, we find that

$$\widetilde{\mathbf{A}}\,\widetilde{\boldsymbol{\lambda}} = \widetilde{\mathbf{F}}, \quad \widehat{\mathbf{A}}\,\widehat{\boldsymbol{\lambda}} = \widehat{\mathbf{F}}, \quad \text{with} \begin{cases} \left(\widetilde{\mathbf{A}}\right)_{i,j} = \langle (Id - T)\psi_j, (Id - T)\psi_i \rangle, & \left(\widetilde{\mathbf{F}}\right)_i = \langle (Id - T)\psi_i, Gf \rangle, \\ \left(\widehat{\mathbf{A}}\right)_{i,j} = \langle (Id - \widehat{T})\psi_j, (Id - \widehat{T})\psi_i \rangle, & \left(\widehat{\mathbf{F}}\right)_i = \langle (Id - \widehat{T})\psi_i, \widehat{G}f \rangle. \end{cases} \tag{B.2}$$

By straightforward calculations, we obtain

$$\widetilde{\boldsymbol{\lambda}} - \widehat{\boldsymbol{\lambda}} = \widetilde{\mathbf{A}}^{-1}\left(\widetilde{\mathbf{F}} - \widehat{\mathbf{F}} - \left(\widetilde{\mathbf{A}} - \widehat{\mathbf{A}}\right)\widehat{\boldsymbol{\lambda}}\right)$$

and thus

$$\|\widetilde{\boldsymbol{\lambda}} - \widehat{\boldsymbol{\lambda}}\|_2 \leq \underbrace{\|\widetilde{\mathbf{A}}^{-1}\|_2}_{=:(\mathrm{I})} \Big(\underbrace{\|\widetilde{\mathbf{A}} - \widehat{\mathbf{A}}\|_2}_{=:(\mathrm{II})} \underbrace{\|\widehat{\boldsymbol{\lambda}}\|_2}_{=:(\mathrm{III})} + \underbrace{\|\widetilde{\mathbf{F}} - \widehat{\mathbf{F}}\|_2}_{=:(\mathrm{IV})} \Big). \tag{B.3}$$

We estimate each term of (B.3) independently: combination of the estimates for (I)-(IV) leads to (5.36).

(I) Recalling the definition of α_{p}, we have $|||\psi - T\psi||| \geq \alpha_{\mathrm{p}}|||\psi|||$; therefore, we have

$$\boldsymbol{\psi}^T \widetilde{\mathbf{A}} \boldsymbol{\psi} = |||\psi - T\psi|||^2 \geq \alpha_{\mathrm{p}}^2 |||\psi|||^2 = \alpha_{\mathrm{p}}^2 \|\boldsymbol{\psi}\|_2^2,$$

which implies (I).

(II) By summing and subtracting $\langle (Id - T)\psi_j, (Id - \widehat{T})\psi_i \rangle$ to $\left| \left(\widetilde{\mathbf{A}}\right)_{i,j} - \left(\widehat{\mathbf{A}}\right)_{i,j} \right|$ and recalling the definitions of $\gamma_{\mathrm{p}}, \widehat{\gamma}_{\mathrm{p}}$ and ε_{T}, we obtain

$$\left| \left(\widetilde{\mathbf{A}}\right)_{i,j} - \left(\widehat{\mathbf{A}}\right)_{i,j} \right| \leq (\gamma_{\mathrm{p}} + \widehat{\gamma}_{\mathrm{p}})\, \varepsilon_{\mathrm{T}}, \quad \forall\, i, j = 1, \ldots, M.$$

Estimate (II) then follows by exploiting the fact that for any $M \times M$ matrix $\mathbf{A}$, we have $\|\mathbf{A}\|_2 \leq M \max_{i,j} |A_{i,j}|$.

(III) Estimate (III) follows directly from the properties of minimum residual formulations of inf-sup stable problems. Indeed, since the bilinear form a_{p} is continuous and inf-sup stable, using the Nečas theorem (see, e.g., [Sal16, Thm 6.42]) we have $\|\widehat{\boldsymbol{\lambda}}\|_2 = \left|\left|\left|\widehat{\lambda}\right|\right|\right| \leq \frac{1}{\widehat{\alpha}_{\mathrm{p}}} \left|\left|\left|\widehat{G}f\right|\right|\right|$ for all $f \in \mathcal{X}'$.

(IV) Proceeding as in (II), we find

$$\left|\left(\widetilde{\mathbf{F}}\right)_i - \left(\widehat{\mathbf{F}}\right)_i\right| \le \widehat{\gamma}_{\mathrm{p}}\varepsilon_{\mathrm{G}} + |||Gf|||\varepsilon_{\mathrm{T}}, \quad \forall\, i = 1,\dots,M,$$

and thus $\|\widetilde{\mathbf{F}} - \widehat{\mathbf{F}}\|_2 \le \sqrt{M}\|\widetilde{\mathbf{F}} - \widehat{\mathbf{F}}\|_\infty \le \sqrt{M}\left(\widehat{\gamma}_{\mathrm{p}}\varepsilon_{\mathrm{G}} + |||Gf|||\varepsilon_{\mathrm{T}}\right).$

□

B.4 Proof of (5.39)

Proof. For the two-subdomain problem, the OS2 statement (5.32) can be stated as:

$$\min_{(\psi_1,\psi_2)\in\mathcal{Z}_1^{\mathrm{p}}\times\mathcal{Z}_2^{\mathrm{p}}} \|\widehat{u}_1(\psi_1) - \widehat{u}_2(\psi_2)\|_{H^{1/2}(\Gamma_1\cup\Gamma_2)} \tag{B.4}$$

where $\widehat{u}_i(\psi_i) = \widehat{u}_i^{\mathrm{b}}(\psi_i) + E_i\psi_i$ and $\widehat{u}_i^{\mathrm{b}}(\psi_i) \in \mathcal{Z}_i^{\mathrm{b}}$ satisfies $a(\widehat{u}_i^{\mathrm{b}}(\psi_i) + E_i\psi_i, v) = f(v)$ for all $v \in \mathcal{Z}_i^{\mathrm{b}}$ and all $\psi_i \in \mathcal{Z}_i^{\mathrm{p}}$, for $i = 1, 2$. If we differentiate (B.4), we obtain the optimality conditions

$$\begin{aligned}&\left(\widehat{u}_1^{\mathrm{p}} - \chi_{\Gamma_1}\left(\widehat{u}_2^{\mathrm{b}}\left(\widehat{u}_2^{\mathrm{p}}\right) + E_2\widehat{u}_2^{\mathrm{p}}\right),\ \psi_1 - \chi_{\Gamma_1}\left(\widehat{u}_2^{\mathrm{b}}(\psi_2) + E_2\psi_2\right)\right)_{H^{1/2}(\Gamma_1)}\\ &+\left(\widehat{u}_2^{\mathrm{p}} - \chi_{\Gamma_2}\left(\widehat{u}_1^{\mathrm{b}}\left(\widehat{u}_1^{\mathrm{p}}\right) + E_1\widehat{u}_1^{\mathrm{p}}\right),\ \psi_2 - \chi_{\Gamma_2}\left(\widehat{u}_1^{\mathrm{b}}(\psi_1) + E_1\psi_1\right)\right)_{H^{1/2}(\Gamma_2)} = 0 \quad \forall\,\psi = (\psi_1,\psi_2) \in \mathcal{Z}_1^{\mathrm{p}}\times\mathcal{Z}_2^{\mathrm{p}},\end{aligned}$$

which can rewritten as in (5.39). □

B.5 Proofs of the estimates in section 5.4.5

In the following, we use the Taylor expansions:

$$e^x \sim 1+x+x^2, \quad \frac{1}{1-x} \sim 1+x+x^2, \quad (1+x)^{1/2} \sim 1+\frac{1}{2}x-\frac{1}{8}x^2, \quad (1+x)^2 \sim 1+2x, \tag{B.5}$$

which are valid for $|x| \ll 1$. We further employ the identiy:

$$\max\{|1-\sigma\lambda_1|,\ |1-\sigma\lambda_2|\} = \begin{cases} 1-\sigma\lambda_1 & \sigma < \frac{2}{\lambda_1+\lambda_2} \\ \sigma\lambda_2 - 1 & \sigma \ge \frac{2}{\lambda_1+\lambda_2} \end{cases} \tag{B.6}$$

that is valid for any $0 \le \lambda_1 \le \lambda_2$.

B.5.1 Problem (5.40a)

It is easy to verify that the local solutions $\widehat{u}_1, \widehat{u}_2$ satisfy

$$\widehat{u}_1(x,\beta) = x^2 - \frac{\delta^2}{1+\delta}(1+x) + \frac{\beta}{1+\delta}(1+x), \quad \widehat{u}_2(x,\beta) = x^2 - \frac{\delta^2}{1+\delta}(1-x) + \frac{\beta}{1+\delta}(1+x). \tag{B.7}$$

By imposing $\beta_1 = \widehat{u}_2(\delta,\beta_2)$ and $\beta_2 = \widehat{u}_1(\delta,\beta_1)$ we obtain the system of equations:

$$\mathbf{A}_\delta\,\boldsymbol{\beta} = \mathbf{F}_\delta, \quad \text{with } \mathbf{A}_\delta = \begin{bmatrix} 1 & -c_\delta \\ -c_\delta & 1 \end{bmatrix}, \ \mathbf{F}_\delta = \begin{bmatrix} d_\delta \\ d_\delta \end{bmatrix},$$

and $c_\delta = \frac{1-\delta}{1+\delta}$, $d_\delta = \frac{2\delta^3}{1+\delta}$. The matrix $\mathbf{A}_\delta$ is symmetric with positive eigenvalues $1 - c_\delta$ and $1 + c_\delta$; we thus have

$$\mathrm{cond}\,(\mathbf{A}_\delta) = \frac{1+c_\delta}{1-c_\delta} = \frac{1}{\delta}, \quad \alpha_\mathrm{p} = 1 - c_\delta = \frac{2\delta}{1+\delta}, \quad \gamma_\mathrm{p} = 1 + c_\delta = \frac{2}{1+\delta}.$$

which are (5.41b) and (5.41c).

Multiplicative OS corresponds to the application of the Gauss-Seidel iterative method to the linear system $\mathbf{A}_\delta\,\boldsymbol{\beta} = \mathbf{F}_\delta$. We thus find

$$\boldsymbol{\beta}^{(k)} = \mathbf{P}_\delta^{\mathrm{os}}\boldsymbol{\beta}^{(k-1)} + \mathbf{F}_\delta^{\mathrm{os}}, \quad \text{with } \mathbf{P}_\delta^{\mathrm{os}} = \begin{bmatrix} 0 & c_\delta \\ 0 & c_\delta^2 \end{bmatrix}, \quad \mathbf{F}_\delta^{\mathrm{os}} = \begin{bmatrix} d_\delta \\ d_\delta + c_\delta d_\delta \end{bmatrix}.$$

We can then verify that the spectral radius of $\mathbf{P}_\delta^{\mathrm{os}}$ is equal to

$$\rho_\delta^{\mathrm{os}} = c_\delta^2 \sim 1 - 4\delta.$$

The OS2 method for (5.40a) reads as

$$\min_{\boldsymbol{\beta}\in\mathbb{R}^2} \frac{1}{2} \sum_{x\in\{-\delta,\delta\}} \left(\widehat{u}_1(x,\beta_1) - \widehat{u}_2(x,\beta_2)\right)^2 = \frac{1}{2}\|\mathbf{A}_\delta\,\boldsymbol{\beta} - \mathbf{F}_\delta\|_2^2. \tag{B.8}$$

If we apply the gradient descent method to (B.8), we obtain

$$\boldsymbol{\beta}^{(k)} = \left(\mathbb{1} - \sigma\mathbf{A}_\delta^T\mathbf{A}_\delta\right)\boldsymbol{\beta}^{(k-1)} + \sigma\mathbf{A}_\delta^T\mathbf{F}_\delta.$$

By tedious calculations, we can verify that the eigenvalues of the transition matrix $\mathbb{1} - \sigma\mathbf{A}_\delta^T\mathbf{A}_\delta$ are equal to $1-\sigma(c_\delta+1)^2$ and $1-\sigma(c_\delta-1)^2$: recalling (B.6), we find that the spectral radius of the transition matrix is minimized by $\sigma = \frac{1}{c_\delta^2+1}$ and is equal to

$$\rho_\delta^{\mathrm{os2}} = \frac{2c_\delta}{c_\delta^2+1} \sim 1 - 4\delta^2.$$

B.5.2 Problem (5.40b)

The local solutions $\widehat{u}_1, \widehat{u}_2$ satisfy

$$\widehat{u}_1(x,\beta) = \beta\frac{e^{\gamma x} - e^{-\gamma}}{e^{\gamma\delta} - e^{-\gamma}}, \quad \widehat{u}_2(x,\beta) = \frac{e^{\gamma x} - e^{-\gamma\delta}}{e^{\gamma} - e^{-\gamma\delta}} + \beta\frac{e^{\gamma} - e^{\gamma x}}{e^{\gamma} - e^{-\gamma\delta}}. \tag{B.9}$$

Exploiting the Taylor expansions in (B.5), we obtain

$$\widehat{u}_1(-\delta,\beta) \sim \beta\left(1 - 2c_\gamma\delta + 2c_\gamma^2\delta^2\right), \quad \widehat{u}_2(\delta,\beta) \sim 2d_\gamma\delta - 2d_\gamma^2\delta^2 + \beta\left(1 - 2d_\gamma\delta + 2d_\gamma^2\delta^2\right)$$

where $c_\gamma := \frac{\gamma}{1-e^{-\gamma}}$ and $d_\gamma := \frac{c_\gamma}{e^\gamma}$. We thus find the (approximate) system of equations

$$\mathbf{A}_\delta\,\boldsymbol{\beta} = \mathbf{F}_\delta, \quad \text{with } \mathbf{A}_\delta = \begin{bmatrix} 1 & \left(-1 + 2d_\gamma\delta - 2d_\gamma^2\delta^2\right) \\ \left(-1 + 2c_\gamma\delta - 2c_\gamma^2\delta^2\right) & 1 \end{bmatrix}, \quad \mathbf{F}_\delta = \begin{bmatrix} 2d_\gamma\delta - 2d_\gamma^2\delta^2 \\ 0 \end{bmatrix}.$$

Therefore, the Gauss-Seidel transition matrix is approximately equal to

$$\mathbf{P}_\delta^{\mathrm{os}} \sim \begin{bmatrix} 0 & -1 + 2d_\gamma\delta \\ 0 & -\left(1 - 2d_\gamma\delta\right)\left(1 - 2c_\gamma\delta\right) \end{bmatrix}$$

and thus

$$\rho_\delta^{\mathrm{os}} \sim 1 - 2\left(c_\gamma + d_\gamma\right)\delta = 1 - 2\frac{e^\gamma + 1}{e^\gamma - 1}\gamma\delta.$$

On the other hand, the eigenvalues of $\mathbf{A}_\delta^T \mathbf{A}_\delta$ are approximately equal to

$$\lambda_1 \sim \frac{(c_\gamma + 2d_\gamma)^2}{4}\delta^2, \quad \lambda_2 \sim 4 - (2c_\gamma + 4d_\gamma)\delta,$$

and thus

$$\alpha_{\mathrm{p}} = \sqrt{\lambda_1} \sim \frac{4(e^\gamma + 2)\gamma\delta}{2(e^\gamma - 1)}, \quad \gamma_{\mathrm{p}} = \sqrt{\lambda_2} \sim 2.$$

Exploiting (B.6), we find that the approximately optimal choice of the step size σ is equal to $\sigma = \frac{1}{2}\left(1 + \left(\frac{c_\gamma}{2} + d_\gamma\right)\delta\right)$ and thus

$$\rho_\delta^{\mathrm{os}2} \sim 1 - \sigma\lambda_1 \sim 1 - \frac{1}{8}\left(c_\gamma + 2d_\gamma\right)^2\delta^2.$$

On the other hand, we obtain that the condition number of $\mathbf{A}_\delta$ is given by

$$\mathrm{cond}(\mathbf{A}_\delta) = \sqrt{\frac{\lambda_{\max}(\mathbf{A}_\delta^T\mathbf{A}_\delta)}{\lambda_{\min}(\mathbf{A}_\delta^T\mathbf{A}_\delta)}} \sim \frac{\sqrt{4 - (2c_\gamma + 4d_\gamma)\delta}}{\frac{(c_\gamma + 2d_\gamma)}{2}\delta} \sim \frac{4}{(c_\gamma + 2d_\gamma)\delta} = \frac{4(e^\gamma - 1)}{4(e^\gamma + 2)\gamma\delta}$$

Bibliography

[Aub91] N. Aubry. “On the hidden beauty of the proper orthogonal decomposition”. In: *Theoretical and Computational Fluid Dynamics* 2.5 (1991), pp. 339–352.

[Bar+04] M. Barrault et al. “An empirical interpolation method: application to efficient reduced-basis discretization of partial differential equations”. In: *Comptes Rendus Mathematique* 339.9 (2004), pp. 667–672.

[BBI09] M. Bergmann, C. H. Bruneau, and A. Iollo. “Enablers for robust POD models”. In: *Journal of Computational Physics* 228.2 (2009), pp. 516–538.

[BCI13] J. Baiges, R. Codina, and S. Idelsohn. “A domain decomposition strategy for reduced order models. Application to the incompressible Navier–Stokes equations”. In: *Computer Methods in Applied Mechanics and Engineering* 267 (2013), pp. 23–42.

[Ber+18] M. Bergmann et al. “A zonal Galerkin-free POD model for incompressible flows”. In: *Journal of Computational Physics* 352 (2018), pp. 301–325.

[BGH21] P. Buchfink, S. Glas, and B. Haasdonk. “Symplectic model reduction of Hamiltonian systems on nonlinear manifolds”. In: *arXiv preprint arXiv:2112.10815* (2021).

[BHL93] G. Berkooz, P. Holmes, and J.L. Lumley. “The proper orthogonal decomposition in the analysis of turbulent flows”. In: *Annual review of fluid mechanics* 25.1 (1993), pp. 539–575.

[Bin+11] P. Binev et al. “Convergence rates for greedy algorithms in reduced basis methods”. In: *SIAM journal on mathematical analysis* 43.3 (2011), pp. 1457–1472.

[BM97] I. Babuka and J. M. Melenk. “The partition of unity method”. In: *International journal for numerical methods in engineering* 40.4 (1997), pp. 727–758.

[BP22] A. Benaceur and A. Patera. “Port-Reduced Reduced-Basis Component Method for Steady State Navier–Stokes and Passive Scalar Equations”. In: (2022).

[BR06] T. J. Bridges and S. Reich. “Numerical methods for hamiltonian pdes”. In: *Journal of Physics A: mathematical and general* 39.19 (2006), p. 5287.

[BR09] P. B. Bochev and D. Ridzal. “An optimization-based approach for the design of PDE solution algorithms”. In: *SIAM journal on numerical analysis* 47.5 (2009), pp. 3938–3955.

[Bra03] M. Brand. “Fast online svd revisions for lightweight recommender systems”. In: *Proceedings of the 2003 SIAM international conference on data mining*. SIAM. 2003, pp. 37–46.

[BTI09] M. Buffoni, H. Telib, and A. Iollo. “Iterative methods for model reduction by domain decomposition”. In: 38 (2009), pp. 1160–1167.

[BTM22] J. Barnett, I. Tezaur, and A. Mota. "The Schwarz alternating method for the seamless coupling of nonlinear reduced order models and full order models". In: *arXiv preprint arXiv:2210.12551* (2022).

[Buf+12] A. Buffa et al. "A priori convergence of the greedy algorithm for the parametrized reduced basis method". In: *ESAIM: Mathematical modelling and numerical analysis* 46.3 (2012), pp. 595–603.

[Buh+20] A. Buhr et al. "Localized model reduction for parameterized problems". In: *Snapshot-Based Methods and Algorithms* (2020), pp. 245–306.

[Car+13] K. Carlberg et al. "The GNAT method for nonlinear model reduction: effective implementation and application to computational fluid dynamics and turbulent flows". In: *Journal of Computational Physics* 242 (2013), pp. 623–647.

[Cas+20] F. Casenave et al. "A nonintrusive distributed reduced-order modeling framework for nonlinear structural mechanicsApplication to elastoviscoplastic computations". In: *International journal for numerical methods in engineering* 121.1 (2020), pp. 32–53.

[Cas+22] A. de Castro et al. "A Novel Partitioned Approach for Reduced Order Model–Finite Element Model (ROM-FEM) and ROM-ROM Coupling". In: *arXiv preprint arXiv:2206.04736* (2022).

[CD16] A. Cohen and R. DeVore. "Kolmogorov widths under holomorphic mappings". In: *IMA Journal of Numerical Analysis* 36.1 (2016), pp. 1–12.

[CDM15] A. Corigliano, M. Dossi, and S. Mariani. "Model order reduction and domain decomposition strategies for the solution of the dynamic elastic–plastic structural problem". In: *Computer Methods in Applied Mechanics and Engineering* 290 (2015), pp. 127–155.

[CDV11] D. Cinquegrana, R.S. Donelli, and A. Viviani. "A hybrid method based on POD and domain decomposition to compute the 2-D aerodynamics flow field". In: *AIMETA, Bologna, Italy* (2011), pp. 1–10.

[CG17] G. Ciaramella and M. J. Gander. "Analysis of the parallel Schwarz method for growing chains of fixed-sized subdomains: Part I". In: *SIAM Journal on Numerical Analysis* 55.3 (2017), pp. 1330–1356.

[Cha+17] T. Chapman et al. "Accelerated mesh sampling for the hyper reduction of nonlinear computational models". In: *International Journal for Numerical Methods in Engineering* 109.12 (2017), pp. 1623–1654.

[Che+21a] S. Chen et al. "A reduced order Schwarz method for nonlinear multiscale elliptic equations based on two-layer neural networks". In: *arXiv preprint arXiv:2111.02280* (2021).

[Che+21b] Y. Chen et al. "An EIM-degradation free reduced basis method via over collocation and residual hyper reduction-based error estimation". In: *Jounral of Computational Physics* 444 (2021).

[CHL91] T. F. Chan, T. Y. Hou, and P. L. Lions. "Geometry related convergence results for domain decomposition algorithms". In: *SIAM Journal on Numerical Analysis* 28.2 (1991), pp. 378–391.

[CS10a] S. Chaturantabut and D. C. Sorensen. *A state space estimate for POD-DEIM Nonlinear Model Reduction*. Tech. rep. Technical report, 2010.

[CS10b] S. Chaturantabut and D. C. Sorensen. "Nonlinear model reduction via discrete empirical interpolation". In: *SIAM Journal on Scientific Computing* 32.5 (2010), pp. 2737–2764.

[DB15] M. DElia and P. B. Bochev. "Optimization–based coupling of nonlocal and local diffusion models". In: *MRS Online Proceedings Library (OPL)* 1753 (2015).

[De 96] R. De Boer. "Highlights in the historical development of the porous media theory: toward a consistent macroscopic theory". In: (1996).

[DH79] L.M. Delves and C.A. Hall. "An implicit matching principle for global element calculations". In: 23 (1979), pp. 223–234.

[DY22] E. Du and M. Yano. "Efficient hyperreduction of high-order discontinuous Galerkin methods: element-wise and point-wise reduced quadrature formulations". In: *Journal of Computational Physics* (2022), p. 111399.

[Far+14] C. Farhat et al. "Dimensional reduction of nonlinear finite element dynamic models with finite rotations and energy-based mesh sampling and weighting for computational efficiency". In: *nternational journal for numerical methods in engineering* (2014).

[Far+21] C. Farhat et al. "Computational bottlenecks for PROMs: Pre-computation and hyperreduction". In: *Handbook on Model Order Reduction. Volume 2: Snapshot-Based Methods and Algorithms. De Gruyter* 2 (2021), pp. 181–244.

[FCA15] C. Farhat, T. Chapman, and P. Avery. "Structure-preserving, stability, and accuracy properties of the energy-conserving sampling and weighting method for the hyper reduction of nonlinear finite element dynamic models". In: *International Journal for Numerical Methods in Engineering* 102.5 (2015), pp. 1077–1110.

[FG20] H. Florez and E. Gildin. "Global/local model order reduction in coupled flow and linear thermal-poroelasticity". In: *Computational Geosciences* 24.2 (2020), pp. 709–735.

[Fic+18] L. Fick et al. "A stabilized POD model for turbulent flows over a range of Reynolds numbers: Optimal parameter sampling and constrained projection". In: *Journal of Computational Physics* 371 (2018), pp. 214–243. ISSN: 0021-9991. DOI: https://doi.org/10.1016/j.jcp.2018.05.027. URL: http://www.sciencedirect.com/science/article/pii/S0021999118303279.

[Fri+18] F. Fritzen et al. "An algorithmic comparison of the hyper-reduction and the discrete empirical interpolation method for a nonlinear thermal problem". In: *Mathematical and computational applications* 23.1 (2018), p. 8.

[GL00] M. D. Gunzburger and H. K. Lee. "An optimization-based domain decomposition method for the Navier–Stokes equations". In: *SIAM Journal on Numerical Analysis* 37.5 (2000), pp. 1455–1480.

[GP05] M. A. Grepl and A. T. Patera. "A posteriori error bounds for reduced-basis approximations of parametrized parabolic partial differential equations". In: *ESAIM: Mathematical Modelling and Numerical Analysis* 39.1 (2005), pp. 157–181.

[GPK99] M.D. Gunzburger, J.S. Peterson, and H. Kwon. "An optimization based domain decomposition method for partial differential equations". In: *Computers & Mathematics with Applications* 37.10 (1999), pp. 77–93.

[GPS07] M. D. Gunzburger, J. S. Peterson, and J. N. Shadid. "Reduced-order modeling of time-dependent PDEs with multiple parameters in the boundary data". In: *Computer methods in applied mechanics and engineering* 196.4-6 (2007), pp. 1030–1047.

[Gra09a] S. Granet. "Modéles de comportement THHM". In: (2009). Official Documentation of Code_Aster.

[Gra09b] S. Granet. "Modélisations THHM, généralités et algorithmes". In: (2009). Official Documentation of Code_Aster.

[Gre+07] M. A. Grepl et al. "Efficient reduced-basis treatment of nonaffine and nonlinear partial differential equations". In: *ESAIM: Mathematical Modelling and Numerical Analysis* 41.3 (2007), pp. 575–605.

[GWW17] Y. Gong, Q. Wang, and Z. Wang. "Structure-preserving Galerkin POD reduced-order modeling of Hamiltonian systems". In: *Computer Methods in Applied Mechanics and Engineering* 315 (2017), pp. 780–798.

[GWZ14] M. D. Gunzburger, C. G. Webster, and G. Zhang. "Stochastic finite element methods for partial differential equations with random input data". In: *Acta Numerica* 23 (2014), pp. 521–650.

[Haa13] B. Haasdonk. "Convergence rates of the pod–greedy method". In: *ESAIM: Mathematical Modelling and Numerical Analysis* 47.3 (2013), pp. 859–873.

[Haa17] B. Haasdonk. "Reduced basis methods for parametrized PDEs–a tutorial introduction for stationary and instationary problems". In: *Model reduction and approximation: theory and algorithms* 15 (2017), p. 65.

[HCC21] C. Hoang, Y. Choi, and K. Carlberg. "Domain-decomposition least-squares Petrov–Galerkin (DD-LSPG) nonlinear model reduction". In: *Computer Methods in Applied Mechanics and Engineering* 384 (2021), p. 113997.

[HCF17] J. A. Hernandez, M. A. Caicedo, and A. Ferrer. "Dimensional hyper-reduction of nonlinear finite element models via empirical cubature". In: *Computer methods in applied mechanics and engineering* 313 (2017), pp. 687–722.

[HK10] R. Herzog and K. Kunisch. "Algorithms for PDE-constrained optimization". In: *GAMM-Mitteilungen* 33.2 (2010), pp. 163–176.

[HKP13] D. B. P. Huynh, D. J. Knezevic, and A. T. Patera. "A static condensation reduced basis element method: approximation and a posteriori error estimation". In: *ESAIM: Mathematical Modelling and Numerical Analysis* 47.1 (2013), pp. 213–251.

[HLR18] C. Himpe, T. Leibner, and S. Rave. "Hierarchical approximate proper orthogonal decomposition". In: *SIAM Journal on Scientific Computing* 40.5 (2018), A3267–A3292.

[HO08] B. Haasdonk and M. Ohlberger. "Reduced basis method for finite volume approximations of parametrized linear evolution equations". In: *ESAIM: Mathematical Modelling and Numerical Analysis* 42.2 (2008), pp. 277–302.

[HPR21] J. S. Hesthaven, C. Pagliantini, and N. Ripamonti. "Structure-preserving model order reduction of Hamiltonian systems". In: *arXiv preprint arXiv:2109.12367* (2021).

[HPR22] J. S. Hesthaven, C. Pagliantini, and N. Ripamonti. "Rank-adaptive structure-preserving model order reduction of Hamiltonian systems". In: *ESAIM: Mathematical Modelling and Numerical Analysis* 56.2 (2022), pp. 617–650.

[HRS+16] J. S. Hesthaven, G. Rozza, B. Stamm, et al. *Certified reduced basis methods for parametrized partial differential equations*. Vol. 590. Springer, 2016.

[Huy09] D. Huybrechs. "Stable high-order quadrature rules with equidistant points". In: *Journal of computational and applied mathematics* 231.2 (2009), pp. 933–947.

[IL14] A. Iollo and D. Lombardi. "Advection modes by optimal mass transfer". In: *Physical Review E* 89.2 (2014), p. 022923.

[IQR16] L. Iapichino, A. Quarteroni, and G. Rozza. "Reduced basis method and domain decomposition for elliptic problems in networks and complex parametrized geometries". In: *Computers & Mathematics with Applications* 71.1 (2016), pp. 408–430.

[IST22] A. Iollo, G. Sambataro, and T. Taddei. "An adaptive projection-based model reduction method for nonlinear mechanics with internal variables: Application to thermo-hydro-mechanical systems". In: *International Journal for Numerical Methods in Engineering* 123.12 (2022), pp. 2894–2918.

[KA12] I. Kalashnikova and S. Arunajatesan. "A Stable Galerkin Reduced Order Model (ROM) for Compressible Flow". In: *10th World Congress for Computational Mechanics (WCCM)*. 2012, pp. 2012–18407.

[Ker+13] P. Kerfriden et al. "A partitioned model order reduction approach to rationalise computational expenses in nonlinear fracture mechanics". In: *Computer methods in applied mechanics and engineering* 256 (2013), pp. 169–188.

[KOH11] S. Kaulmann, M. Ohlberger, and B. Haasdonk. "A new local reduced basis discontinuous Galerkin approach for heterogeneous multiscale problems". In: *Comptes Rendus Mathematique* 349.23-24 (2011), pp. 1233–1238.

[LA03] P. LeGresley and J. Alonso. "Dynamic domain decomposition and error correction for reduced order models". In: *41st Aerospace Sciences Meeting and Exhibit*. 2003, p. 250.

[Lar+20] Y. Larion et al. "Building a certified reduced basis for coupled thermo-hydro-mechanical systems with goal-oriented error estimation". In: *Computational mechanics* 66.3 (2020), pp. 559–573.

[Lar+22] Y. Larion et al. "Using Reduced Basis Approximation for Efficient Surrogate-Based Inverse Identification of Thermo-Hydro-Mechanical Parameters from an In Situ Heating Test". In: *Rock mechanics and rock engineering* 55.9 (2022), pp. 5739–5757.

[Las+14] T. Lassila et al. "Model order reduction in fluid dynamics: challenges and perspectives". In: *Reduced Order Methods for modeling and computational reduction* (2014), pp. 235–273.

[LC20] K. Lee and K.T. Carlberg. "Model reduction of dynamical systems on nonlinear manifolds using deep convolutional autoencoders". In: *Journal of Computational Physics* 404 (2020), p. 108973.

[LF17] M. Leuschner and F. Fritzen. "Reduced order homogenization for viscoplastic composite materials including dissipative imperfect interfaces". In: *Mechanics of Materials* 104 (2017), pp. 121–138.

[LH74] C. L. Lawson and R. J. Hanson. *Solving least squares problems*. Vol. 161. Siam, 1974.

[Li+19] K. Li et al. "D3M: A deep domain decomposition method for partial differential equations". In: *IEEE Access* 8 (2019), pp. 5283–5294.

[Lin+22] P. Lindsay et al. "Preconditioned least-squares petrov-galerkin reduced order models". In: *arXiv preprint arXiv:2203.12180* (2022).

[Lio88] P. L. Lions. "On the Schwarz alternating method. I". In: *First international symposium on domain decomposition methods for partial differential equations*. Vol. 1. Paris, France. 1988, p. 42.

[LK10] O. Le Matre and O. M. Knio. *Spectral methods for uncertainty quantification: with applications to computational fluid dynamics*. Springer Science & Business Media, 2010.

[Luc+01] D. Lucia et al. "Reduced order modeling for a one-dimensional nozzle flow with moving shocks". In: *15th AIAA computational fluid dynamics conference*. 2001, p. 2602.

[MAB22] M. Manucci, J. V. Aguado, and D. Borzacchiello. "Sparse Data-Driven Quadrature Rules via ℓ^p-Quasi-Norm Minimization". In: *Computational Methods in Applied Mathematics* 22.2 (2022), pp. 389–411.

[Mad+15] Y. Maday et al. "A parameterized-background data-weak approach to variational data assimilation: formulation, analysis, and application to acoustics". In: *International Journal for Numerical Methods in Engineering* 102.5 (2015), pp. 933–965.

[MC21] S. McBane and Y. Choi. "Component-wise reduced order model lattice-type structure design". In: *Computer methods in applied mechanics and engineering* 381 (2021), p. 113813.

[MNT04] K. Madsen, H.B. Nielsen, and O. Tingleff. *Methods for non-linear least square problems*. Department of Informatics and Mathematical Modelling, Technical University of Denmark, 2004.

[MRC13] B. Miled, D. Ryckelynck, and S. Cantournet. "A priori hyper-reduction method for coupled viscoelastic–viscoplastic composites". In: *Computers & Structures* 119 (2013), pp. 95–103.

[MTP22] A. Mota, I. Tezaur, and G. Phlipot. "The Schwarz alternating method for transient solid dynamic". In: *International Journal for Numerical Methods in Engineering* in press (2022).

[Nas+22] C. Nasika et al. "Towards real time assessment of earthfill dams via Model Order Reduction". In: *Finite elements in analysis and design* 199 (2022), p. 103666.

[NW06] J. Nocedal and S. J. Wright. *Numerical optimization*. Springer, 2006.

[Peg+21] L. Pegolotti et al. "Model order reduction of flow based on a modular geometrical approximation of blood vessels". In: *Computer Methods in Applied Mechanics and Engineering* 380 (2021), p. 113762.

[PR22] E. J Parish and F. Rizzi. "On the impact of dimensionally-consistent and physics-based inner products for POD-Galerkin and least-squares model reduction of compressible flows". In: *arXiv preprint arXiv:2203.16492* (2022).

[Pru+02] C. PrudHomme et al. "Reliable real-time solution of parametrized partial differential equations: Reduced-basis output bound methods". In: *J. Fluids Eng.* 124.1 (2002), pp. 70–80.

[QMN15] A. Quarteroni, A. Manzoni, and F. Negri. *Reduced basis methods for partial differential equations: an introduction*. Vol. 92. Springer, 2015.

[Qua17] A. Quarteroni. *Numerical models for differential problems*. Springer, 2017.

[QV99] A. Quarteroni and A. Valli. *Domain decomposition methods for partial differential equations*. BOOK. Oxford University Press, 1999.

[RHP08] G. Rozza, D. B. P. Huynh, and A. T. Patera. "Reduced basis approximation and a posteriori error estimation for affinely parametrized elliptic coercive partial differential equations". In: *Archives of Computational Methods in Engineering* 15.3 (2008), pp. 229–275.

[Rif+21] S. Riffaud et al. "The DGDD method for reduced-order modeling of conservation laws". In: *Journal of Computational Physics* 437 (2021), p. 110336.

[Roz+19] G. Rozza et al. "Basic ideas and tools for projection-based model reduction of parametric partial differential equations". In: *arXiv preprint arXiv:1911.08954* (2019).

[RR14] A. Radermacher and S. Reese. "Model reduction in elastoplasticity: proper orthogonal decomposition combined with adaptive sub-structuring". In: *Computational Mechanics* 54.3 (2014), pp. 677–687.

[Ryc05] D. Ryckelynck. "A priori hyperreduction method: an adaptive approach". In: *Journal of computational physics* 202.1 (2005), pp. 346–366.

[Ryc09] D. Ryckelynck. "Hyper-reduction of mechanical models involving internal variables". In: *International Journal for Numerical Methods in Engineering* 77.1 (2009), pp. 75–89.

[Sal16] S. Salsa. *Partial differential equations in action: from modelling to theory*. Vol. 99. Springer, 2016.

[SH11] M. Slawski and M. Hein. "Sparse recovery by thresholded non-negative least squares". In: *Advances in neural information processing systems* 24 (2011).

[Sir87] L. Sirovich. "Turbulence and the dynamics of coherent structures. I.Coherent structures". In: *Quarterly of applied mathematics* 45.3 (1987), pp. 561–571.

[Smi97] B. F. Smith. "Domain decomposition methods for partial differential equations". In: *Parallel Numerical Algorithms*. Springer, 1997, pp. 225–243.

[SP16] K. Smetana and A. T. Patera. "Optimal local approximation spaces for component-based static condensation procedures". In: *SIAM J. Sci. Comput.* 38.5 (2016), A3318–A3356.

[ST22] K. Smetana and T. Taddei. "Localized model reduction for nonlinear elliptic partial differential equations: localized training, partition of unity, and adaptive enrichment". In: *arXiv preprint arXiv:2202.09872* (2022).

[Tad17] T. Taddei. "Model order reduction methods for data assimilation; state estimation and structural health monitoring". PhD thesis. Massachusetts Insitute of Technology, 2017.

[Tad19] T. Taddei. "An offline/online procedure for dual norm calculations of parameterized functionals: empirical quadrature and empirical test spaces". In: *Advances in Computational Mathematics* 45.5-6 (2019), pp. 2429–2462.

[Tad20] T. Taddei. "A registration method for model order reduction: data compression and geometry reduction". In: *SIAM Journal on Scientific Computing* 42.2 (2020), A997–A1027.

[TW04] A. Toselli and O. Widlund. *Domain decomposition methods-algorithms and theory*. Vol. 34. Springer Science & Business Media, 2004.

[TZ21] T. Taddei and L. Zhang. "A discretize-then-map approach for the treatment of parameterized geometries in model order reduction". In: *Computer Methods in Applied Metunics and Engineering* 384 (2021), p. 113956.

[Ver+03] K. Veroy et al. "A posteriori error bounds for reduced-basis approximation of parametrized noncoercive and nonlinear elliptic partial differential equations". In: *16th AIAA Computational Fluid Dynamics Conference*. 2003, p. 3847.

[Vol11] S. Volkwein. "Model reduction using proper orthogonal decomposition". In: *Lecture Notes, Institute of Mathematics and Scientific Computing, University of Graz. see math.uni-konstanz.de/numerik/personen/volkwein/teaching/POD-Vorlesung.pdf* 1025 (2011).

[Wil06] K. Willcox. "Unsteady flow sensing and estimation via the gappy proper orthogonal decomposition". In: *Computers & fluids* 35.2 (2006), pp. 208–226.

[WST09] M. Wicke, M. Stanton, and A. Treuille. "Modular bases for fluid dynamics". In: *ACM Transactions on Graphics (TOG)* 28.3 (2009), pp. 1–8.

[XZ03] J. Xu and L. Zikatanov. "Some observations on Babuvska and Brezzi theories". In: *Numerische Mathematik* 94.1 (2003), pp. 195–202.

[Yan19] M. Yano. "Discontinuous Galerkin reduced basis empirical quadrature procedure for model reduction of parametrized nonlinear conservation laws". In: *Advances in Computational Mathematics* (2019), pp. 1–34.

[Yan21] M. Yano. "Model reduction in computational aerodynamics". In: *Handbook on Model Order Reduction. Volume 3: Applications. De Gruyter* (2021), pp. 201–236.

[YP19a] M. Yano and A. T. Patera. "An LP empirical quadrature procedure for reduced basis treatment of parametrized nonlinear PDEs". In: *Computer Methods in Applied Mechanics and Engineering* 344 (2019), pp. 1104–1123.

[YP19b] M. Yano and A. T. Patera. "An LP empirical quadrature procedure for reduced basis treatment of parametrized nonlinear PDEs". In: *Comput. Methods Appl. Mech. Engrg.* 344 (2019), pp. 1104–1123. ISSN: 0045-7825. DOI: 10.1016/j.cma.2018.02.028. URL: https://mathscinet.ams.org/mathscinet-getitem?mr=3912980.

[ZAF17] M. J. Zahr, P. Avery, and C. Farhat. "A multilevel projection-based model order reduction framework for nonlinear dynamic multiscale problems in structural and solid mechanics". In: *International Journal for Numerical Methods in Engineering* 112.8 (2017), pp. 855–881.